Investigation of Hydrodynamics, Heat Transfer and Drying Characteristics Along the Variable Cross-Sectional Riser of BFBs

A Thesis

Submitted in Partial Fulfilment of the Requirements

for the Award of the Degree of

Doctor of Philosophy

By

Hirakh Jyoti Das

Department of Mechanical Engineering

Indian Institute of Technology Guwahati

Guwahati - 781039, India

May 2022

Dedicated to my parents

Manju Das

&

Jyotish Das

भारतीय प्रौद्योगिकी संस्थान गुवाहाटी
INDIAN INSTITUTE OF TECHNOLOGY GUWAHATI

DECLARATION

I hereby certify that the work compiled in this dissertation is the outcome of the research work, performed by myself, else stated, under the guidance of **Prof. Pinakeswar Mahanta.**

Any part of this work has not been submitted for the award of any degree, diploma, associate fellowship, fellowship, or it's equivalent to any university or institution.

Hirakh Jyoti Das

Date: 09-05-2022

Hirakh Jyoti Das
Registration No. 156103030
Department of Mechanical Engineering
Indian Institute of Technology Guwahati

Department of Mechanical Engineering

भारतीय प्रौद्योगिकी संस्थान गुवाहाटी

INDIAN INSTITUTE OF TECHNOLOGY GUWAHATI

Certificate

It is certified that the work contained in the thesis entitled **"Investigation of Hydrodynamics, Heat Transfer and Drying Characteristics along the Variable Cross-sectional Dryer of BFBs"** submitted by **Hirakh Jyoti Das** to the Indian Institute of Technology Guwahati for the award of the degree of Doctor of Philosophy has been carried out under my supervision in the Department of Mechanical Engineering, Indian Institute of Technology Guwahati. This work has not been submitted elsewhere for the award of any other degree or diploma.

Date: 09-05-2022

Prof. Pinakeswar Mahanta
Professor
Department of Mechanical Engineering
Indian Institute of Technology Guwahati
Guwahati-781039, India

Acknowledgements

If I had worked single-handedly on the research reported in this thesis, I would have never been able to complete it. Herein, I would like to acknowledge all those who supported me in various ways during my doctoral study at the Indian Institute of Technology, Guwahati.

First and foremost, I would like to express my heartfelt gratitude to my supervisor, Prof. Pinakeswar Mahanta, who has unceasingly helped me in my research work with motivation, encouragement and colossal knowledge. His guidance has influenced my basic understanding of this domain up to a greater extent. Without his keen interest and support, I would not have put forth the best foot forward during the current research work. It has been a rewarding experience for me to work with him all these years, and he has inspired me enough in various aspects of research and life for years to come. I am also profoundly indebted to the Director of the Indian Institute of Technology Guwahati for providing such pleasing circumstances for the inception of my research career.

Besides my supervisor, I would like to express my deepest gratitude and humble respect to the doctoral committee members, Prof. Anoop K. Dass, Dr Pranab K. Mondal and Prof. V. S. Moholkar, for their valuable suggestions and informative remarks during the research activities, which have constantly engaged me towards undertaking a meaningful thesis work. I would also like to thank Prof. S. K. Dwivedi, Prof. S. Senthilvelan and Prof. K. S. R. Krishna Murthy, former and present Head of the Department of Mechanical Engineering, IIT Guwahati, and my Administrative Supervisor, Prof. Sukhomay Pal, for encouraging and support throughout my research. I would also like to thank all the faculty members and staff of the Department of Mechanical Engineering for their continued support of my research on various subjects, like material procurement and others.

Special thanks to Mr. N. K. Das, Mr. D. Chetri, Mr. M. Sarma, Mr. J. Kakati, Mr. Sanjib Sarma, Mr. R. Talukdar and Mr. Nip Borah, senior technicians and support staff of the Department of Mechanical Engineering and Central Workshop IIT Guwahati, for their invaluable assistance.

I would deeply thank all my fellow lab-mates in the fluidized bed group: Dr. Mallick, Dr. Saikia, Dr. Mahapatro, Dr. Singh, Mr. Plabon, Mr. Dhananjay, Mr. Sasankar, Ms Munmi and Mr. Rishiraj for all the enriching and meaningful conversations and sleepless nights we had to work together. Without this group, my journey perhaps would have been less enjoyable. From the bottom of my heart, I would like to thank Prof. Nachiketa Tripathi & family, Prof. Utpal

Barua & family, Prof. U. K. Saha & family, Pranjyoti, Nazrul, Birjit, Biswajeet, Dudul and Samar for their companion and for being a part of my small family making me feel like a home away from home. The journey would not have been so smooth without their heartfelt support in my rough times.

I would like to express my sincere gratitude to Dr. M. Syamlal, National Energy Technology laboratory, for giving me the opportunity to learn CFD on multiphase flow, especially for fluidized bed gas-solid flow. I would also like to acknowledge Dr. P. Kalita, Dr. D. K. Rabha, Dr. J. R. Pati, Dr. R. S. Patil, Dr. Shelke for their guidance and support in my student life.

I would also like to thank all the cleaning staff of the hostel as well as the Fluidized-bed lab and the staff of the mess of Dibang hostel for providing day to day needs during my stay at IIT Guwahati.

I would like to express my sincere thanks to Dr. Anita Madam for her continued support and motivation; without her guidance, the journey would not have been possible. I would also like to express my gratitude to Parijat Madam, Aahana, Ting-Tong. Last but not least; I owe my profound gratitude towards my parents Mr. Jyotish Das (Deuta), Mrs. Manju Das (Maa), Mr. Dipak Das (Dada), Mr. Diganta Baishya (Mama), Dr. Mrinal Baishya (Mama), Mr. Utpal Baishya (Mama), Mrs. Barnalee Thakuria, Mrs. Sarala Baishya (Mahi) and Mr. Dhiren Baishya (Maha) for their continuous guidance, and support throughout.

Hirakh Jyoti Das

Abstract

Fluidized bed technology is one of the most promising technologies to harness power due to numerous advantages such as enhanced heat and mass transfer rate, fuel flexibility, supreme gas-solid mixing and emission control ability. Because of its enormous benefits, this technology has found widespread application in many industrial sectors, including the petroleum and refining industries, combustion and gasification industries of coal and biomass, drying industries of various agricultural and pharmaceutical products, etc. Various industrial groups have well recognized the conventional straight type of riser, and studies of various characteristics are well organized in open works of literature. But, the major hindrances associated with this type of riser are elutriation of fine particles, de-fluidization of coarser particles, agglomeration, segregation in size, back mixing of particles, high bed pressure drops and long residence time, etc. Spurred by these challenges, people started conducting research on the conical riser. However, the insight physics of this type of riser is scarcely reported. Therefore, it necessitates extensive research to comprehend the fluid flow behaviour, heat transfer characteristics, drying characteristics etc., when operated under varying parameters. Present work is an attempt to investigate conical bubbling fluidized beds so as to evaluate the bed hydrodynamics, heat transfer and drying characteristics. Hydrodynamics and heat transfer characteristics in three fluidized bed risers of atmospheric bubbling fluidized bed dryers of cone angles 0°, 5° and 10° are studied with sand as inventory initially was studied. Experimental results were validated with numerical results and found to be in good agreement. Furthermore, the drying characteristics of paddy granules have also been studied in these three risers. Finally, thermodynamic analysis of the drying process is carried out in the three risers for different operating parameters such as inlet air velocity, inlet air temperature, the mass of paddy, spiral and cone angle.

As a result of the present investigation, the bed pressure drop is found to decrease by 22.23%, with an increasing cone angle from 0° to 10°, when sand particles are used as bed inventory. Similarly, the bed pressure drop is also observed to decrease by 3.54% with the increase in air velocity. But the bed pressure drop increases by 30% and 24%, respectively, when the bed height and particle size of the sand increase. The interphase heat transfer coefficient is found to be increasing (6.25%) from 288 to 306 W/m^2K with the increase in cone angle. The interphase heat transfer coefficient also increases (8.1%) from 296 to 320 W/m^2K with the increase in air velocity from 1 to 2 m/s. For all operating conditions, the time required for

drying paddy grains in a conical fluidized bed dryer is almost half of the time required for drying the paddy grains in a conventional fluidized bed dryer. A conical bubbling fluidized bed dryer is found to be a better option for energy-saving than any other conventional fluidized bed dryer. The incorporation of a spiral reduces the drying time by 16.67% in a conical dryer of 10° cone angle. A 26.67% reduction in energy consumption of the blower is observed due to the higher degree of cone angle. The percentage of head rice is found to be 63% and 58% for the conical dryer with and without a spiral, respectively, while in conventional dryers, it is approximately 30 to 50% in Asian countries. The addition of a spiral increases the milling recovery by 3%. The EU and EUR are found to increase with the addition of a spiral and an increase in cone angle. The addition of a spiral improves the exergetic efficiency of drying processes in a dryer. It is also seen that there is an improvement in the exergetic efficiency with an increase in the cone angle. The maximum exergy efficiency is found to be 0.41 at an inlet air velocity of 2.1 m/s, inventory of 3 kg and inlet air temperature of 65℃ with spiral and higher cone angle.

Contents

Acknowledgement vii
Abstract ix
Contents xi
Nomenclature xvii
List of Figures xxi
List of Tables xxvii

Chapter 1: INTRODUCTION 1
1.1 MOTIVATION 2
1.2 IMPORTANCE OF DRYING 3
1.2.1 Constant rate period 4
1.2.2 Falling rate period 5
1.3 DIFFERENT TYPES OF DRYERS AND DRYING METHODS 5
1.3.1 Traditional drying 6
1.3.2 Solar drying 7
1.3.2.1 Direct solar dryers 7
1.3.2.2 Indirect solar dryers 8
1.3.2.3 Mixed solar dryers 9
1.3.3 Mechanical dryers 9
1.3.3.1 Heated air drying 9
1.3.3.2 Fluidized bed drying (FBD) 10
1.4 AIM OF THE PRESENT STUDY 11
1.5 OUTLINE OF THE THESIS 12
Chapter 2: LITERATURE REVIEW 13
2.1 INTRODUCTION 14
2.2 NUMERICAL SIMULATION OF FLUIDIZED BEDS 14
2.2.1 Hydrodynamic behaviour of conical fluidized beds 15
2.2.2 Heat transfer study on fluidized beds 18
2.3 EXPERIMENTAL STUDY OF FLUIDIZED BEDS 20
2.4 PARAMETRIC STUDY ON HYDRODYNAMICS AND HEAT TRANSFER 26
2.4.1 Effect of cone angle 27
2.4.2 Effect of static bed height 28

2.4.3 Effect of particle size 28
2.4.4 Effect of superficial air velocity 29
2.4.5 Effect of Particle density 29
2.5 DRYING PHENOMENA IN DIFFERENT TYPES OF DRYERS 30
2.6 ENERGY AND EXERGY ANALYSIS OF DRYING 36
2.7 RESEARCH GAP AND SCOPE FOR THE PRESENT INVESTIGATION 39
2.8 CHAPTER CONCLUSION 41
Chapter 3: NUMERICAL SIMULATION AND PROCEDURE 43
3.1 INTRODUCTION 44
3.2 NUMERICAL SIMULATION OF DRYERS 44
3.3 GOVERNING EQUATIONS AND THEIR CONSTITUTIVE RELATIONS 46
3.4 CFD MODEL AND FORMULATION 51
3.5 NUMERICAL SOLUTION PROCEDURE 52
3.6 CHAPTER CONCLUSION 54
Chapter 4: EXPERIMENTAL SETUP AND PROCEDURE 55
4.1 INTRODUCTION 56
4.2 EXPERIMENTAL SETUP 56
4.3 DETERMINATION OF MINIMUM FLUIDIZATION VELOCITY AND TERMINAL VELOCITY 58
4.4 EXPERIMENTAL PROCEDURE 60
4.5 THERMODYNAMIC ANALYSIS 63
4.5.1 Energy consumption 63
4.5.2 Energy analysis 64
4.5.3 Exergy analysis 65
4.6 MILLING AND DRYING QUALITY 67
4.7 CHAPTER CONCLUSION 68
Chapter 5: PERFORMANCE EVALUATION OF BFB DRYERS WITH SAND AS BED INVENTORY 69
5.1 INTRODUCTION 70
5.2 INTERDEPENDENCE OF GRID FOR 2-D MODEL 71
5.3 VALIDATION OF 2-D SIMULATION RESULTS WITH EXPERIMENTAL RESULTS 72
5.4 GRID AND TIME INDEPENDENCE FOR 3-D MODEL 75
5.5 INCORPORATION OF DRAG MODEL 76

5.6 HYDRODYNAMIC BEHAVIOUR OF THREE DRYERS 77
5.6.1 Pressure analysis in three fluidized bed dryers 77
5.6.2 Bed expansion ratio for three dryers 79
5.6.3 Radial solid volume fraction for three dryers 81
5.6.4 Solid velocity in the radial direction for three dryers 82
5.6.5 Granular temperature with solid volume fraction for three dryers 84
5.7 HEAT TRANSFER CHARACTERISTICS OF THREE DRYERS 85
5.7.1 Temperature distribution of three dryers 85
5.7.2 Interphase heat transfer for three dryers 86
5.8 HYDRODYNAMICS IN A CONICAL DRYER OF 10° CONE ANGLE 87
5.8.1 Bed expansion ratio of the conical dryer 87
5.8.2 Variation of pressure drop on the conical dryer 91
5.8.3 3-D simulation of radial solid volume fraction 94
5.8.4 3-D simulation of the solid and air velocity of the conical dryer 95
5.8.5 3-D simulation of radial granular temperature and solid volume fraction 96
5.9 HEAT TRANSFER CHARACTERISTICS IN A CONICAL DRYER OF 10° CONE ANGLE 97
5.9.1 Experimental result of temperature distribution 97
5.9.2 Validation of 3-D simulation temperature distribution with the experimental temperature distribution 99
5.9.3 Interphase heat transfer coefficient 100
5.10 CHAPTER CONCLUSION 100
Chapter 6: PERFORMANCE EVALUATION OF DRYING CHARACTERISTICS IN BFB DRYERS 103
6.1 INTRODUCTION 104
6.2 HYDRODYNAMIC BEHAVIOUR 104
6.3 DRYING CHARACTERISTICS 109
6.4 ENERGY CONSUMPTION 113
6.4.1 Thermal energy consumption 113
6.4.2 Energy consumption of blower (ECB) 116
6.5 DRYING AND MILLING QUALITY 119
6.6 THERMODYNAMIC (ENERGY AND EXERGY) ANALYSIS 120
6.6.1 Variation in energy utilization (EU) 121

6.6.2 Variation in energy utilization Ratio (EUR) 123
6.6.3 Variation in exergy utilization 125
6.6.4 Variation in exergetic efficiency 127
6.7 CHAPTER CONCLUSION 131
Chapter 7: ECONOMIC ANALYSIS OF DRYERS 133
7.1 INTRODUCTION 134
7.2 COST OF DRYING 134
7.2.1 Fixed cost 134
7.2.2 Variable cost 135
7.3 COST OF ENERGY 135
7.4 COST ANALYSIS OF THREE DRYERS 136
7.4.1 Cost analysis of conical dryer with cone angle 10° 136
7.4.2 Cost analysis of conical dryer with cone angle 5° 137
7.4.3 Cost analysis of cylindrical dryer ($\alpha = 0°$) 138
7.5 SENSITIVITY ANALYSIS 140
7.6 CHAPTER CONCLUSION 143
Chapter 8: CONCLUSIONS AND SCOPE FOR FUTURE WORK 145
8.1 CONCLUSIONS 146
8.1.1 Numerical and experimental investigation of hydrodynamic behaviour and heat transfer characteristics of sand particles in atmospheric bubbling fluidized bed dryers with different cone angles 147
8.1.2 Performance evaluation of drying characteristics of paddy particles in bubbling fluidized bed dryers with different operating parameters 149
8.1.3 Effect of spiral and cone angles on hydrodynamics and drying characteristics of paddy granules in bubbling fluidized bed dryers 151
8.1.4 Thermo-economic study of paddy drying on bubbling fluidized bed dryers 152
8.2 APPLICATION POTENTIAL 154
8.3 SCOPE FOR FUTURE WORK 154
References 155
Appendices 175
A Design of Distributor Plate 176
B Measurement of Mean Particle Size of Sand 179

C Specifications of different Equipments/Instruments used 181
D Calibration of Thermocouple 183
E Uncertainty Analysis 185
List of Publications 189

Nomenclature

Notations

A_c	:	Cross-sectional area of bed (m^2)
C_D	:	Drag coefficient (-)
C_{pg}	:	Specific heat capacity of gas (J/kg-K)
d_p	:	Particle diameter (m)
d_{pm}	:	Average diameter of various particles (m)
D_c	:	Mean diameter of cone (m)
D_{ij}	:	Rate of strain tensor for solid phase (s^{-1})
D_0	:	Inlet diameter of dryer (m)
D_1	:	Outlet diameter of dryer (m)
$\frac{D\overrightarrow{v_g}}{Dt}$	:	Substantial time derivative for gas velocity (m/s^2)
$\frac{D\overrightarrow{v_s}}{Dt}$	:	Substantial time derivative for solids velocity (m/s^2)
e_{ss}	:	Particle–particle restitution coefficient (-)
$\overrightarrow{F_{dg}}$	:	Drag forces for gas phase (N)
$\overrightarrow{F_{d,s}}$	:	Drag forces for solid phase (N)
$\overrightarrow{F_{l,g}}$	:	Lift force for gas phase (N)
$\overrightarrow{F_{l,s}}$	:	Lift force for solid phase (N)
$\overrightarrow{F_{vm,g}}$	:	Virtual masses for gas phase (N)
$\overrightarrow{F_{vm,s}}$	:	Virtual masses for solid phase (N)
g	:	Acceleration due to gravity (m/s^2)
G_f	:	Mass velocity of fluid at fluidization condition (kg/m^2h)
G_{mf}	:	Mass velocity of fluid at minimum fluidization condition (kg/m^2h)
$g_{0,ss}$	:	Solid radial distribution function (-)
h	:	Enthalpy (J)
H	:	Height of bed materials (m)

H_{max}	:	Particles expansion height (m)
H_s	:	Static bed height (m)
h_{sg}	:	Interphase heat transfer coefficient (W/m^2- K)
ΔH	:	Difference in height of water column (m)
I	:	Inventory (kg)
i	:	Current (A)
I_{2D}	:	Second invariant of the deviatory stress tensor (N/m^2)
k_g	:	Thermal conductivity of gas (W/m-K)
k_g^{eff}	:	Effective thermal conductivity of gas (W/m-K)
k_s	:	Thermal conductivity of solids (W/m-K)
k_s^{eff}	:	Effective thermal conductivity of solids (W/m-K)
$\dot{m}$	:	Mass flow rate (kg/s)
m	:	Mass (kg)
Nu_s	:	Solid-phase Nusselt number (-)
P	:	Pressure (Pa)
P_{fr}	:	Frictional pressure (Pa)
P_g	:	Gas-phase pressure (Pa)
∇P_g	:	Gas phase pressure gradient (Pa/m)
P_s	:	Solid-phase pressure (Pa)
ΔP	:	Pressure drop (Pa)
∇P_s	:	Solid phase pressure gradient (Pa/m)
Q	:	Heat input (J)
Q_c	:	Air flow rate (m^3/s)
Q_{sg}	:	Heat transfer between gas and solid phases (J)
R	:	Bed expansion ratio (-)
Re_s	:	Solid Reynold number (-)
$\overline{S_s}$	:	Solid-phase source term (N)
t	:	Drying time (s)
T	:	Temperature (K)

T_b : Bed temperature (K)

T_g : Temperature of gas (K)

T_s : Temperature of solids (K)

T_w : Wall temperature (K)

u Velocity at any section (m/s)

u^* : Non-dimensional air velocity (-)

U_l : Superficial liquid velocity (m/s)

U_{mf} : Minimum fluidization velocity (m/s)

U_0 : Superficial air velocity (m/s)

U_t Terminal velocity (m/s)

V : Input voltage (V)

$\vec{v}$: Velocity vector (m/s)

$\overrightarrow{v_g}$: Local velocity of the gas phase (m/s)

$v_{r,s}$: Relative velocity of solid particles (m/s)

$\overrightarrow{v_s}$: Local velocity of the solid phase (m/s)

$v_s'^2$: Mean square velocity of particles (m^2/s^2)

w : Humidity ratio (kg of moisture/kg of dry air)

W : Power consumer (J/s)

Greek symbols

ρ_s : Density of solid (kg/m^3)

ρ_g : Density of gas (kg/m^3)

ρ_m : Mixture density (kg/m^3)

ε_g : Voidage of gas (-)

ε_s : Volume fraction of the solid phase (-)

$\varepsilon_{s,cr}$: Critical solid volume fraction (-)

$\varepsilon_{s,max}$: Maximum solid volume fraction (-)

ϕ : Angle of internal friction (°)

ϕ_{gs} : Exchange of the fluctuating energy between gas and solid phases (J)

ϕ_s	:	Sphericity of solid particle (-)
ϕ_{sp}	:	Specularity coefficient (-)
β_{gs}	:	Drag coefficient between the gas and solid phase (-)
μ_g	:	Viscosity of gas (N-S/m^2)
μ_s	:	Solid viscosity (N-S/m^2)
$\overline{\overline{\tau_g}}$	:	Gas-phase stress tensor (N/m^2)
$\overline{\overline{\tau_s}}$	:	Solid-phase stress tensor (N/m^2)
k_{Θ_s}	:	Diffusion coefficient (m^2/s)
$k\Theta_s \nabla \Theta_s$	:	The transport of energy due to diffusion (-)
Θ_s	:	Granular temperature (m^2/s^2)
$\gamma\Theta_s$	:	Dissipation of energy due to collision (m^2/s^3)
γ_w	:	Collisional dissipation at the wall (kg/ms^3)
$(-p_s\bar{I} + \bar{\tau}_s): \nabla \overrightarrow{v_s}$	:	Generation of energy by the solid stress tensor (J)
β	:	Diameter ratio = d/D = 0.5
μ	:	Viscosity of air (N-S/m^2)
α	:	Cone angle (°)

Subscripts

av	:	Average
i	:	Inlet
dg	:	Drying gas
fg	:	Vaporisation
g	:	Gas
o	:	Outlet
p	:	Paddy
ref	:	Reference
s	:	Solid
v	:	Vapour

List of Figures

1.1	Drying Process	4
1.2	Schematic diagram of dryer classification	6
1.3	Traditional drying, (a) and (b) Traditional sun drying, (c) Field drying, and (d) Pavement drying	7
1.4	Direct solar dryer	8
1.5	Indirect solar dryer	8
1.6	Types of air heated dryers	10
1.7	Fluidized bed dryer	11
3.1	(a) Geometry, and (b) Mesh for the 2-D model	46
3.2	Configuration of mesh for the 3-D geometries, (a) $\alpha = 0°$, (b) $\alpha = 5°$, (c) $\alpha = 10°$, (d) $\alpha = 15°$ and (e) $\alpha = 20°$	46
4.1	Schematic diagram of an atmospheric bubbling fluidized bed	57
4.2	Configuration of three risers of bubbling fluidized bed, (a) $\alpha = 0°$, (b) $\alpha = 5°$, (c) $\alpha = 10°$, (d) $\alpha = 15°$ and (e) $\alpha = 20°$	57
4.3	An experimental rig of conical bubbling fluidized bed	57
4.4	Schematic of a conical dryer	58
4.5	An attachment of a spiral inside the dryer	63
5.1	Grid independence test at three different grid sizes for 2-D model (Radial solid volume fraction)	71
5.2	Bed pressure drop with different cone angles, (a) 2-D simulation and (b) experimental	72
5.3	Contours of time-averaged solid volume fraction, (a) $\alpha = 0°$, (b) $\alpha = 5°$, and (c) $\alpha = 10°$	73
5.4	Contours of time-averaged solid velocity, (a) $\alpha = 0°$, (b) $\alpha = 5°$, and (c) $\alpha = 10°$	73
5.5	Comparison of bed pressure drop between 2-D simulation and experimental results	73
5.6	Comparison of pressure drop along the height for three dryers, (a) $\alpha = 0°$, (b) $\alpha = 5°$, and (c) $\alpha = 10°$	74
5.7	Grid independence test for the 3-D model ($\alpha = 10°$)	75

5.8	Time independence test for the 3-D model (α = 5°)	76
5.9	Comparison of pressure drop among experimental, Syamlal-O'Brien and Gidaspow drag models	76
5.10	Contours of time-averaged radial solid volume fraction, (a) Syamlal-O'Brien drag model, and (b) Gidaspow drag model	76
5.11	Contours of time-averaged static pressure at different cone angles, (a) α = 0°, (b) α = 5°, and (c) α = 10°	77
5.12	Effect of cone angle on pressure drop along the height of three dryers	78
5.13	Effect of cone angle on bed pressure drop (3-D simulation and experimental)	78
5.14	Comparison of bed expansion ratio between 3-D simulation and experiment	79
5.15	Effect of cone angle on the axial solid volume fraction	80
5.16	Contours of time-averaged solid volume fraction at different cone angles, (a) α = 0°, (b) α = 5°, and (c) α = 10°	81
5.17	Contours of time-averaged solid volume fraction at an axial height of 10 cm at different cone angles, (a) α = 0°, (b) α = 5°, and (c) α = 10°	81
5.18	Effect of cone angle on radial solid volume fraction at the axial height of 10 cm	82
5.19	Contours of time-averaged solid velocity at an axial height of 10 cm at different cone angles, (a) α = 0°, (b) α = 5°, and (c) α = 10°	83
5.20	Effect of cone angle on radial solid velocity at the axial height of 10 cm	83
5.21	Radial granular temperature and solid volume fraction at the axial height of 10 cm for three dryers, (a) α = 0°, (b) α = 5°, and (c) α = 10°	84
5.22	Effect of cone angle on temperature distribution, (a) experimental, and (b) 3-D simulation	85
5.23	Comparison of temperature distribution between 3-D simulation and experiment	86
5.24	Effect of cone angle on interphase heat transfer coefficient	86
5.25	Effect of bed height on bed expansion ratio	88
5.26	Effect of particle size on bed expansion ratio	88

5.27	Effect of inlet air velocity on bed expansion ratio	89
5.28	Axial solid volume fraction at three inlet air velocities	90
5.29	Contours of time-averaged solid volume fraction at three inlet air velocities, (a) 1 m/s, (b) 1.5 m/s, and (c) 2 m/s	90
5.30	Bed pressure drop with bed height	91
5.31	Bed pressure drop with particle size	91
5.32	Bed pressure drop with inlet air velocity	92
5.33	Contours time-averaged static pressure at three inlet air velocities, (a) 1 m/s, (b) 1.5 m/s, and (c) 2 m/s	93
5.34	Effect of inlet air velocity on pressure drop along the height of the conical dryer with 10° cone angle	93
5.35	Contours of time-averaged solid volume fraction at 10 cm axial location at three air velocities, (a) 1 m/s, (b) 1.5 m/s, and (c) 2 m/s	94
5.36	Radial solid volume fraction with different inlet air velocities	94
5.37	Contours of time-averaged solid velocity at 10 cm axial location at three air velocities, (a) 1 m/s, (b) 1.5 m/s, and (c) 2 m/s	95
5.38	Radial solid velocity for three inlet air velocities at a 10 cm axial height	96
5.39	Radial air velocity for three inlet air velocities at a 10 cm axial height	96
5.40	Radial granular temperature and solid volume fraction at an axial height of 10 cm, (a) 1 m/s, (b) 1.5 m/s, and (c) 2 m/s	97
5.41	Bed temperature with bed height	98
5.42	Bed temperature with particle size	98
5.43	Bed temperature with inlet air velocity	98
5.44	Comparison of radial temperature distribution between 3-D simulation and experiment	99
5.45	Interphase heat transfer coefficient with inlet air velocity	100
6.1	Pressure drop along the height of a conical dryer with 10° cone angle at different superficial air velocities	105
6.2	Comparison of pressure drop (a) between sand and paddy particles and (b) between experimental and 3-D simulation	106
6.3	Pressure drop along the height of a conical dryer with 10° cone angle at different bed inventories	106

6.4	Effect of mixing of sand with paddy on pressure drop in a conical dryer with 10° cone angle	107
6.5	Effect of a spiral on pressure drop along the height of a conical dryer with 5° cone angle	108
6.6	Effect of a spiral on pressure drop along the height of a conical dryer with 10° cone angle	108
6.7	Effect of cone angle on pressure drop, (a) without spiral, and (b) with spiral	108
6.8	Effect of inlet air temperature on drying characteristics	109
6.9	Effect of superficial air velocity on drying characteristics	110
6.10	Effect of bed inventory on drying characteristics	110
6.11	Effect of mixing of sand with paddy on drying characteristics	111
6.12	Effect of a spiral on drying characteristics in a conical dryer with 5° cone angle	112
6.13	Effect of a spiral on drying characteristics in a conical dryer with 10° cone angle	112
6.14	Effect of cone angle on drying characteristics, (a) without a spiral, and (b) with a spiral	112
6.15	Thermal energy consumption at different inventories	113
6.16	Thermal energy consumption at different inlet air temperatures	114
6.17	Effect of a spiral on thermal energy consumption in a conical dryer with 5° cone angle at different inlet air temperatures	114
6.18	Effect of a spiral on thermal energy consumption in a conical dryer with 10° cone angle at different inlet air temperatures	114
6.19	Effect of cone angle on thermal energy consumption with a spiral at various inlet air temperatures	115
6.20	Effect of a spiral on thermal energy consumption in a conical dryer with 5° cone angle at various bed inventories	115
6.21	Effect of a spiral on thermal energy consumption in a conical dryer with 10° cone angle at various bed inventories	115
6.22	Effect of cone angle on thermal energy consumption with a spiral at various bed inventories	116

6.23	Effect of cone angle on ECB at (a) different inventories, and (b) different temperatures	116
6.24	Effect of a spiral on ECB in a conical dryer with 5° cone angle at various inlet air temperatures	117
6.25	Effect of a spiral on ECB in a conical dryer with 10° cone angle at various inlet air temperatures	117
6.26	Effect of a spiral on ECB in a conical dryer with 5° cone angle at various bed inventories	118
6.27	Effect of a spiral on ECB in a conical dryer with 10° cone angle at various bed inventories	118
6.28	Effect of cone angle on ECB with a spiral at (a) different inlet air temperatures, and (b) different bed inventories	118
6.29	Variation in EU with inlet air velocity	121
6.30	Variation in EU with the mass of paddy	121
6.31	Variation in EU with inlet air temperature	121
6.32	Variation in EU with and without a spiral	122
6.33	Variation in EU with the cone angle	123
6.34	Variation in EUR with inlet air velocity	124
6.35	Variation in EUR with the mass of paddy	124
6.36	Variation in EUR with inlet air temperature	124
6.37	Variation in EUR with and without a spiral	124
6.38	Variation in EUR with the cone angle	124
6.39	Variation in exergy utilization with inlet air velocity	125
6.40	Variation in exergy utilization with inlet air temperature	126
6.41	Variation in exergy utilization with the mass of paddy	126
6.42	Variation in exergy utilization with and without a spiral	126
6.43	Variation in exergy utilization with the cone angle	126
6.44	Variation in exergetic efficiency with inlet air velocity	127
6.45	Variation in exergetic efficiency with the mass of paddy	128
6.46	Variation in exergetic efficiency with inlet air temperature	128
6.47	Variation in exergetic efficiency with and without a spiral	129
6.48	Variation in exergetic efficiency with the cone angle	129

6.49	Variation in exergetic efficiency with varying inventory and air velocity at inlet air temperature of 55°C	130
6.50	Variation in exergetic efficiency with varying inventory and air velocity at inlet air temperature of 60°C	130
6.51	Variation in exergetic efficiency with varying inventory and air velocity at inlet air temperature of 65°C	130
6.52	Effect of cone angle on the variation in exergetic efficiency with and without a spiral	131
A.1	Design of distributor plate	178
D.1	Calibration curve for temperature readings	184

List of Tables

1.1	Importance of EMC required for different storage periods	5
3.1	Properties and characteristics of the air, sand and paddy used in the simulations	45
3.2	Parameters used in the simulations	53
3.3	Boundary conditions utilized for fluidized bed simulations	54
4.1	Dimensions of bubbling fluidized bed risers	57
4.2	Properties of air, sand and paddy particles	60
4.3	Input variable matrix considered for sand in the dryers	62
4.4	Input variable matrix considered for paddy drying in the dryers	62
4.5	Measurement methods for determining the nutritional contents of paddy grains	68
6.1	Nutritional contents of paddy at different drying times at 60°C temperature	119
6.2	Comparison of nutritional contents of dried paddy with the paddy cultivated in different places of India	119
6.3	Milling quality of paddy materials with spiral and without spiral	120
6.4	Experimental matrix for exergetic analysis	130
7.1	Different costs for the three dryers	136
7.2	One day expenditure for drying of paddy in the conical dryer ($\alpha = 10°$)	137
7.3	One day expenditure for drying of paddy in the conical dryer ($\alpha = 5°$)	138
7.4	One day expenditure for drying of paddy in the cylindrical dryer ($\alpha = 0°$)	139
7.5	Economics of dryers	139
7.6	Input variables, profit/loss and BEP forecast for sensitivity analysis	140
7.7	Input parameter matrix for sensitivity analysis	141
7.8	Sensitivity analysis of profit/year ($\alpha = 10°$)	141
7.9	Sensitivity analysis of profit/year ($\alpha = 5°$)	142
7.10	Sensitivity analysis of profit/year ($\alpha = 0°$)	142
7.11	Sensitivity analysis of BEP ($\alpha = 10°$)	142
7.12	Sensitivity analysis of BEP ($\alpha = 5°$)	143
7.13	Sensitivity analysis of BEP ($\alpha = 0°$)	143

B.1	Measurement of particle size	180
C.1	Specification of instruments	181
D.1	Temperature readings for calibration of thermocouples	183
E.1	Experimental parameters with uncertainty values	185

1

Introduction

1.1 Motivation

1.2 Importance of drying

1.3 Different types of dryers and drying methods

1.4 Aim of the present study

1.5 Organization of thesis

CHAPTER 1

INTRODUCTION

1.1 MOTIVATION

Cereal grain crops are cultivated in large quantities all over the world to meet the food requirement of humans. Amongst the cereal grains, rice is one of the most consumed food grains in Brazil, India, China, Japan and South-East Asian countries. Both traditional and mechanized cultivation of paddy is followed in these countries. It is the major source of caloric providers in developing nations. India is the 2nd highest rice-producing country in the world, followed by China [1]. As per the Indian agriculture survey- 2005, the current population growth rate requires rice production to reach 120 million tons by the year 2025, which will lead to massive pressure on the food supply. One of the challenges with rice grains is the significant amount of wastage at various stages of post-harvest. Nearly 33% of the total food produced is wasted [2]. However, the majority of this loss is due to inefficient drying techniques. Hence, drying is a challenging issue in paddy producing countries. Traditional sun-drying is common in villages, but it results in uneven drying, contamination with dust, soil and foreign particles and huge pilferage due to rodents and birds. Moreover, uneven drying leads to the formation of molds and the nutritional value of the rice is lost [3,4]. Solar assisted dryers are of low capacity. Some examples of high capacity mixed type solar as well as mechanical dryers [5] are continuous flow type LSU (Louisiana state university) dryer [6], super-heated steam drying [7] and spouted bed dryer [8]. But, major disadvantages of these dryers are difficulty in operating, lack of quality control and high operation cost. Therefore, to reduce the difficulties mentioned above, various researchers have carried out their research on the straight type of atmospheric bubbling fluidized bed dryers. These types of dryers are more efficient than conventional dryers and are also widely used in industries [9–11]. Apart from these, there are other benefits such as proper mixing of solid and gas, high heat and mass transfer rate, high thermal efficiency, ease of control of solids, low capital cost and easy handling [12,13]. Nevertheless, due to particle size and inventory changes, the following issues crop up: elutriation of fine particles, de-fluidization of coarser particles, agglomeration, segregation in size, back mixing of particles, high bed pressure drop, and short residence time. Due to these adverse effects of straight type of fluidized bed dryers, the heat transfer rate deteriorates, resulting in lower drying efficiency. Therefore, to overcome the drawbacks aforementioned, a re-design of a fluidized bed dryer is needed so that heat transfer

characteristics can be improved with drying characteristics. Keeping this in mind, the investigator made an attempt to design a conical fluidized bed dryer in which the area of cross-section is increasing along the height. However, very few researchers carried out research on conical beds to overcome the drawbacks mentioned above but is limited. An attempt is made to design and develop a new efficient atmospheric bubbling fluidized bed dryer to overcome the discrepancies associated with conventional atmospheric bubbling fluidized bed dryers with improved heat transfer and drying characteristics.

1.2 IMPORTANCE OF DRYING

Food grains have a considerable amount of moisture content on a wet basis during harvesting in tropical nations [14,15]. This level of moisture content makes the paddy susceptible to fungi and pest attacks, growth of the microorganism and a high rate of respiration. Due to the higher rate of respiration, grains may get damaged and change colour, resulting in a loss of nutritional values. Because of these adverse effects of the high moisture content, the selling price of grains may go down, resulting in considerable loss to the farmers and entrepreneurs. Hence, the reduction of moisture content up to the desired value is indispensable for its storage for a longer period [16–18].

Drying is a process of moisture removal from solid particles by evaporation. It helps to protect food from fungus and germs and makes it easier to be stored for a longer duration, with minimum damage. Different methods are adopted to dry the food granules, such as steam or freeze-drying, infrared drying, chemical drying, microwave drying, mechanical and fluidized bed assisted drying etc. The fluidization drying method is the most convenient and economical method in which hot air is circulated through the inlet of the dryer. The surface of the food grains is brought into contact with the hot air, which causes moisture to evaporate from the grain surface [19]. The hot air forms a steep thermal boundary layer with the solid surface resulting in both heat and mass transfer taking place simultaneously in the process leading to the decrease in the moisture content of the grain with time. The hot air required may be generated by heating the surface of the inlet pipe with an electric circuit. However, if a fluidized bed is used in conjunction with a thermal power unit, the waste heat may be used to generate hot air.

In order to understand the drying phenomenon, a typical drying curve is shown in Fig. 1.1, in which the moisture content of particles decreases over time [20]. There are two phases to the drying process. In the first phase, the moisture is removed from the surface of the particles, and

in the second phase, the internal moisture from the particles is removed. Two drying rules of operation can be seen in this curve: (1) constant rate period A-B and (2) Falling rate period B-C.

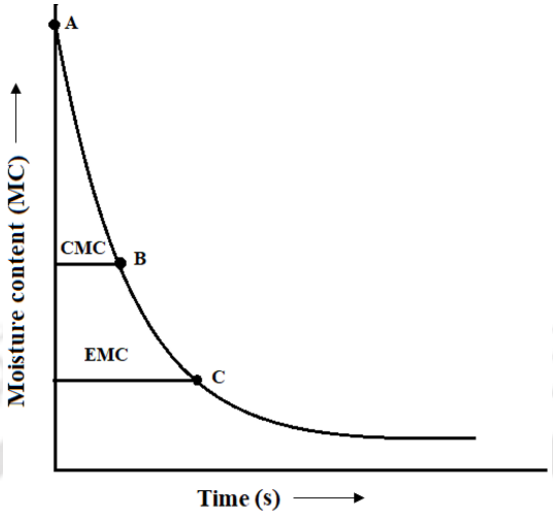

Figure 1.1: Drying Process [20]

In Fig. 1.1, point B is the product's critical moisture content (CMC). It is the average moisture content of the material at which the drying rate begins to decline. This point evolves the continuation of constant drying rate until evaporation of surface moisture content from grains. After crossing point B, the falling rate period begins. Here, point C is known as equilibrium moisture content (EMC), in which grain particles are neither absorbing nor losing moisture. At this point, the moisture content of particles reaches equilibrium with the reference surrounding. A deep understanding of these two points necessitates a thorough description of constant rate and falling rate periods. The value of critical moisture content (CMC) of paddy is reported to be about 18-24% (WB) [21]. Similarly, the value of equilibrium moisture content (EMC) of paddy is about 12-14% (WB), as reported by Chakravarty et al. (1994) [21].

1.2.1 Constant rate period

During the constant rate period, the gradience of moisture removal rate remains constant, as the name implies. In this period, the grain's surface is still wet, and the drying rate is regulated by surface moisture evaporation. The drying rate is influenced by particles' shape, size, air velocity and temperature [22]. In this period, the vapour pressure on the particle surface equals the saturated vapour pressure at the product's surface temperature. The rate at which moisture removes is determined by the vigorous rate of heat and mass transfer. The convective heat

transfer mode is the most prevalent one in this regime. The rate at which moisture is removed from the particle surface can be given by equation (1.1) [23].

$$\frac{dM}{d\tau} = -kA(M - M_e) \tag{1.1}$$

In the above equation, the term $\frac{dM}{d\tau}$ denotes the moisture gradient, M, M_e, k and τ are the moisture content of the grain, equilibrium moisture content (EMC), drying constant and drying time, respectively.

1.2.2 Falling rate period

This is the second stage of drying, in which the vapour pressure on particles is lower than that of the saturated vapour pressure. As shown in Fig. 1.1, this period occurs after the CMC point. In contrast to the constant rate period, the surface and core temperature of particles rise rather than remain constant. Here, the moisture removal rate is determined by intra-particle diffusion limitation. At this phase, the water evaporation rate from the particle surface exceeds the transfer of water from the inner surface of the particles. The moisture content of particles reaches equilibrium with the reference surrounding. This is referred to as the equilibrium moisture content (EMC). The value of EMC depends on air vapour pressure which further depends on the relative humidity and temperature of air with which it is in contact. Some suggested EMC values for various paddy storage periods are shown in Table 1.1 [24].

Table 1.1 Importance of EMC required for different storage periods [24]

Purpose	EMC for safe storage	Potential problems
2 – 3 weeks	14 – 18%	Molds, discolouration, respiration loss
8 -12 months	13% or less	Insect damage
More than 1 year	9% or less	Loss of viability

It is important to note that the structure of solid particles influences the transition between the two phases and their relative significance. On the other hand, the constant rate period is not affected by the properties of solid particles.

1.3 DIFFERENT TYPES OF DRYERS AND DRYING METHODS

There are numerous drying processes and technologies available for the drying of wet particles. Nonetheless, none of them meets the drying requirements, promoting the development of dryers that are based on products to be dried. Microwave, vacuum, freeze, and steam drying

techniques are becoming increasingly popular for drying pharmaceutical, chemical, biological, and other high-value materials. However, for cereal crops such as paddy, these dryers are prohibitively expensive and difficult to afford by small and medium-sized farmers. Therefore, people attempted to incorporate simple and convenient drying methods for drying paddy particles. Initially, the paddy drying methods are classified into traditional drying, solar drying, and mechanical drying. These drying methods are further classified into the following types, as illustrated in Fig. 1.2.

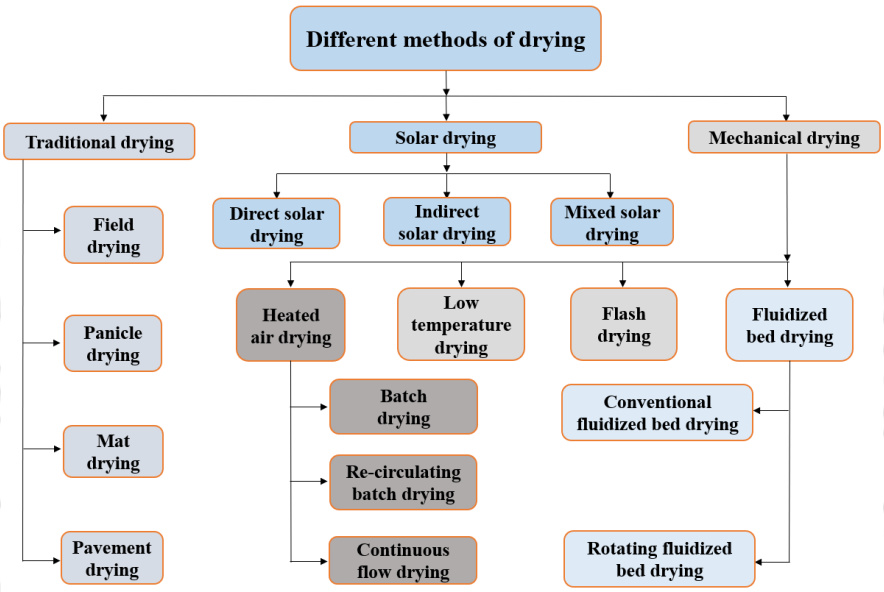

Figure 1.2: Schematic diagram of paddy dryer classification

1.3.1 Traditional drying

This technique is the oldest and simplest method of drying agricultural produce as the particles are directly exposed to sunlight. The surrounding air and the paddy grains get heated due to exposure to sunlight. Although this approach is the easiest and most convenient, it has many drawbacks, including weather dependence and labour intensiveness. Non-uniformity, slowing the process, requiring a large amount of space, and the possibility of fungal growth due to delay in the drying period are other discrepancies encountered with this method. Moreover, major disadvantages are contamination with dust, soil and foreign particles and huge pilferage due to rodents and birds. Due to the passage of time, fungi and pests might proliferate, resulting in poor milling and drying quality. This type of drying method may be classified into the following ways: Field drying, Panicle drying, drying on the woven mat and Pavement drying. It should be noted in this context that the moisture content of paddy can be reduced by 1% per

day with the help of this drying method. Figure 1.3 shows the various types of traditional drying methods.

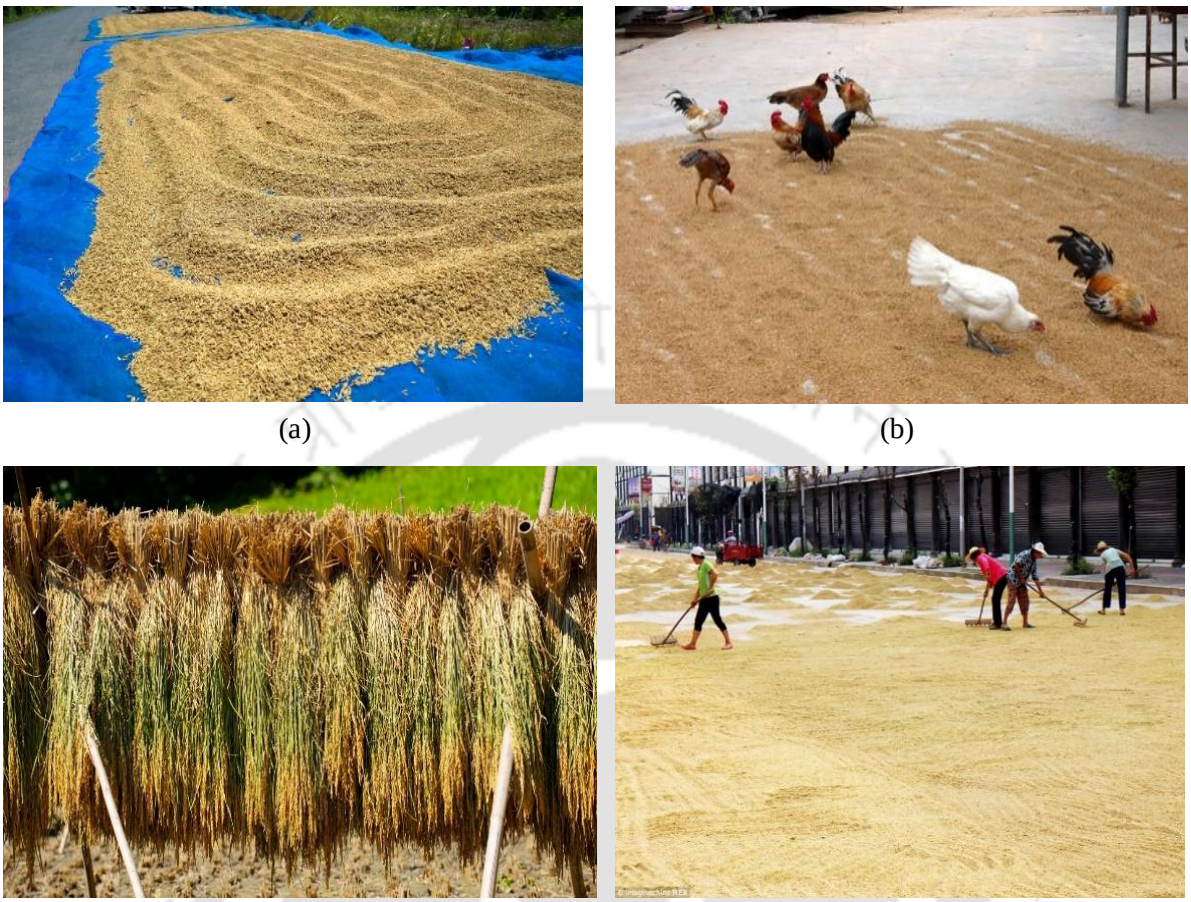

(a) (b)

(c) (d)

Figure 1.3: Traditional drying, (a) and (b) Traditional sun-drying, (c) Field drying, (d) Pavement drying [24]

1.3.2 Solar drying

In this drying, the sun's rays are incident on the transparent roof, which is normally a plastic sheet. The absorber sheets are painted black to absorb as much heat as possible from the sun. Following are the classification of solar dryers:

- Direct solar drying
- Indirect solar drying
- Mixed solar drying

1.3.2.1 Direct solar dryers

In this dryer, a transparent layer is attached above the drying chamber. The sun rays fall on the roof of a transparent layer and pass through it, heating the solid particles within the drying

chamber. The bottom of the dryer is made up of black coated plastic foil to trap the maximum amount of heat. This dryer shows favourable advantages over the traditional sun-drying method, such as lower cost, improved hygiene, and faster drying. However, the key drawbacks of this dryer are its lower drying ability and lack of control.

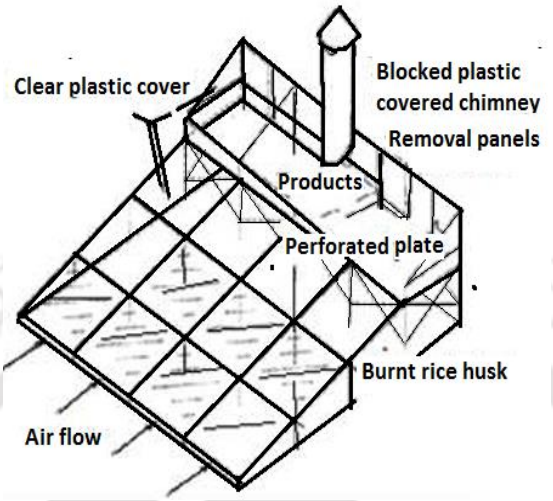

Figure 1.4: Direct solar dryer [25]

1.3.2.2 Indirect solar dryers

The drying chamber in this dryer is different from the solar collector, as shown in Fig. 1.5.

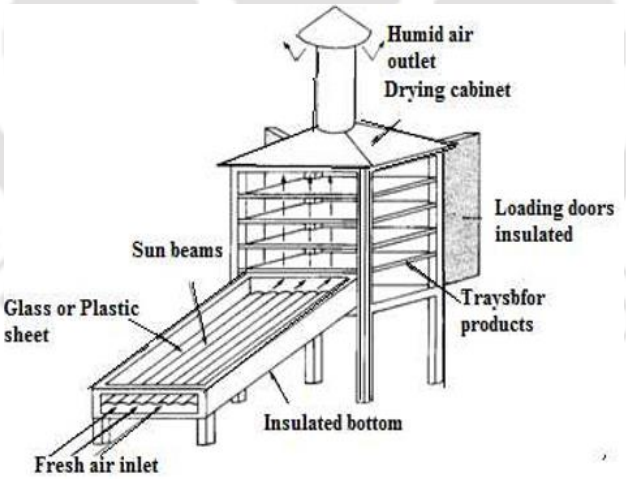

Figure 1.5: Indirect solar dryer [26]

The solar collector consisting of a glass or plastic sheet is connected to the drying chamber. Fresh air is heated in the solar collector by collecting the solar radiation and then passed to the drying chamber through natural convection to dry the products [26]. This dryer cannot be used at night or during the rainy season, as it can induce mold growth. Apart from that, extending

the range of solar dryers without re-building fragile structures is difficult. However, this problem can be overcome by the use of mixed solar dryers.

1.3.2.3 Mixed solar dryers

In this form of the dryer, the air is heated by means of an external source of heat, such as fuel burning or a backup heat source, so that weather conditions do not influence it. In order to dry the products, hot air is blown over the solid products with the aid of a fan, blower and pump. The main benefit of this form of a dryer is that it can dry a variety of solid products. It also has the ability to monitor drying and has a higher drying capacity. However, the cost of this dryer is higher than that of solar dryers. Another downside of this type of dryer may be incomplete fuel burning, which could adversely affect the ecosystem.

1.3.3 Mechanical dryers

These dryers are becoming increasingly important because of their high ability to control. The various parameters, such as temperature, drying rate and moisture rate, can easily be controlled in these dryers. There are various types of mechanical dryers, as shown in Fig. 1.6. Based on their capacity and drying methods, some of them are commercialized, and a list of commercial mechanical dryers are heated air dryers and fluidized bed dryers. The heated air dryers are of three types: fixed batch type dryer, re-circulating batch type dryer, and continuous flow dryer. On the other hand, fluidized bed dryers are the straight type of fluidized bed dryers and rotary type of fluidized bed dryers.

1.3.3.1 Heated air drying

These are drying methods that can be achieved at any time of day or night and can minimize labour costs. As compared to the sun dryer process, these dryers can be used for large scale mass production with reduced time. Uniform grain drying can be achieved by regulating the flow of air. Air heated dryers include batch dryers and continuous flow dryers. The batch dryers are further classified as fixed bed batch dryers and re-circulating batch dryers. In a fixed bed dryer, the wet granules are patched over the perforated bed and drying is done by supplying the hot air produced by burning kerosene or rice husk. The required drying temperature in this type of dryer is kept 10-15°C above the ambient temperature. In such dryers, products are totally exhaled to the drying air under constant drying conditions, i.e., at constant air temperature. In this dryer, the concept of a thin layer arises as a bed of thickness less than 20 cm is better suited for drying.

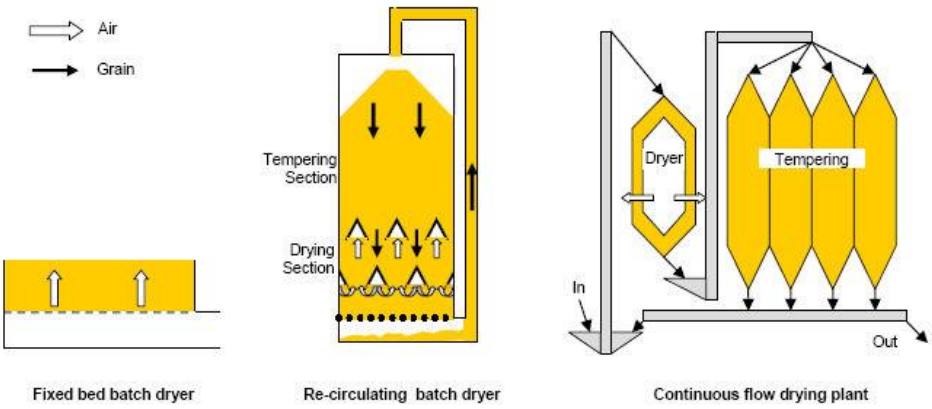

Figure 1.6: Types of air heated dryers [24]

On the one hand, this type of dryer is simple and affordable, and on the other hand, this dryer is labour and cost-intensive. Besides these, the wide variation of moisture gradient along the vertical direction is one of the major disadvantages of this type of dryer. The re-circulating type of dryer is compact in which grains pass through both drying and tempering sections alternately, as shown in Fig. 1.6. Because of the simultaneous action of these two, the moisture gradient in the grains reduces. However, the non-uniformity of drying is the major disadvantage associated with this type of dryer. In a continuous flow dryer, paddy granules are poured at the top and continuously flow across the dryer. Heated air is blown through the paddy as it moves down the bed. It takes 15 to 30 minutes to move across the dryers. This type of dryer is advantageous over the batch type of dryer in terms of drying uniformity and lower operating cost. Nevertheless, the investment cost is higher than those of the batch type of dryer. Sometimes baffles are used to diverge the flow of paddy granules leading to an increase in bed pressure drop.

1.3.3.2 Fluidized bed drying (FBD)

Fluidized bed drying is a relatively new drying technique that has become very popular in recent years. In a fluidized bed, direct interaction between the solid particle and hot air or gas is possible. In a fluidized bed dryer, high-pressure hot air passes through the distributor plate, where it comes into contact with solid particles and dries them. Unlike batch-type dryers, the concept of the thin layer does not come into play as the bed is in a movable condition. There are different types of fluidized bed dryers, such as straight type, rotating type, etc. These dryers are faster, take less time, and improve particle consistency than any other conventional dryers. Because of these, there are numerous advantages inherited with these types of dryers, such as high drying rate due to the good interaction between hot air and solid particles, automatic

operation, high rate of heat as well as mass transfer, better control of temperature and other essential parameters, need less space for installation and lower maintenance costs due to lack of rotating components. A typical fluidized bed dryer is shown in Fig. 1.7.

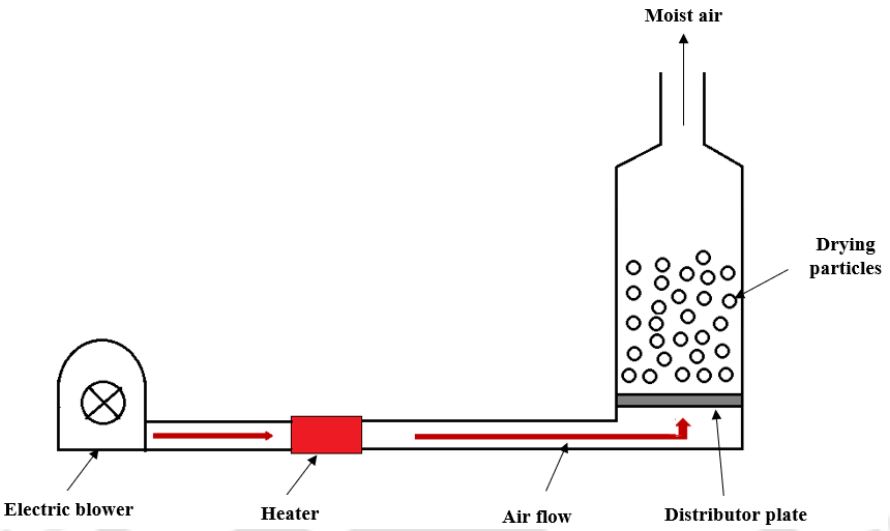

Figure 1.7: Fluidized bed dryer

1.4 AIM OF THE PRESENT STUDY

Although there are many advantages to fluidized bed dryers, the major shortcoming associated with the straight type of atmospheric bubbling fluidized bed dryers is the high velocity at which the solids particles are transported along the height, and elutriation of the bed leads to a shorter residence time, which affects the quality of the product as well as the thermal efficiency of the dryers. On the other hand, it is difficult to fluidize particles with lower velocity in a rotating fluidized bed due to the action of centrifugal force apart from the drag and gravitational force. Therefore, there is a need for alternatives to fluidized bed dryers to reduce these discrepancies. A variable cross-sectional riser of a fluidized bed can minimize these discrepancies, as reported in the literature, in which the superficial velocity gradually decreases with the height of the bed due to an increase in cross-sectional area along the height. Because of the gradual increase in the area of the cross-section along the height of the bed from bottom to top, the velocity is relatively high at the bottom, ensuring the concentration of large particles is relatively low at the top and preventing entrainment of small particles. Similarly, due to the higher velocity at the bottom, the fluidization of coarser particles takes place easily. As a result of this behaviour, the heat transfer characteristics are expected to improve and thereby expect the improvement of drying characteristics, as drying phenomena are inevitably characterized by the heat transfer characteristics in a fluidized bed dryer.

The present investigation aims to design and develop an efficient bubbling fluidized bed riser and to study the hydrodynamics, heat transfer and drying characteristics. In this study, five different atmospheric bubbling fluidized bed dryers with varying cone angles ranging from 0° to 20° (with a change in 5°) are proposed numerically to adjudge the proper cone angle for efficient drying. Based on numerical analysis, the feasible risers will be selected, and a laboratory-scale study will be carried out to find out the best performing dryer using sand particles as bed inventory. Performance of the selected dryers will be carried out, and validation of the experimental results will be done with simulation. Furthermore, the performance of the dryers will also be carried out to assess the drying characteristics of paddy particles. The objectives of the present study will be presented in the subsequent chapter.

1.5 OUTLINE OF THE THESIS

The thesis comprises of seven chapters. Chapter 2 deals with the study of literature review related to the present study, which incorporates hydrodynamics, heat transfer, drying characteristics, and thermo-economic analysis in different aspects of fluidized beds. The scope of the present work based on the research gap is also outlined in this present chapter. Numerical simulation and procedure for the hydrodynamics and heat transfer characteristics of fluidized bed dryers are presented in chapter 3. Chapter 4 describes the experimental setup and procedure for the present study related to hydrodynamics, heat transfer, drying characteristics and thermodynamic analysis. Chapter 5 reports results and discussion of hydrodynamics and heat transfer characteristics of sand particles in the three dryers with varying operating parameters. Chapter 6 investigates the performance of drying characteristics of paddy particles on the developed dryers with varying operating parameters and thermodynamic analysis of the same. Furthermore, the investigation of economic analysis of three dryers using different assumed parameters is described in chapter 7. Finally, the conclusions and future scope of the present work are mentioned in chapter 8.

2

Literature review

2.1 Introduction

2.2 Numerical simulation of fluidized beds

2.3 Experimental study of fluidized beds

2.4 Parametric study on hydrodynamics and heat transfer

2.5 Drying phenomena in different types of drying

2.6 Energy and exergy analysis of drying

2.7 Research gap and scope for the present investigation

2.8 Chapter conclusion

CHAPTER 2

LITERATURE REVIEW

2.1 INTRODUCTION

This chapter deals with the literature about the numerical and experimental study of hydrodynamic behaviour, heat transfer characteristics and drying characteristics of conical and conventional fluidized beds. Section 2.2 is associated with the numerical study of hydrodynamic and heat transfer characteristics. On the other hand, the experimental study of hydrodynamics and heat transfer characteristics is included in section 2.3. The literature analogous to the effect of operating parameters on the same is described in section 2.4. Section 2.5 describes the drying characteristics of different drying granules in different dryers. Similarly, energy and exergy analysis of the drying process of different dryers is rendered in section 2.6. Section 2.7 comprises of research gap within the scope of the present investigation. Finally, the chapter is concluded in section 2.8.

2.2 NUMERICAL SIMULATION OF FLUIDIZED BEDS

This section explores the review related to the numerical simulation of hydrodynamic behaviour in conical fluidized beds and heat transfer characteristics in conventional and conical fluidized beds. The different types of numerical models used in the context of fluidized beds are also discussed. The numerical simulation of the fluidized bed is based on the conservation equations of mass, energy and momentum, incorporated with constitutive equations that depict the interactions between the phases. There are several numerous models developed in recent years for describing the behaviour of gas-solid flow in conventional fluidized beds, such as the Discrete Particle Model (DPM), Discrete element model (DEM), Lattice–Boltzmann model (LBM), and the Two-Fluid Model (TFM) described by Hoef et al. (2008) [27]. However, in the numerical simulation study of conical fluidized beds, the TFM is widely incorporated. The TFM requires a package of physical or empirical models for closure to the governing equations [28].

The two approaches, Eulerian-Eulerian and Eulerian-Lagrangian, are frequently used in the numerical simulation of fluidized beds [29]. The Eulerian-Lagrangian approach describes the DPM and DEM. The DPM is frequently utilized in the freeboard region of the bed. The

freeboard region is the dilute one where a small number of particles with the gas phase are present. On the other hand, DEM is used in complicated geometries for heterogeneous reactions because of the rotational degree of freedom involvement. An enormous number of micron-size particles and above can be simulated by this method, and this method is closely related to molecular dynamics.

2.2.1 Hydrodynamic behaviour of conical fluidized beds

Huilin et al. (2006) [30] numerically compared the gas-solid flow between a tapered-out and a columnar circulating fluidized bed riser. They observed that the existing core annular structure in the columnar riser disappeared when a tapered-out riser was used. Chalermsinsuwan et al. (2010) [31] used the energy-minimization multi-scale (EMMS) model to investigate the gas-solid flow in three risers such as columnar, tapered in and tapered out. They observed that mixing characteristics were improved with the tapered-out riser. However, particle resident time increased, and uniform temperature prevailed when tapered in riser was used. Askaripour and Dehkordi (2016) [32] performed a 2-D simulation by using a TFM coupled with an Eulerian-Eulerian model closed by the kinetic theory of Granular flow. They investigated the effect of static bed height on pressure drop in tapered-in and tapered-out risers. They observed an increase in bed pressure drop with the increase in static bed height in both tapered-in and tapered-out risers. Sau and Biswal (2011) [33] performed a numerical study in a conical fluidized bed riser to investigate the effect of gas velocity on hydrodynamic behaviour, such as pressure drop across the bed and bed expansion ratio. The pressure drop was found to increase first up to a maximum value with the gas velocity and then decrease with a subsequent increase in gas velocity. The numerical simulation was performed with the use of CFD software ANSYS Fluent 6.1.22 [34]. Their results indicated that the bed expansion ratio increases with an increase in superficial air velocity. Similar studies were also carried out for bi-disperse TiO_2 particles by Bahramian and Olazar (2012) [35]. They have considered similar conditions as described by Sau and Biswal (2011) [33]. Besides that, the results obtained were compared for three different wall boundaries for solid materials such as no-slip, partial slip and free slip. Three different drag models as Syamlal-O'Brien (1988) [36], Gidaspow (1994) [37] and Arastoopour (2001) [38], were used in this numerical study and results were compared among all these three different drag models. Among all three different drag models, the Gidaspow drag model was found to be best fitted for experimental results. The results obtained for bed expansion ratio using the free-slip boundary condition were found to be slightly better than

those obtained by implementing the model with the other boundary conditions. The bed expansion ratio and pressure drop was found to increase by increasing gas velocity. However, the bed expansion ratio was found to decrease with the increase in static bed height. Sutar and Das (2012) [39] numerically studied the segregation of particles in a conical fluidized bed, and the results were compared with the experimental results. The simulation was performed by ANSYS Fluent 6.2.16 [34].

Bahramian and Olazar (2021) [40] numerically identified the mutual effects of gas velocity and agglomerate size on the instantaneous pressure, bed pressure drops and bed expansion ratio. The simulations were performed through the CFD-DEM approach. The fluctuation of high pressure was found in the partially fluidized regime, which was associated with high values of bed pressure drop (both average and instantaneous) and low values of bed expansion ratio. In contrast, the spouting flow regime found small pressure fluctuations and enhanced bed expansion ratio. Bahramian and Olazar (2021) [41] also numerically studied the hydrodynamic behaviour of cohesive TiO_2 nanoparticle agglomerates in a conical fluidized bed, and the results were compared with experimental results. The effects of size, particle polydispersity, and airflow velocity were studied in the transition regime from heterogeneous to homogeneous and turbulent fluidization. The CFD-DEM numerical simulation was conducted to explore the interaction between the simple agglomerates. The effects of restitution and friction coefficients, probability density function, and coordination number of agglomerates were studied on the particle velocity profiles in the spout and annular zones. Minor differences in bed hydrodynamics were observed for different values of the restitution coefficient when applied the no-slip and the partial-slip wall boundary conditions. The choice of 0.96 for the restitution coefficient provided the most realistic numerical results in all zone. The effect of the friction coefficient on the particle velocity in the annular zone was greater than in the other zones. Bahramian (2019) [42] studied the reliability and accuracy of numerical results of microparticle (titania powder) fluidization in a conical bed, affected simultaneously by mesh refinement, the grid configuration and the wall boundary condition (BC). The pressure gradients and velocity profiles were studied for a conical bed. The Gidaspow drag correlation and different wall BCs are considered using an Eulerian–Eulerian two-fluid model. Predictions of the pressure fluctuation, power spectra of the corresponding pressure fluctuations, bed pressure drop, minimum fluidization velocity, axial solid velocity, bed expansion ratio, and particle size distribution were compared with experimental data. Simulations showed that significant

savings in terms of computational time were realized by choosing a uniform mesh, while the hexahedral structure, the near-wall mesh refinement, and the free-slip BC give the closest fit to the experimental data. Adnan et al. (2003) [43] reported the hydrodynamics behaviour of a 3-D small-scale cold flow modelling of a gas-solid tapered fluidized bed with the Eulerian-Eulerian two-fluid modelling (TFM) approach. The sensitivity of different modelling parameters, including lift and virtual mass forces, viscous force, gas-solid drag force, granular temperature, granular viscosity, granular pressure, particle-wall specularity coefficient, particle-particle restitution coefficient, and particle-wall restitution coefficient, were systematically investigated to optimize the performance of the present numerical model. The results from different sensitivity analyses revealed that the gas-particle drag force was more important in resolving the correct time-averaged axial and radial solids holdup profiles of the tapered fluidized bed than the other investigated parameters. The highest accuracy possible from simulations was achieved from the Gibilaro drag model followed by the Arastoopour and EMMS/bubbling models. In contrast, all other drag models over-predict the gas-particle interaction force. The assessment of the lift and virtual mass forces, viscous force, granular temperature, granular viscosity, granular pressure, and particle-wall restitution coefficient results revealed that these parameters were less critical for the numerical simulations of the tapered fluidized bed than the gas-solid drag force. However, the assessment of the particle-wall specularity coefficient and particle-particle restitution coefficient revealed that adjusting these parameters in the numerical simulations was helpful in achieving a better agreement between the experimental data and model results. For the higher gas flow rate, this study revealed that a better agreement could be achieved by tuning the parameter values in the standard sub-models than the previously published TFM studies. Meanwhile, for the lower gas flow rate, the accuracy of the present work was slightly lower than the previously published work but acceptable with the experimental measurements. Khongprom et al. (2020) [44] investigated the hydrodynamic behaviour and the performance of catalytic cracking of heavy oil in a circulating fluidized bed reactor using computational fluid dynamics. The two-fluid model incorporated with the kinetic theory of granular flow was applied to predict the hydrodynamic behaviour with a reactive flow. Three reactor geometries were studied, which included a conventional riser, tapered–out riser, and tapered–in riser. The four–lump kinetic model was used to describe the catalytic cracking of heavy oil from waste plastic. A core–annulus flow pattern was found in the three reactor geometries. The solid fraction distribution of the tapered reactor was found to be more uniform than that of the conventional riser. The

tapered–in riser showed the highest heavy oil conversion with the lowest gasoline selectivity. However, the heavy oil conversion and gasoline selectivity of the conventional and tapered–out reactors were not significantly different. Liu et al. (2019) [45] simulated three-dimensional gas-solid flow in tapered-out and tapered-in risers by the two-fluid model using an improved structure-dependent drag based on the EMMS model. The EMMS model was solved at different axial levels to determine different correlations of heterogeneity index with voidage, which were then interpolated between these levels to improve the prediction of varying interphase drag in the tapered risers. Considering the axial variation of the EMMS drag, the simulation predicted much more reasonable flow dynamics in the tapered risers than those coupled with an average EMMS drag or homogeneous drag laws. Koerich and Rosa (2021) [46] carried out numerical simulation to estimate the effect of the shear stress and bioparticles collisions for biofilm development in tapered fluidized bed reactors. The two-fluid Eulerian model was used to conduct the numerical simulation. OpenFOAM software was used to run the simulation. Findings suggested that shear stress had more influence on biofilm maintenance than the frequency of collisions. Both effects occured concomitantly and were stronger in the region near to the walls of the bioreactor. The high value of both parameters could be reduced by increasing the angle of the bioreactor. Nonetheless, the effectiveness analysis indicates that the simulated bioparticles had active biofilms, but thicker biofilms hindered the substrate mass transfer into deeper regions of the biofilm.

2.2.2 Heat transfer study on fluidized beds

Feng and Musong (2014) [47] simulated the spherical particles in a conventional fluidized bed by a direct numerical simulation approach combined with the immersed boundary (DNS–IB) method to study the heat transfer coefficient. The statistical average of particle Nusselt number was found to increase with the increase in fluidization velocity and bed height, and as a result, the heat transfer coefficient increased. However, Banaei et al. (2017) [48] observed that the overall Nusselt number decreases with the air velocity. Bisognin et al. (2016) [49] studied the heat transfer coefficient by considering the effect of the immersed surface geometry. The heat transfer coefficient was found to be highest with the incorporation of a spherical immersed heater. The local heat transfer was found to be enlarging with the superficial air velocity. Liu et al. (2018) [50] investigated the heat transfer mechanism of a coarse grain particle by using CFD-DEM and the coarse-grained particle method (CGPM). Investigation of heat transfer characteristics in a fluidized bed by using the CFD-DEM tool was also studied by Gan et al.

(2016) [51]. They used spherical and ellipsoidal particles to study the conductive, convective and radiative heat transfer in the bed. It was found that spherical particles have higher convective heat transfer rates and lower conductive heat transfer rates when compared with ellipsoids. Dinh et al. (2017) [52] performed a numerical simulation in a bubbling fluidized bed by adopting the Eulerian-Eulerian Multiphase model. Their investigation of heat transfer phenomena included the distribution of solid temperature and heat flux across the fluidized bed. The heat transfer effect was found to be more prevalent in the dense bed region, where solid concentration is more. Nevertheless, the air to particle heat transfer rate was found to be lower with an increase in solid concentration in the study of Ngoh and Lim (2016) [53]. Studies of heat and mass transfer in three-phase fluidized bed were also conducted by Abdel-Aziz et al. (2016) [54] in their numerical investigation. It was observed that the increase in solid particles results in a decrease in a gas hold-up and interfacial contact area between the gas and liquid. The heat transfer investigation conducted by Blaszczuk et al. (2017) [55] showed that the bed to wall heat transfer improved with the use of smaller size particles. The smaller particles also improved the conduction and convection in the bed. Another study by Jia et al. (2019) [56] also observed the improvement of heat transfer characteristics with smaller size particles. Abdelmotalib et al. (2015) [57] investigated the hydrodynamics behaviour and heat transfer characteristics along a conical fluidized bed with 30˚cone angles by considering the effect of two different drag models such as Syamlal-O'Brien and Gidaspow (1985) [58]. The local heat transfer calculated by penetration theory was found to be different from the two drag models. Similarly, Abdelmotalib et al. (2016) [59–61] investigated the heat transfer characteristics in a conical fluidized bed of 0.4 m height with 30˚ cone angles. Their study of heat transfer considered the impact of both gas velocity, granular temperature models, specularity and restitution coefficients. They observed that the local heat transfer coefficient increases with air velocity. However, the use of the partial differential equation (PDE) as the granular temperature model in the investigation of heat transfer characteristics had no impact. Similarly, the heat transfer coefficient was also not influenced by the restitution coefficient. Nonetheless, the heat transfer coefficient was found to decrease with the increase in specularity coefficient.

Gopan et al. (2021) [62] focused on the computational modelling and simulation effect of various parameters like par, stagnant bed height, superficial velocity, minimum fluidization velocity and heat transfer characteristics upon variation in the taper angle of tapered fluidized

bed reactor (TFBR) using Computational Fluid Dynamics (CFD) solver FLUENT. The two-Fluid Model (TFM) was adopted for the simulation studies where both the phases (Solid, Gas) were treated as fluids. The results obtained were compared with simulation conducted for columnar reactor having the same axial length. Simulation results showed that the finer the particle size, the greater the heat transfer by conduction from bed to wall compared to larger particles. The interphase heat transfer from solid air was maximum in the reactor core section. Although the particle volume fraction was observed to be more in the columnar reactor, better fluidization characteristics were observed in the reactor with a taper angle of 4.52°. Zhang et al. (2020) [63] employed DDPM simulation to evaluate the flow behaviours and heat transfer characteristics in a tapered gas-solid fluidized bed with the pulsed flow. The dependence of heat transfer on fluidization was analyzed. The results demonstrate that the inclined wall in a tapered bed greatly enhanced the particle movement inwards so as to improve the fluidization quality and heat transfer. The influence of operating conditions, including taper angle and heater probe location, was also examined. The results revealed that the heat transfer coefficient increased with the decrease of taper angle and the distance from the heater probe to the gas inlet. Different pulsating flow waveforms were also compared. A weaker heat transfer capacity was observed in a tapered fluidized bed with rectangular pulsed flow compared to that with the sinusoidal pulsed flow.

2.3 EXPERIMENTAL STUDY OF FLUIDIZED BEDS

This section describes the experimental investigation conducted by many researchers in the conical fluidized bed. Hydrodynamic behaviours, such as pressure drop and velocity of fluidization at different regimes, fluctuation ratio, the ratio of bed expansion, hysteresis, compressive force, etc., are vigorously investigated. Particle separation, emission characteristics, the efficiency of combustion, and axial and radial voidage of different particle sizes with different static bed heights are reported. This chapter also includes a contrast of conical fluidized beds with other conventional fluidized beds.

Levey et al. (1960) [64] studied the hydrodynamic behaviour in a gas-solid conical fluidized bed and compared it to the cylindrical fluidized bed. They applied a hydrofluorination bed of uranium trioxide and uranium tetrafluoride. He et al. (2017) [65] also compared two fluidized beds, one of which was a conical bed, and the other was a conventional fluidized bed for direct reduction of fine ore concentration. A conical fluidized bed was found to be more versatile in the treatment of fine iron ore concentrate than the cylindrical fluidized bed. It was observed

that the fluidization behaviour with deep beds for the conical fluidized bed was more homogeneous than the cylindrical fluidized bed. Sutherland (1961) [66] recorded fluidization behaviour in gas-solid tapered and mini tapered beds and observed a reduction in the vertical mixing rate of gas-solid particles in deep beds as a result of the increase in the tapered angle. Littman (1964) [67], Venkatesh et al. (1966) [68], and Ridgeway (1965) [69] proposed that the tapering angle had a major impact on solid particle mixing and the occurrence of plug flow, channelling, and agglomeration of particles in the cylindrical fluidized bed could be reduced.

Peng and Fan (1997) [70] studied the hydrodynamics behaviour of Geldart-B type particles in the liquid-solid conical fluidized bed. They observed five different flow regimes for different superficial velocities, such as fixed-bed regime, partially fluidized-bed regime, fully fluidized-bed regime, transition regime and turbulently fluidized-bed regime. However, three different regimes were observed for Geldart B and D type particles in a gas-solid conical fluidized bed [71–76]. Nevertheless, two fluidization regimes were observed for Geldart A-type particles as the partial fluidization regime did not appear [77]. Besides the study of fluidization regime, Zhao et al. (2014) [76] also investigated axial and radial voidage. S-shaped profiles for axial voidage and M-shape profiles for radial voidage were observed. Maruyama and Koyanagi (1993) [78] also used spherical particles to study the hydrodynamic behaviour in various tapered beds, rectangular in cross-section, to develop a mathematical model that predicts bed expansion in slugging flow regime. Sau et al. (2007, 2009, 2010) [79–81] conducted experiments using spherical and non-spherical particles of different sizes and different densities to predict minimum fluidization velocity, maximum pressure drop, and bed fluctuation and expansion ratio. They compared their experimental results with the models of Peng and Fan (1997) [70] and Jing et al. (2000) [71]. The results were found to be in good agreement with these two existing models. Dora et al. (2013) [82] studied the hydrodynamic behaviour, such as minimum fluidization velocity, bed fluctuation ratio and bed expansion ratio of the homogeneous ternary mixture with various particle sizes at varying compositions in a gas-solid conical fluidized bed. Padhi et al. (2016) [83] also conducted studies of the hydrodynamic behaviour of the homogeneous ternary mixture. Their experiments were conducted for a three-phase gas-liquid-solid flow. They used the response surface methodology (RSM) to study the hydrodynamics behaviour, including bed pressure drop, bed fluctuation, and bed expansion ratios. Investigation of hydrodynamic behaviour of a homogeneous and heterogeneous binary mixture of particles in tapered beds was also reported by Sau et al. (2008) [84,85].

Kim et al. (2000) [86] conducted an experimental study in the gas-solid conical fluidized bed to examine fluidization characteristics, such as the size segregation of two different iron ore particles and compared the results with the conventional fluidized bed. The homogeneity of particle size is essential for axial size segregation, and for optimal segregation, there should be a critical taper angle. Beyond that (critical taper angle), coarser particles surface to the top of the bed, and the trend becomes reverse for the lower value of taper angle. If the particle size increases, the taper angle should be increased to obtain the homogeneous axial size distribution. It was also found that the stirring of solids improved with the increase in gas velocity. Moreover, fine particles reside near the wall, confined by downward flow along the wall with the irregular radial distribution. Another study of particle segregation was also carried out by Wormsbecker et al. (2005) [87]. They studied the segregation of particles in the axial and radial direction of a conical fluidized bed. Experiments were carried out with three static bed heights at three different velocities. Particle segregation was observed at the bottom centre of the bed. It was also observed that particles were transported along the centre of the bed and flowed down along the wall of the bed. Consequently, Schaafsma et al. (2006) [88] used two different techniques to investigate the particle flow pattern and the granular particle segregation in a conical fluidized bed and stated similar findings as reported by Wormsbecker et al. (2005) [87] about the upward flow of particles in the centre accompanied by the high velocity of the gas and the downward flow of particles near the wall. Zhou et al. (2009) [89] and Webster and Prerona (1990) [90] had also observed a similar movement of particles.

Fang et al. (2020) [91] first experimentally investigated the effect of particle size and material mass to explore their effects on minimum fluidization velocity and incipient fluidization pressure drop. Then, an Ergun equation modifying method and the dimensional analysis method was used to obtain the modelling correlations of minimum fluidization velocity and incipient fluidization pressure drop by fitting the experimental data. The experimental results showed that minimum fluidization velocity increases significantly with increasing particle size but has little relationship with the material mass; incipient pressure drop increases significantly with increasing material mass but has little relationship with the particle size. Experiments with small particles show a significant increase at large superficial gas velocity; the fitting accuracy of the modified Ergun equation was lower than that of the dimensionless model. When using the Ergun equation modifying method, it was deduced that the gas drag force was approximately 0.8995 times the material total weight at the incipient fluidized state. Fang et al.

(2021) [92] also reported the pressure fluctuations in a conical fluidized bed by using time-series analysis. The standard deviation was found to increase rapidly while the kurtosis value decreased rapidly as the fluidization velocity increased up to the minimum fluidization velocity, indicating that the flow regime changed from fixed bed to bubbling fluidization. As the fluidization velocity continues to increase, standard deviation decreases at certain fluidization velocity values. It was also found that the smaller the material mass was and the smaller the particle size was, the easier it was to enter the turbulent fluidized state. The maximum standard deviation value increased as the material mass increased. Zhang et al. (2020) [93] investigated the surface morphology evolution in the reduction of fine iron ore in a conical fluidized bed reactor under various conditions. The result indicated that it was beneficial to inhibit the formation of iron whiskers under high H_2 content, high gas velocity and low reduction temperature. Kalo et al. (2019) [94] reported the hydrodynamics of binary gas-solid conical fluidized beds experimentally by using radioactive particle tracking data. Time series analysis of the tracer tracks was performed to characterize the chaotic fingerprint and the mixing and segregation features. It was found that the hydrodynamics of the gas-solid conical bed was chaotic and that the degree of chaotic behaviour depends on the gas inlet velocity and bed composition. It was further observed that in the conical bed, different interaction phenomena dominated the behaviour of the bed based on the position inside the column. In the bottom section, gas-solids interaction played a dominating role while, at the top section, particle-particle interaction becomes crucial. In conical fluidized bed, the axial autocorrelation took a longer time to decay compared to radial autocorrelation, which signifies that motion was primarily in the axial direction. Apart from the investigation of hydrodynamics in gas-solid conical fluidized bed reactor, Kalo et al. (2019) [95] also investigated the hydrodynamic behaviour of a conical liquid-solid fluidized bed using mono dispersed particles of two sizes and the 50 wt% binary mixture. The liquid-solid conical fluidized bed was found to be quite homogeneous than the gas-solid conical fluidized bed. It was also observed that the magnitudes of axial and radial RMS velocities were similar at the centre of the column. Hence, the effect of particle-particle interactions in liquid-solid conical fluidized beds was more decisive for the dynamics than the gas-solid conical bed. Bahramian (2019) [96] studied the mutual effects between the mechanical properties and interparticle cohesive forces of the TiO_2 nano particles as well as the fluidization regimes in a conical fluidized bed. Pressure fluctuation analysis exhibited a transition flow regime from a particulate phase to a bubbling, slugging, turbulent fluidization, and spouting regime. The ratio of hydrodynamic to interparticle force

was applied to describe the bed characteristics, while the granular Bond number obtained from settling experiments was used to find the agglomerates fractal dimension. The dependency of the hardness on the fluidization regime showed the interparticle force diminishes with decreasing the asperity radius of agglomerates.

Sahoo and Sarkar (2021) [97] experimentally studied the hydrodynamics of tapered fluidized beds using an image analysis method. The effect of the taper angle and air velocity on the bubble size, shape, fraction, and rise velocity, along with the bed expansion ratio and the unfluidized region, was investigated. A new method was proposed to obtain expanded bed height from an image. The time-averaged bed expansion ratio and bubble fraction increased with the air velocity and decreased with the taper angle, while a reverse trend was observed for the mean unfluidized area fraction. Correlations were proposed for predicting the bubble fraction, bed expansion ratio, and unfluidized area fraction. An imaging method was also proposed and used by Bai et al. (2021) [98] to investigate the effect of bubbles on gas-carbon nanotubes (CNT) particle mixing. It was found that bubbles play different roles in particle mixing at different stages of CNT growth in a tapered fluidized bed reactor (TFBR) without a distributor. The degree of mixing of gas-CNT particles and the degree of particle movement was related to the growth time of the CNT. Investigation of fluidization characteristics of CNT particles in a tapered fluidized bed (TFB) was also made by Bai et al. (2021) [99] without a distributor. The effect of temperature (180 to 680°C) on minimum fluidization velocity and dynamic characteristics of gas–agglomerated CNT particles flow at elevated temperature was studied. Experimental results revealed that the minimum fluidization velocity decreases for agglomerated CNT particles with the increase in temperature. The inhomogeneous dynamic characteristics existed in the bed at elevated temperature in the mesoscale due to the stochastic features of small bubbles or cavities movement. Under different operating conditions, the gas agglomerated CNT particle's flow behaviours showed high sensitivity to the temperatures from the fixed bed to the partial fluidization regime. Bai et al. (2020) [100] also investigated the fluidization behaviour and quality of carbon nanotube particles in a conical fluidized bed reactor without a distributor. The fluidization characteristics such as bed expansion ratio, pressure drop, and fluidization dimensionless time were investigated in a laboratory cold model scale. It was found that the flow regime transition in the conical fluidized bed reactor without a distributor was similar to that of a conical fluidized bed reactor with distributors. From the experiments, it was evident that there was the appearance of four flow regimes, which were

fixed bed (de-fluidization), stable fluidization, bubbling fluidization and particulate fluidization. The fluidization characteristics of particles were found to be similar to those of Geldart group A in the conical fluidized bed reactor without a distributor. The effect of cone angle on fluidization behaviour was also studied. It was observed that the conical fluidized bed reactor with a smaller cone angle had the beneficial effect of fluidizing carbon nanotube particles. Rasteh et al. (2022) [101] reported the effect of Gaussian distribution width, average particle diameter, particle loading, and the tapered angle on minimum fluidization velocity (U_{mf}) by conducting extensive experiments in tapered fluidized beds. Three powders with Gaussian size distribution and different distribution widths were used in the experiments. An increase in U_{mf} with increasing the average particle diameter, particle loading, and the tapered angle was observed. There was also a nonmonotonic behaviour of U_{mf} as the Gaussian distribution width increased. An empirical correlation including dimensionless groups for predicting Umf in tapered beds was developed in which the effect of distribution width was considered. The proposed correlation predictions were in good agreement with the experimental data, with a maximum deviation of 16.5% and average and standard deviations of, respectively, 6.4% and 7.4%.

Padhi et al. (2019) [102] experimentally studied the hydrodynamic characteristics, namely minimum fluidization velocity, maximum bed pressure drop, bed fluctuation and expansion ratios. The effect of tapered angle, superficial air velocity, and particle size on these hydrodynamic parameters was analyzed. Using statistical analysis, correlations were also developed for the responses. The predicted correlations were shown to be in good agreement with the experimental ones. The experimental studies were compared with the values of the responses calculated from various correlations developed by other researchers. The study revealed that the bed pressure drop increases with the increase in tapered angle and decreases with the increase in fine in the ternary mixture. However, the bed fluctuation and expansion ratios were found to decrease with the increase in tapered angle. Nevertheless, the bed fluctuation and expansion ratios were found to increase with the increase in fines in the ternary mixture. Similarly, these two ratios were also shown to increase with the increase in air velocity. Hong et al. (2019) [103] aimed to study the effect of the initial mixing ratio of glass beads and superficial gas velocity on mixing and segregation in a ternary system gas-solids three-sectional tapered fluidized bed with a cone angle of 25°. Flow characteristics and mixing degree in the bottom reaction zone and the top expanded zone were observed based on the

determined composition of the bed according to operating conditions. When gas velocity was increased, the bed provided perfect mixing while the layer separation was decreased. When the initial mass fraction of glass beads was decreased, an increase in the difference between the mass fraction value in the upper expended zone of the bed and the mass fraction value in the lower reaction zone was observed. A comparison of the bed of the bottom reaction zone with that of the top expanded zone showed that segregation occurred with a maximum difference of 25 wt%. The separation efficiency of glass beads was found to increase with an increasing initial mass fraction of glass beads. Karimi et al. (2018) [104] investigated the minimum fluidization velocity (U_{mf}), minimum velocity of full fluidization (U_{mff}), and maximum pressure drop (ΔP_{max}) in the tapered fluidized bed. An artificial neural network (ANN) paradigm was developed for the prediction of these parameters. The ANN model's parameters were adjusted by minimization of the absolute average relative deviation (AARD) and mean square error (MSE) via a back-propagation algorithm. Finally, the proposed model predicted the experimental data of U_{mf}, U_{mff}, and ΔP_{max} with AARD of 1.1%, 1.36%, and 0.89%, respectively, while the best-obtained results by five different empirical correlations were 4.12%, 9.4%, and 5.14% for U_{mf}, U_{mff}, and ΔP_{max}. Hosseini et al. (2021) [105] used smart approaches, namely, Gaussian process regression (GPR), multilayer perceptron (MLP), and genetic programming (GP), for modelling minimum fluidization velocity in the tapered fluidized beds. For validation of the models, 675 experimental data were utilized. Considering the Gaussian distribution width of the fluidizing materials in the model led to a significant improvement in modelling minimum fluidization velocity. Saldarriga et al. (2015) [106] investigated the bed to wall heat transfer coefficient for different compositions of particles in a conical spouted bed. It was observed that the bed to surface heat transfer coefficient was the highest for sand particles and decreased consequently with the amount of sawdust in sand particles. It was also found that the heat transfer coefficient increases with air inlet velocity. Abdelmotalib et al. (2016, 2017) [59,107] investigated the heat transfer characteristics in a conical fluidized bed combustor by considering the effect of superficial air velocity. It was observed that the local heat transfer coefficient at an axial distance of 10 cm of the combustor increases with the increase in superficial air velocity.

2.4 PARAMETRIC STUDY ON HYDRODYNAMICS AND HEAT TRANSFER

The hydrodynamic behaviour and heat transfer characteristics in a conical fluidized bed show an immense difference with the change in operating parameters. In order to understand these

two, it is necessary to know the impact of operating parameters on hydrodynamic behaviour. In this section, the review associated with the changes in hydrodynamic characteristics such as minimum fluidization velocity, maximum pressure drop, minimum velocity of full fluidization, maximum velocity of de-fluidization, fluctuation ratio, bed expansion ratio, compressive force, hysteresis, axial voidage and radial voidage with the operating parameters, namely cone angle, initial static bed height, particle density, particle size and fluid velocity are discussed.

2.4.1 Effect of cone angle

Sutherland was the first to research the influence of cone angle on hydrodynamic behaviour [66]. His aim was to study the impact of cone angle on hydrodynamics and results show that tapering reduces the vertical mixing rate in deep beds. Thereafter, plenty of studies were performed to study the effect of cone angle on hydrodynamic behaviour. Gan et al. (2014) [108] studied the effect of cone angle on minimum fluidization velocity and minimum velocity of full fluidization. Their study revealed that with the increase in cone angle, both minimum fluidization velocity and minimum velocity of full fluidization increase. Similar results were also obtained by Katiyar (2017) [109] for the investigation of the hydrodynamic behaviour of coarse particles. Biswal et al. (1984) [110] and Kaewklum and Kuprianov (2008) [111,112] observed analogous results with Katiyar (2017) [109]. They also indicated that pressure drop corresponding to these two velocities increases with the cone angle. Jing et al. (2000) [71] and Rasteh et al. (2015) [72] observed that there was an increase in maximum pressure drop, minimum fluidization velocity and minimum velocity of full fluidization with an increase in the cone angle. Khani (2011) [74], Sau et al. (2007)[81], and Dora et al. (2013) [82] also observed similar results for maximum pressure drop and minimum fluidization velocity. Apart from investigating the effect of cone angle on maximum pressure drop and minimum fluidization velocity, Dora et al. (2013) [82] also studied the effect of cone angle on bed fluctuation ratio and bed expansion ratio. They found that both bed fluctuation ratio and bed expansion ratio decrease with the increase in cone angle. Padhi et al. (2016) [83] reported similar results as Dora et al. (2013) [82]. However, Padhi et al. (2016) [83] did not investigate the effect of cone angle on the fluctuation ratio. Murthy et al. (2009) [73] reported that peak pressure drop, hysteresis, compressive force, the maximum velocity of de-fluidization and critical fluidization velocity increased with the increase in cone angle. But, the fluctuation ratio was found to decrease with the increase in cone angle. Similar results for fluctuation ratio had also been observed by Sau et al. (2009, 2010) [79,80] and Maruyama and Koyanagi (1993)

[78]. Peng and Fan (1997) [70] conducted a series of experiments in a liquid-solid fluidized bed to study the effect of cone angle on the maximum velocity of full fluidization, minimum velocity of partial fluidization and peak pressure drop and found that with the increase in cone angle, pressured drop, maximum velocity of full fluidization and minimum velocity of partial fluidization increases. Hulin et al. (2006) [30] made a numerical study to investigate the effect of cone angle on a gas-solid flow in the axial and radial direction. Both the gas and particle velocity and particle concentration tended to be more uniformly distributed in the radial direction with the increase in the cone angle. Kim et al. (2000) [86] reported that with the increase in taper angle, expansion height of the bed decreases.

2.4.2 Effect of static bed height

The impact of static bed height on various hydrodynamic behaviour is discussed in this sub-section. The bed pressure drop increases with the increase in static bed height keeping all other parameters constant [32,39,71–73,82,83,109,111]. The spouting pressure drop and minimum spouting velocity increase with the increase in stagnant bed height [71]. The minimum fluidization velocity was also found to increase with the increase in static bed height [35,71–73,82,108,109]. Similarly, the minimum velocity of full fluidization increases with the increase in static bed height [72,73,108,109]. However, some researchers predicted that the minimum fluidization velocity was independent of static bed height [74,81]. But, in the study of Biswal et al. (1985) [111], the minimum fluidization velocity was found to decrease with the rise in initial static bed height. On the other hand, the maximum velocity for de-fluidization [73], hysteresis [73,113] and compressive force [73] in the bed increase with the increase in static bed height. Nevertheless, with the increase in static bed height, the bed fluctuation ratio [73,80,83,114,115] and bed expansion ratio [32,35,79,83,113] decreases.

2.4.3 Effect of particle size

The fluctuation ratio decreases for the single-particle size with an increase in particle diameter [80,114,115]. However, a contradictory result was observed by Murthy et al. (2009) [73]. They observed that the bed fluctuation ratio increases with an increase in particle diameter. The effect of particle size in the binary and ternary mixture on the fluctuation ratio was also studied by Dora et al. (2013) [82] and Padhi et al. (2016) [83]. They observed that the fluctuation ratio decreases with an increase in particle diameter or decrease in the percentage of the fine particle in the mixture. The research was also carried out to study the effect of bed particle size on the bed expansion ratio of single particle size and homogeneous and heterogeneous binary and the

ternary mixture of particles [79,82,83,113]. Similar to the fluctuation ratio, the bed expansion ratio also decreases with an increase in particle diameter for single-particle size and binary and the ternary mixture of particles due to the weight of the particles [79,82,83,113]. The hydrodynamic behaviour, such as pressure drop and velocity corresponding to different regimes of the conical fluidized bed, was characterized by the particle size [73,82,83,108,111]. It was observed that pressure drop increases with the increase in particle size [72–74,82,83,111,112,116]. Nevertheless, Biswal et al. (1985) [111] observed that the pressure drop decreases with particle size increases. The minimum fluidization velocity was found to increase with the particle size [72–74,82,108,111]. However, Sau et al. (2008) [84,117] observed that the critical fluidization velocity decreases with the increase in particle size in the average mixture. The minimum velocity of full fluidization was also found to increase with the particle size [72,74,108,112]. Kaewklum and Kuprianov (2008) [112] and Ali and Ghamin (2014) [116] observed that the hysteresis and the compressive force increased with the particle size. Besides that, the effect of particle size on the local heat transfer coefficient was studied by Abdelmotalib et al. (2015) [57]. They found that with an increase in particle size, the heat transfer coefficient decreases.

2.4.4 Effect of superficial air velocity

The effects of air velocity on hydrodynamic behaviour, such as bed fluctuation and expansion ratio, were studied by many researchers [33,35,57,73,79,80,82,111,118,119]. They observed that with the increase in gas velocity, the bed fluctuation and expansion ratio increase. Researchers also investigated the effect of gas velocity on bed pressure drop [70,71,120,121,72,73,75,81,82,84,85,117]. It was observed that the pressure drop first increases till it attains the maximum value and then decreases with an increase in velocity. Abdelmotalib et al. (2015) [57] analysed the effect of superficial gas velocity on bed expansion ratio, pressure drop, bed height and heat transfer. It was concluded that the bed expansion ratio, pressure drop, bed height and heat transfer coefficient increase with superficial air velocity.

2.4.5 Effect of particle density

Hysteresis increases with the increase in particle density [73,113]. Pressure drop also increases as the particle density increases [73,111]. The critical fluidization velocity was also found to increase with particle density [73,84,117]. Nevertheless, the bed expansion ratio decreases as particle density increases [79,113]. The maximum velocity of full fluidization was found to increase with the increase in particle density [73,122].

2.5 DRYING PHENOMENA IN DIFFERENT TYPES OF DRYERS

Thant et al. (2018) [123] reported the drying characteristics in conventional bubbling fluidized bed dryers and observed that the non-uniform mixing of paddy particles in the radial direction was improved when the dryer was inclined at an angle of 15°. Firouzi et al. (2017) [124] experimentally compared the industrial horizontal rotatory dryer (IHRD) with an industrial batch type bed dryer (IBBD) and found that the IHRD was a better option for energy saving with an improvement in the quality of milled rice at an optimum cost. Islam et al. (2021) [125] assessed the performance of an industrial LSU dryer in terms of drying characteristics and drying efficiency. Quality evaluation in terms of head rice yield (HRY) of the milled product was also analyzed. The results revealed that 7.0–10.0 h drying time was required for reducing the parboiled moisture content to 14% (wet basis). The average drying efficiency of the dryers in the selected drying complexes ranged between 50.30% and 59.80%. HRY of dried products contrasted between 50% and 54%. Yahya et al. (2017) [126] developed a solar-assisted fluidized bed paddy dryer integrated with a biomass furnace and reported that specific energy consumption and drying times of paddy were lower in this dryer than conventional solar dryers. Sivakumar et al. (2016) [127] performed a review on fluidized bed drying and reported that the conventional fluidized bed drying methods were more efficient and required less energy instead of the hybrid FBD drying method. Das et al. (2022) [128] studied the drying kinetics of Raw cashew nuts in a bubbling fluidized bed dryer at ambient temperature with bed inclinations of 0°, 15° and 30° using perforated (18.85%) and semi-circular (50%) opening distributor plates. The superficial velocity ranged from 1.4 m/s to 3.2 m/s for batch sizes of 0.5, 1, 2 and 2 kg raw cashew nuts + 2 kg sand. When fluidized alone, the highest fluidization height of raw cashew nuts was 0.31 m for 2 kg inventory, but when mixed with sand, it was found to be 0.48 m at 15° bed inclination with air velocity as 2.5 m/s in 50% opening distributor plate. Average moisture removal was found to be 14.097 and 16.422% in semi-circular and perforated distributor plates, respectively. Yan et al. (2022) [129] experimentally investigated the drying kinetics of biomass in a fluidized bed dryer using electrostatic sensing and digital imaging techniques under a range of air temperatures from 45°C to 75°C at an air velocity from 0.31 m/s to 0.56 m/s. Biomass in the bubble had a higher moisture diffusivity, which was related to the higher temperature of the hot air in the bubble. The results also found that at an air temperature from 45°C to 75°C, the activation energy of biomass in the bubble increased slightly compared to that at the boundary and exterior of the bubble, indicating the divergence in the drying characteristics at different locations. In addition, compared with the gas-solid mass transfer

coefficients of biomass at the boundary and exterior of the bubble, the mass transfer coefficient of biomass in the bubble was larger, which was attributed to the efficient contacts between the biomass particles and the hot air. Furthermore, it was observed from the experimental results that the gas-solid mass transfer depends on the air temperature and air velocity, while the highest air temperature and the highest air velocity might not be the optimal drying condition. Taskin et al. (2021) [130] investigated the drying kinetics of banana slices in a convective air dryer. The drying period was found to decrease as the drying temperature increased, whereas the drying rates decreased with the increase in the drying period. However, the surface temperature of samples dried by 50°C was significantly less than the samples dried by 60 and 70°C. Results showed that the proper use of convective drying in industrial processing might promote the final quality of the product while reducing the energy requirement.

Anand et al. (2021) [131] dried soybean seeds in a fluidized bed dryer (FBD) and microwave-assisted fluidized bed dryer (MFBD). During FBD, the effect of air temperature (30-50°C) and air velocity (1-7 m/s) on drying parameters and some quality attributes (viz. vigor index, germination, fissure and cracking percentage, and seed coat hardness) of dried seeds were analyzed through response surface method. In MFBD, the effect of air temperature and microwave power levels was studied on the drying kinetics and quality parameters at a constant air velocity of 7 m/s. FBD was able to reduce drying time in comparison to the fixed bed position. The germination potential of the seed was found to be higher under all the drying methods (>77%) and low cracking percentage (<20%). Sarker et al. (2021) [132] aimed to investigate the effect of two-stage drying schemes (first stage: fluidized bed drying at 90°C and second stage: i) fluidized bed drying at 50°C, ii) LSU drying at 50°C, and iii) sun drying) on drying characteristics, milling performance, nutritional and sensory quality of three popular local aromatic rice varieties (Chinigura, Kalizira and Katarivog) in Bangladesh. Results indicated that a shorter drying time (only 1.83 to 5 hrs.) was required in the proposed two-stage drying schemes compared to the sun drying method (14 to 16 hrs.). All the proposed two-stage drying yielded higher or comparable percentage of head rice yield (54.13~64.27%) of the studied rice varieties. Amylose, fat, protein and total ash content varied from 23~25.20%, 0.41~0.54%, 7.20~8.70%, and 0.38~3.37%, respectively. The mineral profile of the milled brown and white aromatic rice and the sensory attributes were not influenced by the two-stage drying methods. Nanvakenari et al. (2021) [133] studied the effect of drying conditions such

as temperature and fluidization velocity, and two different types of drying mechanisms (fluidized bed dryer with and without ventilation) were characterized by the drying time, whiteness index, head rice yield, water uptake ratio, and elongation ratio. Their experimental results indicated that a fluidized bed dryer with ventilation significantly increased the head rice yield (from 30 to 505%) and the whiteness index (from 2 to 17%) compared to a fluidized bed dryer without ventilation. The best optimum conditions were related to the lowest drying time and the highest quality parameters. The optimal drying conditions were found to be: 52 °C inlet temperature, 3.1 m/s inlet fluidization velocity (bubble fluidization regime), and fluidized bed dryer with ventilation. At this optimum condition, the values of the experimental test were found to be 218 min (drying time), 74% (head ice yield), 60.7 (whiteness index), 3.15 (water uptake ratio) and 1.84 (elongation ratio) with desirability factor of 0.695. An investigation of drying kinetics in a fluidized bed dryer was also done by Sandip et al. (2021) [134]. Their investigation was on the strength of moisture content, air temperature and air entry speed on the drying kinetics and fluidization height during fluidized bed drying of soybean using an electric heater as a heating medium. They observed from the experimental results that the height of the fluidized bed increased with the increment in inlet air velocity, and fluidization height decreased with lower inlet air velocity. The reduction in the mass flow rate results in an increase in bed height and vice versa for a high mass flow rate. Fluidized bed drying was able to reduce drying time in comparison to the fixed bed, and hence it could be used to reduce heterogeneity in the bed during drying. In drying kinetics, with the increase in drying parameters, rate constants and diffusivity also increased. Luthra et al. (2021) [135] used a fluidized bed and a fixed bed drying systems to study the effects of dehumidification settings (with and without), air temperature (40°C, 45°C, and 50°C), and drying duration (30 min, 45 min, and 60 min) on rice quality and pasting properties in triplicates. Silica gel was used as a desiccant for ambient air dehumidification. The results showed that the range of moisture removal to be 4.5 to 7.1% (dry basis) for 1 hr in a fluidized bed rice drying. The maximum water absorbed by air achieved 0.382 and 0.434 kg for fluidized bed and fixed bed dryers, respectively, after 60 min of drying, at 50°C, and with air dehumidification. The peak viscosity of rough rice was lower for all fluidized bed experiments than for the fixed bed drying experiments. The results showed that head rice yield and rice whiteness did not reduce fluidized bed drying significantly more than fixed bed drying. Head rice yield was negatively correlated with rice whiteness. Ambient air dehumidification improved moisture removal from rough rice and could be employed during humid conditions. Pasting properties also supported the notion

of attaining good quality rice dried in a fluidized bed system compared with a fixed bed drying system. Head rice yield was positively correlated with the peak and trough viscosities signifying the increase in milling yield with the rice water-absorbing capacity and resistance to cooking textural breakdown.

Barathiraja et al. (2021) [136] studied the drying kinetics, physical and biochemical properties of turkey berry at a fluidizing air velocity of 3.6 and 4.2 m/s along with different temperatures of 70, 80, 90 °C, as well as open sun drying (OSD). The parameters such as drying rate, effective moisture diffusivity, activation energy, shrinkage, total colour changes and Vitamin-C were analyzed in detail. The results indicated that the high temperature of 90 °C with a high fluidized velocity of 4.2 m/s was significantly influencing the drying kinetics such as drying rate, effective moisture diffusivity, and activation energy compared to low inlet air velocity (3.6 m/s) as well as open sun drying (OSD). The maximum effective moisture diffusivity was observed at 90°C with a fluidized velocity of 4.2 m/s, and also low volumetric shrinkage was obtained. However, the Vitamin-C losses were more compared to low inlet air velocity (3.6 m/s) as well as an OSD. The low temperature of 70 °C played a key role in quality perspective like physiochemical properties in which minimal total colour change and Vitamin-C losses were observed when the course of the dehydration process. The maximum colour change of the fruits was observed at OSD rather than the fluidized bed conditions. Sun-drying technique and fluidized bed drying technique were also used by Akhtaruzzaman et al. (2021) [137]. Their investigation was to investigate the effect of two options (first option: fluidized bed drying (120–160°C) + sun-drying; second option: fluidized bed drying (120–160°C) + again fluidized bed drying (65 ± 2°C) of two-stage drying on kinetics, energy consumption, quality of dried maize as colour, nutritional properties, and hardness. The drying time was shorter in the case of the second option than in the first option. Effective moisture diffusivity was found to be higher in both options of two-stage drying than control drying. Specific energy consumption was lower in the first option compared to the second option. The colour of dried maize in two-stage options deteriorated significantly. However, the nutritional qualities of dried grain for two-stage drying technique were similar to the control sample. The hardness of the two-stage dried maize was found to be lesser than the control product. Sadaka et al. (2018) [138] aimed to develop and test a custom-made small-scale fluidized bed dryer suitable for moderate farms and capable of drying small and large size grains from high moisture content to a safe storage moisture content. The fluidized bed dryer was used to dry wheat from an initial

moisture content of 23.3%. The effects of the aspect ratio (bed height to bed diameter ratio) of 2, 3, and 4 m/m, the furnace temperature of no heat, 100°C, 150°C, and 200°C and drying duration of 10, 20, 30, 40, 50, and 60 min on the wheat moisture content, drying rate, and dryer efficiency were investigated. The lowest wheat moisture content of 16.3% was observed at the lowest aspect ratio of 2 m/m, the highest furnace temperature of 200°C, and the longest drying duration of 60 min. Conversely, the highest wheat moisture content of 19.0% was observed at the highest aspect ratio of 4 m/m and the no heat condition. The drying rate of 0.47%/min was observed at the lowest aspect ratio of 2 m/m and the furnace temperature of 200°C after 10 min. The maximum dryer efficiency of 63.2% was achieved at the aspect ratio of 4 m/m, the furnace temperature of 200°C. Two empirical models were developed to predict the moisture content of wheat and the dryer efficiency as affected by the aspect ratio, the furnace temperature and the drying duration with the adjusted coefficient of determination of 0.91 and 0.88, respectively. Mujaffar and Ramsumair (2019) [139] reported the drying of pumpkin seeds for the purpose of making pumpkin seed powders in a fluidized bed dryer at 50–80°C. A moisture content of 4–6% (wb) could be achieved by drying seeds for 135, 110, 60 and 40 min at 50, 60, 70, and 80°C, respectively. The drying behaviour was described by the corresponding drying curves, and the Alibas model was found to successfully predict the moisture ratio data for seeds dried at all temperatures. Increasing the temperature increased the drying rate, and drying occurred in the falling-rate period only, with drying at 60–80°C occurring in two distinct periods. Dried seed powders were found to have high protein, fibre and fat contents. Increasing the temperature from 50 to 80°C had an impact on the lightness of the seed powders, but no browning was observed. Seeds developed a roasted odour at temperatures above 60°C. Novrinaldi et al. (2021) [140] carried out unhulled rice drying using a laboratory-scale fluidized bed dryer. A decrease in significant moisture was observed in the first 5 minutes of drying due to the moisture that was still much in the unhulled rice. Drying unhulled rice with each capacity of 1, 2, and 3 kg has an average initial moisture content of 24% and dried for 45 minutes with a final moisture content of 11.68%, 13.13% and 12.13% for capacities of 1, 2 and 3 kg, respectively. Drying with a capacity of 3 kg evaporated water which was greater by 356.1 gr compared to 2 kg capacity of 217.5 gr and 1 kg capacity by 123.2 gr respectively. However, the largest percentage of water evaporation occurred at a capacity of 1 kg, which was 12.3%, while the mass of 2 and 1 kg of 10.875% and 11.87%. The relative humidity of the drying chamber was greatly influenced by the mass of water that was evaporated from the dried material and also the relative humidity of the surrounding environment. The relative humidity

in the drying chamber was found to rise as the unhulled rice began to be fed, and the temperature decreased.

Apart from comparing fluidized bed dryers with other conventional dryers, researchers have also studied the influence of operating parameters on drying characteristics [22,141–145]. Tohidi et al. (2017) [141] observed better efficiency at higher temperatures and lowered relative humidity, but the higher drying rate leads to damage to the kernel. Khanali et al. (2018) [142] investigated the effects of drying temperature, weir height and inlet dry mass flow rate of solid on drying characteristics and observed that with an increase in the inlet temperature and weir height, the moisture content decreases, whereas the opposite trend was seen for inlet dry mass flow rate of solid. The effect of temperature, particle size and velocity of gas on drying characteristics was also studied by Xia et al. (2017) [22]. They mentioned that the better heat transfer zone was near the gas distributor zone, and in this zone, the system quickly reached thermal equilibrium. Darvishi et al. (2015) [143] reported that the increase in the inlet air temperature and velocity decreased the drying time. However, no significant effect of inlet air velocity was found on the bulk density and shrinkage of the soya bean. Pourbagher et al. (2016) [144] investigated the effect of milling quality and drying rate in a fluidized bed dryer with two types of heaters and reported that in infrared drying, the quality of paddy grain is better in terms of the lower crack than conventional heating. Tatemoto et al. (2018) [145] conducted the drying performance of large particles in a fluidized bed dryer under reduced pressure, and the results were compared with the hot air drying method. It was found to be difficult to measure the drying rate under reduced pressure. So, they injected distilled water with the drying material. The drying rate was found to be higher in fluidized bed drying than in the hot air-drying method. Numerical simulation-based research was also carried out to study the effect of operating parameters on drying characteristics in conventional fluidized bed dryers [146–148].

The above-mentioned literature review focused on the drying characteristics of fluidized bed dryers and other drying techniques. There are a few studies on the drying characteristics of conical fluidized beds available in the literature. Sutar and Kumar (2012) [149] show the effect of the distributor design of a conical fluidized bed dryer and reported that punched plate distributor was a better choice in terms of energy consumption, minimal drying time and proper mixing. Hematian and Hormozi (2015) [150] investigated the drying kinetics of coated sodium percarbonate particles in a conical fluidized bed dryer and reported that the moisture content ratio continuously falls with respect to time. Apart from that, only a few researchers were

associated with the study of internals on drying characteristics in fluidized bed dryers. Srinivasakannan et al. (2012) [151] used an internal to study the drying kinetics as well as mixing behaviour of two phases. They observed that there was a reduction of axial mixing of solids with the use of a spiral as an internal. Thant et al. (2015) [152] reported that the drying time is reduced with the use of a spiral as an internal.

2.6 ENERGY AND EXERGY ANALYSIS OF DRYING

Many researchers studied energy and exergy analysis regarding the different drying materials using different drying techniques. Akpinar (2004) [153] performed a thermodynamic analysis of red pepper slices drying. They observed no significant variation in the exergy efficiency and the energy utilization ratio (EUR) with all drying temperatures. However, energy utilization (EU), exergy inlet, exergy outlet and exergy destructions were found to increase with the increase in drying air temperature. Performance evaluation of a cyclone type dryer through energy and exergy analysis was conducted by Akpinar et al. (2005, 2006) [154,155]. Their results indicated that an increase in air temperature and velocity results in an increase in exergy efficiency. They also observed that the increasing trend of exergy efficiency with drying time was parabolic for potato slice drying, whereas the trend was found to be linear for pumpkin drying [155]. A similar result for exergy efficiency with drying time was also observed by Nazghelichi et al. (2010) [156] in their thermodynamic analysis of carrot cubes drying. They observed that with an increase in drying time, the exergy efficiency increases. However, EU, EUR and exergy destruction for the process decreases continuously with the drying time. Energy and exergy analysis of paddy drying in a fluidized bed dryer was also conducted by Sarker et al. (2015) [157]. They reported that nearly 32-37% of exergy was utilized in the process of paddy drying. Corzo et al. (2008) [158] optimized a drying system for coroba slices by incorporating energy and exergy analysis. They reported that the thermodynamic inefficiency could be reduced by controlling the exergy outflow of the dryer as well as exergy loss of materials. They also suggested that the optimal air temperature and drying air velocity for dying coroba slices are to be maintained at 93°C and 1.18 m/s to stimulate the drying process. Darvishi et al. (2018) [159] conducted a performance evaluation of mushroom drying in a fluidized bed dryer. Their experimental investigation was for three drying temperatures of 30, 40 and 50 °C, respectively, and three air velocities such as 3, 5, and 7 m/s. They observed that the energy consumption and exergy loss increase with an increase in air velocity and temperature. Devani and Yalamerthi (2019) [160] also investigated the energy and exergy

analysis of a multistage fluidized bed dryer. The maximum exergy efficiency was observed to be 0.64. Pattanayak et al. (2019) [161] evaluated the energy and exergy analysis in a vertical fluidized bed paddy dryer. The transient behaviour of EU, EUR and exergy destruction was investigated. It was observed that when the drying time increases, the EU, EUR and exergy destruction decreases. On the other hand, the exergy efficiency was found to increase with drying time. Handayani et al. (2020) [162] conducted energy and exergy analysis of celery leaves to determine the performance of the system, among others, energy utilization, energy efficiency, and efficiency of the exergy. Fresh celery leaves were dried at 50°C, 60°C and 70°C in a continuous vibrating fluidized bed dryer with a dimension of 2350 mm × 300 mm. The energy utilization and energy utilization ratio were found to increase with drying air temperature. Nevertheless, the exergy efficiency decreases with the increase in drying air temperature. The average energy utilization ratio at 50°C is 0.0768, 60°C is 0.1199 and 70°C is 0.1682. Exergy efficiencies decrease with increasing temperature. Average exergy efficiencies were 0.19, 0.16 and 0.17 for 50°C, 60°C and 70°C drying temperatures, respectively. Luthra and Sadaka (2021) [163] carried out energy and exergy analysis in a fluidized bed drying of rough rice by incorporating drying air temperature (40°C, 45°C, 50°C), drying bed condition (fluidized and fixed), drying duration (30 min, 45 min, 60 min), and ambient air dehumidification (yes, no) as parameters. The minimum and maximum EU values were 0.01 kJ/s and 0.55 kJ/s for drying at fixed bed drying at 40°C for 30 min with dehumidification and at 50°C for 60 min under fluidized bed condition without dehumidification, respectively. At the drying process's primary stages, fluidized bed drying had higher exergy efficiency, energy utilization, and energy utilization ratio than the fixed bed drying method. 40°C air temperature using fluidized bed drying with or without ambient air dehumidification was found to be worked best as per the energy and exergy utilization in the drying system. Silva et al. (2021) [164] performed energy and exergy analysis of corn grains in a mixed cabin solar dryer. The dryer operated during four consecutive days in the spring equinox, with and without load and with and without the electrical heater. The thermal efficiency and the exergy efficiency presented opposite trends. Thermal efficiency was found to be increasing with the decrease in exergy efficiency. When comparing the system with and without load, it was observed that the former presented higher thermal efficiency due to the higher humidity of the air and lower exergy efficiency due to the energy required to dry the products. Islam et al. (2021) [125] performed energy and exergy analysis in an industrial LSU dryer. Energy analysis indicated that specific electrical and thermal energy varied between

0.34–0.51 and 14.41–28.81 MJ/kg H_2O evaporated, respectively. Exergy inflow and exergy losses were found to reduce during the last 2.0–3.0 h of drying the parboiled paddy, while exergy outflow gradually increased throughout the drying period. The exergy efficiency of the dryers varied from 43.63% to 67.21% for parboiled paddy drying. Çelik et al. (2021) [165] dealt with the energy and exergy analyses of the drying process of a corn dryer. The energy utilization (EU), energy utilization ratio (EUR), specific energy consumption (SEC), exergy efficiency values were calculated. The results showed that energy utilization ratios increased with the gas velocity, and the maximum exergy efficiency was observed at a high velocity. Taskin et al. (2021) [130] investigated the exergy analysis of banana slices in a convective air dryer. Depending on the drying temperatures, the maximum energy efficiency (22.18%) was attained at 50 °C, while the minimum value (17.41%) was at 70 °C. Mondal et al. (2021) [166] attempted to observe energy and exergy analysis of a mixed flow dryer for drying freshly harvested maize grain. The energy utilization ratio decreased with the increase of drying temperature at 3.0 m/s air velocity, while differing surveillance was noticed for 70 and 80°C at 6.0 m/s air velocity. The energy efficiency of the research mixed flow dryer vacillated from 26.52 to 71.75% over the temperature range. The magnitude of exergy inflow, exergy outflow and exergy loss varied as an increasing trend with the upturn of drying temperature. Beigi et al. (2021) [167] carried out energy and exergy analyses for deep bed drying of paddy in a convective dryer. Drying experiments were carried out at drying air temperatures of 40, 50 and 60 °C, and air flow rates of 0.008, 0.012 and 0.017 $m^3\ s^{-1}$. Energy utilization, energy utilization ratio and energy efficiency were obtained to be in the range of 0.061–0.1412 kJ s^{-1}, 22.41–46.81% and 4.37–8.56%, respectively. Exergy loss decreased continually with drying time, and the average values ranged from 0.019 to 0.081 kJ s^{-1}. Exergy efficiency varied in the range of 32.44–66.91%. Energy and exergy efficiency were improved at low temperature–low flow rate and high temperature–high flow rate, respectively. Golpour et al. (2020) [168] focused on the evaluation of energy and exergy in the convective drying of potato slices. Experiments were conducted at four air temperatures (40, 50, 60 and 70°C) and three air velocities (0.5, 1.0 and 1.5 m/s) in a convective dryer, with circulating heated air. The influence of temperature and air velocity was investigated in terms of energy and exergy (energy utilization [EU], energy utilization ratio [EUR], exergy losses and exergy efficiency). Results indicated that EU, EUR and exergy losses decreased along drying time, while exergy efficiency increased. The specific energy consumption (SEC) varied from 1.94×10^5 to 3.14×10^5 kJ/kg. The exergy loss varied in the range of 0.006 to 0.036 kJ/s, and the maximum exergy efficiency obtained was 85.85%

at 70°C and 0.5 m/s, while minimum exergy efficiency was 57.07% at 40°C and 1.5 m/s. Moreover, the values of exergetic improvement potential (IP) rate changed between 0.0016 and 0.0046 kJ/s and the highest value occurred for drying at 70°C and 1.5 m/s, whereas the lowest value was for 70°C and 0.5 m/s. Suherman et al. (2020) [169] proposed a hybrid solar cassava starch dryer and experimentally analyzed energetic and exergetic efficiencies at three different drying temperatures. The maximum overall energetic efficiency was 20.82%. The fluctuations in exergetic flows were influenced by solar radiation during drying, and the overall exergetic efficiency ranged between 25.1% and 73.8%.

2.7 RESEARCH GAP AND SCOPE FOR THE PRESENT INVESTIGATION

As evident from the literature review, studies on the hydrodynamic behaviour of various particles in conventional fluidized beds have been done experimentally or numerically. Experimental and simulation research on hydrodynamics in conical fluidized beds have been reported by a few researchers. In addition, the effect of cone angle on hydrodynamic behaviour in bubbling fluidized beds by considering different inventories was also studied by a few researchers [74,82,108]. The literature also shows that experimental and numerical investigations of heat transfer characteristics in conical fluidized beds are rare [57,60,61,107]. Nevertheless, the effect of cone angle on heat transfer characteristics in fluidized bed risers is to be explored. Furthermore, the interphase heat transfer coefficient is not deeply understood by previous literatures [57,60,61,107]. It is a fascinating phenomenon in practical applications in industries, such as drying, combustion etc. Again, from the practical application point of view, one of the applications of a fluidized bed riser is the drying process. For that, various aspects of the literature on fluidized bed dryers and other drying techniques have been reviewed. The majority of the available literature was focused on investigations into the performance of drying characteristics and the calculation of energy and exergy of freshly harvested food grains in conventional fluidized beds and other drying techniques. However, drying of paddy in conical fluidized bed dryers along with the effect of the cone angle on the quality of drying has not received much attention. Only a few works of literature were found to deal with the drying characteristics of placebo and coated sodium percarbonate in conical fluidized bed dryers, respectively [149,150]. These literatures did not take into account the investigation of drying characteristics by incorporating the effect of cone angle. Nonetheless, the study of thermal and blower energy consumption in the conical fluidized bed by incorporating different cone angles is seldom reported in the open literature. Its energy

consumption, in the context of fluidized bed drying, is a vital quantity and a reduction of this leads to a decrease in capital cost. Besides that, the nutritional value and milling quality which depends upon the quality of drying, are also essential for human health. As the conical fluidized bed system has given outstanding benefits over the conventional fluidized beds regarding hydrodynamics, hence there is a scope of doing research on bubbling fluidized bed dryers for drying agricultural products by considering different cone angles so that drying time and energy consumption can be reduced. Further, the incorporation of an internal inside a fluidized bed may enhance the drying characteristics and reduce energy consumption. Literature that discusses the effect of a spiral or, for that matter, any internal on the performance of drying characteristics in the context of conical bubbling fluidized bed dryers are limited. Therefore, there is a scope for studying the drying characteristics in fluidized bed dryers by incorporating a spiral as an internal. Also, in the available literature, it is remarked that energy intensiveness is the main issue in the context of the drying process. Energy and exergy analysis provides the necessary information about energy intensiveness. Information regarding conical fluidized bed dryers about exergy and energy analysis is insubstantial. Literature related to investigating the effect of operating parameters such as spiral and cone angles on energy and exergy analysis in conical bubbling fluidized bed paddy dryers is limited. With these outcomes of past studies, the present investigation is therefore taken up with the following objectives-

i. To investigate the hydrodynamic behaviour and heat transfer characteristics of sand particles in atmospheric bubbling fluidized bed risers with different cone angles, numerically and experimentally in order to develop an effective bubbling fluidized bed riser.

ii. To investigate the performance evaluation of drying characteristics of paddy particles with different operating parameters such as inlet air velocity, the mass of paddy and inlet air temperature.

iii. To study the effect of a spiral as an internal and cone angle on hydrodynamics and drying characteristics of paddy granules with varying inlet air temperature, superficial air velocity and bed inventory.

iv. To conduct the thermo-economic study of the paddy drying process under various operating parameters such as inlet temperature, inventory, particle size, spiral and cone angle.

The results and discussion of the first objective will be outlined in chapter 5. The investigation of the second and third objectives will be discussed in chapter 6, and the detailed investigation of the fourth objective will be discussed in chapter 7.

2.8 CHAPTER CONCLUSION

In this chapter, the literature related to numerical simulation and experimental investigation of hydrodynamic behaviour and heat transfer characteristics in the aspect of various fluidized bed risers was employed. The literature analogous to drying characteristics, thermo-economic analysis, milling and drying quality of different agricultural products in various drying chambers was also discussed. In addition, the research gap and scope of the present investigation were also outlined. In the subsequent chapter, the numerical simulation modelling to accomplish the objectives will be discussed.

3

Numerical simulation and procedure

3.1 Introduction

3.2 Numerical simulation of dryers

3.3 Governing equations and their constitutive relationships

3.4 CFD model and formulation

3.5 Numerical simulation procedure

3.6 Chapter conclusion

CHAPTER 3

NUMERICAL SIMULATION AND PROCEDURE

3.1 INTRODUCTION

In this chapter, the numerical simulation of fluidized bed dryers is discussed. Section 3.2 describes the numerical model for the simulation used in the present study. Section 3.3 deals with the governing equations and constitutive equations incorporated with the numerical simulation for all dryers. The CFD model and its formulation are discussed in section 3.4. Further, the solution procedure for the numerical investigation is discussed in section 3.5. Finally, the chapter is summarized in section 3.6.

3.2 NUMERICAL SIMULATION OF DRYERS

Computational fluid dynamic (CFD) simulation was carried out to investigate the hydrodynamics and heat transfer characteristics in the three dryers. Both 2-D and 3-D geometries were modelled, and simulations were carried out at various working parameters. In all simulations, the sand and paddy particles were used as the granular phase, and the air was used to fluidize the sand and paddy particles. The properties of air, sand and paddy particles used in the simulation are displayed in Table 3.1. It ought to be noted that the geometry, generation of mesh, model setup and simulations were made on ANSYS 14.5 software. Ansys is found to be more convenient than any other simulation software for connecting different simulations for multi-phase problems. There are numerous mesh alternatives available, which allows us to fine-tune our mesh and subsequent elements to a high degree than other simulation techniques. The mesh options, when paired with the contact options, allow for the simple and systematic modelling of seemingly complex geometry. We can connect elements with different nodal interfaces using the contact definition. However, with other numerical tools used at work, the mesh must match component interfaces, which adds complexity to the mesh production. Apart from these, Ansys has several advantages over other software, such as it's easier to use, it doesn't require users that necessarily understand either mechanics or finite elements, designXplorer, many parameters on mesh quality can be handled, it has good compatibility with fluid-solid interactions, it saves simulating time with accurate and efficient simulation processing, it provides solutions for industries to reduce overall costs, conserve energy, minimize environmental impacts, meet higher regulatory standards, and streamline product

development and operations through a range of initiatives, it helps us to make faster and better decisions. It provides accurate results and high computing power and validates its quality. Besides, they ensure little to no errors and offer the great possibility to innovate and produce optimized products using industry-grade, efficient solvers.

Initially, the pseudo-2-D model of five dryers ($\alpha = 0°$, 5°, 10°, 15° and 20°) was considered to check the feasibility of the dryers with the use of sand particles as a granular phase. Furthermore, the numerical results of the dryers were compared with the experimental results. The geometry and mesh files of the 2-D model are shown in Fig. 3.1. For the mesh analysis of the 2-D model, quadrilateral mesh with a bias factor of 10 to the wall was used. However, it was anticipated that 3-D simulations would provide more reliable results than 2-D simulations for the experimental results. Therefore, 3-D simulations were also carried out in the five dryers ($\alpha = 0°$, 5°, 10°, 15° and 20°). Furthermore, 3-D numerical simulations were in a conical dryer of 10° cone angle performed under various operating parameters. The mesh files of the 3-D simulation are shown in Fig. 3.2. Inflation function was used for all the dryers with first layer thickness 0.0001 – maximum layers 18 – growth size 1.2. Multizone as hexahedral cells was used in the core region as well as near the wall. A mapped face meshing option was also used for uniform sizing with a maximum face size limit of 0.015.

Table 3.1 Properties and characteristics of the air, sand and paddy used in the simulations

Properties	**Value**
Density of air in kg/m^3	1.225
Density of sand in kg/m^3	2660
Density of paddy in kg/m^3	1200
Thermal conductivity of air in W/m-K	0.025
Thermal conductivity of sand in W/m-K	0.25
Thermal conductivity of paddy in W/m-K	0.0454
Specific heat of air in J/kg-K	1005
Specific heat of sand in J/kg-K	837
Specific heat of paddy in J/kg-K	737
Viscosity of air in Pa-s	1.86×10^{-5}
Solid volume fraction	0.5

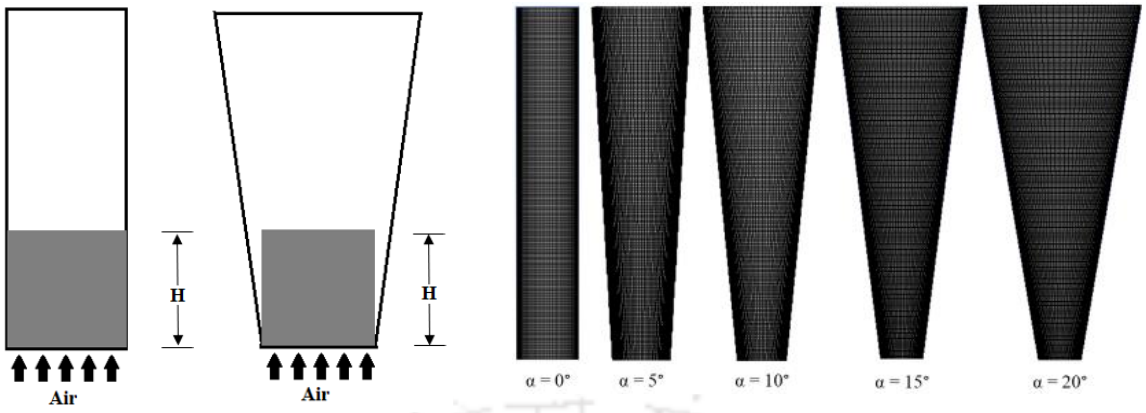

Figure 3.1: (a) Geometry, and (b) mesh for the 2-D model

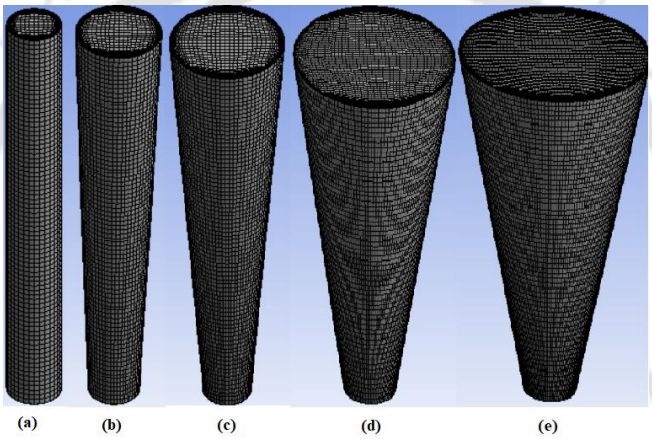

Figure 3.2: Configuration of mesh for the 3-D geometries, (a) α = 0°, (b) α = 5°, (c) α = 10°, (d) α = 15° and (e) α = 20°

3.3 GOVERNING EQUATIONS AND THEIR CONSTITUTIVE RELATIONS

The description of gas-solid fluidized beds as two interpenetrating continua is the principle of two-fluid models. One continuum represents the gas phase in the bed, while the other represents the particle phase (also known as the particulate or solid phase). This enables the Eulerian description of both phases without the need for specific Lagrangian tracking of each particle in the bed. As a result, when using the two-fluid approach for a fluidized bed reactor, the governing equations of continuity, momentum, and thermal energy balance for the gas and particle phases can be employed to describe the phenomena mathematically. In this aspect, the particle phase was assumed as a fluid with efficient transport qualities in the momentum equations. In general, the conservation equations of mass, momentum and thermal energy balance for each phase were solved together with a differential equation for granular temperature transfer based on KTGF to simulate the behaviour of fluidized bed reactors.

Therefore, the governing equations for each phase and constitutive equations associated with the governing equations are provided in this section as follows. The equations were taken from Ansys.

Continuity equation:

For gas,

$$\frac{\partial}{\partial t}\left(\varepsilon_g \rho_g\right)+\nabla.\left(\varepsilon_g \rho_g \vec{v}_g\right)=0 \tag{3.1}$$

For solid,

$$\frac{\partial}{\partial t}\left(\varepsilon_s \rho_s\right)+\nabla.\left(\varepsilon_s \rho_s \vec{v}_s\right)=0 \tag{3.2}$$

Volume fraction equation:

$$\varepsilon_g+\varepsilon_s=1 \tag{3.3}$$

Momentum equation:

For gas,

$$\frac{\partial}{\partial t}\left(\varepsilon_g \rho_g \vec{v}_g\right)+\nabla.\left(\varepsilon_g \rho_g \vec{v}_g \vec{v}_g\right)=-\varepsilon_g \nabla P_g+\nabla \bar{\bar{\tau}}_g+\varepsilon_g \rho_g \vec{g}+\vec{F}_{d.g}+\vec{F}_{\mathrm{l}.g}+\vec{F}_{\mathrm{vm}.g} \tag{3.4}$$

For solid,

$$\frac{\partial}{\partial t}\left(\varepsilon_s \rho_s \vec{v}_s\right)+\nabla.\left(\varepsilon_s \rho_s \vec{v}_s \vec{v}_s\right)=-\varepsilon_s \nabla P_g-\nabla P_s+\nabla \bar{\bar{\tau}}_s+\varepsilon_s \rho_s \vec{g}+\vec{F}_{d.\mathrm{s}}+\vec{F}_{\mathrm{l.s}}+\vec{F}_{\mathrm{vm.s}}+\bar{S}_s \tag{3.5}$$

Energy equation:

For gas,

$$\frac{\partial}{\partial t}\left(\varepsilon_g \rho_g h_g\right)+\nabla.\left(\varepsilon_g \rho_g \vec{v}_g h_g\right)=\nabla.\left(\varepsilon_g k_g{}^{eff} \nabla T_g\right)+Q_{sg} \tag{3.6}$$

For solid,

$$\frac{\partial}{\partial t}\left(\varepsilon_s \rho_s h_s\right)+\nabla.\left(\varepsilon_s \rho_s \vec{v}_s h_s\right)=\nabla.\left(\varepsilon_s k_s \nabla T_s\right)-Q_{sg} \tag{3.7}$$

k-epsilon turbulence model:

The k-epsilon models were used to govern the turbulence model as it is widely used in two-phase gas-solid fluidized bed turbulent flow models. This equation is defined as follows-

$$\frac{\partial}{\partial t}(\rho_m k)+\nabla.(\rho_m \vec{v}_m k)=\nabla.(\alpha_k \mu_t \nabla k)+G_{k,m}-\rho_m \varepsilon \tag{3.8}$$

$$\frac{\partial}{\partial t}(\rho_m \varepsilon)+\nabla.(\rho_m \vec{v}_m \varepsilon)=\nabla.(\alpha_\varepsilon \mu_t \nabla \varepsilon)+\frac{\varepsilon}{k}(c_{1\varepsilon}G_{k,m}-c_{2\varepsilon}\rho_m \varepsilon) \tag{3.9}$$

where,

$C_{1\varepsilon}$=1.44, and $C_{2\varepsilon}$=1.9.

The conical fluidized bed is divided into two main regimes: a dilute region in the core and hump (top surface) and a dense region near the wall. In this type of bed, additional stresses are developed by the sidewall, which is accompanied by a reduced pressure gradient. However, in the conventional fluidized bed, the development of stress is not seen. These additional stresses are introduced into the solid phase momentum equation and expressed as the solid source term (S_s). The solid source term expression for both these two regimes is expressed as [32,33,122,170]:

$$S_s=(K-1)\varepsilon_s \rho_s g \tag{3.10}$$

$$K=\begin{cases} K_a & \varepsilon_g < 0.8 \\ K_c & \varepsilon_g \geq 0.8 \end{cases} \tag{3.11}$$

where, K_a is defined as the ratio of the pressure drop in a tapered fluidized bed to that in a columnar bed. Previous studies show that the numerical results agree with the experimental results for the value of K_a = 0.7, so in the present study K_a = 0.7 is considered. On the other hand, the parameter K_c is a function of some operating parameters. For solving problems, the value K_c was assumed to be a constant value of 1 in the present study.

$$K_a=\frac{\Delta P_{tapered}}{\Delta P_{columnar}} \tag{3.12}$$

$$K_c=f(\varepsilon_g,\rho_s,d_s,\rho_g,\mu_g,\vec{v}_g) \tag{3.13}$$

$$\vec{F}_{d.g}=\beta_{gs}(\vec{v}_s-\vec{v}_g),\quad \vec{F}_{d.s}=-\vec{F}_{d.g} \tag{3.14}$$

$$\vec{F}_{l.g}=0.5\rho_g \varepsilon_s(\vec{v}_s-\vec{v}_g).(\nabla\times\vec{v}_g),\quad \vec{F}_{l.s}=-\vec{F}_{l.g} \tag{3.15}$$

$$\vec{F}_{vm.s}=-\vec{F}_{vm.g} \tag{3.16}$$

Syamlal-O'Brien drag model (1988) [36]:

$$\vec{F}_{\text{vm}.g} = 0.5\rho_g \varepsilon_s \left(\frac{D\vec{v}_s}{Dt} - \frac{D\vec{v}_g}{Dt} \right) \tag{3.17}$$

$$\beta_{gs} = \frac{3}{4} \frac{\varepsilon_g \varepsilon_s \rho_g}{v_{r,s}^2 d_s} C_D \left(\frac{\text{Re}_s}{v_{r,s}} \right) \left| \vec{v}_s - \vec{v}_g \right| \tag{3.18}$$

$$C_D = \left(0.63 + \frac{4.8}{\sqrt{\text{Re}_s / v_{r,s}}} \right)^2 \tag{3.19}$$

$$v_{r,s} = 0.5 \left[A - 0.06\,\text{Re}_s + \sqrt{(0.06\,\text{Re}_s)^2 + 0.12\,\text{Re}_s\,(2B - A) + A^2} \right] \tag{3.20}$$

$$A = \varepsilon_g^{4.14} \text{ and } B = 0.8\varepsilon_g^{1.28} \text{ for } \varepsilon_g \le 0.85 \text{ and } B = \varepsilon_g^{2.65} \text{ for } \varepsilon_g > 0.85 \tag{3.21}$$

As the thermodynamic temperature of the gas can be determined by the random fluctuation and collision of gas particles, similar to that, the granular temperature of solid particles can also be determined. It is defined as the one-third of the square of fluctuation velocity of particles, i.e.

$$\Theta_s = \frac{1}{3} v_s'^2 \tag{3.22}$$

Kinetic fluctuation energy:

$$\frac{3}{2} \left[\frac{\partial}{\partial t} (\rho_s \varepsilon_s \Theta_s) + \nabla . (\rho_s \varepsilon_s \vec{v}_s \Theta_s) \right] = (P_s \bar{\bar{I}} + \bar{\bar{\tau}}_s) : \nabla \vec{v}_s + \nabla . (k\Theta_s \nabla \Theta_s) - \gamma \Theta_s + \phi_{gs} \tag{3.23}$$

Fluctuating energy exchange between gas and solid:

$$\phi_{gs} = -3\beta_{gs}\Theta_s \tag{3.24}$$

Collisional dissipation of energy:

$$\gamma \Theta_s = \frac{12(1 - e_{ss}^2) g_{o,ss}}{d_s \sqrt{\pi}} \rho_s \varepsilon_s^2 \Theta_s^{3/2} \tag{3.25}$$

Diffusion coefficient of energy:

$$k\Theta_s = \frac{150\rho_s d_s \sqrt{\Theta_s \pi}}{384(1 + e_{ss}) g_{o,ss}} \left[1 + \frac{6}{5} g_{o,ss} \varepsilon_s (1 + e_{ss}) \right]^2 + 2\rho_s \varepsilon_s^2 d_s (1 + e_{ss}) g_{o,ss} \sqrt{\frac{\Theta_s}{\pi}} \tag{3.26}$$

Solid pressure:

$$P_s = \rho_s \varepsilon_s \Theta_s + 2\rho_s (1 + e_{ss}) \varepsilon_s^2 g_{o,ss} \Theta_s \tag{3.27}$$

Radial distribution function:

$$g_{o,ss} = \frac{1+2.5\varepsilon_s + 4.59\varepsilon_s^2 + 4.52\varepsilon_s^3}{\left[1-\left(\frac{\varepsilon_s}{\varepsilon_{s,\max}}\right)^3\right]^{0.678}} \tag{3.28}$$

Collision viscosity:

$$\mu_{s.\mathrm{col}} = \frac{4}{5}\varepsilon_s d_s \rho_s (1+e_{ss}) g_{o,ss}\sqrt{\frac{\Theta_s}{\pi}} \tag{3.29}$$

Solids bulk viscosity [171]:

$$k_s = \frac{4}{3}\varepsilon_s d_s \rho_s (1+e_{ss}) g_{o,ss}\sqrt{\frac{\Theta_s}{\pi}} \tag{3.30}$$

The frictional viscosity, as defined by Schaeffer [172] is

$$\mu_{s.\mathrm{fr}} = \frac{P_{fr}\sin(\phi)}{\sqrt{I_{2D}}} \tag{3.31}$$

where, P_{fr} is the frictional pressure and can be determined from an equation given by Johnson and Jackson (1987) [173].

$$P_{fr} = Fr\frac{(\varepsilon_s - \varepsilon_{s,cr})^n}{(\varepsilon_{s,\max} - \varepsilon_s)^p},\ Fr = 0.05,\ n = 2,\ p = 5 \tag{3.32}$$

where, *Fr*, *n* and *p* are empirical constants.

$$I_{2D} = \frac{1}{6}\left[(D_{xx}-D_{yy})^2 + (D_{yy}-D_{zz})^2 + (D_{zz}-D_{xx})^2\right] + D_{xy}^2 + D_{yz}^2 + D_{zx}^2 \tag{3.33}$$

$$D_{ij} = \frac{1}{2}\left[\nabla\vec{v}_s + (\nabla\vec{v}_s)^T\right] \tag{3.34}$$

The interphase heat transfer characteristic plays an important role in predicting the wall to bed heat transfer coefficient. In the simulation, the following equation was used to calculate the interphase heat transfer coefficient, which is strongly dependent upon the Nusselt number of solid particles. Nevertheless, it is difficult to calculate the interphase heat transfer coefficient experimentally.

$$h_{sg} = \frac{Nu_s k_g^{eff}}{d_s} \tag{3.35}$$

where, Nu_s is the solid phase Nusselt number, and Gunn's (1978) [174] expression was used to calculate this non-dimensional number showing as a function of air voidage, Reynold number and Prandtl number.

$$Nu_s = \left(7 - 10\varepsilon_g + \varepsilon_g^2\right)\left(1 + 0.7\,\mathrm{Re}_s^{0.02}\,\mathrm{Pr}^{1/3}\right) + \left(1.33 - 2.4\varepsilon_g + 1.2\varepsilon_g^2\right)\mathrm{Re}_s^{0.7}\,\mathrm{Pr}^{1/3} \tag{3.36}$$

$$\mathrm{Re}_s = \frac{\rho_g d_s \varepsilon_g \left|\vec{v}_s - \vec{v}_g\right|}{\mu_g} \tag{3.37}$$

$$\mathrm{Pr} = \frac{\mu_g C_{p,g}}{k_g} \tag{3.38}$$

$$k_g^{eff} = \left(1 - \sqrt{\varepsilon_s} \Big/ \varepsilon_g\right) k_g \tag{3.39}$$

3.4 CFD MODEL AND FORMULATION

In this context, the Eulerian-Eulerian approach, coupled with the kinetic theory of Granular flow (KTGF), was employed to analyze the hydrodynamic behaviour and heat transfer characteristics across the fluidized beds. Similar to the kinetic theory of gases, the kinetic theory of granular flow (KTGF) helps us to determine the solid pressure, bulk viscosity, and collision frequencies among particles. They are substantially dependent upon granular temperature. The granular temperature of solid particles makes it feasible to explore the hydrodynamic behaviour and heat transfer characteristics across the fluidized bed dryers. In this approach, both the primary and secondary phases are mathematically considered as continuous interpretations. In the simulation of two-phase problems, the volume fraction of both phases cannot hold the same regions simultaneously, and the sum of both phase's volume fractions is considered one.

One set of momentum, mass and energy equations was solved for each phase, in which the right-hand side of the momentum equations was interconnected by interphase exchange term. The interphase drag coefficient was modelled by using the Syamlal-O'Brien [58] drag model, and the reason for considering the drag model will be described in the next chapter. The lift force was not considered in this present investigation. Its effect is prominent only when the diameter of particles is much larger, whereas the largest diameter of particles in the present study was taken as 600 μm only. The virtual mass was also neglected. The bulk viscosity was

assessed from an equation provided by Lun et al. (1984) [171], which accounts for particles' resistance to expansion and contraction. Schaeffer's (1987) [172] equation was applied for the frictional viscosity model. This equation is applicable for the very dense flow of particles when the volume fraction of particles approaches the maximum packing limit, which is 0.63. Since the secondary phase density is much higher than that of the primary phase, therefore, Schaeffer equation was used. The solid pressure comprises two terms: the primary term being the kinetic term, and the subsequent term originates from particle collisions. In fluidized bed simulation, solid pressure was determined from a state equation similar to the state equation for gases in the Van der Waals equation, as Pidduck et al. (1939) [175] suggested.

3.5 NUMERICAL SOLUTION PROCEDURE

The conservation equations were solved by available software ANSYS FLUENT 14.5. In ANSYS FLUENT, the finite volume method is used to discretize the equations. Both hydrodynamic behaviour and heat transfer characteristics across the three fluidized bed dryers were investigated with proper initial and boundary conditions. A phase coupled SIMPLE algorithm was used for pressure velocity coupling. However, for the unsteady formulation, the second-order implicit scheme was used. The convergence criteria for residual between two iterations for mass and momentum are set to 10^{-3} and energy to 10^{-6}. The time step used for performing the simulation was taken as 10^{-3} s. In the first instance, the 2-D numerical investigations of hydrodynamic behaviours such as bed pressure drop of five dryers (α = 0°, 5°, 10°, 15° and 20°) were investigated, and the results were compared. After that, the 2-D numerical investigations of hydrodynamic behaviours such as bed pressure drop and the pressure drop along the height of five dryers were investigated and compared with the experimental results. The simulations for hydrodynamics were carried out for 30 s in which solutions were converged at 10 s, and afterwards, the time-average value from 10 to 30 s was taken.

In this 3-D numerical analysis, simulations were performed on five dryers with three inlet air velocities such as 1, 1.5 and 2 m/s and a one-bed height of 30 cm. Sand particle with an average size of 435 µm was used for this simulation. The hydrodynamic behaviour such as bed expansion ratio, pressure drop, axial solid volume fraction, radial solid volume fraction and radial solid velocity was calculated for all these operating parameters, and probable numerical results were compared with the experimental results. In order to study the heat transfer characteristics, constant hot air at 65°C was applied through the inlet of the dryer at the three

air velocities. The temperatures at the bed and wall were estimated, and the results were compared. The simulations were converged at 150 s then, the time-average value from 150 to 200 s was taken. Furthermore, the numerical comparison of hydrodynamic behaviour between paddy and sand particles was carried out with the same bed height (10 cm). In this regard, the 3-D simulations were carried out on a conical dryer with a cone angle of 10° for the operating parameter of air velocities such as 1.1 and 1.6 m/s. The bed height and particle size of the paddy were taken as 10 cm and 0.0025 m, respectively. Similarly, the bed height and particle size of sand were 10 cm and 435 µm, respectively. The pressure drop along the height of the conical dryer was compared between these two different particles. The parameters used in the present simulations are described in Table 3.2.

Table 3.2 Parameters used in the simulations

Parameters	**Description**
Type of flow	Turbulent, k-epsilon model
Two-phase approach	Eulerian-Eulerian, with KTGF
Time step used	10^{-3} s
Criteria of convergence	10^{-3} for continuity and momentum 10^{-6} for energy
Under-relaxation factors	Pressure = 0.5 Momentum = 0.2 Volume and granular temperature = 0.2
Packing limit (maximum)	0.63
Specularity coefficient	0.5
Particle to particle restitution coefficient	0.9
Pressure-velocity coupling	SIMPLE
Scheme for discretization	Second-order upwind
Air velocity for sand particles (m/s)	1, 1.5 and 2
Bed height of sand particles (cm)	10, 20 and 30
Bed height of paddy particles (cm)	10
Static bed height of sand particles (cm)	9.15, 16.5 and 23.2
Sand particle size (micron)	300, 435 and 600
Paddy particle size (mm)	2.5
Air velocity for paddy particles (m/s)	1.1, 1.6 and 2.1

The boundary conditions of both 2-D and 3-D models were the same, as shown in Table 3.3, as the inlet velocity at the bottom of the fluidized bed dryer. At the same time, the pressure

outlet was at the top, which corresponds to the gauge pressure, equal to zero. The other parts of the fluidized bed were considered as the wall, where there was the no-slip condition for the gas phase and a partial slip condition for the solid phase. However, the normal component of the velocity of solid particles was imposed as zero.

Table 3.3 Boundary conditions utilized for fluidized bed simulations

Description	Type	Comments
Inlet	Velocity inlet	Uniform distribution for gas phase No entry of solid phase
Outlet	Pressure outlet	Atmospheric
Wall	Stationary	No-slip for gas phase Partial slip for solid phase

3.6 CHAPTER CONCLUSION

The numerical simulation procedure for hydrodynamic and heat transfer characteristics of two phases on the bubbling fluidized bed dryers was described in the present chapter. Both 2-D and 3-D model geometries were used for the present investigation. The geometry and mesh files for both 2-D and 3-D simulations were provided. The governing equations and constitutive equations related to the governing equations were discussed. The k-epsilon turbulence models were used to describe the flow in which c_μ was a function of mean strains and rotation rates. The numerical formulation and probable models used for the present study were also explained in detail. In the next chapter, the experimental setup and procedure will be discussed.

4

Experimental setup and procedure

4.1 Introduction

4.2 Experimental setup

4.3 Determination of minimum fluidization velocity and terminal velocity

4.4 Experimental procedure

4.5 Thermodynamic analysis

4.6 Milling and drying quality

4.7 Chapter conclusion

CHAPTER 4

EXPERIMENTAL SETUP AND PROCEDURE

4.1 INTRODUCTION

In this chapter, the experimental setup, material and procedure for experiments are discussed. Section 4.2 provides details on the experimental setup fabricated at the technology complex of the Indian Institute of Technology (IIT) Guwahati. The procedure for determining the minimum fluidization velocity for sand and paddy particles is described in section 4.3. The experimental procedure used for the hydrodynamic behaviour, heat transfer and drying characteristics in the dryer columns is described in section 4.4. Section 4.5 deals with the thermodynamic analysis of the paddy drying process. On the other hand, the methods for drying and milling quality are explained in section 4.6. Finally, the chapter conclusion of the chapter is presented in section 4.7.

4.2 EXPERIMENTAL SETUP

Five experimental setups with different risers of cone angles were made in the technology complex of IIT Guwahati. One was a conventional cylindrical riser, and the other four were conical risers having cone angles 5°, 10°, 15° and 20°, respectively. The bottom diameter (D_1) of all three risers was taken as 15 cm. The area of the cross-section was increasing along the height of the risers to maintain the desired cone angles. However, the axial height (L) of all three risers was taken as 120 cm. The D_1/L ratio was considered 0.125 for all the risers. A schematic diagram of an atmospheric bubbling fluidized bed is shown in Fig. 4.1. The risers were made up of MS sheets of a thickness of 1.5 mm (Thermal conductivity – 45 W/m-K, Density – 7850 kg/m^3). The dimensions of the setup are explained in Table 4.1. The risers were mounted on a plenum chamber, as shown in Fig. 4.1. A suitably designed distributor plate was placed between the bottom part of a riser and the uppermost part of the plenum chamber. The design of the distributor is shown in appendix A. A 40-size wire mesh was placed above the distributor plate to prevent solid particles from entering the plenum chamber. The pictorial representation of the risers of bubbling fluidized beds is shown in Fig. 4.2. An experimental rig is also provided in Fig. 4.3. These risers were used as dryers for investigating the hydrodynamics, heat transfer and drying characteristics.

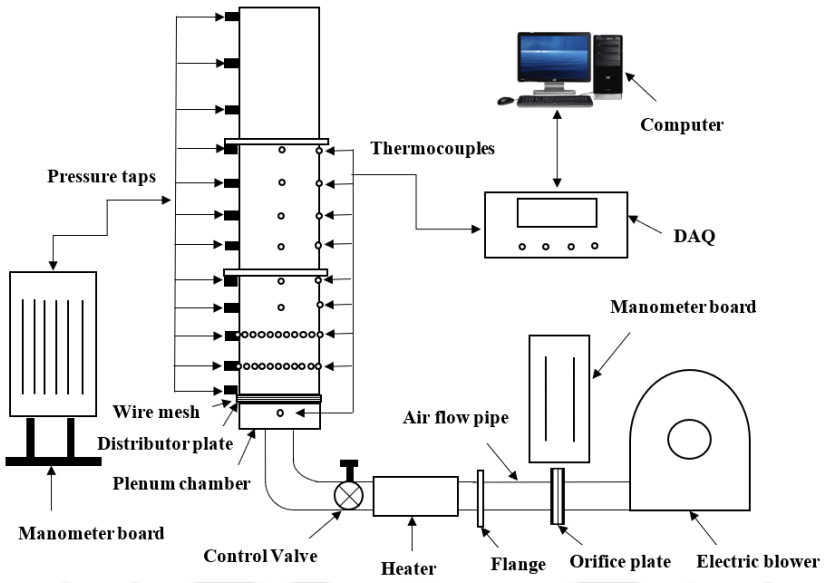

Figure 4.1: Schematic diagram of an atmospheric bubbling fluidized bed

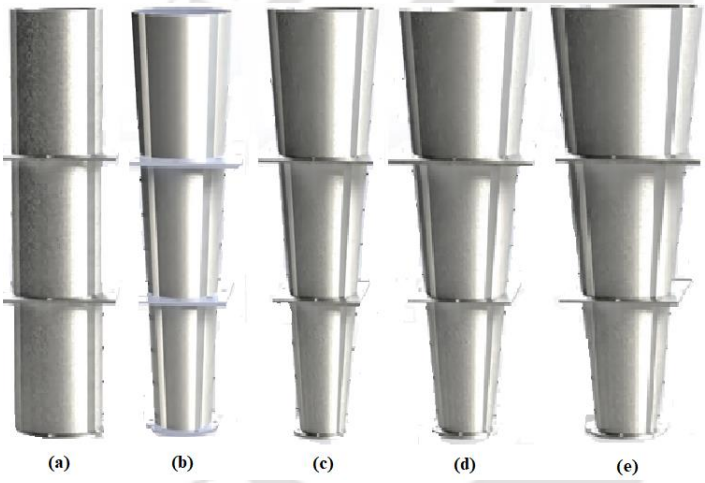

Figure 4.2: Configuration of three risers of bubbling fluidized bed, (a) α = 0°, (b) α = 5°, (c) α = 10°, (d) α = 15° and (e) α = 20°

Figure 4.3: An experimental rig of a conical bubbling fluidized bed

Table 4.1 Dimensions of bubbling fluidized bed risers

Sl. No.	Cone angle (°)	Inlet diameter (cm)	Outlet diameter (cm)	Height of dryer (cm)
1	0°	15	15	120
2	5°	15	25.48	120
3	10°	15	36	120
4	15°	15	46.6	120
5	20°	15	57.32	120

4.3 DETERMINATION OF MINIMUM FLUIDIZATION AND TERMINAL VELOCITY

At the onset of fluidization, the upward force exerted on particles equals the effective weight of particles, i.e.

Buoyancy force on particles = Weight of particles

[Pressure drop] × [Cross-sectional area of the bed] = [Volume fraction of solids] × [specific weight of solid] × [Volume of bed]

In a conical fluidized bed, the area of cross-section increases along the height. Therefore, the mechanics associated with the conical fluidized bed vary from those associated with the cylindrical bed.

Figure 4.4 shows a conical dryer with a bottom radius of r_0, and r_1 is the radius up to which particles are filled. The static bed height between r_0 and r_1 is H_s. A small layer with radius r and thickness dh was considered at the height of h_0 from the bottom. Then the buoyancy force exerted on this layer of particles is given by dF.

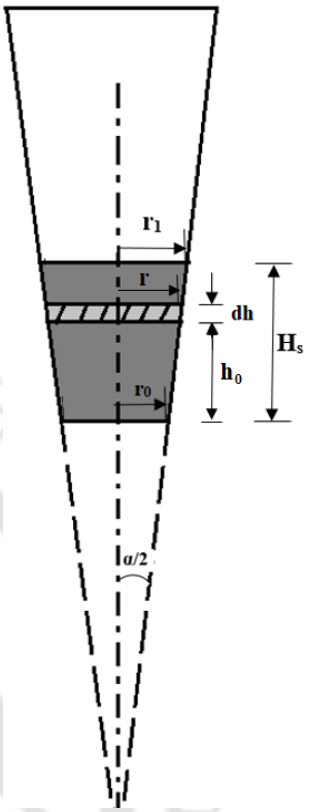

Figure 4.4: Schematic of a conical dryer

$$dF = \pi r^2 dP \tag{4.1}$$

where, dP is the pressure drop at the bed. In the fixed bed, the pressure drop is given by the Ergun equation-

$$dP = \left(Au + Bu^2 \right) dh \tag{4.2}$$

where,

$$A = 150\frac{\left(1-\varepsilon_g\right)^2}{\varepsilon_g^{\,3}}\frac{\mu_g}{\left(\phi_s d_p\right)^2} \text{ and } B = 1.75\frac{\left(1-\varepsilon_g\right)}{\varepsilon_g^{\,3}}\frac{\rho_g}{\phi_s d_p}$$

In a fixed bed, the air volume fraction is assumed to be constant. Air existing in the layer with velocity u can be written as-

$$\frac{u}{r^2} = \frac{v_g}{r_0^{\,2}} \tag{4.3}$$

If the cone angle is α, then from the geometry of the figure, it can be written as-

$$\tan\frac{\alpha}{2} = \frac{r - r_0}{h_0} \tag{4.4}$$

which becomes

$$r = r_0 + h_0 \tan\frac{\alpha}{2} \tag{4.5}$$

So, the equation (4.3) becomes,

$$u = \frac{\nu_g \left(r_0 + h_0 \tan\frac{\alpha}{2} \right)^2}{r_0^2} \tag{4.6}$$

$$\text{Now, } dF = \pi \left[A\nu_g r_0^2 + \frac{B\nu_g^2 r_0^4}{\left(r_0 + h\tan\frac{\alpha}{2} \right)^2} \right] dh \tag{4.7}$$

Integrating the equation (4.7) along the height, it becomes

$$F = \pi r_0^2 H_s \left(A\nu_g + B\nu_g^2 \frac{r_0}{r_1} \right) \tag{4.8}$$

At the same time, the effective weight of the particles in the layer is given by

$$dG = \left(1 - \varepsilon_g\right)\left(\rho_s - \rho_g\right) g\pi r^2 dh \tag{4.9}$$

Integrating the equation (4.9) over the height H_s, the equation becomes

$$G = \left(1 - \varepsilon_g\right)\left(\rho_s - \rho_g\right) g\pi H_s \frac{r_0^2 + r_0 r_1 + r_1^2}{3} \tag{4.10}$$

Rearranging the equation (4.10), it becomes

$$G = \left(1 - \varepsilon_g\right)\left(\rho_s - \rho_g\right) g\pi r_0^2 H_s \frac{r_0^2 + r_0 r_1 + r_1^2}{3r_0^2} \tag{4.11}$$

If equations (4.8) and (4.11) are equated, the minimum fluidization velocity can be calculated using the following equation.

$$B\frac{r_0}{r_1} U_{mf}^{\ 2} + AU_{mf} - \left(1 - \varepsilon_g\right)\left(\rho_s - \rho_g\right) g \frac{r_0^2 + r_0 r_1 + r_1^2}{3r_0^2} = 0 \tag{4.12}$$

Equation (4.12) is in a quadratic form. The equation was solved for three dryers, and minimum fluidization velocity was determined for sand and paddy particles. For sand particles with bed heights of 10, 20 and 30 cm, the minimum fluidization velocities were 0.48, 0.54 and 0.62 m/s, respectively. Similarly, the minimum fluidization velocity for paddy particles was determined and found to be 0.51 m/s.

The terminal velocity of a single particle was determined by the following equation

$$U_t = \left(\frac{1.78\times10^{-2} \times \left\{ g\left(\rho_s - \rho_g\right)\right\}^2}{\rho_g \mu} \right)^{1/3} \left(d_p\right) \tag{4.13}$$

The terminal velocity for three different sand particle sizes (300, 435 and 600 µm) was calculated as 2.41, 3.49 and 4.8 m/s. Similarly, the terminal velocity for the paddy particle was calculated, and its value was 3.1 m/s.

4.4 EXPERIMENTAL PROCEDURE

The experimental procedure is divided into two phases. In the first phase, the procedure to investigate the hydrodynamic behaviour and heat transfer characteristics of sand particles across the three dryers is demonstrated. The sand particles were used as most of the existing literature reported using sand particles to study the hydrodynamic and heat transfer behaviour of sand particles in fluidized bed dryers due to their abundance and easy availability. In the second phase, the procedure for hydrodynamic behaviour and drying characteristics of paddy particles are illustrated. The properties of air, sand and paddy particles are shown in Table 4.2.

Table 4.2 Properties of air, sand and paddy particles

Sl. No.	Properties	Unit	Value
1	Density of air	kg/m^3	1.225
2	Thermal conductivity of air	W/m-K	0.024
3	Specific heat of air	J/kg-K	1005
4	Density of sand	kg/m^3	2660
5	Thermal conductivity of sand	W/m-K	0.25
6	Specific heat of the sand	J/kg-K	0.837
7	Density of paddy	kg/m^3	1200
8	Thermal conductivity of paddy	W/m-K	0.0454
9	Viscosity of air	Pa-s	1.86×10^{-5}
10	Air volume fraction	-	0.5

For the first case, experiments were carried out to investigate the hydrodynamic behaviour and heat transfer characteristics of sand particles in a conventional cylindrical dryer with an air velocity of 1.5 m/s and a 30 cm bed height. For this experiment, an average particle size of 435 μm (appendix B) was chosen. Furthermore, experiments were conducted in four conical dryers with cone angles of 5°, 10°, 15° and 20°, respectively, for the same operating parameters, and results were compared to the cylindrical dryer to investigate the effect of cone angle. Once the results were validated and conclusive evidence identified, experiments were performed in a conical dryer of 10° cone angle with three different superficial air velocities (1, 1.5 and 2 m/s) with three average particle sizes of sand (300, 435 and 600 μm) as indicated in Table 4.3, in order to optimize the features of the conical dryer. In this study, three static bed heights (H_s) of 9.15, 16.5 and 23.2 cm were used, corresponding to bed heights (H) of 10, 20 and 30 cm, respectively. Air was introduced as a primary phase supplied from the high pressure and high discharge blower via pipes through the designed distributor plate with an opening area of 24.16%. The air flow rate was regulated by the controlling valve installed below the plenum chamber. An installed D-D/2 orifice plate was used to determine the differential height of the water U-tube manometer to calculate the flow rate of air by the following equation.

$$Q_c = 0.035\sqrt{\Delta H} \tag{4.14}$$

where, Q_c is the air flow rate at the dryer inlet and ΔH is the differential height of the water column across the orifice plate. After calculating the air flow rate, then superficial air velocity was determined by the following equation-

$$U_0 = \frac{Q_c}{A_c} \tag{4.15}$$

Twelve pressure taps separated by 10 cm were inserted along the dryer height to determine the pressure drop. In order to investigate the heat transfer characteristics, hot air at a constant temperature of 65°C was supplied through the dryer inlet. The air was heated by means of four ceramic band heaters with a capacity of 1.25 kW attached to the main pipe of the setup. A mica sheet wrapped over the inlet pipe acts as an insulator over which the heaters were placed. Another mica sheet and ceramic wool were wrapped over the heater section to minimize the heat loss to the surrounding. For heat transfer study, the measurement of bed and surface temperatures is essential. So, twenty-two pre-calibrated K type thermocouples were inserted in a row to measure the surface and bed temperatures. These thermocouples were connected to

the Data Acquisition System (appendix C), from which temperature readings were noted, and results were compared. The calibration of thermocouples is shown in appendix D.

Table 4.3 Input variable matrix considered for sand in the dryers

Sl. No.	Input	Unit	Matrix
1	Inlet air velocity	m/s	1, 1.5, 2
2	Static bed height	cm	9.15, 16.5, 23.2
3	Temperature of inlet air	℃	65
4	Average particle size of sand	µm	300, 435, 600

In the second phase, drying characteristics were studied using the locally available paddy as a batch material with a moisture content of 42% (WB). Initially, at the time of harvesting, the moisture content in the paddy was about 24-28%. Before drying, it was boiled, which increases its moisture content to 42% (measured by digital grain moisture meter; make: Indosaw, model: handy data logging moisture meter, the accuracy of ±0.5). The experiments were carried out for varying bed inventory between 1 to 3 kg with three different inlet air velocities such as 1.1, 1.6 and 2.1 m/s and three inlet drying temperatures (55°, 60° and 65°C), as shown in Table 4.4.

Table 4.4 Input variable matrix considered for paddy drying in the dryers

Sl. No.	Input	Unit	Matrix
1	Inlet air velocity	m/s	1.1, 1.6, 2.1
2	Bed inventory	Kg	1 – 3
3	Temperature of drying air	°C	55, 60, 65
4	Initial moisture content	Wet basis	42 %

Different masses and air velocities were considered because, as mentioned in the literature [22,141–143], the hydrodynamics and drying characteristics changes with the change in mass of materials and air velocity. The different drying temperatures (55℃, 60℃ and 65℃) were selected as an operating parameter because the quality of paddy is good after drying for those operating parameters, as the literature stated [21,176]. So, different masses, air velocity and air temperature were considered in order to study the changes in these operating parameters on hydrodynamics and drying characteristics. An experiment was started by switching on the high-pressure, high discharge blower. An energy meter (AC, 3 phase, 4 wire, static energy meter; Type: BBLSM-T44, Frequency 50 Hz, Class 1.0, 10-40A, 3×240 V, Temperature 27°C, Bentex control & Switchgear Co.) was attached to the power supply line to the blower to measure the energy consumption of the bower. Once it was ON, the air flowed from the blower

and passes through the airflow pipes. The airflow rate was regulated by an adjustable gate valve installed on the flow pipes. For the electrical heating, electric heaters of rating 1.25 kW were used just before the inlet to the fluidized bed dryer and wrapped over the main pipe covered by a layer of mica sheets to provide electrical insulation. Regulated current was supplied to heaters through an electrical circuit consisting of an autotransformer, voltmeter and ammeter. The autotransformer regulates the power supplied to the heater to maintain the inlet air temperature at 55°, 60° and 65°C, respectively. The paddy particles were fed to the fluidized bed dryer in different batch sizes. The inlet air velocity was set to 2 or 2.5 times above the minimum fluidization velocity to maintain the bubbling regimes. A set of pressure tapings of the copper tube having an internal diameter of 10 mm were inserted along the height of the dryer and were connected to a water-filled differential U-tube manometer. The difference of two consecutive pressure taps provides the pressure drop between two subsequent locations along the dryer. In order to study the effect of a spiral inside the dryer column, a spiral of 10 cm axial length fabricated out of mild steel was installed inside the fluidized bed dryers. An attachment of the spiral inside a dryer is shown in Fig. 4.5. The attachment of the spiral was done by welding it to the internal surface of the dryer just above the distributor plate. A small amount of paddy grain (10 g approx...) was taken out from the top of the dryer after every 5-minutes interval to check the moisture content until it reaches equilibrium moisture content (EMC), i.e. 12-14% (WB), which is a required parameter for further processing of dried paddy. For all cases, the experiments were repeated for three times and error analysis was performed, as indicated in appendix E.

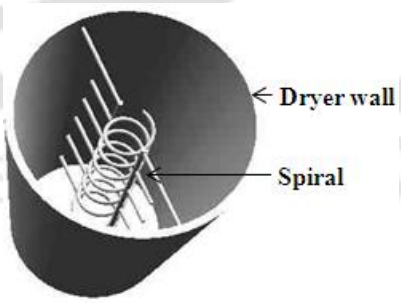

Figure 4.5: An attachment of a spiral inside the dryer

4.5 THERMODYNAMIC ANALYSIS

4.5.1 Energy consumption

The energy consumption of a dryer is the sum of energy consumed to heat the air and drive the blower. The heat input to the dryer is given by-

$$Q = Vit \times P.F. \times 60 \times 10^{-6} \text{ MJ/kg} \tag{4.16}$$

4.5.2 Energy analysis

Energy is associated with the first law of thermodynamics. The first law of thermodynamics states that energy is always conserved. By using the first law of thermodynamics, the energy utilization (EU) was determined as the difference of energy at the inlet and outlet. The equation to determine the EU is given by Cengel (2004) [177]:

$$EU = \dot{m}_g \left(h_{gi} - h_{go} \right) \tag{4.17}$$

where, $\dot{m}_g$ is the mass flow rate of drying air per unit time and h_g is the net enthalpy of dry air and water vapour. The mass flow rate was used to determine the energy utilization ratio (EUR) and humidity ratio and can be calculated by the following equation:

$$\dot{m}_g = \rho_g U_0 A_c \tag{4.18}$$

where, ρ_g, U_0 and A_c are the density of air, air velocity and inlet cross-sectional area of beds, respectively. The density of air was taken from the literature, and air velocity was measured. The cross-sectional area of the bed can be determined in the following way-

$$A_c = \frac{\pi}{4} D_0^2 \tag{4.19}$$

where, D_0 is the inlet diameter of bed. Net enthalpy of dry air and water vapour can be calculated from the following expression [156]:

$$h_g = C_{pg} \left(T - T_{ref} \right) + h_{fg} w \tag{4.20}$$

where, C_{pg} , T, T_{ref}, h_{fg} and w are the specific heat of air, outlet temperature of beds at different operating conditions, temperature of surrounding, latent heat of evaporation and humidity ratio, respectively. The specific heat of drying air was determined by considering the heat content in dry air and water vapour present in the moist air used for drying. It is strongly dependent on humidity ratio, the specific heat of dry air and water vapour. Depending on the drying temperature, the following is the equation used for determining the specific heat of the drying air [156]:

$$C_{pg} = 1.004 + 1.88w \tag{4.21}$$

The outlet temperature of beds and temperature of surrounding were measured. The latent heat of evaporation was calculated from the steam table. The humidity ratio is again a strong

function of relative humidity and partial pressure of water vapour. By the addition of humidity ratio due to moisture evaporated from paddy with the humidity ratio at dryer inlet, the humidity ratio at dryer outlet was determined. The humidity ratio of drying air at the outlet of the drying chamber was determined by using the following relationship [156]:

$$w_{go} = w_{gi} + \frac{\dot{m}_v}{\dot{m}_g} \tag{4.22}$$

where, $\dot{m}_v$ is the moisture evaporation rate and was calculated by the flowing expression [156]:

$$\dot{m}_v = \frac{M_t - M_{t+\Delta t}}{\Delta t} \tag{4.23}$$

The energy utilization ratio (EUR) is determined by an expression provided by Nazghelichi et al. (2010) [156]:

$$EUR = \frac{\dot{m}_g \left(h_{gi} - h_{go}\right)}{\dot{m}_g \left(h_{gi} - h_{ge}\right)} \tag{4.24}$$

4.5.3 Exergy analysis

Effective thermal analysis through improved drying material efficiency is a key market quality index. Increasing efficiency can often contribute to a significant reduction in the system's irreversibility loss. This conveys the idea of exergy as one of the most important concepts for optimal drying conditions. An energy analysis of an energy conversion system is essentially an accounting of the energies entering and exiting. The exiting energy can be broken down into products and wastes. Efficiencies are often evaluated as ratios of energy quantities and are often used to assess and compare various systems. The thermodynamic losses or inefficiencies and the magnitude of them that occur within a system often are not accurately identified and assessed with energy analysis through the first law of thermodynamics. The system energy balance is not sufficient for the possible finding of the system imperfections. Therefore, the second law assessment can be expressed as a powerful tool that can help us to optimize the system design and improve its energy conversion. Simply put, it is a kind of helpful approach for clarifying the distinction between energy wasted on the environment and internal irreversibility in the system. In fact, any sort of irreversibility detrimentally affects the energy conversion of the drying chamber, including heat loss by the wall of the drying chamber. Exergy analysis is a thermodynamic analysis technique based on the second law providing an alternative and illuminating approach for investigating energy processes rationally and

meaningfully, and it imparts a qualitative study of thermodynamic processes via efficiency rather than quantitative. Unlike energy, exergy analysis provides the available energy or work potential of a system. Features like system optimization and system components comparison can be accomplished by proper exergy analysis, which contributes to perceiving effective ways to enhance processes. The stimulation of a plant by assessing the operating cost, energy conservation, and fuel versatility is the key challenge for researchers. Exergy analysis leads to the determination of the effectiveness of the plant by providing useful information. It reveals how a thermal system is designed more effectively by eliminating the existing irreversibility associated with the sources. The exergy concept has gained considerable interest in the thermodynamic analysis of thermal processes and plant systems since it has been seen that the first law analysis has been insufficient from an energy performance standpoint.

The importance of exergy analysis is numerous compared to energy analysis. Some of the more significant ones follow below:

- Exergy efficiencies are always the measures of the approach to true ideality and provide more meaningful information when assessing the performance of energy systems. Also, exergy losses clearly identify the locations, causes, and sources of deviations from ideality in a system.
- Exergy methods can help evaluate the thermodynamic values of the product energy forms in complex systems with multiple products (e.g., cogeneration and trigeneration plants).
- Exergy-based methods can be used to improve economic and environmental assessments.
- Exergy can improve understanding of terms like energy conservation and energy crisis.

The exergy analysis is the total exergy of inflow, outflow and losses due to the irreversibility of the processes. The second law analysis of thermodynamics provides the basic concept of exergy analysis. The exergy analysis of fluidized bed dryer is exergy flow values at steady-state points and variation of exergy processes due to the loss of irreversibility [153,156,158,178]. The loss of irreversibility is due to the heat transfer through a finite temperature difference. By implementing the first law energy balance concept, the exergy flow values were calculated [156]. The present work uses the first law of energy balance to calculate the exergy flow values.

The steady-state exergy at any location of the dryer is the maximum potential work obtainable from drying air concerning the surrounding, and it is evaluated from the second law of thermodynamics. The total exergy of drying air is the summation of the heat content of drying air due to the electrical heating and kinetic energy of drying air due to forced convection. In the exergy analysis, the thermodynamic properties include mass flow rate, specific heat, velocity and temperature of drying air is the combination of dry air and water vapour. The following expression was used to determine the exergy of drying air at the inlet and the outlet of the dryers.

$$\dot{E}x = \dot{m}_g C_{pg}\left[\left(T - T_{ref}\right) - T_{ref}\ln\frac{T}{T_{ref}}\right] + \frac{\dot{m}_g U_0^{\,2}}{2000} \tag{4.25}$$

Once the exergy of drying air at the inlet and outlet of the dryers were calculated by using the above relationship, the exergy destruction was determined by the difference between exergy at the inlet and outlet, which was described in equation 4.26. In the process of drying, a substantial amount of exergy was destroyed by the evaporation of water from the drying product. The rate of evaporation is the useful energy used for the evaporation of moisture content from paddy grains. Therefore, it can be thought of as a measure of exergy utilization. The exergy utilization was determined for the three dryers, and the results will be compared in chapter 6.

Unlike the first law efficiency, the second law efficiency provides a precise measurement of the drying characteristics performance. The second law efficiency or exergy efficiency is defined as the ratio between exergy at the outlet and exergy at the inlet. In this present study, the exergy efficiency was also determined for the three dryers by equation 4.27, and the results will be compared in chapter 6. The expression exergy efficiency is described in equation 4.27 [153,158]:

$$\dot{E}x_{destruction} = \dot{E}x_{inlet} - \dot{E}x_{outlet} \tag{4.26}$$

$$Ex_{efficiency} = \frac{\dot{E}x_{inlet} - \dot{E}x_{destruction}}{\dot{E}x_{inlet}} = \frac{\dot{E}x_{outlet}}{\dot{E}x_{inlet}} \tag{4.27}$$

4.6 MILLING AND DRYING QUALITY

The milling quality of paddy was tested in terms of head rice, broken rice and milling recovery for both the conditions with a spiral and without a spiral. The following expressions were used for milling quality.

$$\text{Head rice} = \frac{\text{Weight of whole grains after milling}}{\text{Weight of paddy samples}} \times 100\% \quad (4.28)$$

$$\text{Broken rice} = \frac{\text{Weight of broken grains after milling}}{\text{Weight of paddy samples}} \times 100\% \quad (4.29)$$

$$\text{Milling recovery} = \frac{\text{Weight of milled rice}}{\text{Weight of sample used}} \times 100\% \quad (4.30)$$

The drying quality of paddy rice was determined in terms of fibre, protein, fat and carbohydrate percentage. Different measurement methods are required to assess this dietary quantity of paddy grains, and a list of them is included in Table 4.5.

Table 4.5 Measurement methods for determining the nutritional contents of paddy grains [179]

Sl. No.	**Nutritional contents of paddy**	**Measurement methods** [179]
1	Fibre	Crude fibre estimation method
2	Protein	Kjeldahl method
3	Fat	Soxhlet extraction method
4	Carbohydrate	Anthrone method

4.7 CHAPTER CONCLUSION

A cylindrical and two conical fluidized bed dryers having dimensions given in Table 4.1 were developed at IIT Guwahati. The necessary instrumentation and data acquisition system were incorporated into the setup. Three dryers were fabricated to study the effect of various operating parameters like the superficial velocity of air, bed height of sand, particle size and cone angle on hydrodynamic behaviour and heat transfer characteristics. The minimum fluidization velocity for these three dryers was calculated by using the holding relationship for the conical fluidized bed. Experimental procedures for investigating hydrodynamic behaviour, heat transfer characteristics of sand particles and the hydrodynamic behaviour and drying characteristics of paddy particles were also described. Significant equations relevant to this investigation were also explained. The next chapter will discuss the results and discussion of experimental and numerical simulation of sand particles' hydrodynamics and heat transfer characteristics.

5

Performance evaluation of BFB dryers with sand as bed inventory

5.1 Introduction

5.2 Independence of grid for 2-D model

5.3 Validation pf 2-D simulation results with experimental results

5.4 Grid and time independence for 3-D model

5.5 Incorporation of drag model

5.6 Hydrodynamic behaviour of three dryers

5.7 Heat transfer characteristics of three dryers

5.8 Hydrodynamics in a conical dryer of 10° cone angle

5.9 Heat transfer characteristics in a conical dryer of 10° cone angle

5.10 Chapter conclusion

CHAPTER – 5

PERFORMANCE EVALUATION OF BFB DRYERS WITH SAND AS BED INVENTORY

5.1 INTRODUCTION

As a part of the present investigation, the experimental and numerical studies of hydrodynamic behaviour and heat transfer characteristics of sand particles in the fluidized bed dryers are discussed in this chapter. The study of heat transfer characteristics is important as it inevitably influences the drying characteristics. These heat transfer and drying characteristics are further affected by the hydrodynamics. As a result, the hydrodynamic behaviour and heat transfer characteristics were studied in present dryers. Initially, the five dryers (α = 0°, 5°, 10°, 15° and 20°) were modelled through 2-D simulation for the operating parameter such as inlet air velocity (1.5 m/s), bed height (30 cm) and particle size (435 µm) and then compared the results of hydrodynamics with the experimental results. Hydrodynamic behaviour such as bed pressure drop and pressure drop along the height of the dryers obtained through 2-D simulation were compared with the experimental results. Once conclusive evidence was made, experiments and 3-D simulations were also carried out to investigate the hydrodynamic behaviour and heat transfer characteristics to validate the 3-D simulation results with the experimental results. In addition, experiments were also done in a conical dryer with a cone angle of 10° to investigate the hydrodynamic behaviour and heat transfer characteristics for the different operating parameters of bed height (10, 20 and 30 cm), particle size (300, 435 and 600 µm) and air velocity (1, 1.5 and 2 m/s). Similarly, to validate the simulation results with the experimental results, 3-D simulations were carried out in the conical dryer with a cone angle of 10° for different air velocities keeping bed height and particle size constant. For the heat transfer study, a constant air temperature of 65°C was introduced through the inlet of the dryer under the operating parameters mentioned above. The grid independence test was performed for all the dryers to study the effect of grid sizes on simulation results. Pressure drop, axial and radial solid volume fraction and the interphase heat transfer coefficient were calculated at different locations of the three dryers for the inlet air temperature of 65°C. This chapter comprises 10 sections. Section 5.2 explains grid independence for the 2-D model. Section 5.3 describes the validation of 2-D simulation results with experimental results. The grid and time independence

test for the 3-D model is described in section 5.4. Section 5.5 introduces the incorporation of the drag model in the modelling of dryers. Section 5.6 explains the hydrodynamic behaviour of three dryers. Similarly, the heat transfer characteristics of the three dryers are also explained in section 5.7. Sections 5.8 and 5.9 describe the study of hydrodynamic behaviour and heat transfer characteristics in the conical dryer of 10° cone angle, respectively. Finally, the chapter is concluded in section 5.10.

5.2 INTERDEPENDENCE OF GRID FOR 2-D MODEL

Spurred by the challenges of solving the non-linear equation of momentum conservation, there is a need to stress the numerical simulation techniques. As a result, the grid independence test was performed for the 2-D model of the three dryers to ensure that the simulation results were independent of grid sizes. However, the test for the cylindrical dryer is shown in this context. The test was carried out for distinct grid sizes with rectangular cells of 8800, 14400 and 25600. The rectangular mesh is advantageous over other meshes as it seems physically sensible to have edges that follow the flow direction, which is achieved by the lateral faces of the rectangle. Radial solid volume fraction profiles for these three grid sizes are plotted as shown in Fig. 5.1.

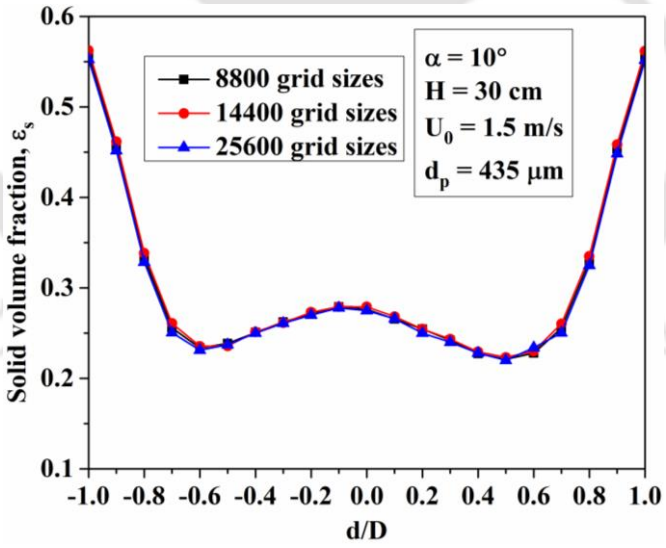

Figure 5.1: Grid independence test at three different grid sizes for 2-D model (Radial solid volume fraction)

It was observed that there was no significant difference between the three different numbers of grid cells. Therefore, 14400 grid cells were used for all further simulations.

5.3 VALIDATION OF 2-D SIMULATION RESULTS WITH EXPERIMENTAL RESULTS

First of all, the 2-D numerical simulations were carried out to check the feasibility of the five fluidized bed dryers. For that, one inlet air velocity was considered, i.e. 1.5 m/s. The bed height of material and particle size was considered as 30 cm and 435 µm, respectively. The simulations for all the models were run for 30 s, in which the solution reached a quasi-steady state at 10 s. Then time average value was taken from 10 to 30 s. Experiments were also carried out under similar operating parameters to test the viability of the dryers. The bed pressure drop for the five dryers was investigated numerically and experimentally, as shown in Figs. 5.2 (a) and (b).

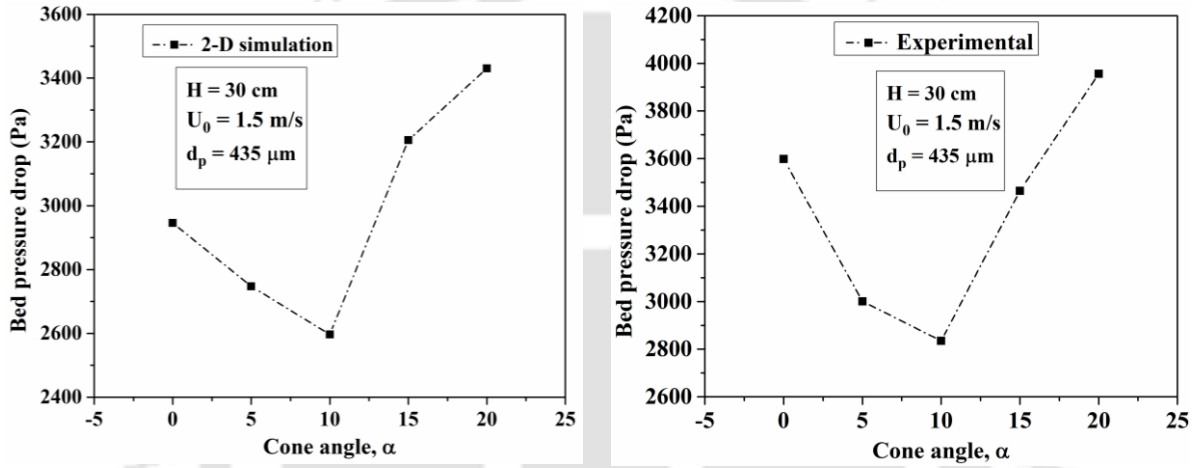

(a) (b)

Figure 5.2: Bed pressure drop with different cone angles, (a) 2-D simulation and (b) experimental

It was observed from the figure that the bed pressure drop was found to be lowest at a 10° cone angle. Subsequently, when the cone angle was increased above 10° and up to 20°, the bed pressure drop increased by 23% and 28%, respectively, at 15° and 20° cone angles in 2-D simulation conditions. Similarly, an increase in pressure drop of 22% and 39.54%, respectively, at 15° and 20° cone angles were observed in experimental conditions. The increasing pressure drop in the fluidized bed is not viable as it does not ensure the smooth fluidization of particles which is the disadvantage of a fluidized bed [57,60]. Hence, the limiting cone angle of 10° was used in both experimental and simulation conditions for all subsequent purposes. As a result, the three dryers having cone angles of 0°, 5° and 10° were considered for the present study.

Once the dryers were modelled and validated, other hydrodynamic characteristics for the three dryers (α = 0°, 5° and 10°) were compared between 2-D simulation and experimental results

under the same operating parameters. The bed pressure drop and the pressure drop along the height for the three dryers from the 2-D simulation were compared with the experimental results. The contours of the time-averaged solid volume fraction profile and solid velocity for the three dryers are shown in Figs. 5.3 and 5.4 to study the fluidization characteristics of sand particles.

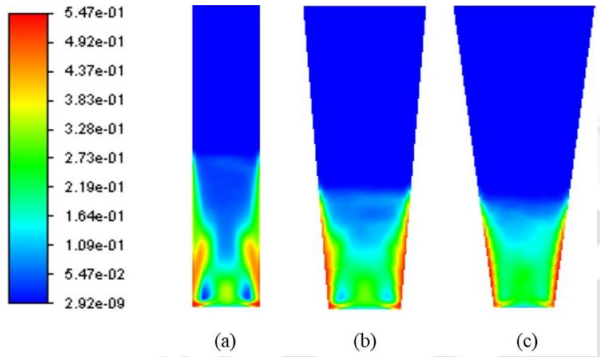

Figure 5.3: Contours of time-averaged solid volume fraction, (a) α = 0°, (b) α = 5°, and (c) α = 10°

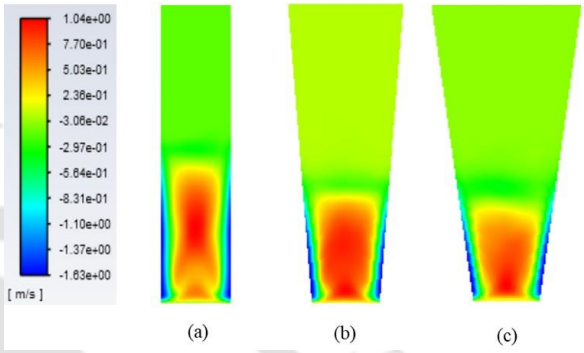

Figure 5.4: Contours of time-averaged solid velocity, (a) α = 0°, (b) α = 5°, and (c) α = 10°

It was observed from the contour plot that the uniformity of particle fluidization increases when the cone angle increases from 0 to 10°. The solid particles occupy mostly the wall of the dryers than the core of the dryers. Similar patterns were also reported by Basu and Nag (1987) [180], Basu (1990) [181] and Basu et al. (1996) [182]. However, the effective height of the solid volume fraction and solid velocity decreases when the cone angle increases. The solid velocity at the wall was observed to be minimum for all the dryers considered [59,183,184].

Bed pressure drop observed for three dryers under 2-D simulation and experiment is shown in Fig. 5.5. The pressure drop along the height of the three dryers is also demonstrated in Fig. 5.6.

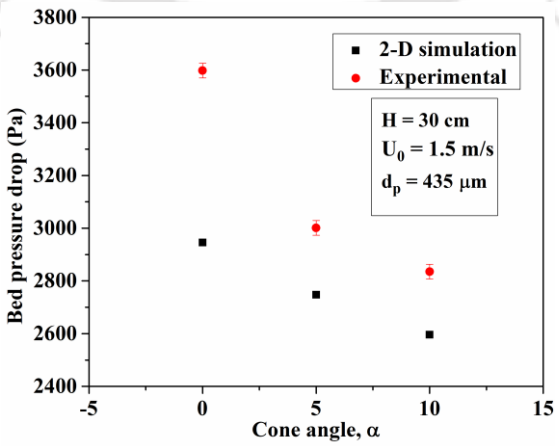

Figure 5.5: Comparison of bed pressure drop between 2-D simulation and experimental results

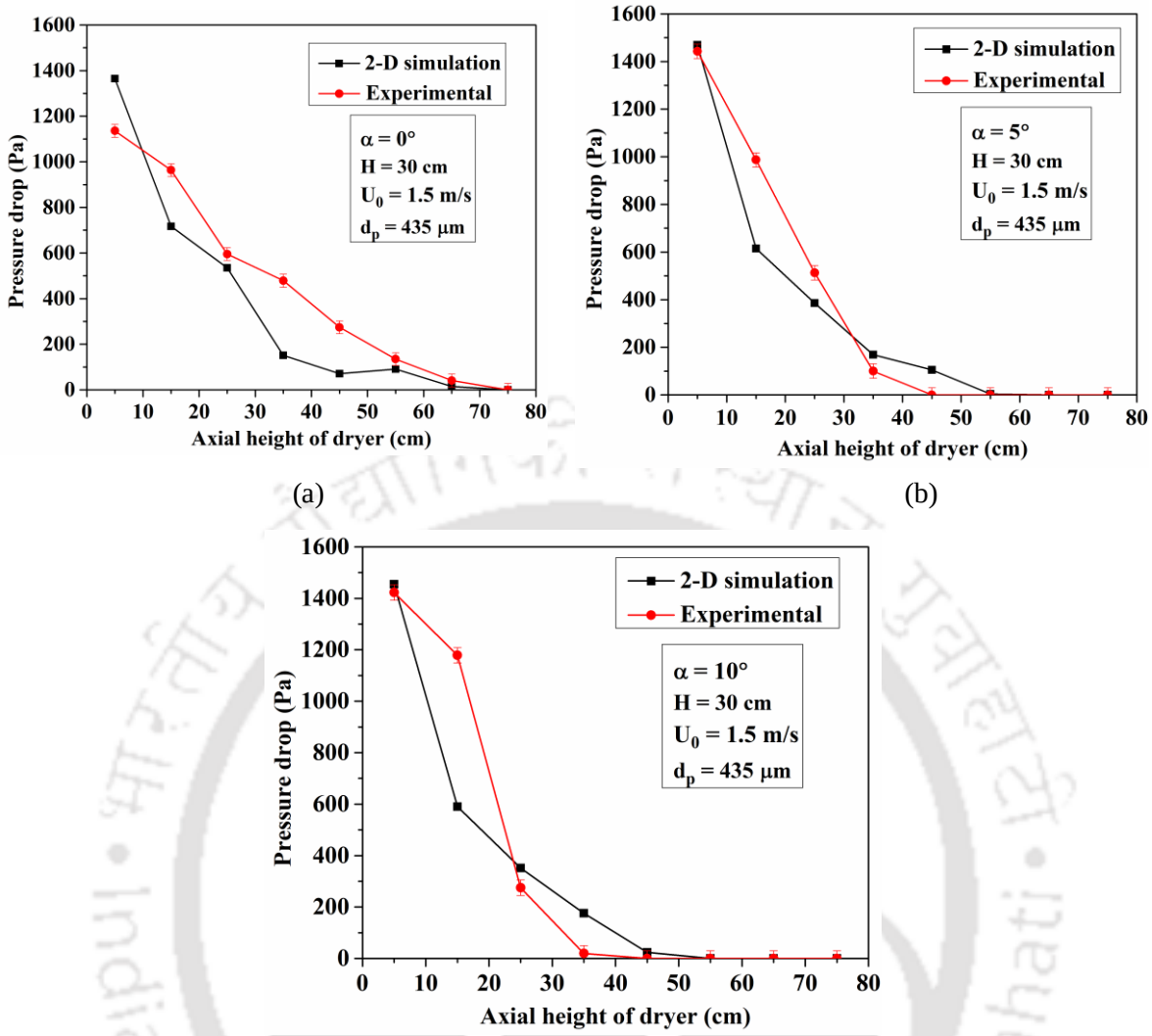

Figure 5.6: Comparison of pressure drop along the height for three dryers, (a) α = 0°, (b) α = 5°, and (c) α = 10°

It was observed that the 2-D simulation results of bed pressure drop and pressure drop along the height of three dryers deviated significantly from the experimental results. However, the trends remained the same. It was because 2-D simulations were usually done by ignoring the continuity equation in one spatial direction. Similarly, the momentum equations for both phases in that direction were also assumed to be zero. Hence, no convective accelerations and surface and body forces were expected in that direction. Therefore, mixing and diffusion characteristics do not happen purely in 2-D simulations. On the other hand, the 2-D modelling of fluidized bed dryers does not consider the shape (square, prismatic or circular) of the cross-sectional area. Hence, in order to compare the experimental results, a 3-D simulation is necessary. For instance, 3-D simulation was carried out in the three dryers to validate the simulation results

with the experimental results. The hydrodynamic behaviour and heat transfer characteristics were investigated in the three dryers, and the results were compared.

5.4 GRID AND TIME INDEPENDENCE FOR 3-D MODEL

Similar to the 2-D simulation, a grid independence test was also conducted with three grid sizes 94336, 140049, and 232704, for the 3-D simulation. The meshing was done in ANSYS 14.5 software. Multizone as hexahedral cells was used in the core region as well as near the wall. The inflation function option was used for all the dryers with first layer thickness 0.0001 – maximum layers 18 – growth size 1.2. The mapped face meshing option was also used for uniform sizing with a maximum face size limit of 0.015. These hexahedral cells were used as the angle between faces can be kept close to 90°. In the simulation of fluidizing problem, we need very fine spacing in the wall-normal direction. Hex grids make very fine wall-normal spacing but without large face skewness. As shown in Fig. 5.7, a profile of time-averaged radial solid velocity for these three grid sizes has been plotted for 1 m/s.

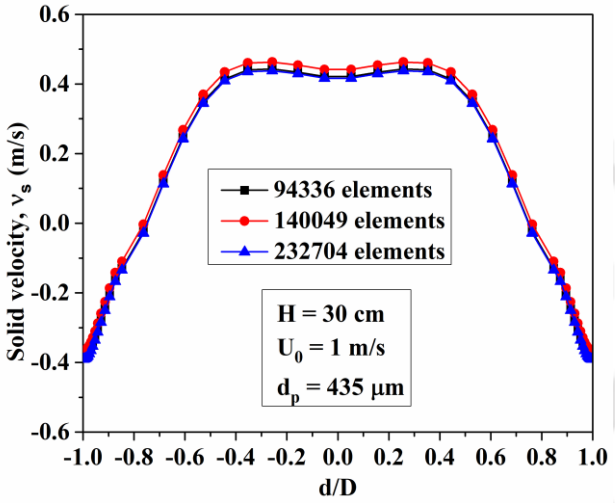

Figure 5.7: Grid independence test for the 3-D model (α = 10°)

The time-averaged local solid velocity profiles for these three cells were found to be close to one another. Thus, 140049 grid sizes were used for further simulations in order to achieve relatively close results to the experimental results. Similarly, for the time independence study, three different time step sizes, such as 2.5×10^{-3} s, 1×10^{-3} s and 2.5×10^{-4} s, were considered, and time-averaged radial solid velocity is shown for 3-D simulation. However, in this present study, investigation of time step sizes is shown for only conical riser of 5° cone angle. Figure 5.8 depicts the time-averaged radial solid velocity of the conical riser with a 5° cone angle for three-time step sizes.

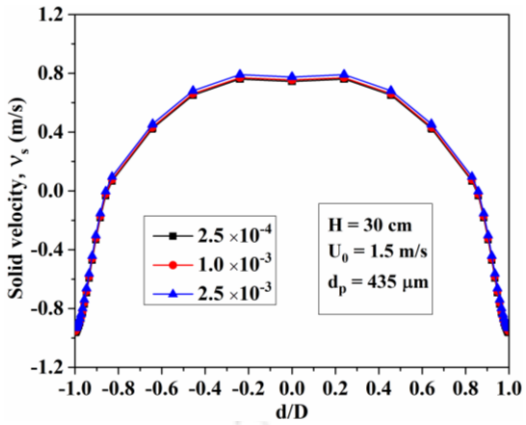

Figure 5.8: Time independence test for the 3-D model (α = 5°)

The results observed by using 2.5 ×10^{-3} s deviate slightly from 1×10^{-3} and 2.5 ×10^{-4} s -time step sizes. Nonetheless, the results between 1×10^{-3} and 2.5 ×10^{-4} s -time step sizes were closed to each other. As a result, 1×10^{-3} s was used for further simulation to ensure precision and lessen physical simulation time.

5.5 INCORPORATION OF DRAG MODEL

There are different types of drag models, such as the Schiller and Naumann model, Wen and Yu model, Syamlal-O'Brien model, and Gidaspow model. The Syamlal-O'Brien model and the Gidaspow model are widely incorporated for interphase exchange coefficient in gas-solid dense flow. Hence, these two drag models were used in the present study for the conical riser (α = 10°) and the comparison of bed pressure drops was made with the experimental results as in Fig. 5.9. The results obtained by the Syamlal-O'Brien model were closer to the experimental results than the Gidaspow model. Also, the uniform distribution of particles prevailed through the riser column with the adoption of the Syamlal-O'Brien drag model, as shown in Fig. 5.10

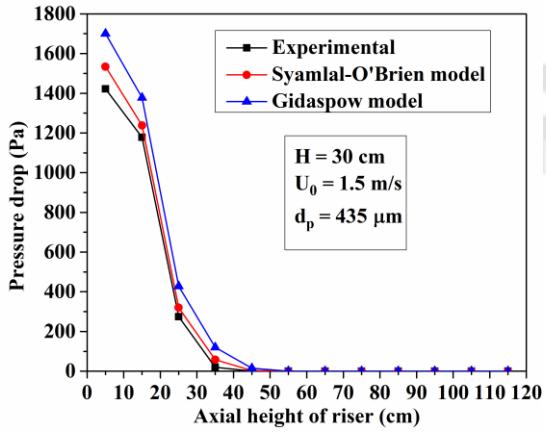

Figure 5.9: Comparison of pressure drop among experimental, Syamlal-O'Brien and Gidaspow drag models

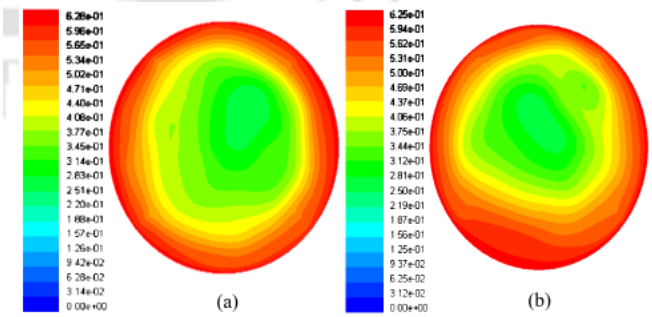

Figure 5.10: Contours of time-averaged radial solid volume fraction, (a) Syamlal-O'Brien drag model, and (b) Gidaspow drag model

As a result, the Syamlal-O'Brien drag was used to describe the interphase exchange coefficient of the drag force equation during the entire simulation [36].

5.6 HYDRODYNAMIC BEHAVIOUR OF THREE DRYERS

This section deals with the experimental and numerical investigation of hydrodynamic behaviour such as bed pressure drop, bed expansion ratio, the pressure drop along the height of three dryers. The radial profile of solid volume fraction, solid velocity and temperature at an axial height of 10 cm for all three dryers are also investigated numerically in this section. However, experimental investigation of these behaviours is difficult due to the variation in operating parameters. The axial distance of 10 cm is considered, as most particles remain in the lower region, and interesting phenomena occur in an atmospheric bubbling fluidized bed [57,59].

5.6.1 Pressure analysis in three fluidized bed dryers

In the analysis of pressure across the three dryers, the contours of time-averaged static pressure are shown in Fig. 5.11. The static pressure was observed to be higher at the lower region for all the dryers and consequently decreases with the dryer's height, which can be explained by the pressure drop profile along the height of the dryers, as shown in Fig. 5.12.

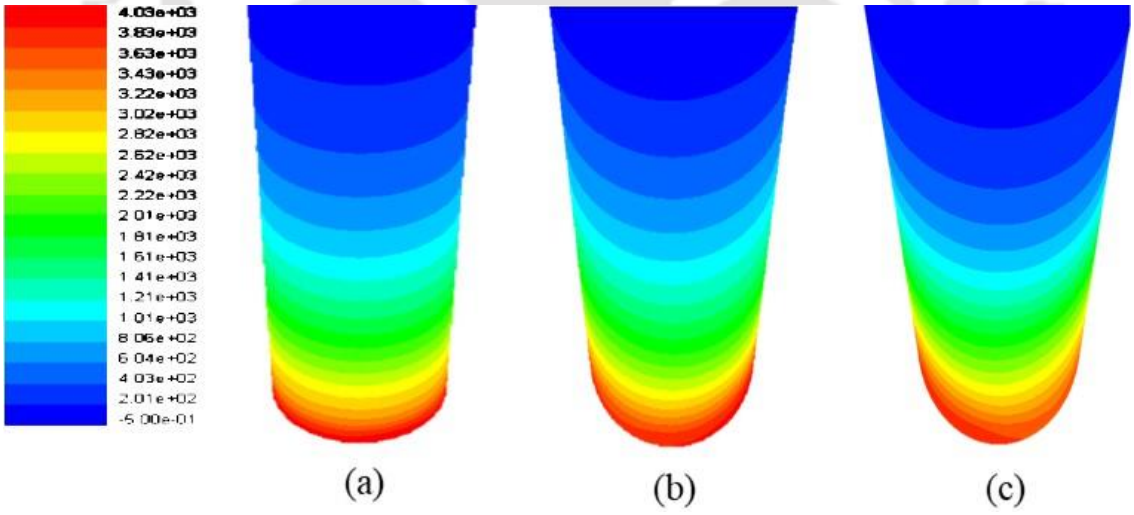

Figure 5.11: Contours of time-averaged static pressure at different cone angles, (a) α = 0°, (b) α = 5°, and (c) α = 10°

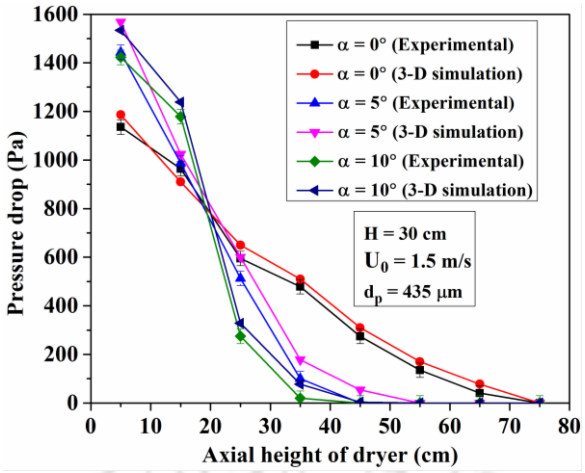

Figure 5.12: Effect of cone angle on pressure drop along the height of three dryers

It was observed from the figure that the pressure drop decreased along the height of the three dryers. The decrease in pressure drop along the height of the dryers is due to the decrease in the weight of the particles per unit cross-sectional area along the height. It was also observed from Fig. 5.12 that the effective height of the pressure drop was lesser in a higher degree of the conical dryer ($\alpha = 10°$) than in the other two dryers. The reason may be attributed to the fact that for the same height of bed particles, as the cone angle increases, the area of the cross-section along the height of the dryer increases, causing the velocity gradient to decrease along the height. As a result, there was a decrease in the expansion of particles along the height. Hence, the effective height of the pressure drop was lesser for a large cone angle.

The behaviour of particle expansion can be described by the solid volume fraction and bed expansion ratio, which is shown in the subsequent subsection. The bed pressure drop for the three dryers was investigated both experimentally and numerically and shown in Fig. 5.13.

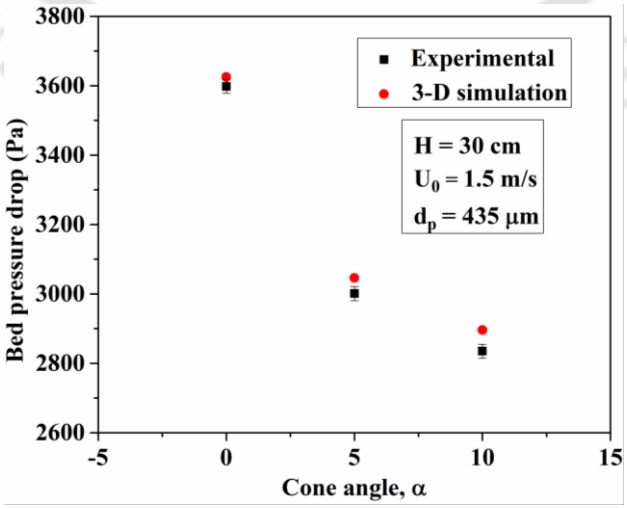

Figure 5.13: Effect of cone angle on bed pressure drop (3-D simulation and experimental)

It was observed that the bed pressure drop decreases with the increase in cone angle. When the cone angle was increased from 0° to 10°, the bed pressure drop was reduced by 22.23%. For the same amount of bed materials, as the cross-sectional area increases due to a higher cone angle, the average weight of particles per unit area of cross-section and resistance to gas flow reduces, resulting in reduced friction of the particulate to the wall. As a consequence, the bed pressure drop was found to decrease with an increase in the cone angle. Similar results were also reported by Rao and Reddy (2012) [113], Sari et al. (2012) [185] and Sahoo and Sarkar (2021) [97]. The observed results in previous literatures were due to a decrease in gas flow resistance. However, Jing et al. (2000) [71] and Sau et al. (2007) [81] observed opposite trends. This is due to the increase in mass flow rate with the area of cross-section of the bed. As shown in Fig. 5.13, the 3-D simulation results of the bed pressure drop for the three dryers are reasonably close to the experimental results.

5.6.2 Bed expansion ratio for three dryers

The bed expansion ratio is a salient hydrodynamic behaviour in the area of fluidization research to know the expansion of bed materials. It is defined by the ratio between the height of the expansion of solids and the static bed height. This behaviour determines the mixing behaviour of two-phase flow, which would affect the heat transfer phenomena. Hence, this behaviour must be acknowledged. Figure 5.14 shows the effect of cone angle on the bed expansion ratio for the same amount of bed materials.

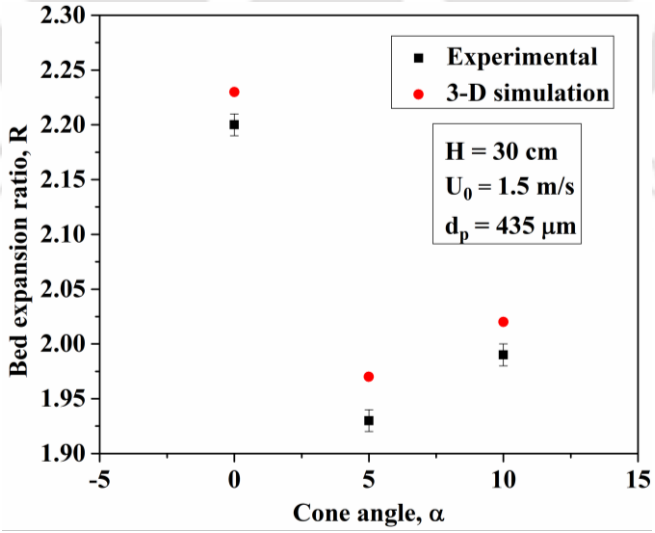

Figure 5.14: Comparison of bed expansion ratio between 3-D simulation and experiment

It was observed that the expansion ratio from the 3-D simulation results was analogous to the experimental results. It was also observed that the bed expansion ratio was higher for the

cylindrical dryer and lowered for the conical dryer at a 5° cone angle. In the cylindrical dryer, the expansion height of particles was more, which can be accompanied by the axial solid volume fraction profile in Fig. 5.15.

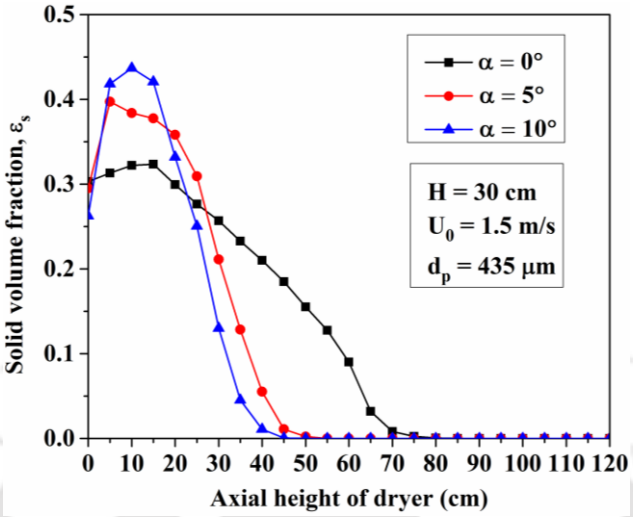

Figure 5.15: Effect of cone angle on the axial solid volume fraction

The more is the expansion of particles for the static bed height, the higher is the bed expansion ratio, as it is defined by the ratio between the expansion height of particles to the static bed height of particles. In the conical dryer of 5° cone angle, the static bed height decreases, and the expansion of height also reduces. But the relative ratio between these quantities drops. But the expansion ratio increases with a further increase in cone angle. Although the static bed height and expansion height of particle decreases, the rate at which the static bed height decreases is higher than that of the expansion height. Therefore, the bed expansion ratio was higher for the conical riser at 10° than for the conical riser at 5°. Figure 5.15 concludes that the expansion of bed height decreases as the cone angle increases for the same amount of bed materials. This may be due to a reduction in velocity gradient along the conical dryer's height when the cone angle increases. In a conical bed, the existence of the velocity gradient was more as the cone angle increased, which does not happen in a cylindrical bed. Hence, particle flow height was less for a higher degree of cone angle. It was also observed from the axial solid volume fraction that more solid particles reside across a lower region with the increase in cone angle. For visualization of this, the contour plot of the time-averaged solid volume fraction is shown in Fig. 5.16.

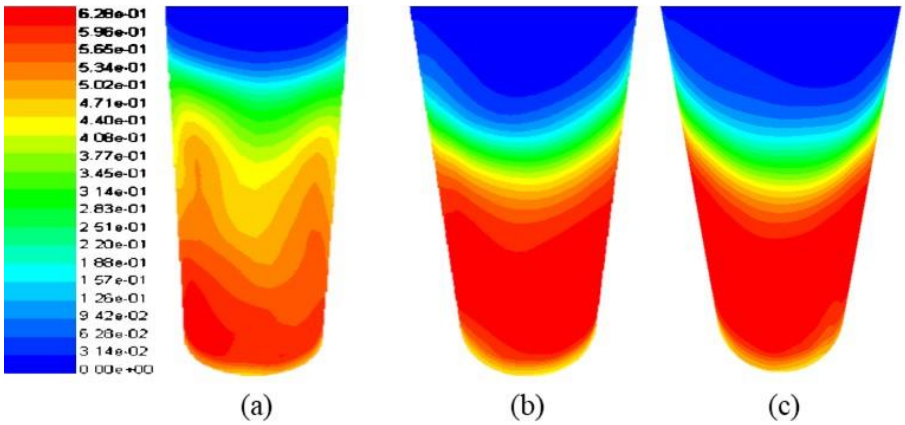

Figure 5.16: Contours of time-averaged solid volume fraction at different cone angles, (a) α = 0°, (b) α = 5°, and (c) α = 10°

It is observed from the contour of the solid volume fraction that the uniform distribution of solid particles prevails in the conical riser of the higher degree of cone angle. The solid volume fraction at the wall region was also found to increase with the increase in cone angle.

5.6.3 Radial solid volume fraction for three dryers

The investigation of radial solid volume fraction profile is important to understand the occurrence of particle concentration in a region. In this investigation, the numerical simulation of the radial solid volume fraction profile is shown. Figure 5.17 depicts the contours of the time-averaged solid volume fraction profile at an axial position of 10 cm of the dryers.

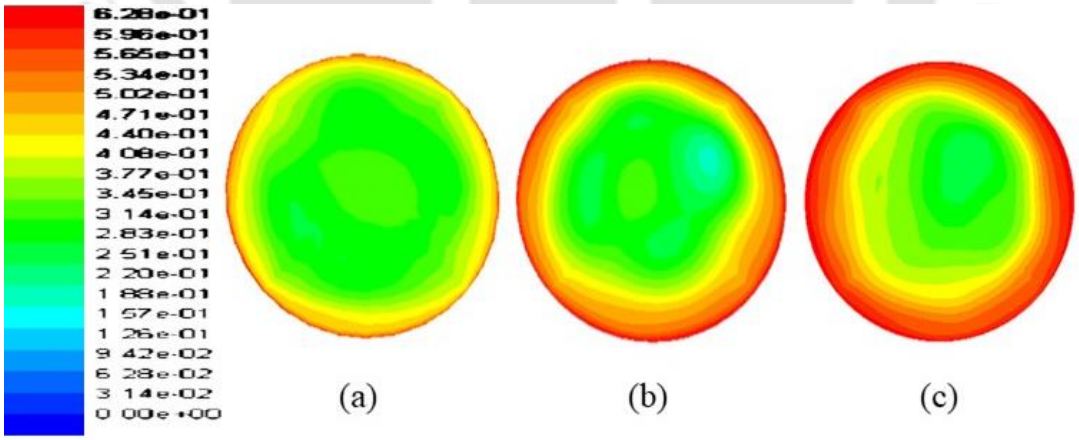

Figure 5.17: Contours of time-averaged solid volume fraction at an axial height of 10 cm at different cone angles, (a) α = 0°, (b) α = 5°, and (c) α = 10°

A core annular structure was prominently observed for all three dryers [183,184]. It can also be observed from the figure that there was an increasing amount of solid particles near the wall as the cone angle increased. The core-annular structure of solid volume fraction can be

interpreted with the help of the radial solid volume fraction plot for the three dryers in Fig. 5.18.

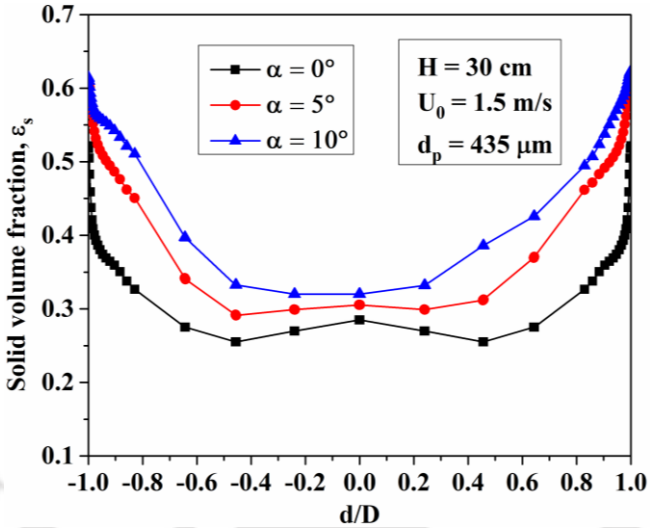

Figure 5.18: Effect of cone angle on radial solid volume fraction at the axial height of 10 cm

This figure exhibits the variation of time-averaged radial solid volume fraction with the cone angle for the same height of solid particles. The radial solid volume fraction profile for the cylindrical dryer was of W type, as shown in Fig. 5.18. However, it transformed into a U type when the cone angle increased. The W-shaped profile observed could be attributed to the formation of bubbles in the region between the centre and the dryer wall. On the other hand, with the increase in cone angle, the bubbles burst and occupy the solid particles in that region due to a decrease in velocity gradient along the height. The solid particles are dragged up axially by the continuous upward moving air, and gravity causes the solid particles to fall through the dryer's walls. This process takes place on a periodic basis for the same height of particles and inlet air velocity. However, the fraction of volume occupied by solid was more at that of axial location as the cone angle increased. This occurs due to a drop in solid velocity and the existence of a large velocity gradient with the increase in cone angle as the area of cross-section increases along the height. The reduction in solid velocity is presented by the radial solid velocity profile in subsection 5.6.4.

5.6.4 Solid velocity in the radial direction for three dryers

The contour plot of time-averaged solid velocity at an axial position of 10 cm is shown in Fig. 5.19.

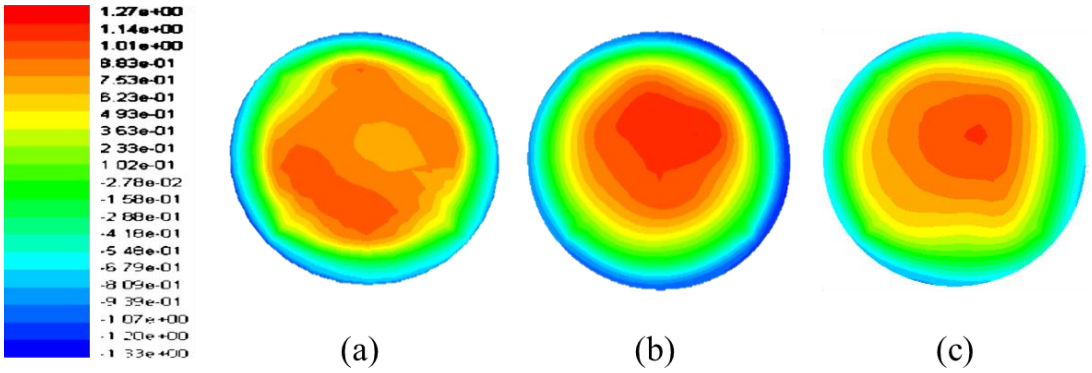

Figure 5.19: Contours of time-averaged solid velocity at an axial height of 10 cm at different cone angles, (a) α = 0°, (b) α = 5°, and (c) α = 10°

It was seen from the figure that the solid velocity was more at the core and less at the wall. The profile of radial solid velocity at an axial distance of 10 cm for the same bed height is also shown in Fig. 5.20.

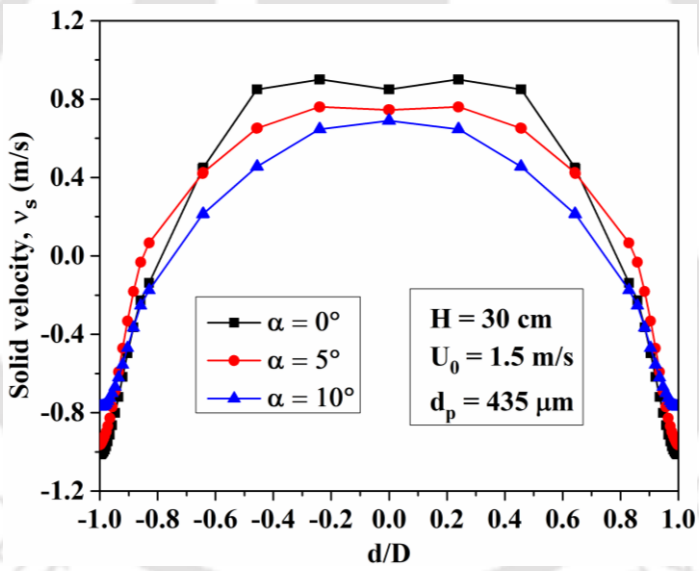

Figure 5.20: Effect of cone angle on the radial solid velocity at the axial height of 10 cm

An inverted W type profile of radial velocity of solid was clearly seen for the cylindrical dryer. Similarly, for the conical dryer of 10° cone angle, an inverted U type profile of the radial velocity of solid was observed, indicating that the solid velocity was higher in the core region and consequently lower near the wall of the dryer. It was because the drag force of air increases in the core region and decreases near the wall region for all the dryers. From Fig. 5.20, it can also be concluded that as the cone angle increases, the profile of radial solid velocity becomes inverted U type from inverted W type. The solid velocity in the core region as well as near the wall was also found to decrease with the increase in cone angle. The increase in the cone angle

results in an increase in cross-sectional area, which results in the existence of a velocity gradient along the height of the dryer. As a result, the flow separation takes place in the conical dryer, which becomes more prominent when the cone angle increases.

5.6.5 Granular temperature with solid volume fraction for three dryers

The granular temperature of the solid determines the fluctuation of solid velocity. It represents the loss of energy due to the inelasticity of the collisions, which is responsible for the existence of steady granular shear fluxes. In this subsection, the granular temperature profiles with solid volume fractions are investigated for three dryers. However, the experimental investigation of granular temperature is difficult due to the need for sophisticated instruments. The variation of radial granular temperature and percentage of solid at an axial location of 10 cm is plotted for the three dryers in Figs. 5.21 (a), (b) and (c).

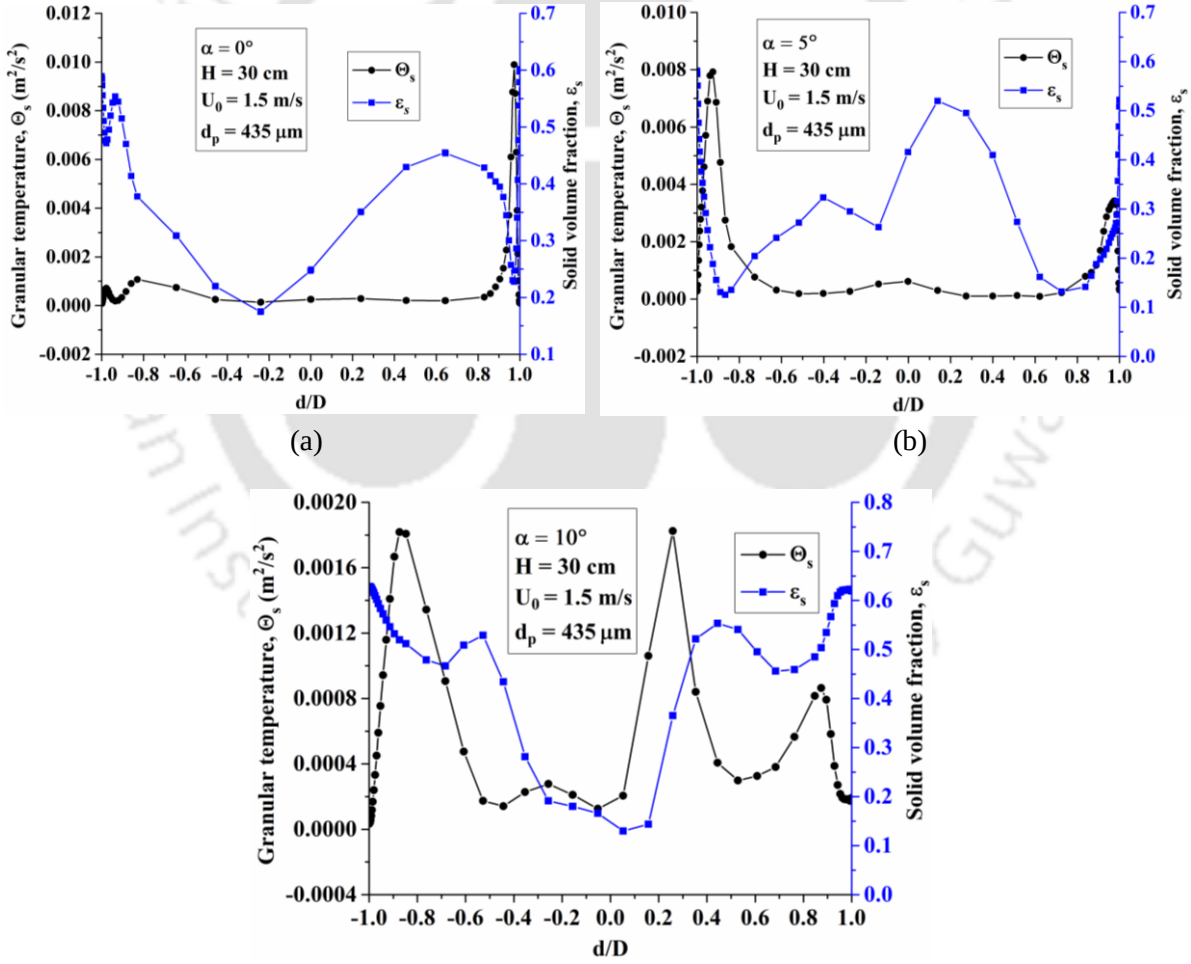

Figure 5.21: Radial granular temperature and solid volume fraction at the axial height of 10 cm for three dryers, (a) α = 0°, (b) α = 5°, and (c) α = 10°

The profiles show that the granular temperature increases as the solid volume fraction decreases. The decrease in solid volume fraction increases the mean free path of particles, increasing the fluctuation of solid velocity or the difference between instantaneous and mean velocities. Because the granular temperature is governed by the square of the solid velocity fluctuation, the granular temperature increases as the fluctuation of solid velocity increases. The rise in solid velocity results in the indication of the growth of bubbles representing higher air voidage. Moreover, particles falling and rising were higher due to the large particle shear stress. Apart from this, the results also indicated that the granular temperature near the wall decreases for all dryers. The decrease in granular temperature near the wall may be due to the frictional wall resistance to particles governed by the boundary condition imposed on the wall.

5.7 HEAT TRANSFER CHARACTERISTICS OF THREE DRYERS

After investigating the hydrodynamic behaviour, the heat transfer characteristics were studied in the three dryers for the same operating parameter as mentioned in subsection 5.1. The temperature distribution in the radial direction and interphase heat transfer coefficient were determined, and the effect on the three dryers is observed in the subsection as follows.

5.7.1 Temperature distribution of three dryers

The experimental and simulation results of temperature distribution for the three dryers are investigated at an axial location of 10 cm and are plotted radially in Figs. 5.22 (a) and (b).

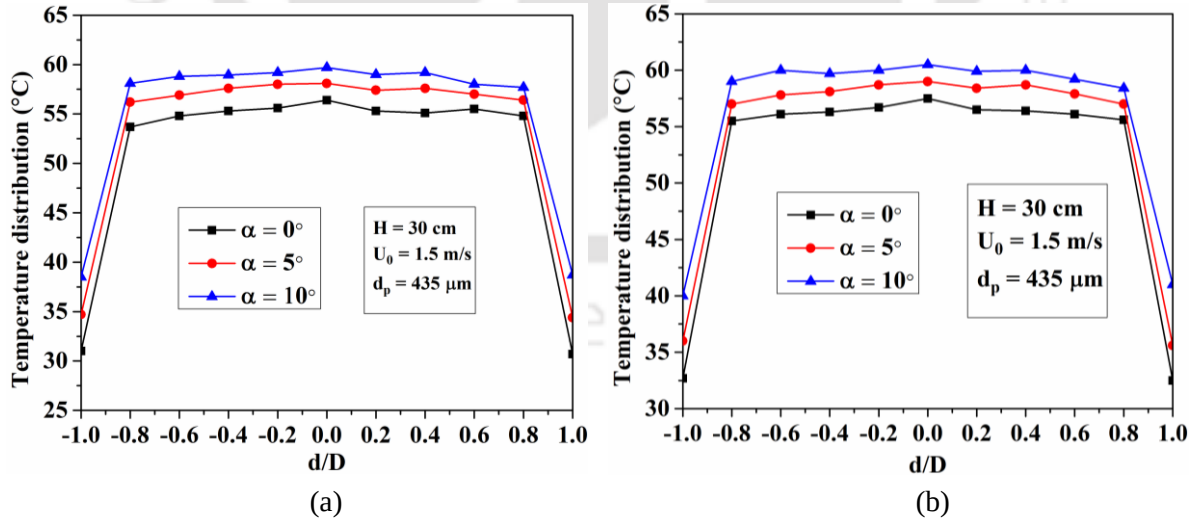

Figure 5.22: Effect of cone angle on temperature distribution, (a) experimental, and (b) 3-D simulation

It was observed from the figure that the bed and wall temperature increases with an increase in cone angle for the same air velocity. It may be due to higher conductive heat transfer between

solid particles, as the percentage of solid was more in the higher degree of the conical dryer. It may also be due to the higher gas to particle heat transfer. As the cone angle increases, the gradient of velocity decreases along the height. As a result, the solid volume increases, which results in a higher value of the Nusselt number. On the other hand, due to the lower gradient of the velocity field, the particle Reynold number decreases, which in turn reduces the Nusselt number. Nonetheless, the former counterpoises the effect of the latter. Hence, gas to particle heat transfer increases with an increase in cone angle. The results of the experimental study and numerical simulation study are compared in Fig. 5.23. The 3-D simulation temperature distribution results were found to be in strong agreement with the results of the experimental temperature distribution.

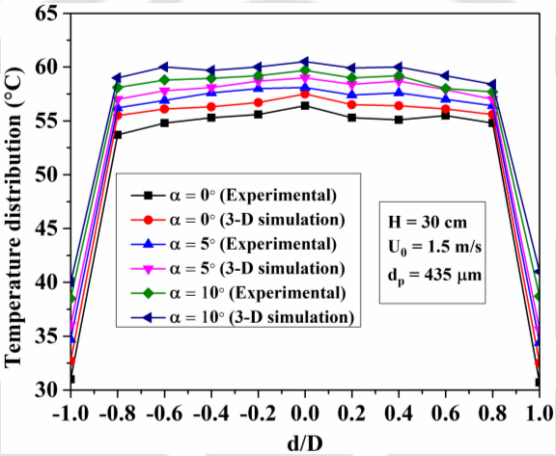

Figure 5.23: Comparison of temperature distribution between 3-D simulation and experiment

5.7.2 Interphase heat transfer for three dryers

The interphase heat transfer coefficient at an axial location of 10 cm for the three dryers is determined, and a graph of this is shown in Fig. 5.24.

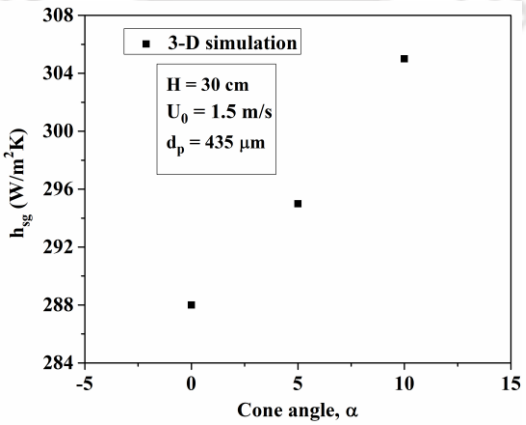

Figure 5.24: Effect of cone angle on interphase heat transfer coefficient

The interphase heat transfer coefficient increases from 288 to 306 W/m^{2}K, with the increase in cone angle from 0° to 10°, for the same air velocity and height of bed material. The reason for this is explained in the previous section.

From the above investigations, it may be concluded that the conical dryer of a higher degree cone angle has a higher interphase heat transfer coefficient than the other two dryers. As a consequence, the conical dryer having a 10° cone angle was taken to be an efficient dryer. However, in this analysis, only one operating parameter was considered, such as air velocity of 1.5 m/s, bed height of 30 cm and particle size of 435 µm. Therefore, there is a scope for a detailed analysis of the hydrodynamic behaviour and heat transfer characteristics of the efficient dryer with varying operating parameters. It was evident from the previously published literature that the hydrodynamic behaviour and heat transfer characteristics of fluidized beds are inevitably influenced by bed inventory, air velocity and particle size. Thus, experiments were carried out in the efficient dryer at three-bed heights such as 10, 20 and 30 cm and three superficial air velocity values of 1, 1.5 and 2 m/s. Similarly, the analysis referred to above was also carried out in accordance with three average particle sizes of 300, 435 and 600 µm. Furthermore, the 3-D simulation results were compared with the experimental results for the operating parameter of air velocity. The hydrodynamic behaviour such as bed pressure drop, bed expansion ratio, and pressure drop along the height of the dryer was studied, and results were compared. Similarly, the radial solid volume fraction, solid velocity in the radial direction and granular temperature at an axial height of 10 cm was investigated numerically for the operating parameter of air velocity.

5.8 HYDRODYNAMICS IN A CONICAL DRYER OF 10° CONE ANGLE

In this section, the hydrodynamic behaviour and heat transfer characteristics were studied in the conical dryer with a higher degree of cone angle by considering different operating parameters. As observed from the previous study, the higher degree of the conical dryer is considered due to the increase in bed temperature and interphase heat transfer coefficient. The bed expansion ratio, pressure drop, solid volume fraction, solid velocity, granular temperature and heat transfer characteristics are studied for the different operating parameters.

5.8.1 Bed expansion ratio of the conical dryer

In this subsection, the impact of the height of bed materials and particle size on the bed expansion ratio was investigated experimentally. Similarly, the bed expansion ratio was also

investigated experimentally and numerically for different air velocities. Figure 5.25 describes the impact of bed height on the bed expansion ratio.

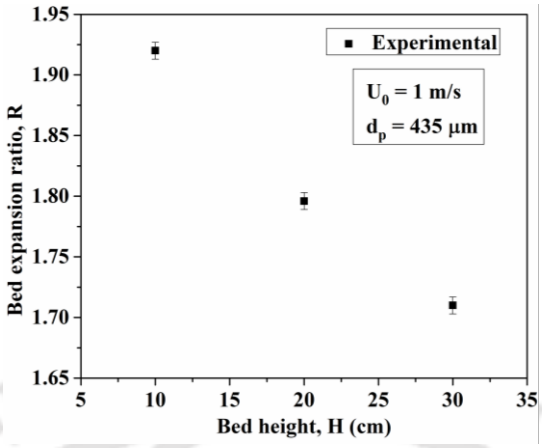

Figure 5.25: Effect of bed height on bed expansion ratio

It can be concluded from Fig. 5.25 that this behaviour decreases with an increase in bed height across the conical dryer for the constant value of velocity 1 m/s and particle size 435 µm. The experimental study shows that the ratio of bed expansion decreases by 14.7% when the bed height increases from 10 to 30 cm. Similar results were also observed by Sau et al. (2010) [79], Bahramian and Olazar (2012) [35], Padhi et al. (2016) [83], Dora et al. (2013) [82], Rao and Reddy (2012) [113] and Askaripour and Dehdorki (2016) [32] in their experimental study. The reason for this can be attributed to the increase in the amount of bed materials with an increase in bed height which increases its weight, ultimately requiring higher drag force to expand the particles than that for the less amount of bed materials. Consequent breaking of bubbles may be another cause of this observation. Similarly, the particle size effect on the bed expansion ratio across the conical dryer was investigated in Fig. 5.26.

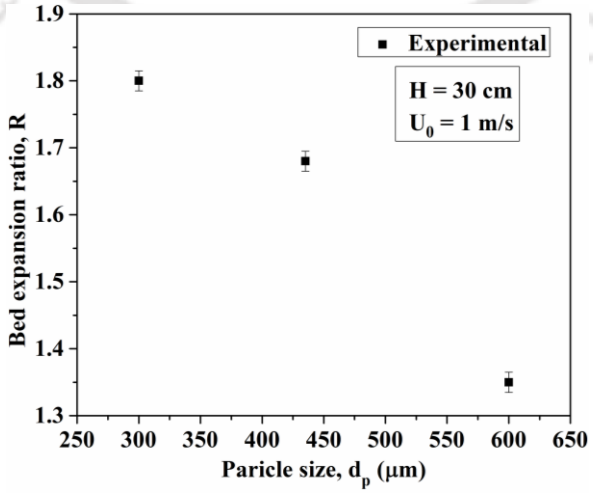

Figure 5.26: Effect of particle size on bed expansion ratio

As observed in Fig. 5.26, when particle size was increased from 300 to 600 µm, the bed expansion ratio decreased by 23.24%. Dora et al. (2013) [82], Padhi et al. (2016) [83], Sau et al. (2010) [79], and Rao and Reddy (2012) [113] also observed similar results in their experimental investigations for single particle size. The solid particles expand less due to the lower effect of gas-solid momentum influenced by larger particle size. As the expansion of solid particles is less, the expansion ratio is also less since the dryer's bed height and air velocity are constant. The bed expansion ratio at three distinct air velocities along the dryer height is shown in Fig. 5.27.

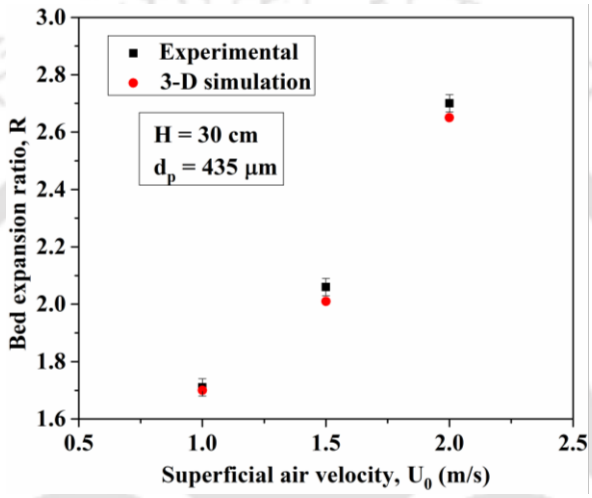

Figure 5.27: Effect of inlet air velocity on bed expansion ratio

An amount of 38.4% increase in expansion ratio was observed in the experimental study. Abdelmotalib et al. (2015) [57], Sau and Biswal (2011) [33], Sau et al. (2010) [79], Sahoo and Sarkar (2021) [97], Bai et al. (2021) [99], Bahramian and Olazar (2012) [35], Bahramian (2019) [42], Bahramian and Olazar (2021) [40], Padhi et al. (2019) [102] and Sau et al. (2011) [33] observed similar results in their study. The reason may be attributed to an increase in drag force with the rise in air velocity, where more bubbles form and grow. The growth of bubbles makes the bed particles expand more for the same amount of bed height. The expansion of bed height can be explained by the axial solid volume fraction profile shown in Fig. 5.28.

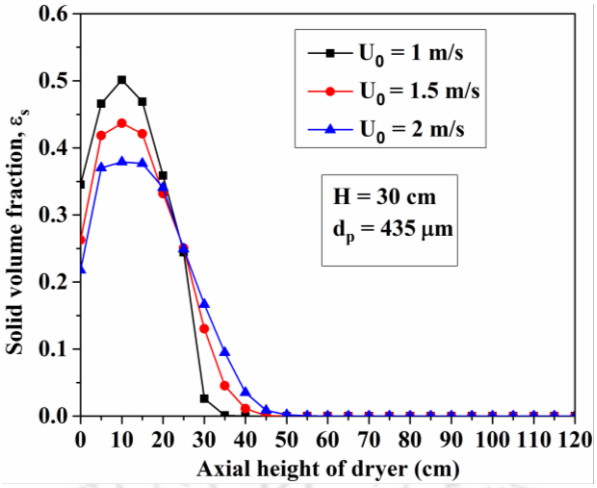

Figure 5.28: Axial solid volume fraction at three inlet air velocities

It was observed from the figure that the effective height of solid particles is higher at the higher value of air velocity, i.e. 2 m/s. The fraction of volume occupied by the solid particles was lower up to 30 cm of bed height at this operating velocity. The contours of time-averaged axial solid volume fraction are also provided to visualize the fluidization of solid particles and are shown in Fig. 5.29.

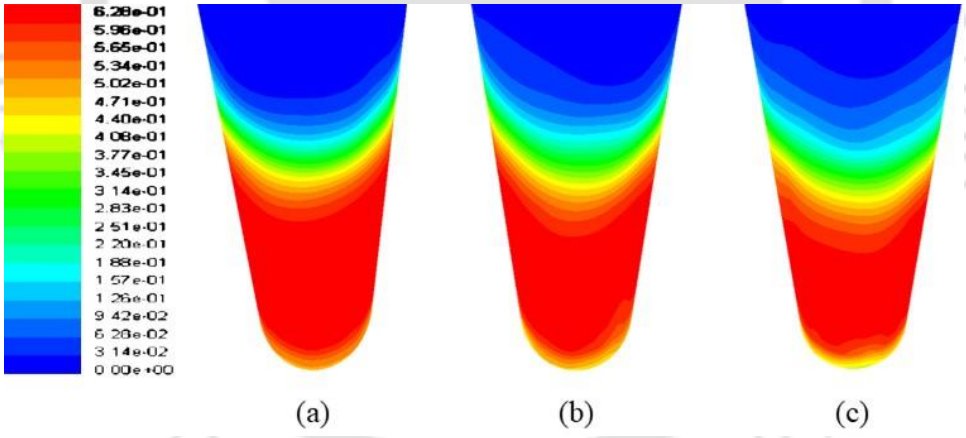

Figure 5.29: Contours of time-averaged solid volume fraction at three inlet air velocities, (a) 1 m/s, (b) 1.5 m/s, and (c) 2 m/s

The contour plot showed that the solid particles expanded more when the superficial air velocity increased, and the solid volume fraction at the wall was lower with the increase in superficial air velocity. It was observed that the 3-D simulation results of bed expansion ratio are close to the experimental results. The difference between the experimental and 3-D simulation result was just 2.34%.

5.8.2 Variation of pressure drop on the conical dryer

Bed pressure drop was investigated experimentally for three different operating parameters as aforementioned. The validation of the simulation results was also studied for different air velocities. Figure 5.30 shows the variation of bed pressure drop for the operating parameter of bed height.

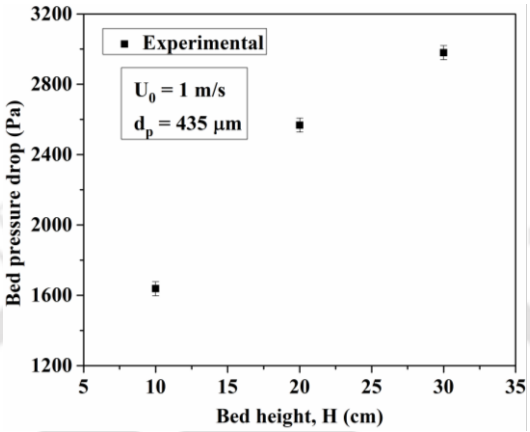

Figure 5.30: Bed pressure drop with bed height

It is seen from the figure that the bed pressure drop increases with bed height. Similar results were also observed by Jing et al. (2000) [71], Rasteh et al. (2015) [72], Katiyar (2017) [109], Murthy et al. (2009) [73], Padhi et al. (2016) [83], Dora et al. (2013) [82], Askaripour and Dehdorki (2016) [32], and Sutar and Das (2012) [39]. The pressure drop increases by 30% when bed height increases from 10 to 30 cm. This is because of the increased amount of particles as the bed height increases. The increased amount of particles increases the weight of particles across the fluidized bed dryer. As a result, the resistance to gas flow increases, resulting in increased friction of the particulate to the wall. Similarly, the effect of particle size on bed pressure drop is investigated experimentally in Fig. 5.31.

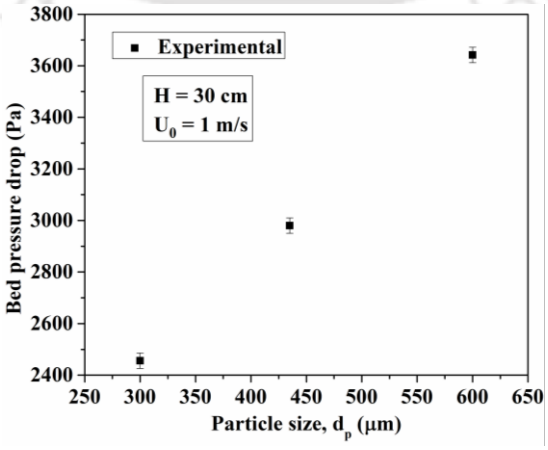

Figure 5.31: Bed pressure drop with particle size

In this figure, the bed pressure drop is found to increase with the particle size. The reason is that the larger size of particles can not be exhaled at the same air velocity. It necessitates a high velocity. As a result, a significant amount of pressure is required to lift the large particles. Hence, the pressure drop increases with the increase in particle size. The increase in particle size from 300 to 600 µm causes a nearly 24% increase in bed pressure drop. Rasteh et al. (2015) [72], Murthy et al. (2009) [73], Dora et al. (2013) [82], Padhi et al. (2016) [83], Khani (2011) [74], Kaewklum and Kuprianov (2008) [112] and Ali and Ghamin (2014) [116] reported the similar results. The bed pressure drop is also investigated for the operating parameter of air velocity, as shown in Fig. 5.32.

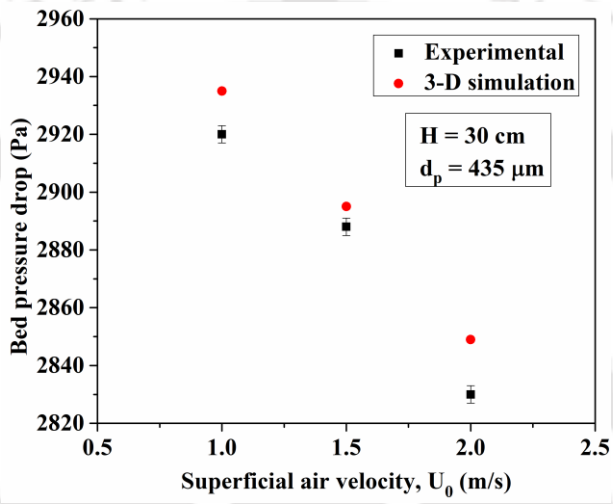

Figure 5.32: Bed pressure drop with inlet air velocity

The bed pressure drop is observed to decrease with the air velocity for both experimental and numerical conditions. As the air velocity is increased from 1 to 2 m/s, the bed pressure drop decreases by 3.54%. The reason is that, with the rise in air velocity, the solid particles are mostly influenced by the momentum exchange and inertia. Because of that, the gas holdup increases, ensuring uniform distribution of particles and thereby decreasing the density of particles. Since the density is lower, the buoyancy force increases, thus reducing the drag. Hence, the pressure drop is witnessed to decrease with the increase in inlet air velocity. Similar observations have also been made by Dora et al. (2013) [186], Bahramian (2019) [42], Bahramian and Olazar (2021) [40], and Padhi et al. (2016) [187]. The 3-D simulation results are found to be in good agreement with the experimental pressure drop.

The pressure analysis along the height of the dryer was also investigated for the three air velocities. For that, a contour plot of the time-averaged static pressure is shown in Fig. 5.33.

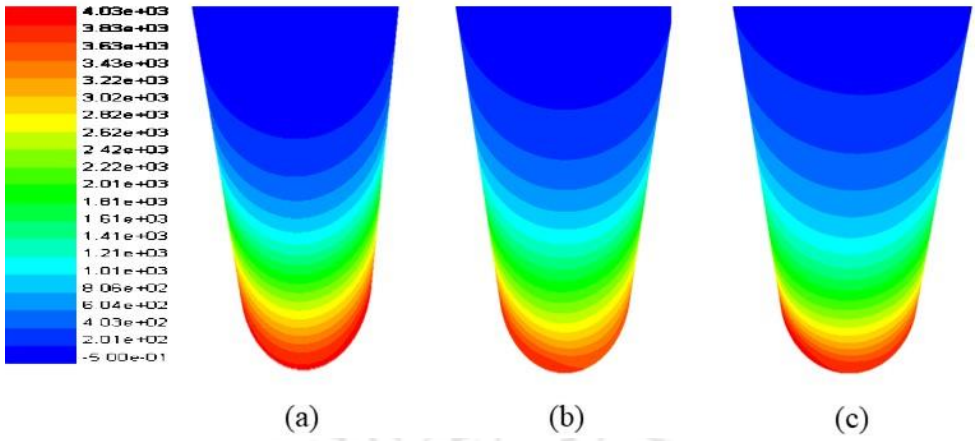

Figure 5.33: Contours of time-averaged static pressure at three inlet air velocities, (a) 1 m/s, (b) 1.5 m/s, and (c) 2 m/s

It was observed from the contour plot that the time-averaged static pressure decreases with the height of the dryer for all velocities. It was also observed from the contour plot that the static pressure at the lower region decreases with the increase in air velocity. In order to investigate the proper analysis of the pressure, the pressure drop profile for three velocities is shown in Fig. 5.34.

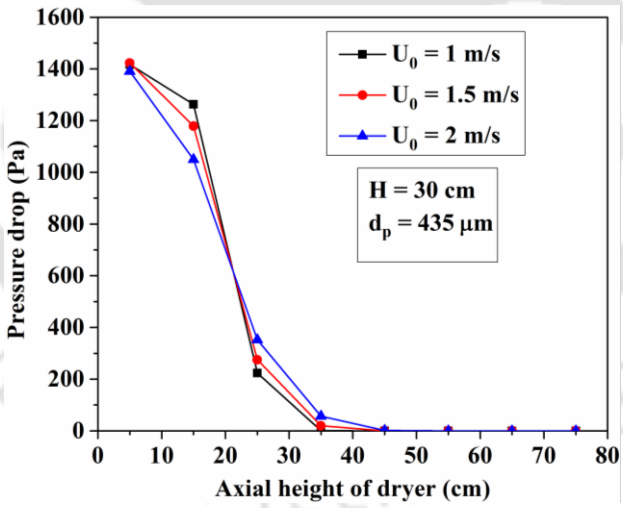

Figure 5.34: Effect of inlet air velocity on pressure drop along the height of the conical dryer with 10° cone angle

It was observed that the pressure drop height increases with the increase in the air velocity. The effective height of pressure drop is 45 cm for the higher value of air velocity. At higher air velocity, the expansion of particles is more due to the higher drag force, as discussed in the previous subsection. As a result, the pressure drop height is more for the higher value of air velocity.

5.8.3 3-D simulation of radial solid volume fraction

In this subsection, the radial solid volume fraction at an axial location of 10 cm is discussed for the three air velocities. The contours of time-averaged solid volume fraction at an axial location of 10 cm are shown in Fig. 5.35.

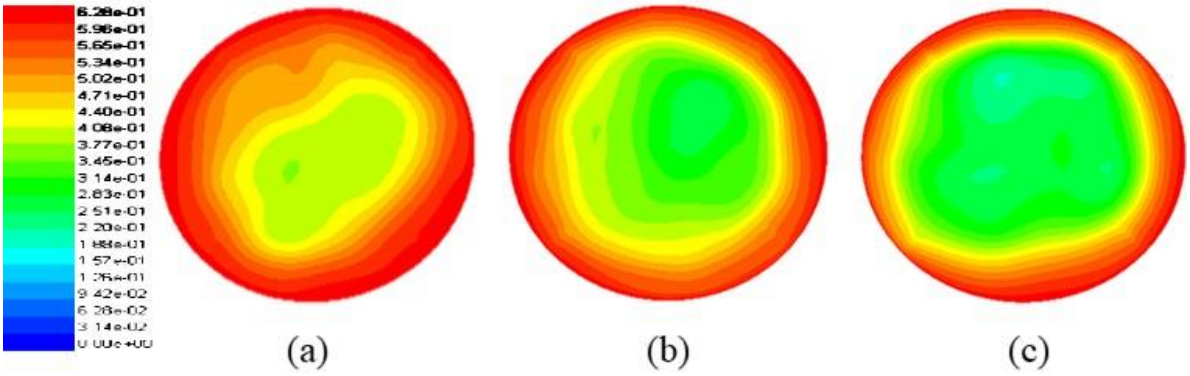

Figure 5.35: Contours of time-averaged solid volume fraction at 10 cm axial location at three air velocities, (a) 1 m/s, (b) 1.5 m/s, and (c) 2 m/s

It is seen from the figure that there is a significant difference in solid volume fraction contour with the variation of air velocity for all other parameters being constant (H = 30 cm and d_p = 435 µm). The solid particles reside near the wall than in the centre for all values of air velocities. It was also observed that the thickness of particles from the wall to the centre decreases when the superficial air velocity increases. The reason for this is that the higher the value of air velocity, the greater the influence on the bed as the interphase momentum exchanges more. In order to investigate this, a radial solid volume fraction profile is shown for three air velocities. Figure 5.36 shows the profile of simulated radial solid volume fraction at three air velocities.

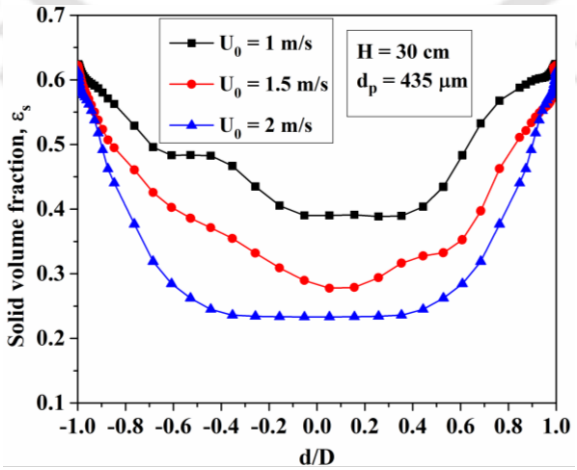

Figure 5.36: Radial solid volume fraction with different inlet air velocities

It was observed from the figure that the radial solid volume fraction profiles for three air velocities are of U type, which means that the solid particles remain more near the wall than the core of the dryer. This is due to the increased drag force in the core region, where solid particles are transported and fall by touching the wall of the dryer due to gravity. Along the wall, the drag force on sand particles is not appreciable and tends to accumulate there. The higher is the drag force; the lower is the solid volume fraction in the region of 10 cm. It is also observed that solid particles tend to reside less towards the bottom of the dryer when the air velocity is higher. As the air velocity is higher, the solid velocity is also higher, which causes the emergence of large bubbles and their growth. In addition, the solid particles are transported more rapidly as the velocity of air increases. Hence, the solid volume fraction is lower for the higher value of velocity.

5.8.4 3-D simulation of the solid and air velocity of the conical dryer

Figure 5.37 shows the 3-D simulation contours of time-averaged axial solid velocity for the three air velocity values in the radial direction.

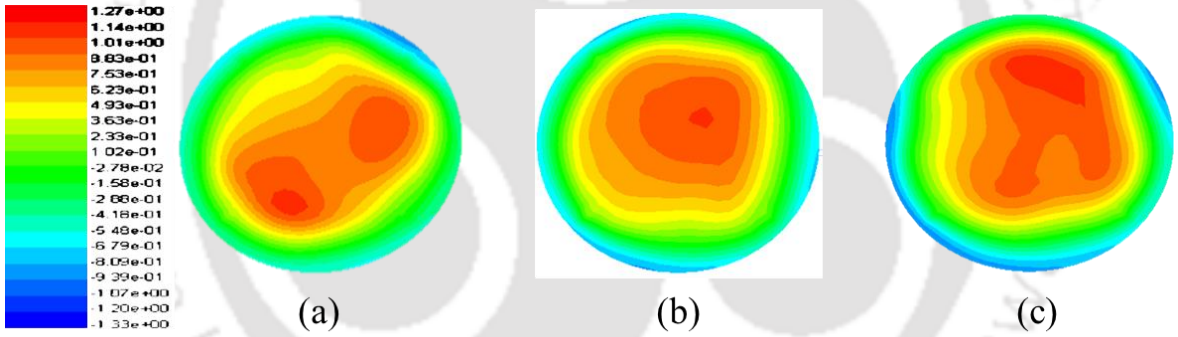

Figure 5.37: Contours of time-averaged solid velocity at 10 cm axial location at three air velocities, (a) 1 m/s, (b) 1.5 m/s, and (c) 2 m/s

It is observed from the figure that the solid velocity is maximum in the core region than the dryer's wall. To analyze the result of solid velocity, a profile of solid velocity in the radial direction is depicted in Fig. 5.38. It is seen that the solid velocity is higher in the core region than that of the wall of the dryer for all three air velocities. To analyze the result of solid velocity, a profile of radial air velocity is also depicted in Fig. 5.39.

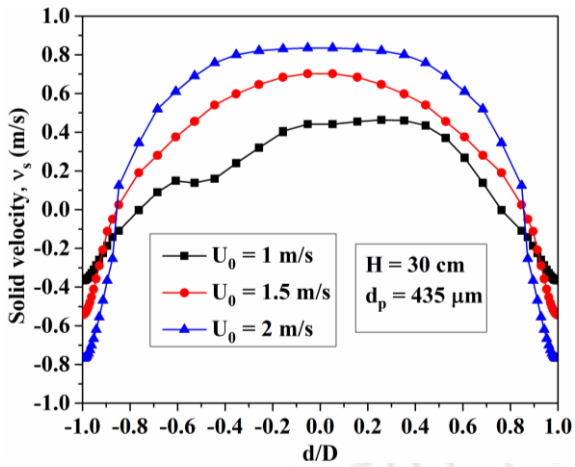

Figure 5.38: Radial solid velocity for three inlet air velocities at a 10 cm axial height

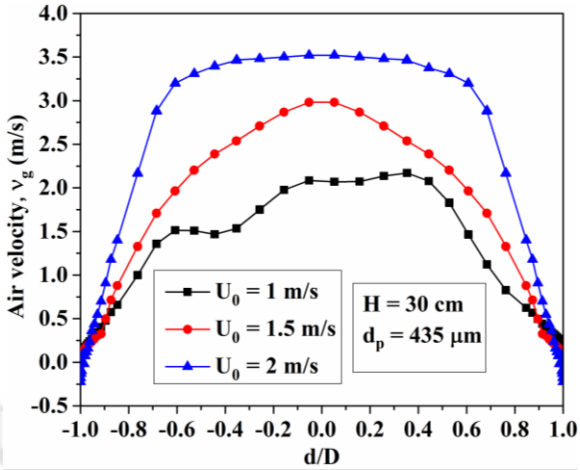

Figure 5.39: Radial air velocity for three inlet air velocities at a 10 cm axial height

In the core region, the drag force of the fluidizing air is higher, which carries sand particles at a higher velocity. The results also indicate that the solid velocity is higher at higher air velocity. The explanation for this could be that as air velocity rises, the interphase exchange momentum and the gas phase velocity field have a greater influence on the particles. Hence, maximum solid velocity is obtained at higher air velocity. It is also observed from Fig. 5.38 that particles descend along the walls at smaller downward velocities at 1.0 m/s than at higher air velocities. At a lower value of velocity, particles do not expand to a greater height due to less momentum exchange, and as a result, more particles are accumulated to a shorter height, which can be seen from the radial solid volume fraction profile in Fig. 5.36, due to which collision frequency between particles is less. The reduction in particles collision frequency results in a decrease in granular temperature, which can be described by the radial profile of granular temperature with solid volume fraction in the subsequent subsection. Moreover, the boundary condition imposed on the wall is no-slip for air and for the lower value of air velocity, the hydrodynamic boundary layer is thicker, which corresponds to less impact on solid particles by the air. Hence, particles descend along the wall at a smaller downward air velocity of 1.0 m/s than the other two air velocities (1.5 and 2 m/s).

5.8.5 3-D simulation of radial granular temperature and solid volume fraction

Similar to the previous subsection 5.6.5, the granular temperature for three velocities is investigated and shown in Figs. 5.40. Figure 5.40 (a), (b) and (c) exhibit the 3-D simulation profile of radial granular temperature and solid volume fraction for three velocities at 20 s.

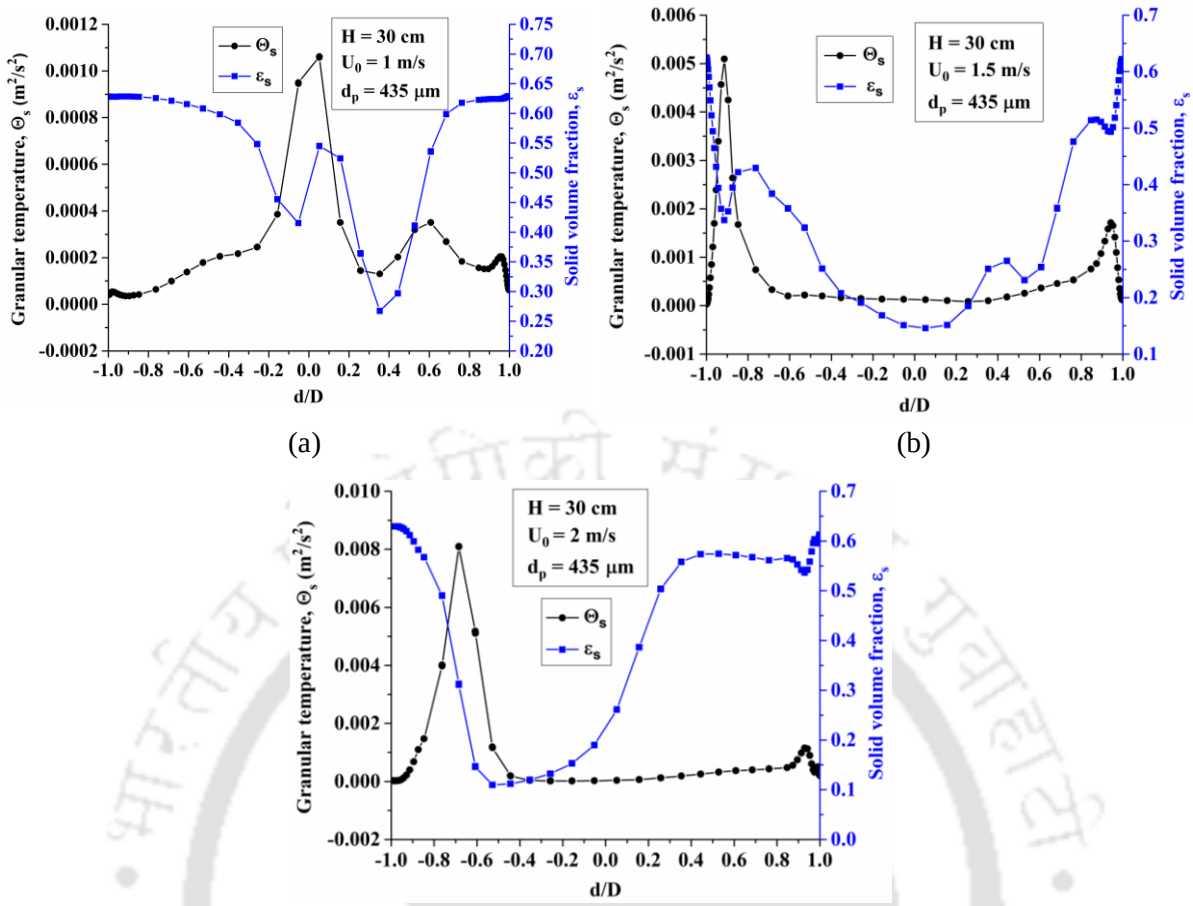

Figure 5.40: Radial granular temperature and solid volume fraction at an axial height of 10 cm, (a) 1 m/s, (b) 1.5 m/s, and (c) 2 m/s

It is reflected that for all the cases, the granular temperature increases where the solid volume fraction decreases. The reason for this was explained already in subsection 5.6.5.

5.9 HEAT TRANSFER CHARACTERISTICS IN A CONICAL DRYER OF 10° CONE ANGLE

The heat transfer characteristics of the conical dryer are carried out experimentally and numerically with the same operating parameters as the hydrodynamic behaviour. Temperature distribution in the radial direction is investigated experimentally. Similarly, the experimental results are compared with the 3-D simulation results for the operating parameter of air velocity. The interphase heat transfer coefficient is also determined numerically for the inlet air velocity.

5.9.1 Experimental result of temperature distribution

This subsection illustrates the variation of bed temperature at an axial distance of 10 cm in the radial direction. In this regard, air at 65°C was applied through the inlet of the dryer, and the

initial temperature of the wall and outlet before the experiment was 27°C. The bed temperature in the radial direction for the three operating parameters is investigated in Figs. 5.41-5.43.

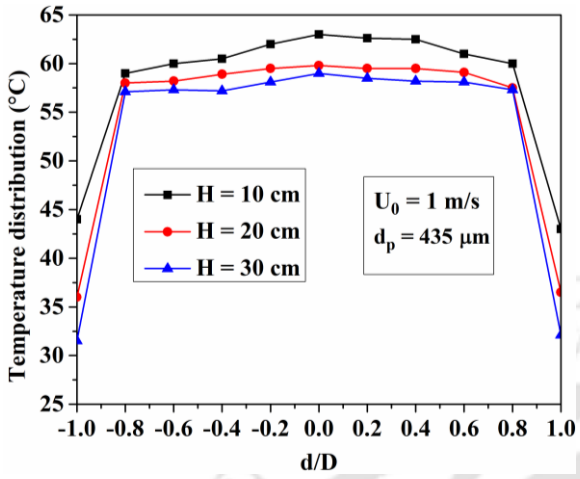

Figure 5.41: Bed temperature with bed height

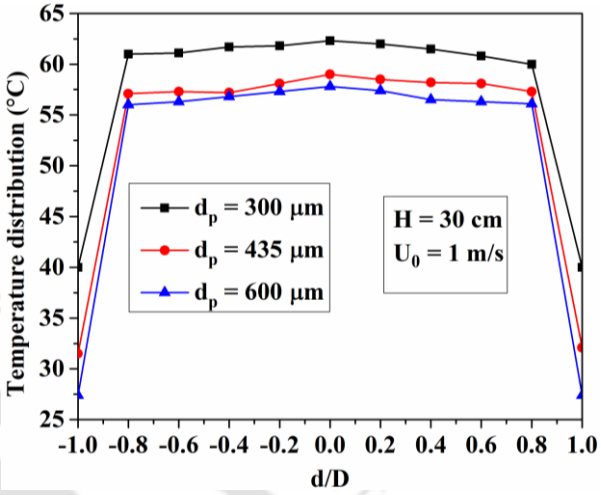

Figure 5.42: Bed temperature with particle size

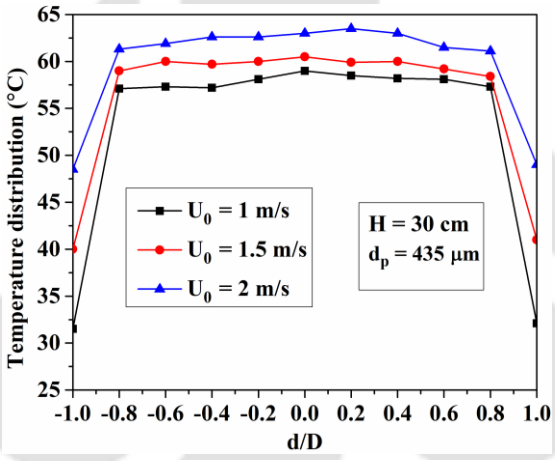

Figure 5.43: Bed temperature with inlet air velocity

It is observed from the above three figures that the temperature in the core region is higher than the temperature at the wall. Since the core region has a lower solid volume fraction than the wall of the dryer, the mixing of air and solid particles is improved, allowing for more convective heat transfer between the air and solid particles. As a result, temperature increases in the core region. On the other hand, particle-particle heat conduction at the wall is lesser than that of the convective heat transfer between air and solid particles. Particles accumulate as the solid volume fraction increases, indicating a higher thermal resistance. Figure 5.41 shows the radial bed temperature for the three different bed heights. It is observed from the figure that the bed temperature decreases from 63 to 58.3 ℃ with the increase in bed height of particles from 10 to 30 cm. If the bed height increases, the solid volume fraction increases, reducing the surface area of solid particles in contact with the air. Furthermore, increasing the solid volume

fraction reduces convective heat transfer between air and solid particles. Hence, bed temperature decreases with the bed height of particles. Similarly, the bed temperature also drops (from 62.3 to 57.8 ℃) as the particle size increases from 300 to 600 µm, as seen in Fig. 5.42. This may be due to the decrease in interphase momentum exchange and change in the velocity field. The interphase momentum exchange has little impact on particles of larger sizes, so the majority of particles remain in this field. As a result, particles of a greater size cannot be readily disposed of in hot air. Because of that, they do not absorb as much heat as smaller particles. Hence, bed temperature decreases with particle size. However, the bed temperature is found to increase with air velocity in Fig. 5.43. The increase in air velocity increases collision frequency, indicating improved particle agitation and mixing characteristics between particles and the hot air. As a result, convective heat transfer between air and solid particles and particle to particle increases. It is also observed that the wall temperature increases with air velocity. More solid particles move upward as the air velocity increases, and they appear to be distributed in the radial direction. As a consequence, a cluster of particles forms at the wall. Further, as the velocity increases, these clusters of solids break up into smaller sizes, and the solid volume fraction decreases, allowing hot air to encounter solid particles. Hence, wall temperature increases with air velocity. As air velocity increases from 1 to 2 m/s, the temperature of the bed rises by 6.34 %.

5.9.2 Validation of 3-D simulation temperature distribution with the experimental temperature distribution

In this subsection, a comparative result of experimental and simulation temperature distribution in the radial direction is investigated for three velocities and the results are shown in Fig. 5.44.

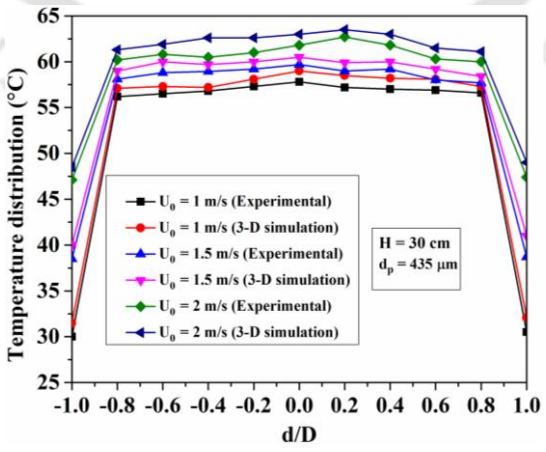

Figure 5.44: Comparison of radial temperature distribution between 3-D simulation and experiment

The 3-D simulation of temperature is found to be in good agreement with the experimental results. However, the numerical results deviate by a maximum of 2.3% from that of experimental results.

5.9.3 Interphase heat transfer coefficient

In the 3-D numerical simulation, the gas to particle heat transfer coefficient for three velocities was calculated at an axial location of 10 cm of the conical dryer; a graph of that is shown in Fig. 5.45.

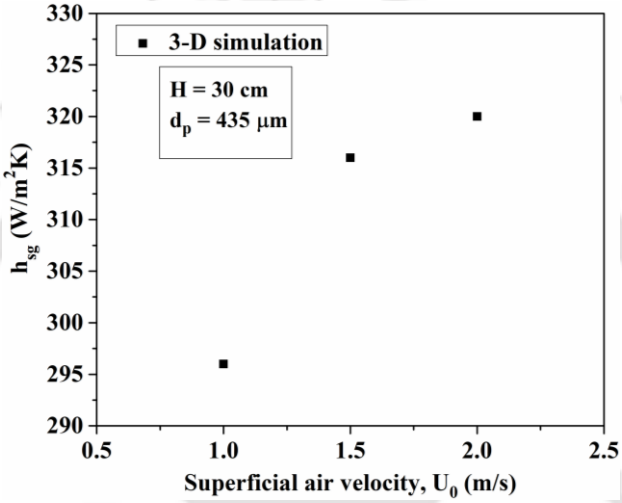

Figure 5.45: Interphase heat transfer coefficient with inlet air velocity

It has been observed that the interphase heat transfer coefficient increases from 296 to 320 W/m^{2}K with an increase in air velocity from 1 to 2 m/s. For the constant temperature, as the air velocity increases, the relative velocity between the air and solid increases, which in turn increases the particle Reynold number. The increase in particle Reynold number increases the interphase heat transfer coefficient. The amount of heat content supplied through the dryer's inlet also increases when the air velocity increases. Hence, the interphase heat transfer increases with the inlet air velocity for the constant inlet air temperature.

5.10 CHAPTER CONCLUSION

In the present investigation, the hydrodynamic behaviour and heat transfer characteristics of sand particles in five bubbling fluidized bed dryers were investigated experimentally and numerically. At the onset of the present investigation, the 2-D simulation was carried out to model the fluidized bed dryers for the operating parameter of one height of bed particles, air velocity and particle size. Experiments were also carried out based on numerical results of hydrodynamic behaviour, and results were analysed. It was observed that the 2-D simulation results deviate

from the experimental results by an average of 12.53%. However, the trend remains the same with the experimental results. After validation, the hydrodynamic behaviour and heat transfer characteristics were investigated experimentally. The 3-D simulations were also carried out to validate the simulation results with the experimental results. The simulation results were reasonably in good agreement with experimental results. Furthermore, the experiments were carried out in a conical dryer at a 10° cone angle to investigate the hydrodynamics and heat transfer characteristics with varying operating parameters. Similarly, the heat transfer characteristics were also investigated for the same operating parameters and compared with the 3-D simulation. However, to compare the experimental results with 3-D simulation results, one operating parameter was considered, which was varying inlet air velocity. The bed temperature at a central location of dryer height of 10 cm was investigated experimentally and numerically. It is intriguing to note that the 3-D numerical simulation results were in excellent agreement with the experimental investigation for bed expansion ratio, bed pressure drop and bed temperature. It was found that the interphase heat transfer coefficient increases from 288 to 306 W/m^2K with increasing cone angle. It was also observed that the interphase heat transfer coefficient increases from 296 to 320 W/m^2K when the air velocity increases from 1 to 2 m/s.

It was observed from this chapter that the conical dryer of cone angle 10° has a higher heat transfer coefficient with increasing superficial air velocity. Therefore, the higher degree of the conical dryer can be regarded as an efficient dryer. This chapter studied only the hydrodynamics and heat transfer characteristics of sand particles. It was reported in the literature that the heat transfer characteristics influence the drying performance inside a dryer [188,189]. So, keeping the interphase heat transfer coefficient and temperature distribution analysis of sand particles in mind, the present dryers were utilized to study the drying characteristics of agricultural produce. Paddy is one of the cereal crops which is largely available in Assam, as described in chapter 1. So, the drying characteristics of paddy particles were investigated in the present dryers with varying operating parameters. The next chapter devotes to the effect of various operating parameters on the drying characteristics of paddy particles.

6

Performance evaluation of drying characteristics in BFB dryers

6.1 Introduction

6.2 Hydrodynamic behaviour

6.3 Drying characteristics

6.4 Energy consumption

6.5 Drying and milling quality

6.6 Thermodynamic (energy and exergy) analysis

6.7 Chapter conclusion

CHAPTER 6

PERFORMANCE EVALUATION OF DRYING CHARACTERISTICS IN BFB DRYERS

6.1 INTRODUCTION

In this chapter, the hydrodynamic behaviour and drying characteristics of the paddy drying process are experimentally investigated to study the effect of different operating parameters in a conical bubbling fluidized bed dryer with a cone angle of 10°. The energy consumption such as thermal and energy consumption of blower are also studied in the fluidized bed dryer. The effect of a spiral and cone angle on three bubbling fluidized bed dryers is also studied. Energy and exergy analyses are performed in the three dryers with operating parameters to optimize the performance of dryers. Experiments were conducted at three different superficial air velocities of 1.1, 1.6 and 2.1 m/s with bed inventories ranging from 1 to 3 kg. Three different inlet air temperatures of 55, 60 and 65°C were maintained to evaluate the drying process. The hydrodynamic behaviour in terms of pressure drop is discussed in section 6.2. The drying characteristics of paddy particles are also investigated and discussed in section 6.3. Section 6.4 describes the thermal and blower energy consumption in the paddy drying process. Similarly, in section 6.5, the drying and milling quality of dried paddy is investigated and analyzed. Section 6.7 demonstrates the energy and exergy analysis of the drying characteristics. Finally, the chapter is summarized in section 6.8.

6.2 HYDRODYNAMIC BEHAVIOUR

In order to investigate the bed hydrodynamics, preliminary experiments were carried out to calculate the pressure drop along the height of the three dryers. Experiments were carried out with three inlet air velocities (1.1, 1.6 and 2.1 m/s) and four-bed inventories (1, 2, 2.5 and 3 kg) and the results were compared. Numerical simulations were also carried out to compare the pressure drop between sand and paddy particles with the same operating parameters. The pressure drop of the two conical dryers was compared with the results of Thant et al. (2018) [123]. Furthermore, the effect of a spiral on pressure drop was investigated in the two conical dryers. Finally, the effect of cone angle with a spiral on pressure drop was investigated, and results were compared. In order to study the effect of the spiral on pressure drop, only one set of parameters was considered, i.e. m_p = 2.5 kg and U_0 = 1.6 m/s. For all investigations, the

difference in pressure drop was measured using water-filled differential U-tube manometers. Twelve pressure taps separated by 10 cm were inserted above the distributor plate along the height of the three dryers, and the differential height was measured between two successive pressure taps. From the differential height, the pressure drops were calculated.

Figure 6.1 shows the variation of experimental and numerical pressure drops between two consecutive pressure taps along the height of the conical dryer ($\alpha = 10°$) at different superficial air velocities (1.1, 1.6 and 2.1 m/s) and a constant bed inventory ($m_p = 2$ kg).

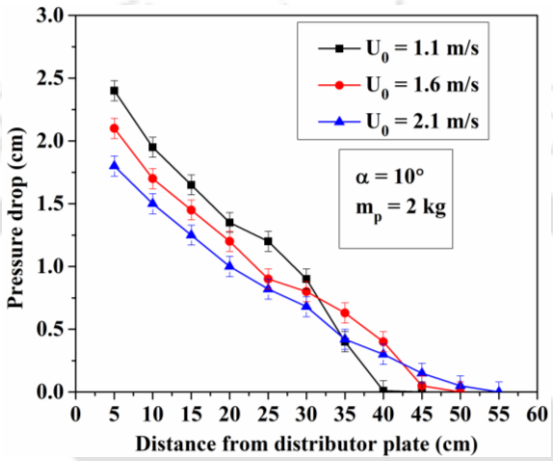

Figure 6.1: Pressure drop along the height of a conical dryer with 10° cone angle at different superficial air velocities

It was observed from the figure that there was a decrease in pressure drop with an increase in the height of the dryer for all velocities. At a particular height of the dryer, the pressure drop was lower for higher superficial velocity. In Fig. 6.1, it was also observed that at dryer heights of 30 cm to 45 cm, the pressure drop was steeper for lower superficial velocity because the increasing air velocity continues to raise the gas volume fraction, which reduces the concentration of the bed material. Figure 6.1 also concludes that the effective bed height for increased superficial velocity is higher. Furthermore, the pressure drop between paddy and sand particles was compared numerically along the height of the conical dryer at a 10° cone angle with the operating parameter of air velocity. In this investigation, two air velocities, such as 1.1 m/s and 1.6 m/s, were considered. The bed height of both materials was taken as 10 cm. The size of paddy and sand particles were taken as 2.5 mm and 0.435 mm, respectively. Nonetheless, the influence of humidity and paddy moisture content was not taken into account. Similarly, the experimental pressure drop of paddy was also compared with the numerical simulation. As a result, the graph of the pressure drop as a function of dryer height is shown in Figs. 6.2 (a) and (b).

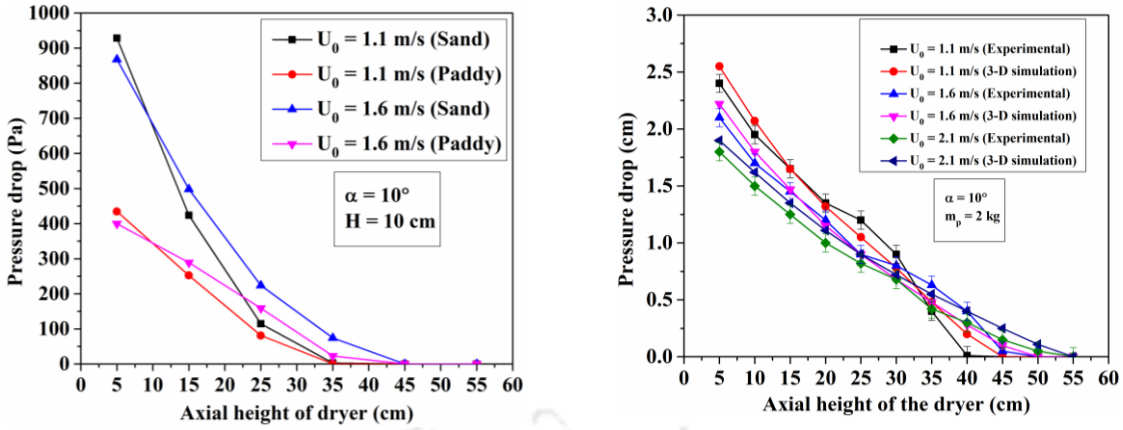

(a) (b)

Figure 6.2: Comparison of pressure drop (a) between sand and paddy particles and (b) between experimental and 3-D simulation

It was observed from figure 6.2 (a) that the pressure drop for the sand particles was higher, as its density was higher than that of the paddy particles. Despite the fact that sand particles have a smaller particle size than paddy particles, the pressure drop for sand particles was higher due to their higher density. But the trend of pressure drops along the height of the dryer for both the particles remains the same. In Fig. 6.2 (b), the pressure drop along the height of the dryer for the three air velocities between experimental and simulation conditions were found to be in good agreement.

Pressure drops along the dryer's height were also investigated for varying bed inventories, as shown in Fig. 6.3.

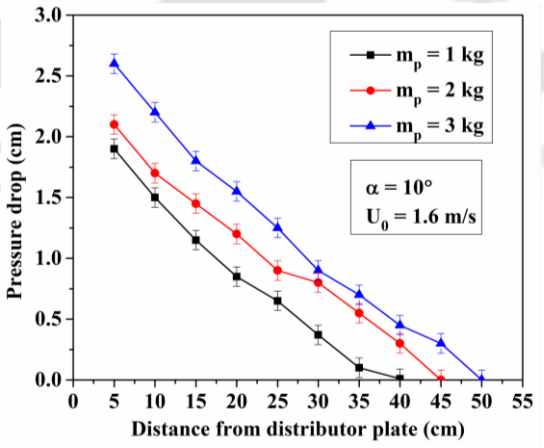

Figure 6.3: Pressure drop along the height of a conical dryer with 10° cone angle at different bed inventories

It was observed that pressure drop between two successive distances decreases with dryer height for all inventories. This is because the concentration of bed particles is higher at the

bottom of the conical fluidized bed dryer, and it decreases with the height of a dryer. The figure also shows that the pressure drop increases as bed inventory increases for a constant superficial air velocity. Static pressure is defined as the weight per unit of cross-sectional area, and an increase in bed inventory increases the weight of bed inventory per unit of cross-sectional area.

Furthermore, the effect of mixing sand particles with paddy on pressure drop along the height of the conical dryer having a cone angle of 10° is investigated. Figure 6.4 shows the effect of mixing sand and paddy on pressure drop along the height of the conical dryer at a 10° cone angle.

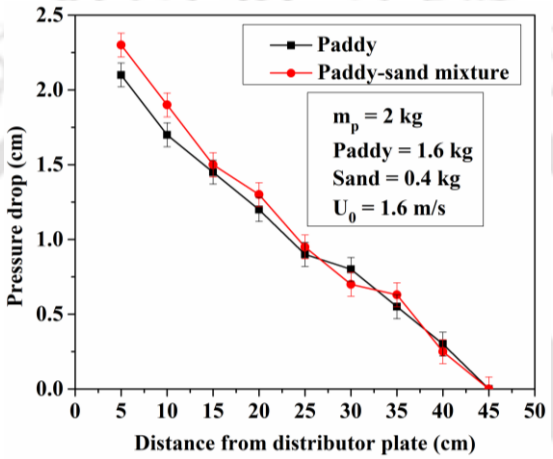

Figure 6.4: Effect of mixing of sand with paddy on pressure drop in a conical dryer with 10° cone angle

The prime intention of mixing was to shorten the drying time. The hydrodynamic behaviour of the fluidized bed dryer must be understood in order to investigate the drying characteristics. To achieve a constant bed inventory of 2 kg, 0.4 kg of sand was mixed with 1.6 kg of paddy. The figure reveals that the pressure drop increased when sand was mixed with paddy for the same amount of bed inventory. The explanation for this is that the density of the sand particles is higher than that of the paddy, so the interphase momentum influence is less. Similar to the previous studies, the effect of a spiral on pressure drop in the two conical dryers was investigated, and the results are presented in Figs. 6.5 and 6.6.

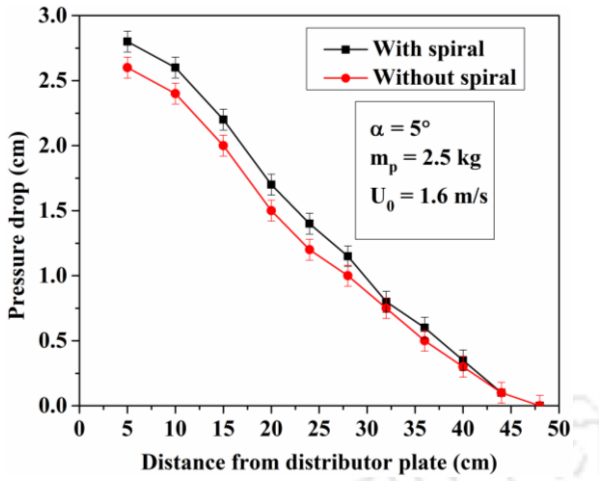

Figure 6.5: Effect of a spiral on pressure drop along the height of a conical dryer with 5° cone angle

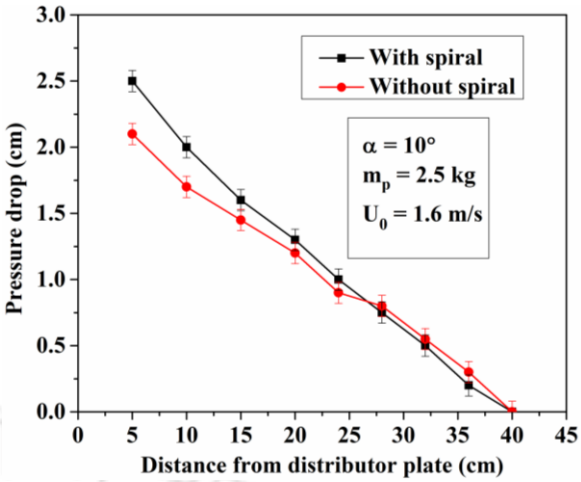

Figure 6.6: Effect of a spiral on pressure drop along the height of a conical dryer with 10° cone angle

The pressure drops increase with the use of a spiral for both dryers, as seen from the figures. The reason for this behaviour is the vigorous agitation of particles along the height of dryers. The reason may also be due to the increased expansion and contraction of particles to the wall of the dryers. The effect of cone angle on pressure drop without and with a spiral is shown in Figs. 6.7 (a) and (b).

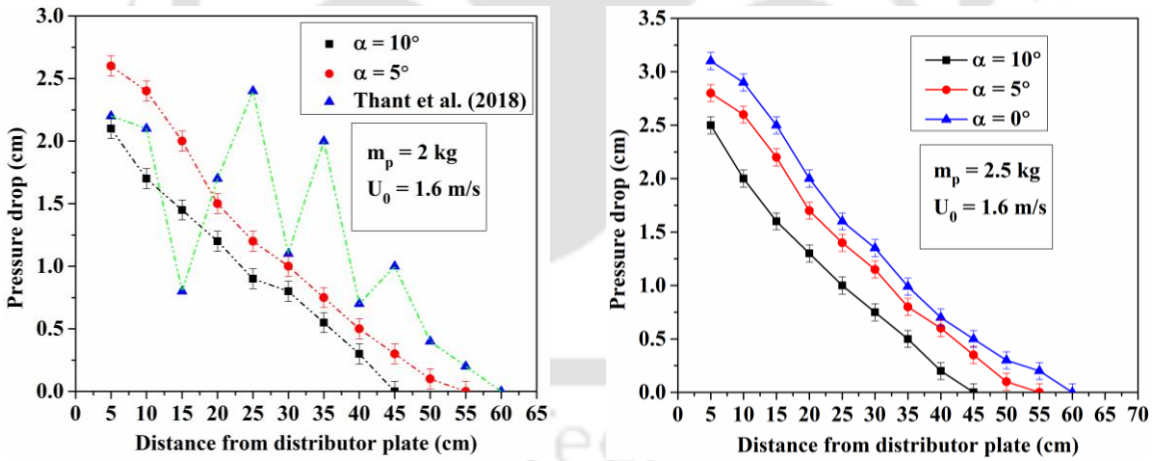

(a) (b)

Figure 6.7: Effect of cone angle on pressure drop, (a) without a spiral and (b) with a spiral

In Fig. 6.7 (a), the results of pressure drop for two conical dryers were compared with the result of Thant et al. (2018) [123]. The work of Thant et al. (2018) [123] shows vigorous fluctuation in pressure drops, whereas the current experiments show a gradual pressure drop with the height of the dryer. The reason for this characteristic can be attributed to good particle mixing and less fluctuation in particle compression and expansion to the wall. Pressure drop in conical

bed was found to be lower at different subsequent taps than the pressure drop of Thant et al. (2018) [123]. The pressure drop in both cases (with and without a spiral) decreases with the increase in cone angle [Figs. 6.7 (a) and (b)]. For the same mass of particles, as the cone angle increases, the area of the cross-section along with the height of the dryer increases, causing the concentration of paddy per unit area of the cross-section to decrease. Because of the different cross-sectional areas, the static bed height of particles differs for all dryers when the same amount of bed inventory is used. As a result, the pressure drop was found to be lower in a dryer with a large cone angle. From the figures, it can also be revealed that the effective height of pressure drop was lower for the larger degree of cone angle. This was because the velocity gradient along the height of a conical dryer increases as the cone angle increases due to the increase in cross-sectional area along the height. As a result, the paddy particles were unable to expand to a higher height. Hence, the effective height of the pressure drop was lower for the larger degree of cone angle conical dryer.

6.3 DRYING CHARACTERISTICS

The drying characteristics of paddy particles in the fluidized bed dryers under various operating conditions are explained in this section. Figure 6.8 shows the effect of inlet air temperature on drying characteristics in a conical fluidized bed dryer with a cone angle of 10°.

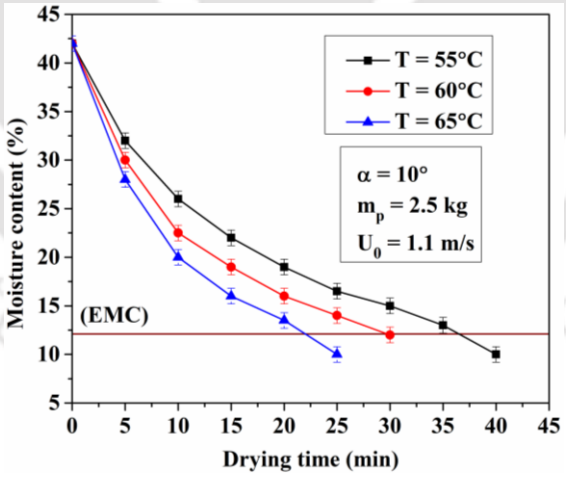

Figure 6.8: Effect of inlet air temperature on drying characteristics

For this, air temperature varies from 55 to 65°C with a step increase of 5°C. This was accomplished by adjusting an autotransformer connected to the power supply circuit. The inventory and the superficial air velocity were also kept constant. According to the figure, the paddy required lesser time to dry when the inlet air temperature was higher. As the temperature of the inlet air rises, the amount of heat content increases, reducing the drying time. A 28.57%

reduction in drying time prevailed when the inlet air temperature increased from 55 to 65°C. The effect of superficial air velocity on drying characteristics is also shown in Fig. 6.9.

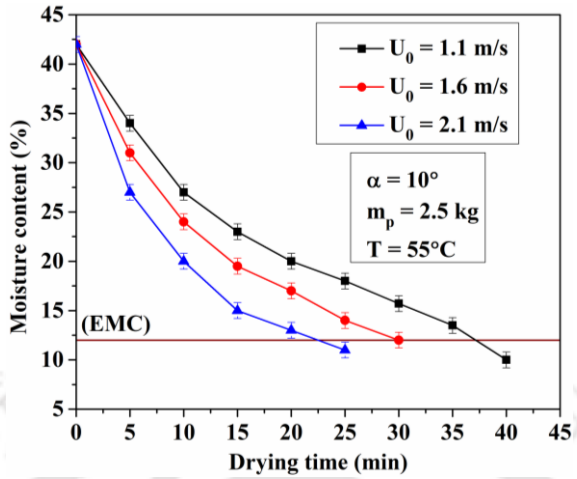

Figure 6.9: Effect of superficial air velocity on drying characteristics

For the comparison, three different superficial velocities of air were considered: 1.1, 1.6 and 2.1 m/s. However, the paddy inventory and temperature were kept at 2.5 kg and 55°C, respectively. It was revealed from the figure that as the superficial air velocity increases, the drying time decreases. The drying time of paddy grains was approximately 22.5 mins for the highest value of air velocity. However, for a superficial air velocity of 1.1m/s, it takes nearly 37 mins to dry the paddy grains. This is due to the fact that at high values of superficial air velocity, more heat is carried by the flowing air and vigorous mixing of air and paddy particles prevails, resulting in high heat transfer between air and paddy grains. As a result, drying time was reduced at high-velocity values. Apart from this, the effect of bed inventory on drying characteristics is also presented in Fig. 6.10.

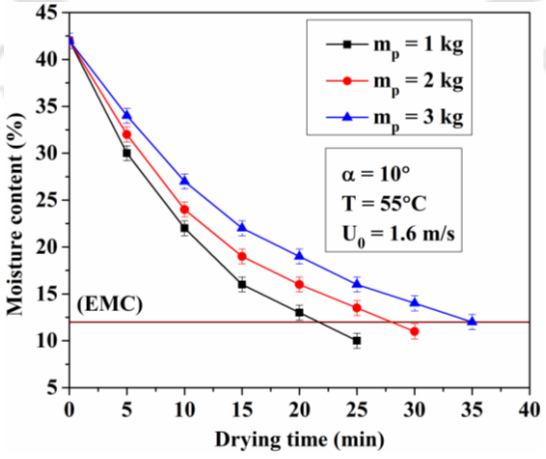

Figure 6.10: Effect of bed inventory on drying characteristics

For that, the bed temperature and superficial velocity of air were kept constant at 55°C and 1.6 m/s, respectively. It was observed from the figure that as the bed inventory was increased with constant velocity and inlet air temperature, the drying time increased. This is because when the bed inventory increases at a constant velocity, the turbulence of particles and air decreases which is accompanied by the decreasing fluctuation ratio, resulting in less vigorous mixing of particles and the air. The distribution of paddy per unit cross-sectional area was more for an increased amount of bed inventory, and thus, heat transfer between air and paddy was lower at a constant velocity. The effect of mixing sand with paddy on drying characteristics is shown in Fig. 6.11.

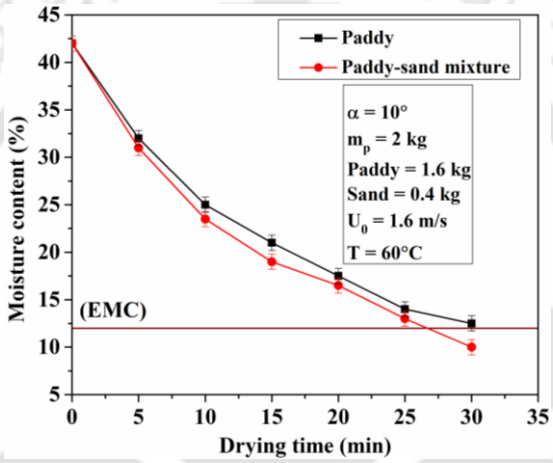

Figure 6.11: Effect of mixing of sand with paddy on drying characteristics

It is seen from the experimental results that mixing sand with paddy takes less time to reduce the moisture content. The sand particles have a higher heat capacity than paddy particles, allowing them to retain more heat from hot inlet air, increasing interphase heat transfer. Moreover, conduction heat transfer also increases between particles, as the thermal conductivity of sand is higher than that of paddy particles. Furthermore, due to the smaller size of sand particles than paddy particles, the sand particles are easily exhaled by the hot air, and as they are in contact with the paddy particles, the sand particles transfer heat to the paddy particles. As a result, the drying time was reduced when sand particles were mixed with paddy particles. When the sand was combined with paddy particles, the drying time was reduced by 13.33%. The drying characteristics plots in terms of moisture content vs drying time graph with spiral and without a spiral are presented in Figs. 6.12 and 6.13.

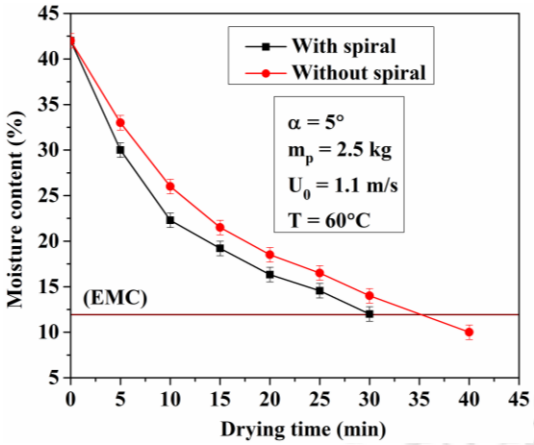

Figure 6.12: Effect of a spiral on drying characteristics in a conical dryer with 5° cone angle

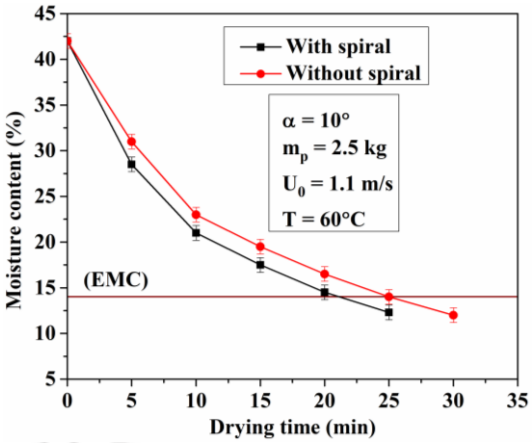

Figure 6.13: Effect of a spiral on drying characteristics in a conical dryer with 10° cone angle

The results showed that the incorporation of a spiral improves the drying characteristics of both dryers. The particles were in direct contact with the spiral inside the dryer, resulting in unsteady-state heat conduction. However, for a dryer without a spiral, heat transfer takes place between particles and heated air only. Furthermore, the spiral increases the turbulence in mixtures and makes the heat transfer rate faster. Hence, drying time was reduced in the case of the dryer with a spiral. When a spiral was used, there was a nearly 16.67% reduction in drying time. The effect of cone angle on drying characteristics without and with a spiral is shown in Figs. 6.14 (a) and (b).

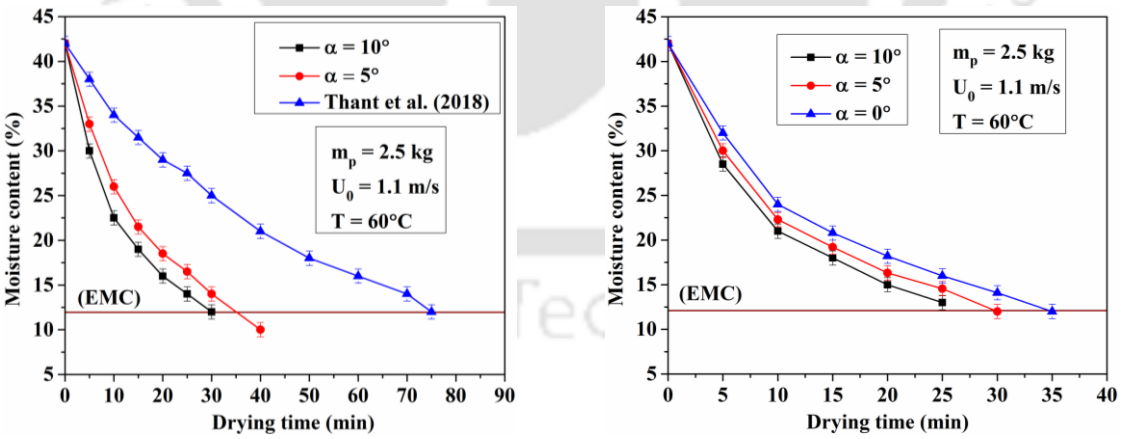

(a) (b)

Figure 6.14: Effect of cone angle on drying characteristics, (a) without a spiral, and (b) with a spiral

In Fig. 6.14 (a), the result of two conical dryers was compared with Thant et al. (2018) [123]. It is seen from Figs. 6.14 (a) and (b) that a higher cone angle reduces the drying time for the same amount of bed inventory. When the same amount of inventory was used at a higher value

of cone angle, the static bed height was less. Due to the lower static bed height, the turbulence of particles is more for a conical dryer with a higher cone angle which enhances the heat transfer between the fluid phase and particulate phase. Hence, faster is the drying rate. It was observed that a higher cone angle dryer with a spiral had a drying time of 25 mins. However, a conical dryer with a smaller cone angle takes almost 30 mins to dry, i.e. 20% more drying time than that of the larger cone angle conical dryer. On the other hand, the cylindrical dryer takes nearly 34 mins to get the desired drying.

6.4 ENERGY CONSUMPTION

6.4.1 Thermal energy consumption

This subsection investigates the significance of bed inventory and inlet air temperature on the thermal energy consumption of the three dryers with and without a spiral. The effect of cone angle on the same was also investigated, and the possible results were compared with Thant et al. (2018) [123]. Figure 6.15 shows the thermal energy consumption at different bed inventories.

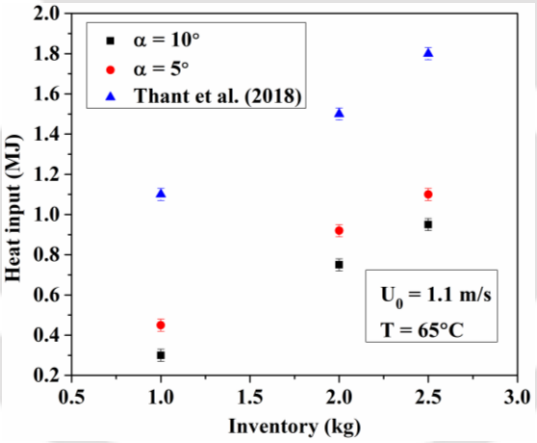

Figure 6.15: Thermal energy consumption at different inventories

It is clear from the figure that energy consumption increases with the inventory. Since thermal energy consumption is directly dependent upon the time required for drying and drying time increases with an increase in inventory, thermal energy consumption also increases with an increase in bed inventory. It was observed that in a conical fluidized bed dryer with a cone angle of 10°, the thermal energy required for drying was less, which was also lower than that of Thant et al. (2018) [123]. The average thermal energy consumption was reduced by nearly 50% when the conical dryer with a higher degree of the cone angle was used. Consumption of thermal energy at different inlet air temperatures is also shown in Fig. 6.16.

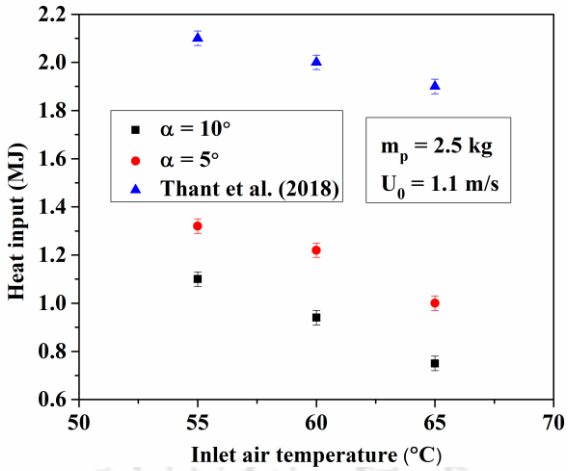

Figure 6.16: Thermal energy consumption at different inlet air temperatures

It is seen that less input is required at high-temperature drying because an increase in the inlet air temperature results in a decrease in the drying time. The average thermal energy consumption was also observed to reduce by about 48% with the increase in cone angle.

Figures 6.17 and 6.18 illustrate the thermal energy consumption of the heater for the two conical dryers with and without a spiral at U_0 = 1.1 m/s and m_p = 2.5 kg.

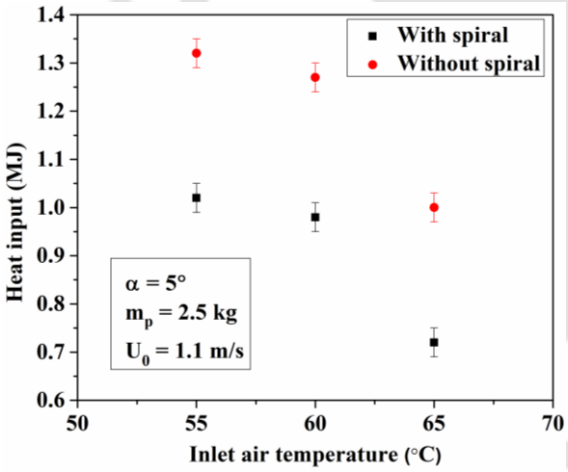

Figure 6.17: Effect of a spiral on thermal energy consumption in a conical dryer with 5° cone angle at various inlet air temperatures

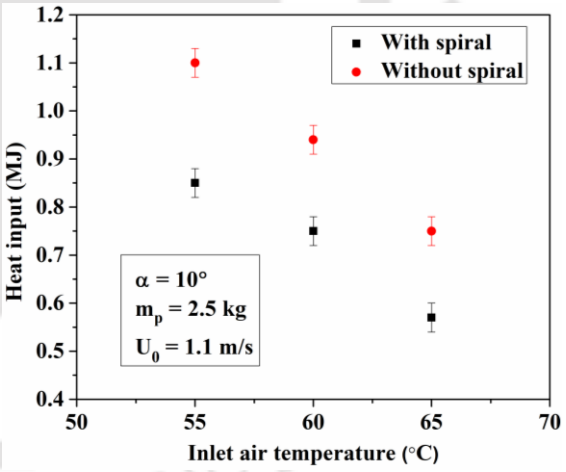

Figure 6.18: Effect of a spiral on thermal energy consumption in a conical dryer with 10° cone angle at various inlet air temperatures

It can be concluded that the thermal energy consumption was lower for the heater with a spiral than without a spiral, which indicates that the time needed for removing moisture content was less for the dryer with a spiral. Drying time was reduced because of the higher heat transfer inside the bed with a spiral due to turbulence and the rapid mixing of particles with hot air. Since the thermal energy consumption was directly related to the time required for drying, it

was lower for the heater with a spiral. Similarly, the effect of cone angle on the thermal energy consumption for the heater with a spiral was also studied and shown in Fig. 6.19.

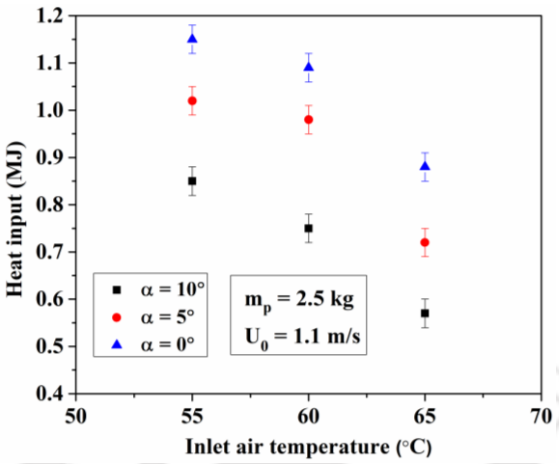

Figure 6.19: Effect of cone angle on thermal energy consumption with a spiral at various inlet air temperatures

The thermal energy consumption was lower in the case of the 10° cone angle of the conical dryer. This is due to the lesser amount of drying time. It was found that nearly 19.26% of thermal energy consumption was reduced for a higher degree of cone angle. However, the reduction in heat energy consumption due to the use of spiral was found to be nearly 23% in all cases. Subsequently, the thermal energy consumption for three-bed inventories at T = 65°C and U_0 = 1.1 m/s is shown in Figs. 6.20 and 6.21.

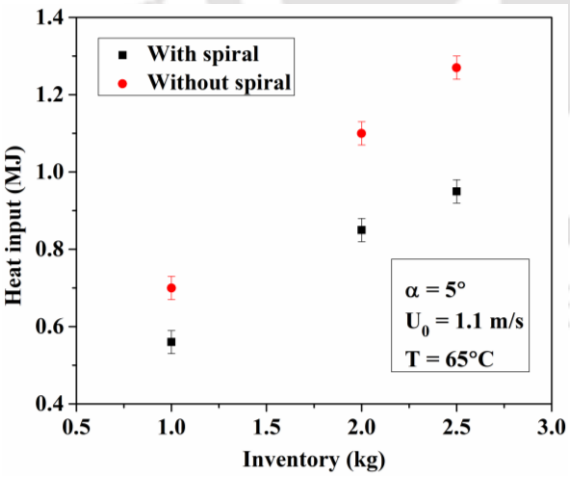

Figure 6.20: Effect of a spiral on thermal energy consumption in a conical dryer with 5° cone angle at various bed inventories

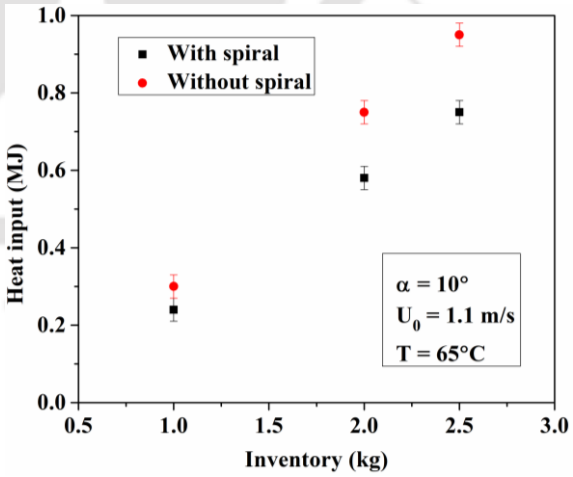

Figure 6.21: Effect of a spiral on thermal energy consumption in a conical dryer with 10° cone angle at various bed inventories

The same trend was observed as in the previous case. Thermal energy consumption was lower for the heater with a spiral than without a spiral. In Fig. 6.22, the impact of cone angle on thermal energy consumption at 65°C and 1.1 m/s is also shown. A similar result was also found, as observed in Fig. 6.19, where the thermal energy consumption decreases with an increase in the cone angle.

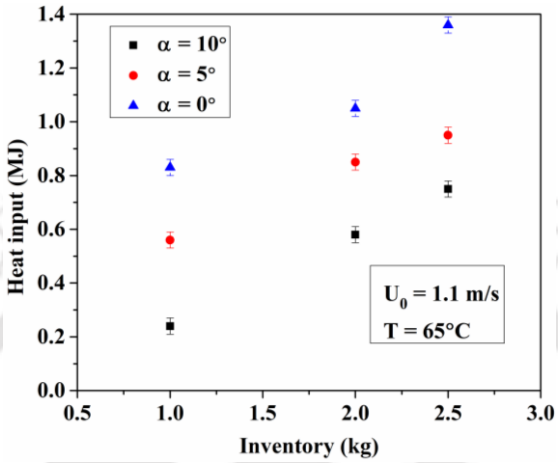

Figure 6.22: Effect of cone angle on thermal energy consumption with a spiral at various inventories

6.4.2 Energy consumption of blower (ECB)

Energy consumption of blower (ECB) was studied for different inventories. Effects of different temperatures, cone angles and spiral were also investigated, and results were compared. Figures 6.23 (a) and (b) show the ECB at three different inventories and inlet air temperatures.

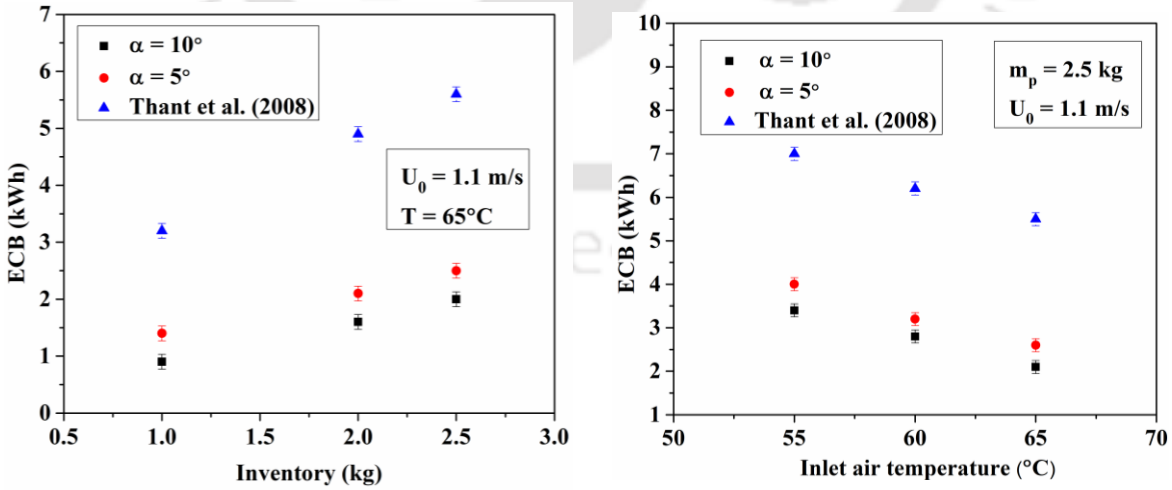

(a) (b)

Figure 6.23: Effect of cone angle on ECB at (a) different inventories, and (b) different inlet air temperatures

It can be seen that ECB is a direct function of time. If the drying rate is higher, the ECB is less. The ECB was found to be higher for the increased value of inventory. On the other hand, the ECB decreases with an increase in inlet air temperature. The ECB in a conical fluidized bed dryer was lower than that of a cylindrical fluidized bed dryer. Similarly, the ECB was investigated with and without a spiral and results were compared. Figures 6.24 and 6.25 show the ECB with a spiral and without a spiral for two conical dryers at varying inlet air temperatures.

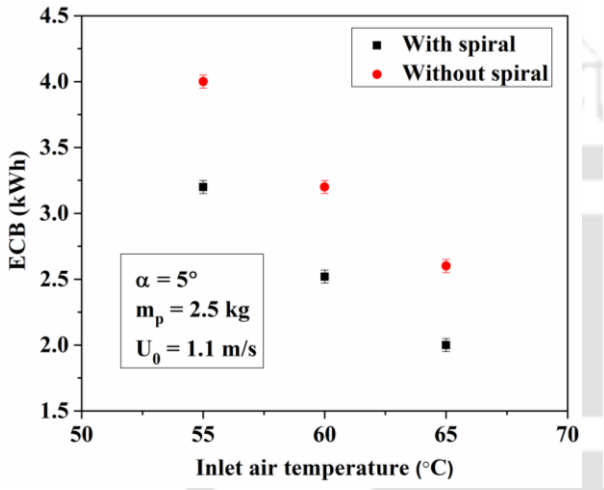

Figure 6.24: Effect of a spiral on ECB in a conical dryer with 5° cone angle at various inlet air temperatures

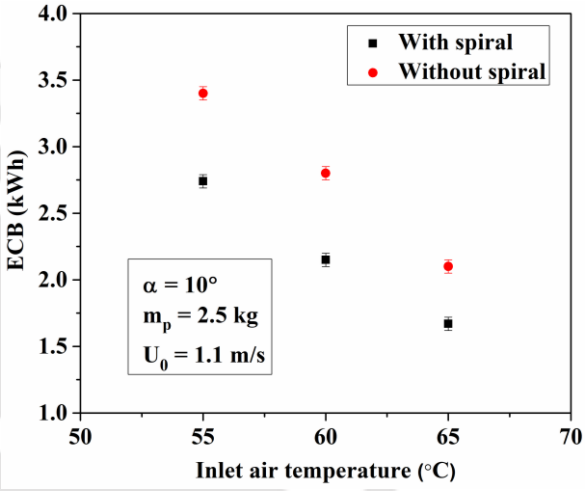

Figure 6.25: Effect of a spiral on ECB in a conical dryer with 10° cone angle at various inlet air temperatures

In this investigation, the bed inventory and superficial air velocity were kept constant as m_p = 2.5 kg and U_0 = 1.1 m/s, respectively. As shown in Figs. 6.24 and 6.25, the energy consumption of the blower was lower for the dryer with a spiral than without a spiral. The energy consumption of the blower was reduced by 18% due to the incorporation of a spiral. This consumption of energy is dependent upon drying time and heat transfer characteristics. The greater the heat transfer between two phases, the lower the drying time. Incorporating the spiral leads to vigorous mixing of particles, enhancing gas to particle heat transfer. As a result, the drying time required to achieve the EMC decreases by incorporating a spiral. Hence, the energy consumption of the blower was lower. A similar kind of investigation was also made for varying inventory and shown in Figs. 6.26 and 6.27.

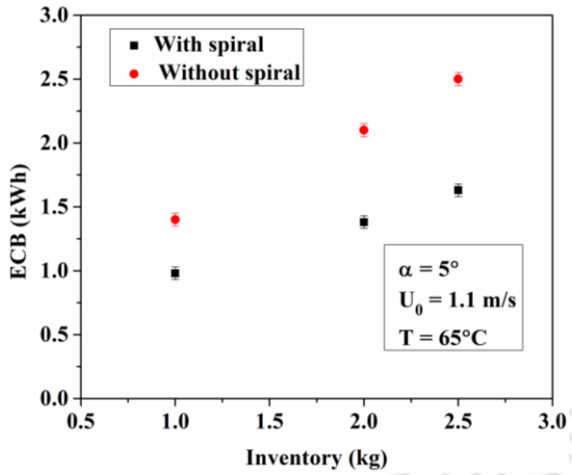

Figure 6.26: Effect of a spiral on ECB in a conical dryer with 5° cone angle at various bed inventories

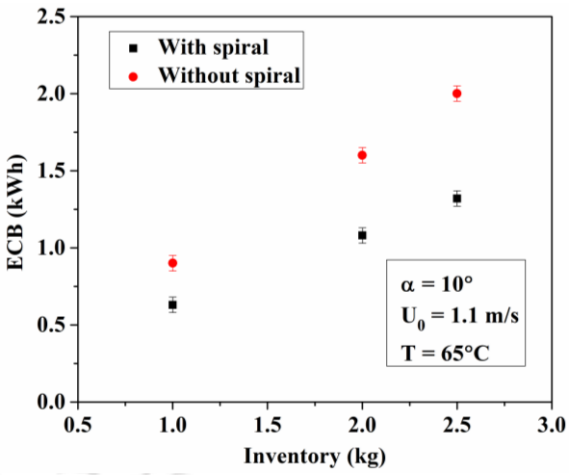

Figure 6.27: Effect of a spiral on ECB in a conical dryer with 10° cone angle at various bed inventories

In this case, the inlet air temperature and velocity were constant as T = 65˚C and U_0 = 1.1 m/s. Figures conclude that there was a reduction of ECB for a conical dryer with a higher cone angle and a spiral.

Furthermore, the effect of cone angle on energy consumption of blower with a spiral for varying inlet air temperature and varying bed inventory is explained in Figs. 6.28 (a) and (b), respectively.

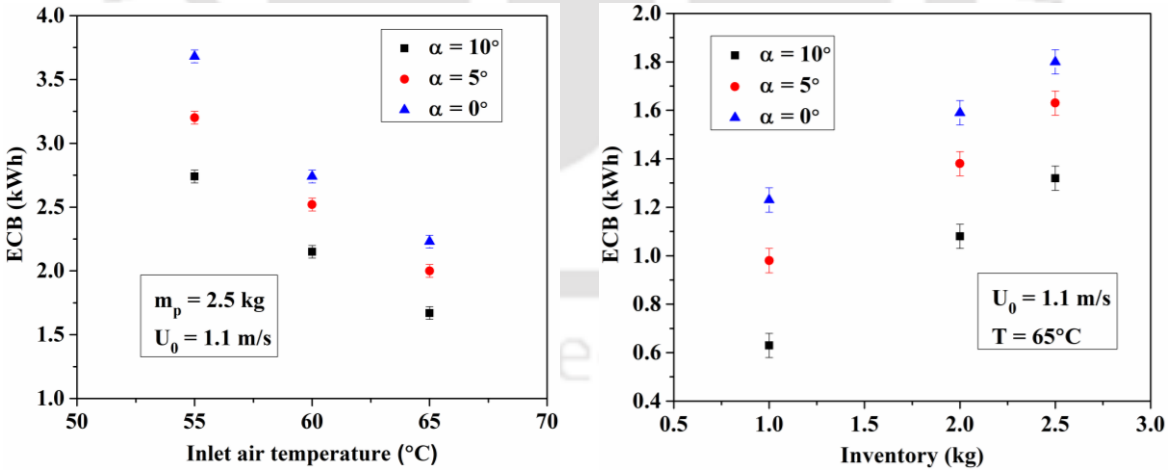

(a) (b)

Figure 6.28: Effect of cone angle on ECB with a spiral at (a) different inlet air temperatures and (b) different bed inventories

As described in section 6.3, drying time was shorter for a conical dryer with a higher degree of cone angle. Hence, the energy consumption of the blower was found to be decreasing with an

increase in cone angle, as the energy consumption of the blower is also dependent upon drying time. The reduction in ECB due to the higher cone angle was found to be 26.67%. However, the difference in energy consumption of blower between spiral and without spiral was more prominent when the air velocity increased.

6.5 DRYING AND MILLING QUALITY

The drying quality of locally available Ranjit paddy was assessed with respect to the nutritional value found in the paddy grains. The nutritional contents in the paddy grains consist of a percentage of carbohydrate, protein, fat and fibre. In this context, the nutritional value of different quantities at 60°C temperature was determined at four different drying times, one was at 0 minutes, and the other three were at 10, 20 and 30 minutes, respectively. The value of the nutritional contents is shown in Table 6.1. Furthermore, these nutritional values of dried paddy were compared with the Ranjit rice cultivated in different places of India, which is shown in Table 6.2 [190,191].

Table 6.1 Nutritional contents of paddy at different drying times at 60°C temperature

Sample Type	% Crude Fibre content	% Protein content	% Fat content	% Carbohydrate content
0 minutes	2.84	13.96	2.42	82.72
10 minutes	2.24	12.82	1.82	77.92
20 minutes	1.90	12.21	1.53	76.32
30 minutes	1.65	11.88	1.46	75.20

Table 6.2 Comparison of nutritional contents of dried paddy with the paddy cultivated in different places of India

Sample Type	Present value	Values from Prasad et al. (2018) [190] and Verma and Srivastav (2017) [191]
% Crude Fibre content	1.65	1.71
% Protein content	11.88	12.01
% Fat content	1.46	1.55
% Carbohydrate content	75.20	75.055

It was observed from Table 6.1 that the percentage of all nutritional contents decreases with increasing drying time [179,192], i.e., drying plays a vital role in making paddy grains more digestible. However, drying results in a decrease in the macronutrient content of grains caused by biochemical changes. A chemical reaction between amino acids is known as the Maillard

reaction, due to which the protein and carbohydrate contents in paddy decrease. The protein content also gets reduced due to the conversion of tannins to complexes. The Maillard reaction and reducing sugars both together give a distinctive flavour to browned food. It was proposed by Cho et al. (2008) [193] and Savage et al. (2002) [194] that because of oxidation, the percentage of protein content is getting reduced due to drying. It was observed from Table 6.2 that the nutritional value of dried paddy in the present study was found to be in good agreement with the previously published literatures [190,191].

The milling quality was checked for dried paddy for conical dryer having cone angle 10°. The inlet air velocity and temperature for milling quality were taken as 1.1m/s and 60°C. The weight of milled rice is the summation of the weight of head rice and broken rice. One hundred grams of paddy samples were used to check the milling quality, and a conical bubbling fluidized bed dryer recovered around 75% of milled rice. Similarly, the milling quality for the same dryer was compared in Table 6.3 with and without a spiral.

Table 6.3 Milling quality of paddy materials with and without a spiral

Milling quality	With a spiral	Without a spiral
Weight of paddy sample	100 gm	100 gm
% Head rice	63	58
% Broken rice	12	14
% Milling recovery	75	72

As observed in the above table, the percentage of head rice was 63% and 58% for a dryer with and without a spiral, respectively, while in a conventional dryer, it was around 30 to 50% for Asian countries. The table shows that the incorporation of a spiral increases the milling recovery by 3%.

6.6 THERMODYNAMIC (ENERGY AND EXERGY) ANALYSIS

In this section, variation in energy utilization (EU) and energy utilization ratio (EUR) are studied in three dryers. Similarly, the exergy utilization and exergetic efficiency are also determined in the three dryers. Five different operating parameters were used for this analysis. The operating parameters were inlet air velocity, the mass of paddy particles, inlet air temperature, spiral and cone angle. Experiments were carried out for three inlet air velocities, such as 1.1, 1.6 and 2.1 m/s as well as three inlet air temperatures, 55°C, 60°C and 65°C. The above experiments have been accomplished with three different bed inventories, such as 1, 2

and 3 kg. In order to study the effect of the spiral on the thermodynamic analysis, a passive spiral was inserted into all three dryers.

6.6.1 Variation in energy utilization (EU)

The variation of energy utilization regarding drying time for five different operating parameters is investigated. Figure 6.29 depicts the trend of the EU with inlet air velocity.

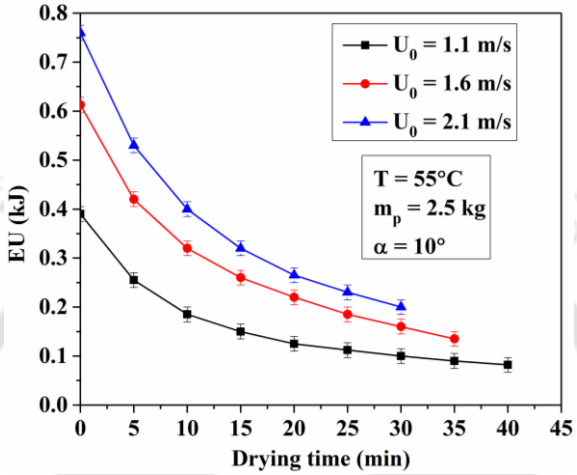

Figure 6.29: Variation in EU with inlet air velocity

The variation in EU with time was observed to be increasing with an increase in the inlet air velocity [158]. It is due to the drying air's increased enthalpy. Increased air velocity causes an increase in mass flow rate, which raises the enthalpy of drying air. Increasing enthalpy raises the heat and mass transfer. As a result, as air velocity increases, so does the EU.

The effect of the mass of paddy and inlet air temperature on the variation of EU is also investigated in Figs. 6.30 and 6.31.

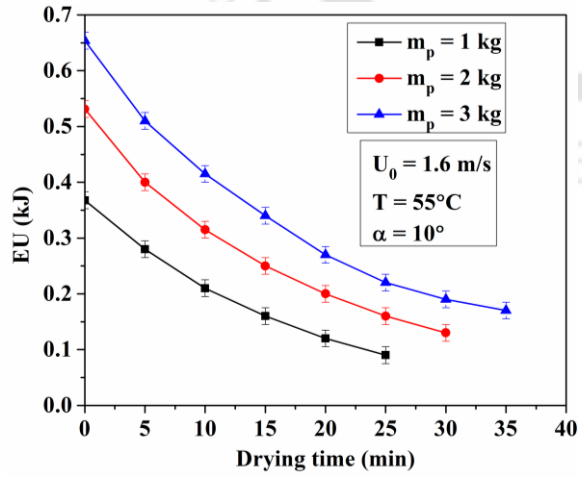

Figure 6.30: Variation in EU with the mass of paddy

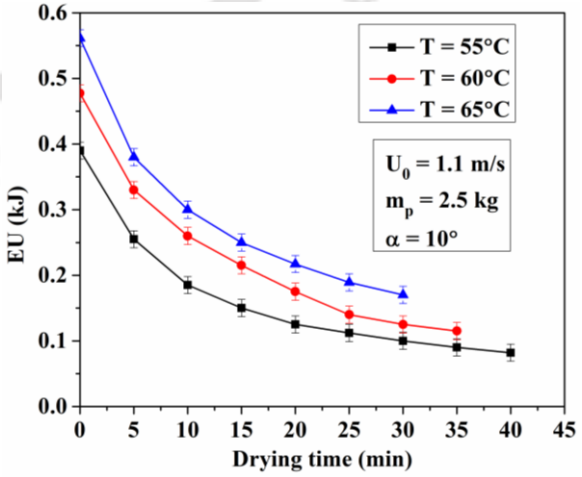

Figure 6.31: Variation in EU with inlet air temperature

In Figs. 6.30 and 6.31, the EU was seen to be increasing with the increase in the mass of the paddy and the inlet air temperature. Similar patterns were also observed by Nazghelichi et al. (2010, 2011) [156,195] and Pattanayak et al. (2019) [161]. If the amount of paddy particles increases, then the energy needed to extract the moisture content will also increase. The utilization of energy was, therefore, higher while the mass of paddy increased. Similarly, when the inlet air temperature rises, the enthalpy at the inlet of a dryer also increases. As a result of an increase in enthalpy, there was an increase in the EU [153,158,162] since the EU is a direct function of enthalpy.

Analogous to other operating parameters, the influence of an incorporated spiral on the variation of EU is depicted in Fig. 6.32.

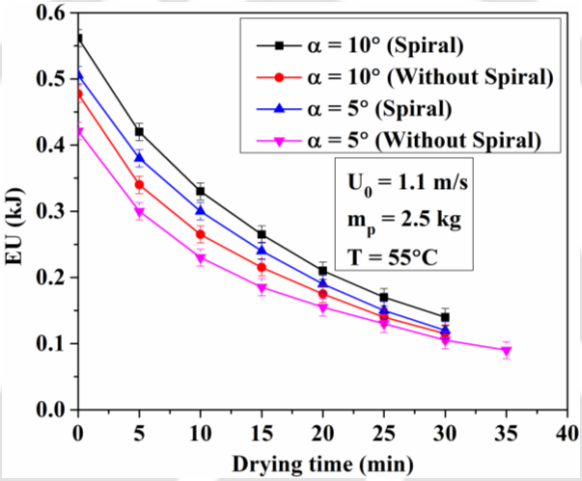

Figure 6.32: Variation in EU with and without a spiral

For this investigation, two different tapered fluidized bed dryers with cone angles of 5° and 10° were considered, and the EU pattern with and without spiral is shown. It can be interpreted that the EU was more with a spiral than non-spiral for both the dryers. This is due to the rapid extraction of moisture from paddy due to the turbulence of gas-solid flow produced by the spiral.

Furthermore, the effect of cone angle on the variation of EU is investigated in Fig. 6.33.

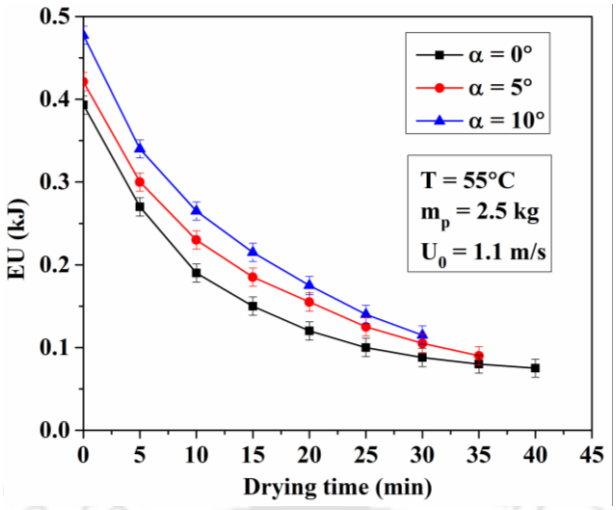

Figure 6.33: Variation in EU with the cone angle

It was observed from Fig. 6.33 that the trend of the EU was in accordance with an increase in the cone angle. In order to investigate the impact of the cone angle on the EU, two conical dryers and one cylindrical dryer were considered. The increase in the cone angle increases the angle of divergence of a dryer, accompanied by the existence of the gradient of velocity. As a result, the solid volume fraction was more at a cross-section and mixing characteristics were superior. Therefore, the rate of moisture removal from paddy particles was high. Hence, the EU increased with an increase in cone angle.

Nonetheless, All figures from 6.29 to 6.33 indicated a decreasing trend of EU with drying time [161,168]. The energy consumption due to the evaporation of surface moisture was more likely to be high at the beginning of the process. Nevertheless, the continuous evaporation of moisture at the centre of the paddy leads to a decrease in energy consumption over time.

6.6.2 Variation in energy utilization ratio (EUR)

As discussed in the previous section, the same operating parameters were used to investigate EUR variation. All figures indicate that the trend of EUR was similar to the trend of the EU with respect to drying time [161,168]. Figures 6.34-6.38 reveal the influence of inlet air velocity, the mass of paddy inlet, inlet air temperature, spiral and cone angle on the change of EUR.

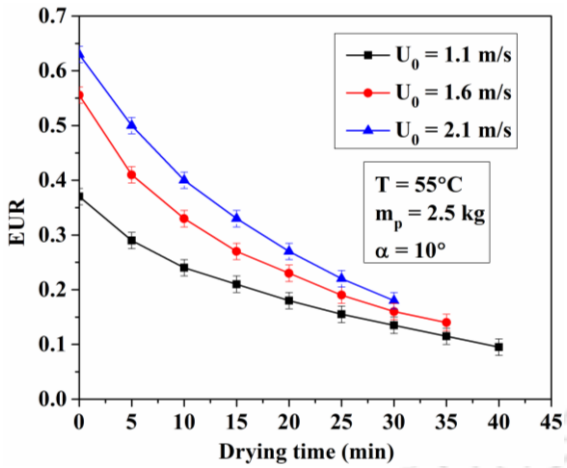

Figure 6.34: Variation in EUR with inlet air velocity

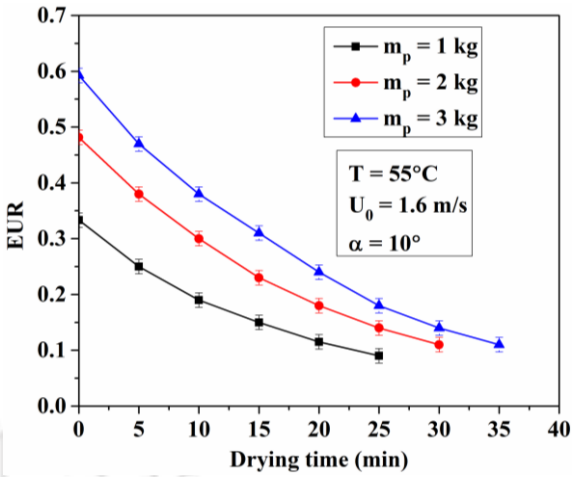

Figure 6.35: Variation in EUR with the mass of paddy

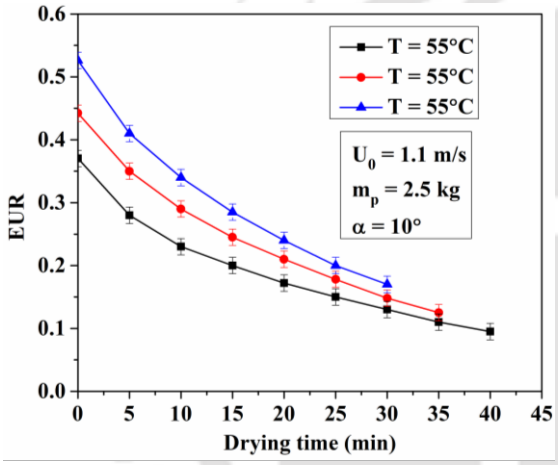

Figure 6.36: Variation in EUR with inlet air temperature

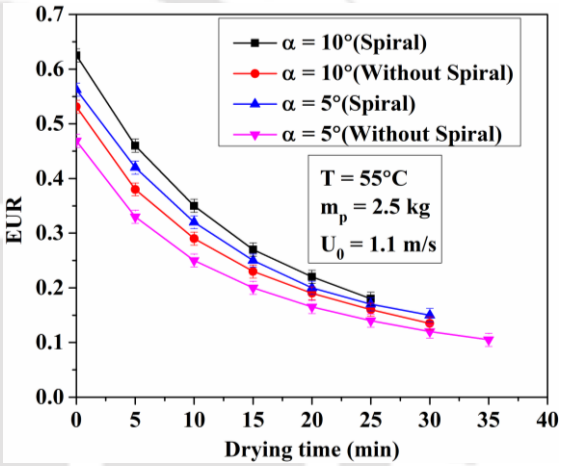

Figure 6.37: Variation in EUR with and without a spiral

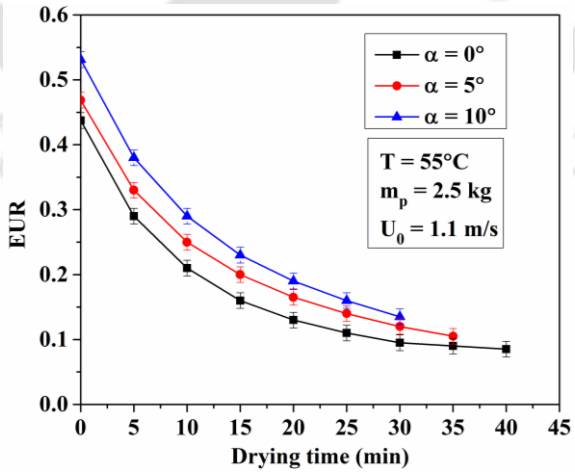

Figure 6.38: Variation in EUR with the cone angle

It was evident that the EUR increased with an increase in inlet air velocity [158,165], the mass of paddy inlet and inlet air temperature [156,158,162], which is analogous to that of the

variation in the EU. Similarly, the EUR also increases with the incorporation of a spiral and increase in cone angle. The explanation for the observations is the same as the reason for the variation in the EU.

6.6.3 Variation in exergy utilization

In this subsection, the exergy utilization is investigated at the various operating parameters mentioned in the previous subsection. Figure 6.39 describes the exergy utilization for variations in the operating parameter, air velocity.

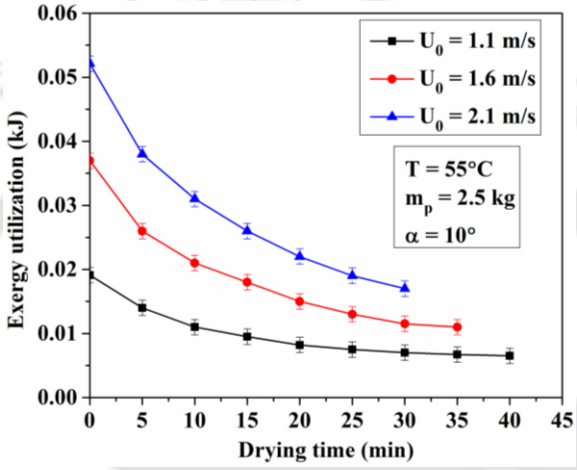

Figure 6.39: Variation in exergy utilization with inlet air velocity

Exergy utilization was observed to decrease with an increase in drying time. The presence of moisture for evaporation gradually declines as drying progresses. However, exergy utilization was found to increase as the air velocity increased [158]. Increased air velocity contributes to a rapid fluctuation of air and paddy particles, which leads to the development of turbulence motion. As a result, a greater amount of moisture is extracted from the paddy particles, which means more exergy utilization.

Similar to air velocity, there was also an increase in the use of exergy with inlet air temperature and mass of paddy (Figs. 6.40 and 6.41).

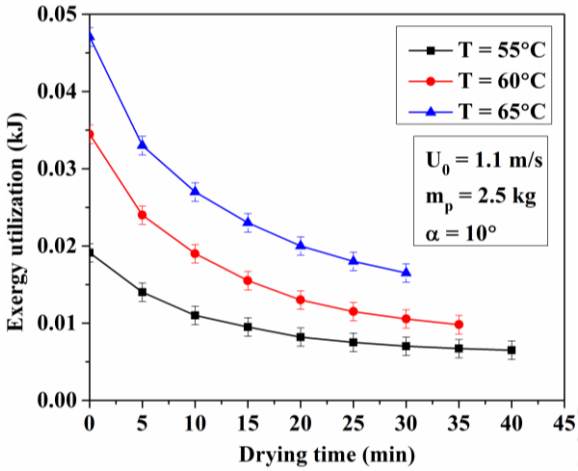

Figure 6.40: Variation in exergy utilization with inlet air temperature

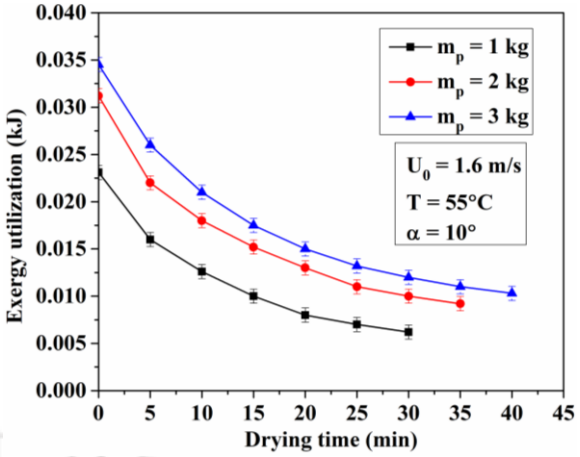

Figure 6.41: Variation in exergy utilization with the mass of paddy

As the inlet air temperature rises, the enthalpy and entropy rise, which means that the exergy required to evaporate the moisture increases, leading to an increase in exergy utilization during the drying process. Similarly, a significant amount of exergy was also required to remove moisture from particulate matter when the mass of paddy increases. Hence, the utilization of exergy increases with the rise in inlet air temperature and amount of paddy. Nazghelichi et al. (2010) [156] and Pattanayak et al. (2019) [161] found similar results for inlet air temperature [153,158] and mass of paddy. The effect of a spiral and cone angle on exergy utilization is represented in Figs. 6.42 and 6.43.

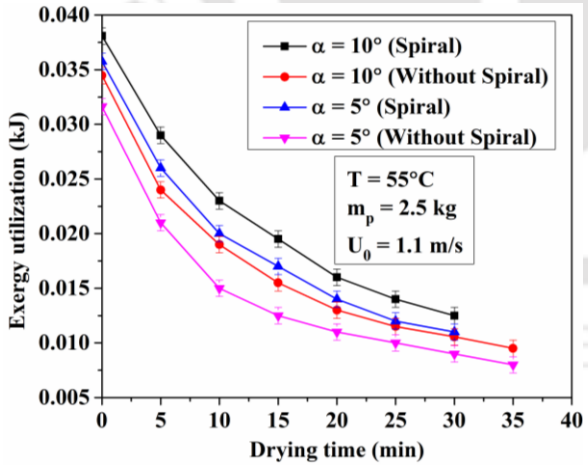

Figure 6.42: Variation in exergy utilization with and without a spiral

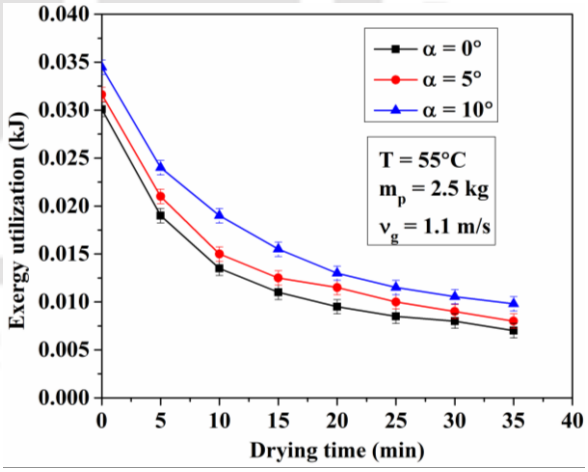

Figure 6.43: Variation in exergy utilization with the cone angle

In Fig. 6.42, it was observed that the use of a spiral raises the amount of exergy utilization compared to that without a spiral. The use of a spiral promotes gas-solid mixing resulting in better drying characteristics, which ensures that the utilization of exergy is higher. Figure 6.43

also indicates that exergy utilization increases with an increase in the cone angle. Increased cone angle results in a lower pressure drop across the dryer, resulting in improved drying characteristics. Improving the drying characteristics signifies that the evaporation of the moisture from the particles increases, which means an increase in exergy utilization.

6.6.4 Variation in exergetic efficiency

Similar to the energy analysis, exergy analysis such as exergy efficiency was determined in the three dryers at the same operating parameters. The exergetic efficiency is described by the ratio between exergy used and exergy inflow to the dryer. Figure 6.44 reveals the effect of air velocity on exergetic efficiency.

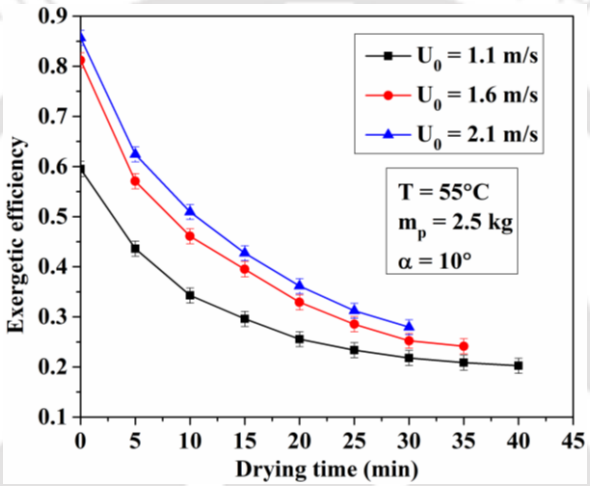

Figure 6.44: Variation in exergetic efficiency with inlet air velocity

It can be seen from Fig. 6.44 that the exergetic efficiency increases with an increase in air velocity. A similar result was also observed by Celik et al. (2021) [165]. The utilization of exergy increases with the increase in inlet air velocity, as shown in Fig. 6.39. The exergy inflow to the dryer also increases when the air velocity increases. But the counter effect of these two results in an improvement of exergetic efficiency. Analogous to this, exergy efficiency increases with the increase in the mass of the paddy, which can be seen in Fig. 6.45.

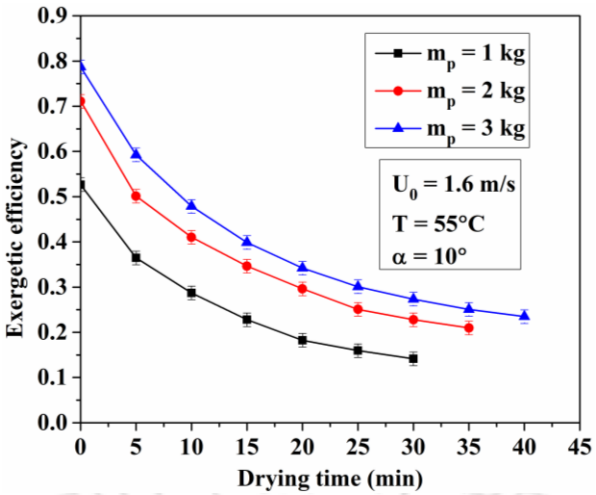

Figure 6.45: Variation in exergetic efficiency with the mass of paddy

The reason for this is the decrease in exergy outflow and increase in the utilization exergy with an increase in the mass of paddy. However, the exergy inflow to the dryer is the same. Analogous results have been reported by Dincer and Sahin (2004) [196] in their thermodynamic analysis of drying processes. Similar results were also observed for the inlet air temperature [156], as shown in Fig. 6.46.

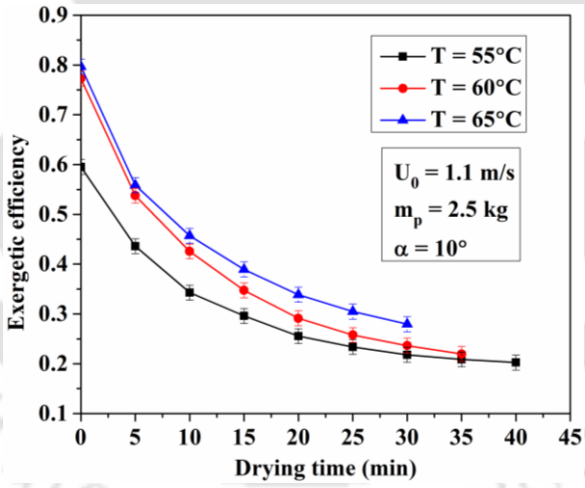

Figure 6.46: Variation in exergetic efficiency with inlet air temperature

It is because of the increase in the utilization of exergy. There is a decrease in the exergy outflow, and at the same time, the exergy inflow into the drying chamber also increases at a lower rate than that of the exergy utilization. As a result, the exergy efficiency increases with the increase in inlet air temperature.

Exergetic efficiency with respect to drying time is plotted in Fig. 6.47 for a dryer with and without a spiral.

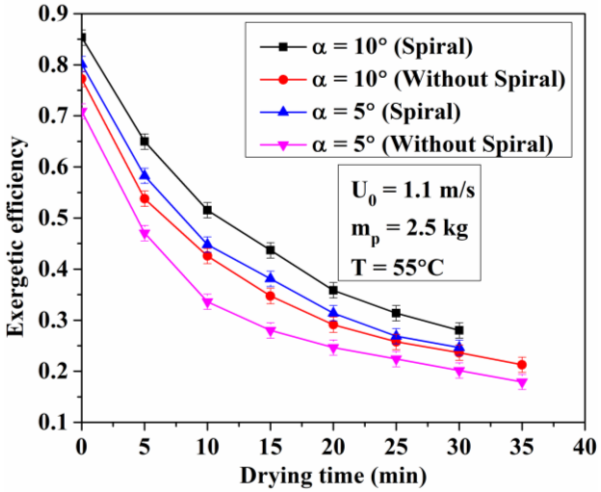

Figure 6.47: Variation in exergetic efficiency with and without a spiral

It was observed that the exergy efficiency increases with the introduction of a spiral. A spiral in a fluidized bed increases the heat transfer to the particles and increases the exergy utilization. This results in an improvement in the exergetic efficiency of the drying process.

Figure 6.48 also shows the effect of cone angle on exergy efficiency with drying time.

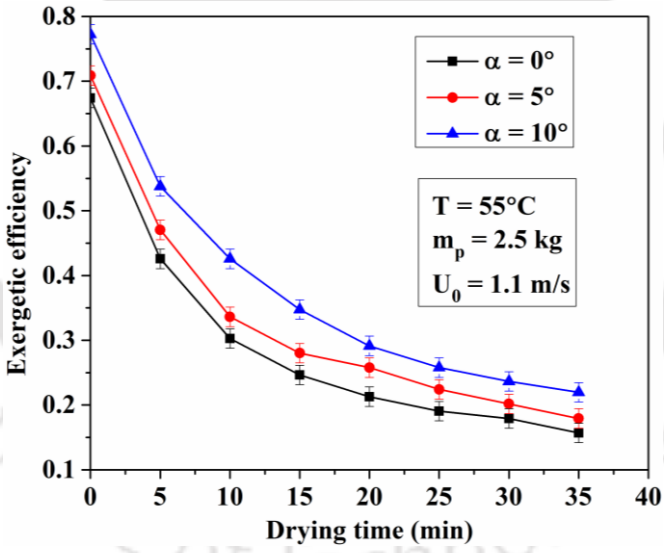

Figure 6.48: Variation in exergetic efficiency with the cone angle

An increase in exergy efficiency with an increase in cone angle has been observed. The reason for this can be attributed to a decrease in the amount of exergy outflow, which eventually increases the dryer's exergy utilization with an increase in the cone angle. As a consequence, the exergetic efficiency increases with an increase in the cone angle. The exergetic efficiency was also investigated at the ECM point for the operating parameter of inlet air velocity, the

mass of paddy and inlet air temperature. As a result, the experimental matrix is provided in Table 6.4.

Table 6.4 Experimental matrix for exergetic analysis

Sl. No.	Inlet air velocity (m/s)	Mass of paddy (kg)	Inlet air temperature (°C)
1	1.1, 1.6, 2.1	1, 2, 3	55, 60, 65
2	1.1, 1.6, 2.1	1, 2, 3	55, 60, 65
3	1.1, 1.6, 2.1	1, 2, 3	55, 60, 65

Figures 6.49, 6.50 and 6.51 show the impact of these three operating parameters on exergetic efficiency at ECM points for a conical dryer of 10° cone angle.

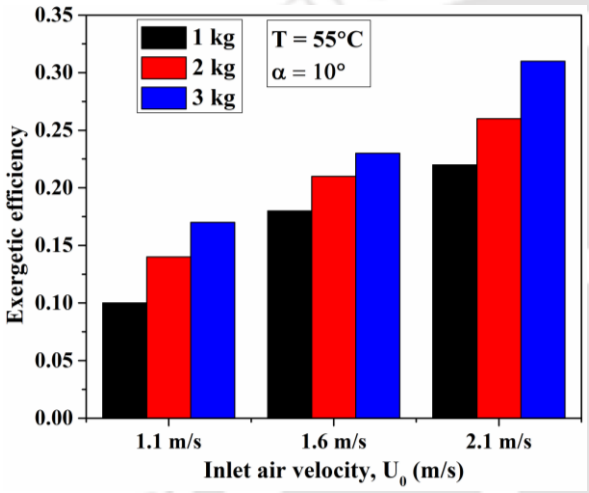

Figure 6.49: Variation in exergetic efficiency with varying inventory and air velocity at an inlet air temperature of 55°C

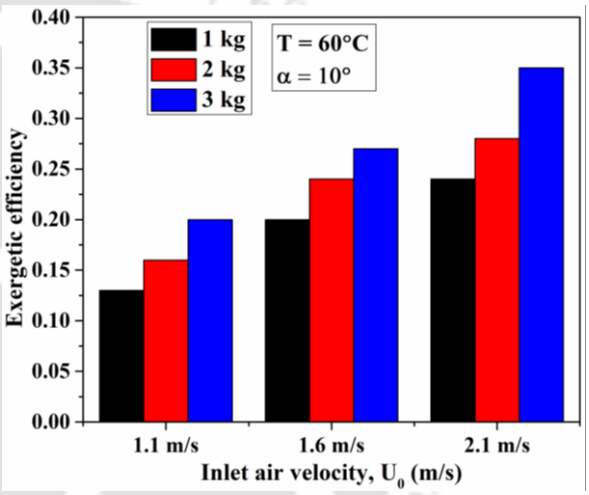

Figure 6.50: Variation in exergetic efficiency with varying inventory and air velocity at an inlet air temperature of 60°C

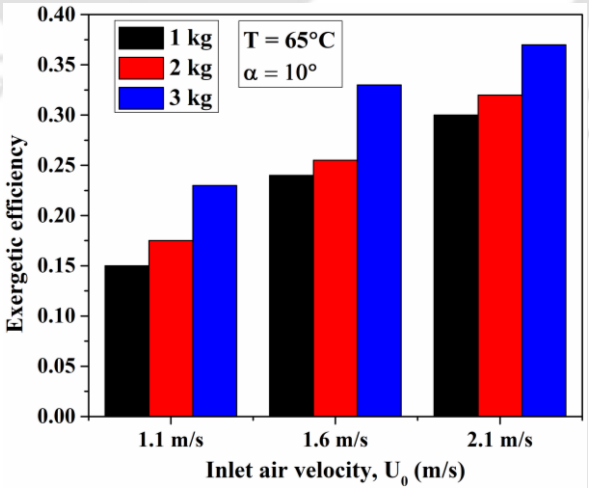

Figure 6.51: Variation in exergetic efficiency with varying inventory and air velocity at an inlet air temperature of 65°C

The exergetic efficiencies were found to be increasing with the increase in inlet air velocity, the mass of paddy and inlet air temperature. The reason for this was explained in Figs. 6.44, 6.45 and 6.46. The maximum exergetic efficiency was found to be at the air velocity of 2.1 m/s and inlet air temperature of 65°C for the mass of paddy of 3 kg. However, it was found to be minimum at the inlet air velocity of 1.1 m/s. As the maximum exergetic efficiency was obtained at the air velocity of 2.1 m/s and inlet air temperature of 65°C for the mass of paddy of 3 kg thus, the effect of cone angle on exergetic efficiency with and without a spiral was also investigated at this operating parameter.

Figure 6.52 shows the effect of cone angle on exergetic efficiency with and without a spiral.

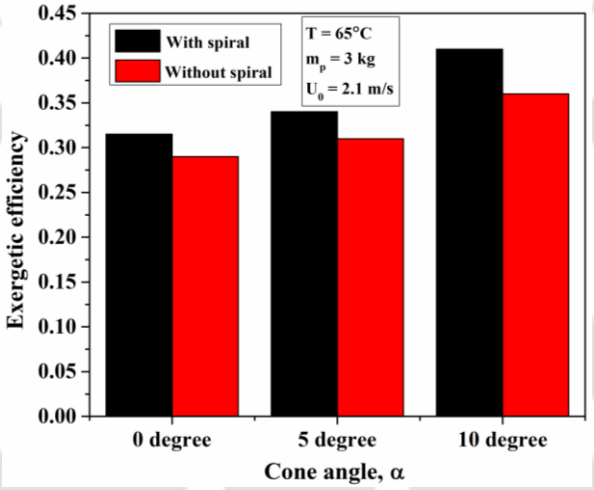

Figure 6.52: Effect of cone angle on the variation in exergetic efficiency with and without a spiral

It was observed that the conical dryer of a higher degree cone angle shows higher exergetic efficiency with a spiral than the other two with a spiral. It was also observed that when a spiral is inserted into a dryer, the efficiency increases. Therefore, it can be said that the conical dryer of a higher degree cone angle has a higher exergetic efficiency with a spiral. When a spiral is incorporated, the exergy efficiency increases by 28% as the cone angle increases. The maximum exergetic efficiency was found to be 0.41.

6.7 CHAPTER CONCLUSION

In the present chapter, the hydrodynamic behaviour and drying characteristics of paddy in two conical bubbling fluidized bed dryers of cone angle 5° and 10° and one cylindrical bubbling fluidized bed dryer was experimentally investigated at different operating conditions such as temperature, inlet superficial air velocity and bed inventory. The effect of cone angle and incorporation of a spiral on the same was also investigated in this study. Furthermore, the

pressure drop along the height of the dryer was also compared numerically between sand and paddy particles. The thermal energy consumption and ECB were calculated for all operating parameters, and results were compared. Furthermore, the results of the present study were compared with the results published by Thant et al. (2018) [123]. The drying and milling quality of paddy was also checked, and results were compared with previously published literature. Once these investigations were made, thermodynamic analysis was performed for three dryers to understand the feasibility of the systems. In all investigations, the pressure drop was found to be decreasing with the height of the dryer. The maximum pressure drop was found to be about 2.5 cm of water column for all operating conditions. The addition of a spiral to a fluidized bed dryer produced a more desirable effect on drying characteristics, energy consumption and drying quality than without a spiral. The higher the cone angle for the same inlet diameter, the lower the drying time for all operating parameters. The conical dryer consumes lesser energy than a conventional fluidized bed dryer. It was also observed that the conical dryer having a 10° cone angle has higher exergetic efficiency with a spiral than other dryers without a spiral. Hence, a conical bubbling fluidized bed dryer is a better energy-saving option than any conventional fluidized bed dryer. In the next chapter, the economic analysis of the three dryers will be presented.

7

Economic Analysis of Dryers

7.1 Introduction

7.2 Cost of drying

7.3 Cost of energy

7.4 Cost analysis of three dryers

7.5 Sensitivity analysis

7.6 Chapter conclusion

CHAPTER – 7

ECONOMIC ANALYSIS OF DRYERS

7.1 INTRODUCTION

In this chapter, the economic analysis of paddy drying in three atmospheric bubbling fluidized dryers are discussed by assuming different costs associated with the dryers. The economic study was carried out in order to acknowledge the viability of the developed dryers. The fixed cost, variable cost, cost of energy, payback period or break-even period (BEP) and profit per year were determined. Section 7.2 describes the cost of drying, which includes both fixed and variable costs. Section 7.3 illustrates the cost of energy associated with the dryers. Section 7.4 deals with the cost analysis of three dryers which includes one cylindrical dryer and two conical dryers having cone angles of 5° and 10°, respectively. Section 7.5 contains the sensitivity analysis of the present results. Finally, the chapter is concluded in section 7.6.

7.2 COST OF DRYING

The cost of drying consists of fixed and variable costs. The fixed cost includes the cost of the rate of interest, depreciation, the cost of repair and opportunity cost. On the other hand, the variable cost is associated with electricity, fuels and labour costs. The drying cost can be expressed either by the per-unit cost of weight or annual cost, depending on the objective of drying. In the present calculation, the drying cost was assumed to be one metric ton of food grain (paddy). The total cost of drying has been determined as given below:

$$C_D = C_F + C_V \tag{7.1}$$

where, C_D, C_F, and C_V are total cost, fixed cost and variable cost, respectively.

7.2.1 Fixed cost

Fixed costs, often known as indirect costs or overhead costs, are expenses that do not vary with the level of commodities. They are usually recurrent, such as monthly interest or rent. These costs also tend to be capital costs. The fixed costs were determined by the following relationship:

$$C_F = C_{system} + C_{instrumentation} + C_{depreciation} + C_{others} \tag{7.2}$$

where,

C_F = Fixed cost (Rs./kg)

C_{system} = System cost (Rs./kg)

$C_{instrumentation}$ = Instrumentation cost (Rs./kg)

$C_{depreciation}$ = Depreciation cost (Rs./kg)

C_{others} = Others cost (Rs./kg)

7.2.2 Variable cost

The variable cost is an operating cost of the drying system, which consists of several expenses such as labour cost, fuel cost, electricity cost and other minor costs related to unforecastable. The variable cost was determined by the following relationship:

$$C_V = C_{labour} + C_{electricity} + C_{others} \tag{7.3}$$

where,

C_v = Variable cost (Rs./kg)

C_{labour} = Labour cost (Rs./kg)

$C_{electricity}$ = Electricity cost (Rs./kg)

C_{others} = Others cost (Rs./kg)

7.3 COST OF ENERGY

The average net present cost of electricity generation for a generating plant during its lifetime is measured as the cost of energy. It is utilised for investment planning as well as comparing different ways of electricity generation on a regular basis. The cost of energy was calculated by the following relationship:

$$C_{energy} = \frac{EC.C_e}{m_{dry}} \tag{7.4}$$

where,

C_{energy} = Cost of energy (Rs./kg)

EC = Energy consumption (Units/batch)

C_e = Electricity cost per unit (Rs./unit)

m_{dry} = Weight of dried grain per batch (1 kg/batch)

Hence, energy cost consumed is Rs. 18.80

7.4 COST ANALYSIS OF THREE DRYERS

In this section, the cost analysis of three dryers is investigated. The fixed cost, variable cost, selling price, payback period and profit per year were all determined. When performing cost analysis, numerous assumptions associated with various costs were taken into account. The assumptions were taken based on the experimental evaluations and market survey conducted in Assam, the North-Eastern region of India. The assumptions for the cost of paddy drying computation are shown in Table 7.1.

Table 7.1 Different costs for the three dryers

Calculation parameters	**Conical dryer (α = 10°)**	**Conical dryer (α = 5°)**	**Cylindrical dryer (α = 0°)**
Wet paddy rate (100 kg)	Rs. 1200.00	Rs. 1200.00	Rs. 1200.00
Dry paddy rate (100 kg)	Rs. 2000.00	Rs. 2000.00	Rs. 2000.00
Electricity kWh	@ 5.10	@ 5.10	@ 5.10
Unskilled Labour	Rs. 313.00/day	Rs. 313.00/day	Rs. 313.00/day
Interest rate	10% of investment	10% of investment	10% of investment
Repair & Maintenance	5% of investment	5% of investment	5% of investment
Dryer Utilization	300 days/year	300 days/year	300 days/year
Dryer Cost	Rs. 15000.00	Rs. 13500.00	Rs. 13000.00
Dryer service life	10 years	10 years	10 years
Instrumentation	Rs. 25000.00	Rs. 25000.00	Rs. 25000.00
Drying of paddy @ hour	10 kg	8 kg	5 kg
Dryer running 8 hours	51 kg/day	43 kg/day	36 kg/day
Drying time	28 mins	33 mins	40 mins

7.4.1 Cost analysis of conical dryer with cone angle 10°

The blower mass flow rate and electric heater power were calculated by the following equation

$$\text{CFM} = 1.75 \times (\text{Watt} / \text{Temperature Difference}) \quad (7.5)$$

According to the above formula, the use of total electricity used for one hour was 2.5 kW for the drying paddy.

Total cost of dryer = Dryer + Investment (cost) = Rs. (15000.00 + 25000.00) = Rs. 40,000.00.

Assuming the total life span of the dryer as 10 years.

The total interest of investment per year @10% = Rs. 4,000.00.

So, for one year, the fixed and the interest cost will be equal to Rs. 4,000.00.

So, the total fixed cost for one year = Rs. (4000.00 + 4000.00) = Rs. 8000.00.

Annual maintenance and repairing cost @ 5% of investment = Rs. 2,000.00.

After calculating the annual expenditure, the one-day expenditure for drying of paddy in the conical dryer of 10° cone angle is evaluated by dividing the number of days and shown in Table 7.2, which helps to determine the annual profit and BEP.

Table 7.2 One day expenditure for drying of paddy in the conical dryer (α = 10°)

Parameters	**Cost**
Fixed cost per day	Rs. 27.00
Maintenance per day	Rs. 7.00
Electricity per day	Rs. 102.00
Unskilled labour per day	Rs. 313.00
Total expenditure per day	**Rs. 449.00**

For one day, a total of 51 kg of paddy is dried with the expenditure of Rs. 449.00.

The cost of a dryer per kg of paddy is **Rs. 8.80.**

The total collected dry paddy is 38 kg from 51 kg of wet paddy.

The volume of dry paddy in one year is 38×300 = 11400 kg.

The selling price of dry paddy per kg is more than that of wet paddy by twenty rupees.

Therefore, total money collected by selling 38 kg @ Rs 20.00 = Rs. 760.00.

Profit = Selling price of paddy - Expenditure price for drying of paddy.

Profit = Rs. 760.00 - Rs. 449.00 = Rs. 311.00 per day

Therefore, (considering 300 days as working days), the profit will be Rs. 311.00 × 300 = Rs. 93400.00.

Payback period or BEP (Break-even period):

$$N^* = \frac{A}{S} \tag{7.6}$$

where, S is the net annual saving or profit, A is the capital cost or investment per year, and N^* is the payback period per year.

N^* = 40,000.00/93,400.00 = **0.43.**

The cost of one kg wet paddy and the payback period is Rs. 8.80 and 0.43 years, respectively.

7.4.2 Cost analysis of conical dryer with cone angle 5°

Total cost of dryer = Dryer + Investment (cost) = Rs. (13500.00 + 25000.00) = Rs. 38,500.00.

Assuming the total life span of the dryer as 10 yrs.

The total interest of investment per year @10% = Rs. 3,850.00.

So, for one year, the fixed and the interest cost will be equal to Rs. 3,850.00.

So, the total fixed cost for one year = Rs. (3850.00 + 3850.00) = Rs. 7,700.00.

Annual maintenance and repairing cost @5% of investment = Rs. 1,925.00.

Similar to Table 7.2, one-day expenditure for paddy drying in the conical dryer of 5° cone angle is also calculated by dividing the number of days to determine the annual profit and BEP and is shown in Table 7.3

Table 7.3 One day expenditure for drying of paddy in the conical dryer (α = 5°)

Parameters	**Cost**
Fixed cost per day	Rs. 25.00
Maintenance per day	Rs. 6.00
Electricity per day	Rs. 102.00
Unskilled labour per day	Rs. 313.00
Total expenditure per day	**Rs. 446.00**

For one day, a total of 43 kg of paddy is dried with the expenditure of Rs. 446.00.

The cost of a dryer per kg of paddy is **Rs. 10.37.**

The total collected dry paddy is 35 kg from 43 kg of wet paddy.

The volume of dry paddy in one year is 35×300 = 10500 kg.

Total collected dry paddy per kg is more than that of wet paddy by twenty rupees. Therefore, total money collected by selling 35 kg @Rs 20.00 = Rs. 700.00.

Profit = Selling price of paddy - Expenditure price for drying of paddy

= Rs. 700.00 - Rs. 446.00 = Rs. 254.00 per day.

Therefore, (considering 300 days as working days), the profit will be Rs. 254.00 × 300 = Rs. 76,200.00.

Payback period or BEP (Break-even period):

N^* = 38,500.00/76,200.00 = **0.505**

The cost of one kg wet paddy and the payback period is Rs 10.37 and 0.505 years, respectively.

7.4.3 Cost analysis of cylindrical dryer (α = 0°)

Total cost of Dryer = Dryer + Investment (cost) = Rs. (13,000.00 + 22,000.00) = Rs. 35,000.00.

Assuming the total life span of the dryer as 10 years.

The total interest of investment per year @10% = Rs. 3,500.00.

So, for one year, the fixed and the interest cost will be equal to Rs. 3,500.00.

So, the total fixed cost for one year = Rs. (3500.00 + 3500.00) = Rs. 7000.00.

Annual maintenance and repairing cost @5% of investment = Rs. 1,750.00.

Analogous to Tables 7.2 and 7.3, one-day expenditure for drying of paddy in the cylindrical dryer is shown in Table 7.4 to determine the annual profit and BEP.

Table 7.4 One day expenditure for drying of paddy in the cylindrical dryer (α = 0°)

Parameters	**Cost**
Fixed cost per day	Rs. 23.00
Maintenance per day	Rs. 5.00
Electricity per day	Rs. 102.00
Unskilled labour per day	Rs. 313.00
Total expenditure per day	**Rs. 443.00**

For one day, a total of 36 kg paddy is dried with the expenditure of Rs. 443.00.

The cost of a dryer per kg of paddy is **Rs. 12.33.**

The total collected dry paddy is 28 kg from 36 kg of wet paddy.

The volume of dry paddy in one year is 28×300 = 8400 kg

Total collected dry paddy per kg is more than that of wet paddy by twenty rupees. Therefore, total money collected by selling 28 kg @Rs 20.00 = Rs. 560.00.

Profit = Selling price of paddy - Expenditure price for drying of paddy

= Rs. 560.00 - Rs. 443.00 = Rs. 117.00 per day

Therefore, (considering 300 days as working days), the profit will be Rs. 117.00 × 300 = Rs. 35100.00.

Payback period or BEP (Break-even period):

N^* = 35,000.00/35,100.00 = **0.997**

The cost of one kg wet paddy and the payback period is Rs 12.33 and 0.997 years, respectively. After calculating all the parameters, the economics of dryers are presented in Table 7.5.

Table 7.5 Economics of dryers

Calculation parameters	**Conical dryer (α = 10°)**	**Conical dryer (α = 5°)**	**Cylindrical dryer (α = 0°)**
Total cost of a dryer	Rs. 40,000.00	Rs. 38,500.00	Rs. 35,000.00
Total fixed cost/ year	Rs. 8000.00	Rs. 7,700.00	Rs. 7,000.00
Profit/day	Rs. 311.00	Rs. 254.00	Rs. 117.00
Profit/year	Rs. 93400.00	Rs. 76,200.00	Rs. 35100.00
BEP	0.43	0.505	0.997

The BEP was found to be lower than Yahya et al. (2016) [197], Singh (2021) [198] and Pati (2016) [199] and profit/year was found to be higher than that of Yahya et al. (2016) [197],

Singh (2021) [198] and Pati (2016) [199]. The reason for this is due to the enhanced drying characteristics and consumption of less energy in the context of bubbling fluidized bed dryers.

7.5 SENSITIVITY ANALYSIS

Sensitivity analysis is a tool used in financial modelling to analyze how the different values of a set of independent variables affect a specific dependent variable under certain specific conditions. In this section, sensitivity analysis is carried out to study the effect of input parameters on the present results. The effect of selling price/kg and variable cost price/kg on profit per year and break-even period of three dryers has been investigated. As a result, the input variables, calculation of profit & loss and BEP for three dryers are provided in Table 7.6. Based on the input variables, the profit/loss and BEP are determined for the sensitivity analysis. Once the calculations of profit & loss and BEP for three dryers are completed based on the input variables, the sensitivity of the input variables on profit & loss and BEP for the three dryers is determined.

Table 7.6 Input variables, profit/loss and BEP forecast for sensitivity analysis

Parameters	**Conical dryer (α = 10°)**	**Conical dryer (α = 5°)**	**Cylindrical dryer (α = 0°)**
Input variable:			
Volume of paddy/year	11400 kg	10500 kg	8400 kg
Interest of investment rate	10%	10%	10%
Selling price/kg	Rs. 20.00	Rs. 20.00	Rs. 20.00
Variable Cost price/kg	Rs. 11.11	Rs. 12.01	Rs. 14.99
Profit & Loss and BEP forecast:			
Revenue/year	Rs. 2,28,000.00	Rs. 2,10,000.00	Rs. 1,68,000.00
Variable cost/year	Rs. 1,26,600.00	Rs. 1,26,100.00	Rs. 1,25,900.00
Instrument and dryer cost for 10 years	Rs. 40,000.00	Rs. 38,500.00	Rs. 35,000.00
Instrument and dryer cost for 1 year	Rs. 4,000.00	Rs. 3,850.00	Rs. 3,500.00
Service cost/year	Rs. 4,000.00	Rs. 3,850.00	Rs. 3,500.00
Fixed cost/year	Rs. 8,000.00	Rs. 7,700.00	Rs. 7,000.00
Total cost/year	Rs. 1,34,600.00	Rs. 1,33,800.00	Rs. 1,32,900.00
Profit/year	Rs. 93,400.00	Rs. 76,200.00	Rs. 35,100.00
BEP	0.43	0.505	0.997

The input parameters in the above table were the volume of paddy/year, interest on investment rate, selling price/kg and variable cost/kg. The volume of paddy was constant for the three dryers as the calculation was for one year. It was calculated for the three dryers as shown in previous sub-sections. The other three could change. If the interest of investment rate varies, so does the fixed cost, which has an impact on output results, i.e. profit/loss and BEP. Similarly, changes in the selling price/kg and variable cost/kg have an impact on output results. But due to table reduction, the influence of interest on investment rate on output results was not shown. It was assumed as constant. Only the effect of selling price/kg and variable cost/kg on output results for the three dryers was studied. As a result, the six sets of input parameters were considered, and a matrix of this is shown in Table 7.7. The input parameter matrix was considered in such a way that the value of selling price/kg and variable cost/kg should be either lower or higher than the present value. The selling price/kg value changes from Rs. 5.00 to Rs. 30.00 in Rs. 5.00 increments. Similarly, the variable cost price/kg changes from Rs. 8.00 to Rs. 18.00 with a step increase in Rs. 2.00.

Table 7.7 Input parameter matrix for sensitivity analysis

Sl. No.	Selling price/kg (Rs.)	Variable cost/kg (Rs.)
1	5.00	8.00
2	10.00	10.00
3	15.00	12.00
4	20.00	14.00
5	25.00	16.00
6	30.00	18.00

The sensitivity analysis was performed for the three dryers with the change in input parameters. Tables 7.8, 7.9 and 7.10 show the sensitivity analysis of profit/loss per year for two conical dryers having cone angles of 10° and 5° and a cylindrical dryer, respectively.

Table 7.8 Sensitivity analysis of profit/year (α = 10°)

Selling Price/kg (Rs.)	Profit/year (Rs.) vs Cost price/kg (Rs.)					
	8.00	10.00	12.00	14.00	16.00	18.00
5.00	- 42,200.00	- 65,000.00	- 87,800.00	- 1,10,600.00	- 1,33,400.00	- 1,56,200.00
10.00	14,800.00	- 8,000.00	- 30,800.00	- 53,600.00	- 76,400.00	- 99,200.00
15.00	71,800.00	49,000.00	26,200.00	3,400.00	- 19,400.00	- 42,200.00
20.00	1,28,800.00	1,06,000.00	83,200.00	60,400.00	37,600.00	14,800.00
25.00	1,85,800.00	1,63,000.00	1,40,200.00	1,17,400.00	94,600.00	71,800.00
30.00	2,42,800.00	2,20,000.00	1,97,200.00	1,74,400.00	1,51,600.00	1,28,800.00

Table 7.9 Sensitivity analysis of profit/year (α = 5°)

Selling Price/kg (Rs.)	Profit/year (Rs.) vs Cost price/kg (Rs.)					
	8.00	10.00	12.00	14.00	16.00	18.00
5.00	- 39,200.00	- 60,200.00	- 81,200.00	- 1,02,200.00	- 1,23,200.00	- 1,44,200.00
10.00	13,300.00	- 7,700.00	- 28,700.00	- 49,700.00	- 70,700.00	- 91,700.00
15.00	65,800.00	44,800.00	23,800.00	2,800.00	- 18,200.00	- 39,200.00
20.00	1,18,300.00	97,300.00	76,300.00	55,300.00	34,300.00	13,300.00
25.00	1,70,800.00	1,49,800.00	1,28,800.00	1,07,800.00	86,800.00	65,800.00
30.00	2,23,300.00	2,02,300.00	1,81,300.00	1,60,300.00	1,39,300.00	1,18,300.00

Table 7.10 Sensitivity analysis of profit/year (α = 0°)

Selling Price/kg (Rs.)	Profit/year (Rs.) vs Cost price/kg (Rs.)					
	8.00	10.00	12.00	14.00	16.00	18.00
5.00	- 32,200.00	- 49,000.00	- 65,800.00	- 82,600.00	- 99,400.00	- 1,16,200.00
10.00	9,800.00	- 7,000.00	- 23,800.00	- 40,600.00	- 57,400.00	- 74,200.00
15.00	51,800.00	35,000.00	18,200.00	1,400.00	- 15,400.00	- 32,200.00
20.00	93,800.00	77,000.00	60,200.00	43,400.00	26,600.00	9,800.00
25.00	1,35,800.00	1,19,000.00	1,02,200.00	85,400.00	68,600.00	51,800.00
30.00	1,77,800.00	1,61,000.00	1,44,200.00	1,27,400.00	1,10,600.00	93,800.00

It is seen from the table that when the variable cost/kg increases, the profit/year drops from left to right for all the dryers. The rate at which the selling price increases raises the annual profit in all cases. The negative sign in the table indicated that a loss had occurred. It was also observed that in order to make a profit, the selling price should be greater than Rs. 15.00 per kg for the highest value of variable cost price.

Similarly, the sensitivity analysis of BEP with changes in selling price/kg and variable cost price/kg is also provided in Tables 7.11, 7.12 and 7.13.

Table 7.11 Sensitivity analysis of BEP (α = 10°)

Selling Price/kg (Rs.)	BEP vs Cost price/kg (Rs.)					
	8.00	10.00	12.00	14.00	16.00	18.00
5.00	-0.95	-0.62	-0.46	-0.36	-0.30	-0.26
10.00	2.70	-5.00	-1.30	-0.75	-0.52	-0.40
15.00	0.56	0.82	1.53	11.76	-2.06	-0.95
20.00	0.31	0.38	0.48	0.66	1.06	2.70
25.00	0.22	0.25	0.29	0.34	0.42	0.56
30.00	0.16	0.18	0.20	0.23	0.26	0.31

Table 7.12 Sensitivity analysis of BEP (α = 5°)

Selling Price/kg (Rs.)	BEP vs Cost price/kg (Rs.)					
	8.00	10.00	12.00	14.00	16.00	18.00
5.00	-0.98	-0.64	-0.47	-0.38	-0.31	-0.27
10.00	2.89	-5.00	-1.34	-0.77	-0.54	-0.42
15.00	0.59	0.86	1.62	13.75	-2.12	-0.98
20.00	0.33	0.40	0.50	0.70	1.12	2.89
25.00	0.23	0.26	0.30	0.36	0.44	0.59
30.00	0.17	0.19	0.21	0.24	0.28	0.33

Table 7.13 Sensitivity analysis of BEP (α = 0°)

Selling Price/kg (Rs.)	BEP vs Cost price/kg (Rs.)					
	8.00	10.00	12.00	14.00	16.00	18.00
5.00	-1.09	-0.71	-0.53	-0.42	-0.35	-0.30
10.00	3.57	-5.00	-1.47	-0.86	-0.61	-0.47
15.00	0.68	1.00	1.92	25.00	-2.27	-1.09
20.00	0.37	0.45	0.58	0.81	1.32	3.57
25.00	0.26	0.29	0.34	0.41	0.51	0.68
30.00	0.20	0.22	0.24	0.27	0.32	0.37

According to the tables, when the selling price exceeds Rs. 15.00, the BEP decreases. Over this selling price, the BEP is seen to increase with the variable cost/kg. As a result, the selling price should be greater than Rs. 15.00/kg in order to have profit. In addition, tables show that BEP is negative at the price of the negative profit.

7.6 CHAPTER CONCLUSION

In this chapter, an economic analysis of three atmospheric bubbling fluidized dryers was performed to accept the viability of dryers under various assumed dryer costs. The economic study determined the fixed cost, variable cost, cost of energy, break-even period and profit/year. It was observed that the conical dryer of 10° cone angle had lower BEP and higher profit/year than the other two dryers. The sensitivity analysis of profit/loss and BEP with response to the change in selling price/kg and variable cost/kg reveals consistent trends across all dryers. In all dryers, as variable cost/kg increases, profit/year declines from left to right. However, the annual profit in all dryers rises as the selling price/kg rises. When the selling price exceeds Rs. 15.00/kg, the BEP was seen to drop in all dryers. As a result, the selling price should be higher than Rs. 15.00/kg for more profit and less BEP. In the next chapter, conclusions and the future scope of the present investigation will be presented.

8

Conclusions and scope for future work

8.1 Conclusions

8.2 Application potential

8.3 Scope for future work

CHAPTER – 8

CONCLUSIONS AND SCOPE FOR FUTURE WORK

8.1 CONCLUSIONS

A comparative study on flow behaviour, heat transfer and drying characteristics in atmospheric bubbling fluidized bed dryers was investigated experimentally and numerically for five different cone angles, 0°, 5°, 10°, 15° and 20°, in the present work. Initially, 2-D numerical simulations with sand as bed inventory was carried out to model the five dryers. The Eulerian-Eulerian model incorporating the kinetic theory of granular flow (KTGF) was employed for the simulation study. Based on the simulation results, the experiments were carried out on the dryers, and the results were compared. It was found that increasing the cone angle beyond 10° increased the bed pressure drop by 23% and 28%, respectively, at 15° and 20° cone angles in 2-D simulation conditions. Similarly, an increase in bed pressure drop was also observed in experimental conditions above 10° cone angle. The increasing bed pressure drop is the disadvantage of a fluidized bed. As a result, the entire investigation was carried out for the limiting cone angle of 10°. The hydrodynamic behaviour such as bed pressure drop, axial solid volume fraction, radial solid volume fraction, radial solid velocity and granular temperature were studied in the dryers. The temperature distribution and interphase heat transfer coefficient were also investigated. Similarly, the 3-D simulation was carried out to compare the experimental results with the simulation results. In this comparative study, the bed height of sand particles and air velocity were kept as 30 cm and 1.5 m/s, respectively, for all dryers. The average particle size of the sand particle of 435 µm was considered. Subsequently, the impact of the height of bed materials (10, 20 and 30 cm), superficial air velocity (1, 1.5 and 2.1 m/s) and size of the particle (300, 435 and 600 µm) on the hydrodynamic behaviour such as bed expansion ratio, radial solid volume fraction profile, granular temperature profile and heat transfer coefficient have been explored experimentally, in a conical dryer of 10° cone angle. Furthermore, the experimental results of the conical dryer were validated against the 3-D simulation results. A constant air temperature of 65°C was applied through the inlet of the dryers to explore the heat transfer phenomena. After the characterization of the conical dryer by investigating hydrodynamics and heat transfer characteristics, it was used for drying the

paddy granules since paddy is widely available in the North-Eastern region of India. The trend in energy consumption (both thermal and blower), the hydrodynamic behaviour and drying characteristics were investigated in the dryers. A spiral was inserted into these dryers, and the results were analysed. Experiments of drying paddy in the dryers were conducted under various operating conditions such as inlet air velocity (1.1, 1.6 and 2.1 m/s), inlet air temperature (55, 60 and 65°C) and bed inventory (1, 2, 2.5 and 3 kg). The drying quality of paddy in terms of milling and nutritional contents was also determined for a conical dryer of 10° cone angle, and results were compared to previously published literature. Finally, energy analysis in terms of energy utilization and energy utilization ratio was also investigated for the same operating parameters described above. The exergy analysis for exergy use and exergy efficiency was also reported for the same operating parameters. The novelty of the current study is that it investigates heat transfer characteristics by including varied cone angles, as well as the effect of spiral and cone angles on hydrodynamics, drying characteristics, energy consumptions (both thermal and blower), thermodynamic analysis (energy and exergy), milling and drying quality of paddy. Objective-wise conclusions are presented in the following sub-sections:

8.1.1 Numerical and experimental investigation of hydrodynamic behaviour and heat transfer characteristics of sand particles in atmospheric bubbling fluidized bed dryers with different cone angles

The experimental and simulation results of hydrodynamic behaviour and heat transfer characteristics in bubbling fluidized bed dryers are summarized in this subsection. Air was used as the primary phase, with sand particles as the fluidizing material. Experiments were carried out at the same bed height of particles (30 cm), air velocity (1.5 m/s) and particle size (435 µm). The pressure drops, bed expansion ratio, radial solid volume fraction, radial solid velocity, bed temperature and interphase heat transfer coefficients were determined. Furthermore, experimental and numerical investigations of hydrodynamic behaviour and heat transfer characteristics of the conical dryer with a 10° cone angle were also discussed for various operating parameters such as bed height, particle size and inlet air velocity. The effect of cone angle on heat transfer characteristics, as well as the performance analysis of a conical riser with various operating parameters, are novel aspects of this objective. The key results are demonstrated below:

- The bed pressure drop was found to decrease by 22.23%, with an increasing cone angle from 0° to 10° with a step increase of 5° for both conditions. The bed pressure drop in

the conical dryer at a 10° cone angle was also observed to decrease by 3.54% with the air velocity in experimental conditions. The effective height of pressure drop was found to be 45 cm for the higher value of air velocity. The pressure drop increases by 30% when the bed height increases from 10 to 30 cm. Similarly, the increase in particle size from 300 to 600 µm causes a nearly 24% increase in bed pressure drop. The 3-D simulation results of the bed pressure drop coincide with the experimental result.

- The expansion of solid particles was less for the higher cone angle of conical dryers. The effective bed height for the cylindrical dryer was 65 cm. However, it was about 45 cm for the higher cone angle of the conical dryer, which was nearly 30.76% lesser than the cylindrical dryer. The bed expansion ratio was observed to decrease by 14.7%, with an increment of bed height from 10 to 30 cm for a conical dryer of 10° cone angle. Similarly, the bed expansion ratio also decreases by 23.24% when particle size increases from 300 to 600 µm. However, the trend was reversed, i.e., it increases from 1.7 to 2.8 (38.4%) for increasing superficial air velocity from 1 to 2 m/s. The experimental result of the bed expansion ratio for superficial air velocity was in excellent agreement with 3-D simulation results.
- Data for radial solid volume fraction collected at an axial height of 10 cm indicates a rising trend with the cone angle. It was also seen that there exists a core annular structure in all dryers. There was an increasing amount of solid particles near the wall with an increase in cone angle. It was observed that the thickness of particles from the wall to the centre decreases when the superficial air velocity increases in the conical dryer at a 10° cone angle. There was a decrease in solid volume fraction in the radial direction with the rise in air velocity. The 3-D simulation result of radial solid volume fraction profile showed that the profile is of U type, which means that the solid particles remain more near the wall than the core of the dryer and the percentage of solid decreases with an increase in the air velocity at the axial location of 10 cm.
- The solid velocity embraces a decreasing trend with the cone angle. The solid velocity was found to be maximum in the core region than the wall of the conical dryer at a 10° cone angle for the operating parameter of air velocity. The solid velocity was found to be higher at the higher value of the air velocity.

- For all the cases, the granular temperature, which is equivalent to the square of solid fluctuation velocity, increases, whereas the solid volume fraction decreases. The granular temperature at the wall was also found to decrease as the solid volume fraction increased at the wall for all operating conditions.

- The higher cone angle was observed to have a beneficial effect on the bed temperature and interphase heat transfer coefficient for the same height of bed material as the solid temperature increases with an increase in cone angle. The interphase heat transfer coefficient was found to be increasing (6.25%) from 288 to 306 W/m^2K with the increase in cone angle. There was an increase in interphase heat transfer coefficient from 296 to 320 W/m^2K (8.1%) in the conical dryer at a 10° cone angle when the air velocity increased from 1 to 2 m/s.

- The temperature at the core region was higher than the wall of the conical dryer at a 10° cone angle for all cases. The bed temperature increases with the superficial air velocity. The bed temperature decreases from 63 to 58.3 °C with an increase in the bed height of particles from 10 to 30 cm. Similarly, the bed temperature also drops (from 62.3 to 57.8 °C) as the particle size increases from 300 to 600 µm. The 3-D simulation results of temperature were found to be in good agreement with the experimental results. However, the difference between simulation and experimental results is 2.3%.

8.1.2 Performance evaluation of drying characteristics of paddy particles in bubbling fluidized bed dryers with different operating parameters

In this investigation, performance evaluation of the drying process of paddy was experimentally investigated in two conical bubbling fluidized bed dryers with cone angles of 5° and 10°, and the results were compared with the results of Thant et al. [123]. The experiments were conducted at three different superficial air velocities of 1.1, 1.6 and 2.1 m/s with bed inventories between 1 to 3 kg. Three different inlet air temperatures of 55, 60 and 65°C were maintained for the evaluation of the drying process. Both hydrodynamic behaviour and drying characteristics have been investigated under these operating conditions, and results were compared among the dryers. Numerical simulations were also carried out to validate the pressure drop between sand and paddy particles for the operating parameter of superficial air velocity. The energy consumptions in the drying of paddy, which incorporates both thermal and the blower, were also investigated for the operating parameters of inventory and constant inlet air temperature, and results were compared. Similarly, the performance of drying and milling quality of dried paddy was studied

in a conical dryer of 10° cone angle and results were compared with available literature under similar operating parameters. The significance of the research is to compare the drying characteristics, energy consumptions (thermal and blower), drying and milling quality of paddy particles between conical bubbling fluidized bed dryers and straight bubbling fluidized bed dryers. The results of this investigation are summarized below:

- The pressure drop decreases with the height of the dryers in all operating parameters. The maximum pressure drop was found to be about 2.5 cm of the water column. It was also found that with an increase in superficial air velocity, the pressure drop decreases. Pressure drop also decreases with the higher cone angle of the conical dryer. But, the effective height of the pressure drop was higher when the superficial air velocity increased. However, the pressure drop was found to be increasing with an increase in bed inventory. The pressure drop was found to be higher for sand particles than that of paddy particles. It was also found that the pressure drop increases when the sand is mixed with paddy particles.

- Drying time was found to be lower for a higher value of air velocity. However, for the higher value of static bed inventory, it showed the opposite trend. The use of a conical fluidized bed dryer had a more desirable effect on drying characteristics than a conventional fluidized bed dryer. The drying rate was also found to be increasing with the mixing of sand with paddy. The reduction in drying time was found to be nearly 13.33% when sand was mixed with paddy particles. For all operating conditions, the time required for drying paddy grains in a conical fluidized bed dryer was almost half of the time required for drying the paddy grains in a conventional fluidized bed dryer.

- The conical fluidized bed dryer with a higher degree of cone angle consumed less thermal and energy consumption of blower than a conventional fluidized bed dryer. When a higher degree of the conical dryer was used, the average thermal energy consumption was lowered by 50%. Hence, a conical bubbling fluidized bed dryer is a better energy-saving option than any conventional fluidized bed dryer.

- A minor reduction of all nutritional contents was observed with an increase in the drying time. The nutritional value of the dried paddy sample for 30 minutes of drying contained 1.65% crude fibre, 11.88% protein, 1.46% fat and 75.20% carbohydrate.

- The milling quality of the drying product was tested, and 75% of milled rice was found to be recovered by a conical bubbling fluidized bed dryer having a cone angle of 10°.

8.1.3 Effect of spiral and cone angles on hydrodynamics and drying characteristics of paddy granules in bubbling fluidized bed dryers

In this objective, the influence of spiral and cone angles on hydrodynamic behaviour, drying characteristics, thermal energy consumption, ECB, drying and milling quality of paddy products were studied experimentally. Experiments were carried out with two different inlet air velocities (1.1 and 1.6 m/s) and three different inlet air temperatures (55°C, 60°C and 65°C), using a 1-3 kg batch size of paddy as a bed inventory. The essence of the work is that it gives an insight into hydrodynamics, drying characteristics, energy consumptions (both thermal and blower), milling and drying quality of paddy by including the effect of spiral and cone angles. The key outcomes from this study are presented below:

- The pressure drop increases with the use of a spiral in all the dryers. The maximum reduction of pressure drop was found to be 5 mm in the water column for both conical dryers. The pressure drops were also found to decrease with an increase in cone angle. When using a 10° cone angle conical dryer, the reduction in pressure drop was 10 mm in the water column.

- For all cases, the drying time was found to be lower with the use of spiral than without spiral. In a conical dryer with a cone angle of 5°, when a spiral was inserted into the dryer, the maximum drying time to reach the EMC was 30 mins, which was 25% lower than without a spiral (40 mins). Similarly, the drying time was 16.67% lower with the spiral than without the spiral in the conical dryer at a 10° cone angle.

- The drying time decreases with an increase in cone angle for the spiral. The required drying time was 25 mins for a higher degree of cone angle. A conical dryer with a smaller cone angle took almost 30 mins to dry, which was 20% more than that of a larger cone angle conical dryer. On the other hand, the cylindrical dryer took nearly 34 mins to achieve the desired moisture content.

- The trend of thermal energy consumption for these two types of dryers (5° and 10°) showed that the incorporation of a spiral in the dryers decreases energy consumption by about 23%. The thermal energy consumption was also lower in the 10° cone angle

of the conical dryer. When a larger degree of the cone angle was employed for the conical dryer, nearly 19.26% of energy consumption was reduced.

- The energy consumption of the blower was lower for the dryer with a spiral than without a spiral. The energy consumption of the blower was decreased by 18% due to the introduction of a spiral. The energy consumption of the blower was also shown to decrease with an increase in cone angle. A 26.67% reduction in energy consumption of the blower was observed due to the higher degree of cone angle. However, when the air velocity increases, the difference in energy consumption of blower between spiral and without spiral was more prominent.

- The drying quality of paddy materials in terms of milling and nutritional contents for conical dryers with a cone angle of 10° was examined for spiral and without spiral. For the milling quality, head rice was weighed, and the percentage was determined. As observed, the head rice for the dryer with and without a spiral was 63% and 58%, respectively, but in conventional dryers, it was around 30 to 50% in Asian countries. The addition of a spiral increases the milling recovery by 3%. The percentage of all nutritional values decreases with an increase in drying time.

8.1.4 Thermo-economic study of paddy drying on bubbling fluidized bed dryers

After careful investigation of hydrodynamic behaviour, drying characteristics, energy consumption and drying quality of paddy product in the dryers under various operating parameters, the thermo-economic analysis was carried out in the dryers with five different operating parameters. Energy utilization (EU), energy utilization ratio (EUR), exergy utilization and exergy efficiency were determined. The operating parameters were inlet air velocity, the mass of paddy, inlet air temperature, spiral and cone angle. For the economic analysis, the break-even period and profit per year for the dryers were investigated. Further, the economic analysis was subjected to sensitivity analysis. The important aspect of this objective is the effect of cone angles and spiral on energy and exergy analysis as well as the economic analysis by incorporating the same. After an analysis of the results, the following conclusions are made:

- The trend of EU and EUR was found to decline with drying time. However, the EU and EUR increase with an increase in inlet air velocity, inlet air temperature and mass of paddy particles.
- The EU and EUR also increase with the addition of a spiral and an increase in cone angle from 0° to 10° at a step of 5°.
- Similar to the EU and EUR, the exergy utilization was also decreasing with the drying time. However, the utilization of exergy in the process of drying was observed to increase with the increase in inlet air velocity, inlet air temperature and mass of paddy particles.
- The spiral's incorporation into the dryer leads to a higher exergy utilization of the drying process. Similarly, the exergy utilization also increases with an increase in cone angle.
- The pattern of exergetic efficiency showed a decreasing order with an increase in drying time. The exergetic efficiency improves with the increase in inlet air velocity, inlet air temperature and mass of paddy.
- The addition of a spiral improves the exergetic efficiency of drying processes in a dryer. It was also seen that there was an improvement in the exergetic efficiency with an increase in the cone angle. When a spiral was incorporated, the exergy efficiency increased by 28% as the cone angle increased. The maximum exergetic efficiency was found to be 0.41.
- The break-even period was found to be lesser for a conical dryer of 10° cone angle. However, the profit per year was found to be higher for the conical dryer at a 10° cone angle. Hence, it can be said that the conical dryer of 10° cone angle is the most economical dryer.
- The sensitivity analysis of profit/loss reveals that when the variable cost/kg increases, the profit/year drops from left to right for all the dryers. The rate at which the selling price increases raises the annual profit in all cases. It was also observed that in order to make a profit, the selling price should be greater than Rs. 15 for the highest value of variable cost price.

- The BEP was also found to decrease when the selling price exceeds Rs. 15. Over this selling price, the BEP was seen to increase with the variable cost/kg. As a result, the selling price should be greater than Rs. 15/kg in order to make a profit.

After a critical analysis of the present investigation, it is recommended that a significant amount of exergy was lost at the end of a drying process. So, this loss of exergy can be reutilized as drying air by dehumidifying the exhaust air.

8.2 APPLICATION POTENTIAL

The dryers were successfully tested under laboratory conditions and have the potential to be used on the pilot scale in a commercial unit. The drying products obtained from the conical dryer have a higher yield and slightly improved nutritional contents. The outcome of the present investigation will help the researchers to get a brief idea about the conical bubbling fluidized bed's heat transfer and drying characteristics.

8.3 SCOPE FOR FUTURE WORK

- Performance analysis of paddy drying was carried out in the present dryers. The dryers can also be utilized to study the performance analysis of different drying materials such as tea, cardamom, ginger and different agricultural products etc., and results can be compared with the present study.

- The present risers were used for investigating the hydrodynamics, heat transfer and drying characteristics of sand and paddy particles, respectively. The risers may also be used to study the gasification characteristics by considering different feed materials such as coal and coal with biomasses.

- The present study was carried out to study the drying characteristics and energy consumption by incorporating a passive spiral as an internal. A similar study can also be carried out by introducing different internals, and the results can be compared with the passive spiral.

- The maximum D_1/L ratio of the risers was considered 0.125 in the present study. The scale-up study can be carried out by enlarging the D_1/L ratio to meet the mitigation of the deviation between laboratory-scale units and real processes industries.

References

[1] B. Roy, D.T. Surje, S. Mahato, Biodiversity of farmers' varieties of rice (Oryza Sativa L.) at respository of Uttar banga krishi viswavidyalaya:A reservoir of important characters, J. Environ. Sci. 4 (2013) 145–151.

[2] P. Kalita, T.J. Deka, S. Das, D. Das, R. Kataki, Design, development and performance evaluation of a fluidized bed paddy dryer, J. Energy Environ. Sustain. 6 (2018) 18–23.

[3] A. Fudholi, M.Y. Othman, M.H. Ruslan, K. Sopian, Drying of Malaysian Capsicum annuum L. (Red Chili) Dried by Open and Solar Drying, Int. J. Photoenergy. 2013 (2013) 1–9. https://doi.org/10.1155/2013/167895.

[4] V. Palled, S.R. Desai, M. Anantachar, Field evaluation of solar tunnel dryer for grapes drying, Ecol. Environ. Conserv. 20 (2014) 1665–1668.

[5] A.S. Kassem, A.Z. Shokr, A.R. El-Mahdy, A.M. Aboukarima, E.Y. Hamed, Comparison of drying characteristics of Thompson seedless grapes using combined microwave oven and hot air drying, J. Saudi Soc. Agric. Sci. 10 (2011) 33–40. https://doi.org/10.1016/j.jssas.2010.05.001.

[6] W. Jittanit, N. Saeteaw, A. Charoenchaisri, Industrial paddy drying and energy saving options, J. Stored Prod. Res. 46 (2010) 209–213. https://doi.org/10.1016/j.jspr.2010.04.005.

[7] W. Rordprapat, A. Nathakaranakule, W. Tia, S. Soponronnarit, Comparative study of fluidized bed paddy drying using hot air and superheated steam, J. Food Eng. 71 (2005) 28–36. https://doi.org/10.1016/j.jfoodeng.2004.10.014.

[8] W. Zhonghua, A.S. Mujumdar, Simulation of the Hydrodynamics and Drying in a Spouted Bed Dryer, Dry. Technol. 25 (2007) 59–74. https://doi.org/10.1080/07373930601160775.

[9] S. Tirawanichakul, S. Prachayawarakorn, W. Varanyanond, S. Soponronnarit, Drying Strategies for Fluidized-Bed Drying of Paddy, Int. J. Food Eng. 5 (2009). https://doi.org/10.2202/1556-3758.1401.

[10] A. Karbassi, Z. Mehdizadeh, Drying rough rice in a fluidized bed dryer, J. Agric. Sci. Technol. 10 (2008) 233–241.

[11] Somchart Soponronnarit, Fluidised-bed paddy drying, ScienceAsia. 25 (1999) 51–56.

[12] A.S. Mujumdar, Some recent developments in drying technologies appropriate for postharvest processing, Int. J. Postharvest Technol. Innov. (2006). https://doi.org/10.1504/ijpti.2006.009185.

[13] D. Kunii, O. Levenspiel, Fluidization Engineering, Butterworth-Heinemann, 1991.

[14] J.M. Beeny, C.S.N. Basil, Multipass drying of paddy (rice) in the humid tropics, J. Agric. Eng. Res. 15 (1970) 364–374. https://doi.org/10.1016/0021-8634(70)90096-X.

[15] C. Igathinathane, P.K. Chattopadhyay, L.O. Pordesimo, Moisture diffusion modeling of parboiled paddy accelerated tempering process with extended application to multi-pass drying simulation, J. Food Eng. 88 (2008) 239–253. https://doi.org/10.1016/j.jfoodeng.2008.02.014.

[16] S. Suherman, M. Djaeni, A.C. Kumoro, Drying Kinetics of Paddy in Fluidized Bed with Immersed Heating Element, Adv. Sci. Lett. 23 (2017) 2364–2366. https://doi.org/10.1166/asl.2017.8672.

[17] Y. Tirawanichakul, S. Prachayawarakorn, W. Varanyanond, S. Soponronnarit, Simulation and grain quality for in-store drying of paddy, J. Food Eng. (2004). https://doi.org/10.1016/j.jfoodeng.2003.09.001.

[18] K. Luthra, S.S. Sadaka, G.G. Atungulu, Exploration of rough rice head yield subjected to drying and retention durations in a fluidized bed system, Appl. Eng. Agric. (2018). https://doi.org/10.13031/aea.12925.

[19] S. V. Jangam, An Overview of Recent Developments and Some R&D Challenges Related to Drying of Foods, Dry. Technol. 29 (2011) 1343–1357. https://doi.org/10.1080/07373937.2011.594378.

[20] A.S. Mujumdar, Research and Development in Drying: Recent Trends and Future Prospects, Dry. Technol. 22 (2004) 1–26. https://doi.org/10.1081/DRT-120028201.

[21] A. Chakraverty, Post-harvest technology of cereals, pulses and oil seeds, Third, Oxford and IBH, 1994.

[22] L. Xia, H. Zhang, B. Wang, C. Yu, X. Fan, Experimental and numerical analysis of oil shale drying in fluidized bed, Dry. Technol. 35 (2017) 802–814. https://doi.org/10.1080/07373937.2016.1218345.

[23] M.. Basunia, T. Abe, Thin-layer solar drying characteristics of rough rice under natural convection, J. Food Eng. 47 (2001) 295–301. https://doi.org/10.1016/S0260-8774(00)00133-3.

[24] International Rice Research Institute, (2005). www.irri.org.

[25] A. Ayensu, Dehydration of food crops using a solar dryer with convective heat flow, Sol. Energy. 59 (1997) 121–126.

[26] D. Pangavhane, Design, development and performance testing of a new natural convection solar dryer, Energy. 27 (2002) 579–590. https://doi.org/10.1016/S0360-5442(02)00005-1.

[27] M.A. van der Hoef, M. van Sint Annaland, N.G. Deen, J.A.M. Kuipers, Numerical Simulation of Dense Gas-Solid Fluidized Beds: A Multiscale Modeling Strategy, Annu. Rev. Fluid Mech. 40 (2008) 47–70. https://doi.org/10.1146/annurev.fluid.40.111406.102130.

[28] J. Sun, Y. Zhou, C. Ren, J. Wang, Y. Yang, CFD simulation and experiments of dynamic parameters in gas–solid fluidized bed, Chem. Eng. Sci. 66 (2011) 4972–4982. https://doi.org/10.1016/j.ces.2011.06.035.

[29] Y. Li, J. Zhang, L.-S. Fan, Numerical simulation of gas–liquid–solid fluidization systems using a combined CFD-VOF-DPM method: bubble wake behavior, Chem. Eng. Sci. 54 (1999) 5101–5107. https://doi.org/10.1016/S0009-2509(99)00263-8.

[30] L. Huilin, Z. Yunhua, S. Zhiheng, J. Ding, J. Jiying, Numerical simulations of gas-solid flow in tapered risers, Powder Technol. 169 (2006) 89–98. https://doi.org/10.1016/j.powtec.2006.07.023.

[31] B. Chalermsinsuwan, P. Kuchonthara, P. Piumsomboon, CFD modeling of tapered circulating fluidized bed reactor risers: Hydrodynamic descriptions and chemical reaction responses, Chem. Eng. Process. Process Intensif. 49 (2010) 1144–1160. https://doi.org/10.1016/j.cep.2010.08.016.

[32] H. Askaripour, A. Molaei Dehkordi, Effects of initial static bed height on fractional conversion and bed pressure drop in tapered-in and tapered-out fluidized bed reactors, Int. J. Multiph. Flow. 79 (2016) 50–61. https://doi.org/10.1016/j.ijmultiphaseflow.2015.08.006.

[33] D.C. Sau, K.C. Biswal, Computational fluid dynamics and experimental study of the hydrodynamics of a gas–solid tapered fluidized bed, Appl. Math. Model. 35 (2011) 2265–2278. https://doi.org/10.1016/j.apm.2010.11.037.

[34] Fluent 6.1.22, User's Guide, 20.4, Eulerian Model, Fluent Inc. (2005).

[35] A. Bahramian, M. Olazar, Fluidization of micronic particles in a conical fluidized bed: Experimental and numerical study of static bed height effect, AIChE J. 58 (2012) 730–744. https://doi.org/10.1002/aic.12621.

[36] M. Syamlal, T.J. O'Brien, Simulation of granular layer inversion in liquid fluidized beds, Int. J. Multiph. Flow. 14 (1988) 473–481. https://doi.org/10.1016/0301-9322(88)90023-7.

[37] D. Gidaspow, Multiphase Flow and Fluidization: Continuum and Kinetic Theory Descriptions, Academic Press, New York, 1994.

[38] H. Arastoopour, Numerical simulation and experimental analysis of gas/solid flow systems: 1999 Fluor-Daniel Plenary lecture, Powder Technol. 119 (2001) 59–67. https://doi.org/10.1016/S0032-5910(00)00417-4.

[39] H. Sutar, C.K. Das, Mixing and Segregation Characteristics of Binary Granular Material in Tapered Fluidized Bed: A CFD Study, Engineering. 04 (2012) 215–227. https://doi.org/10.4236/eng.2012.44029.

[40] A. Bahramian, M. Olazar, Evaluation of elastic and inelastic contact forces in the flow regimes of Titania nanoparticle agglomerates in a bench-scale conical fluidized bed: A comparative study of CFD-DEM simulation and experimental data, Chem. Eng. Res. Des. 176 (2021) 34–48. https://doi.org/10.1016/j.cherd.2021.09.027.

[41] A. Bahramian, M. Olazar, Influence of restitution and friction coefficients on the velocity field of polydisperse TiO2 agglomerates in a conical fluidized bed by the adhesive CFD-DEM simulation, Powder Technol. 386 (2021) 491–504. https://doi.org/10.1016/j.powtec.2021.03.068.

[42] A. Bahramian, Simultaneous effects of mesh refinement, grid configuration and wall boundary condition on prediction of pressure gradients and velocity profiles of microparticles in a conical fluidized bed, Particuology. 43 (2019) 123–136. https://doi.org/10.1016/j.partic.2018.04.003.

[43] A. Midilli, H. Kucuk, Mathematical modeling of thin layer drying of pistachio by using solar energy, Energy Convers. Manag. 44 (2003) 1111–1122. https://doi.org/10.1016/S0196-8904(02)00099-7.

[44] P. Khongprom, T. Whansungnoen, P. Pienduangsri, W. Wanchan, S. Limtrakul, Catalytic Cracking of Heavy Oil from Waste Plastic in Tapered Circulating Fluidized Bed Riser Reactor, E3S Web Conf. 141 (2020) 01012. https://doi.org/10.1051/e3sconf/202014101012.

[45] X. Liu, M. Zhao, S. Hu, W. Ge, Three-dimensional CFD simulation of tapered gas-solid risers by coupling the improved EMMS drag, Powder Technol. 352 (2019) 305–313. https://doi.org/10.1016/j.powtec.2019.04.070.

[46] D.M. Koerich, L.M. da Rosa, Analysis of hydrodynamic effects on biofilm thickness in fluidized-bed tapered bioreactors, Particuology. 58 (2021) 48–57. https://doi.org/10.1016/j.partic.2021.01.011.

[47] Z.-G. Feng, S.G. Musong, Direct numerical simulation of heat and mass transfer of spheres in a fluidized bed, Powder Technol. 262 (2014) 62–70. https://doi.org/10.1016/j.powtec.2014.04.019.

[48] M. Banaei, J. Jegers, M. van Sint Annaland, J.A.M. Kuipers, N.G. Deen, Effect of Superficial Gas Velocity on the Solid Temperature Distribution in Gas Fluidized Beds with Heat Production, Ind. Eng. Chem. Res. 56 (2017) 8729–8737. https://doi.org/10.1021/acs.iecr.7b00338.

[49] P.C. Bisognin, J.M. Fusco, C. Soares, Heat transfer in fluidized beds with immersed surface: Effect of geometric parameters of surface, Powder Technol. 297 (2016) 401–408. https://doi.org/10.1016/j.powtec.2016.04.028.

[50] W. Liu, P. Liu, J.B. Wang, N.B. Zheng, Z.C. Liu, Exergy destruction minimization: A principle to convective heat transfer enhancement, Int. J. Heat Mass Transf. 122 (2018) 11–21. https://doi.org/10.1016/j.ijheatmasstransfer.2018.01.048.

[51] J. Gan, Z. Zhou, A. Yu, Particle scale study of heat transfer in packed and fluidized beds of ellipsoidal particles, Chem. Eng. Sci. 144 (2016) 201–215. https://doi.org/10.1016/j.ces.2016.01.041.

[52] C.-B. Dinh, C.-C. Liao, S.-S. Hsiau, Numerical study of hydrodynamics with surface

heat transfer in a bubbling fluidized-bed reactor applied to fast pyrolysis of rice husk, Adv. Powder Technol. 28 (2017) 419–429. https://doi.org/10.1016/j.apt.2016.10.013.

[53] J. Ngoh, E.W.C. Lim, Effects of particle size and bubbling behavior on heat transfer in gas fluidized beds, Appl. Therm. Eng. 105 (2016) 225–242. https://doi.org/10.1016/j.applthermaleng.2016.05.165.

[54] M.H. Abdel-Aziz, M.Z. El-Abd, M. Bassyouni, Heat and mass transfer in three phase fluidized bed containing high density particles at high gas velocities, Int. J. Therm. Sci. 102 (2016) 145–153. https://doi.org/10.1016/j.ijthermalsci.2015.11.020.

[55] A. Blaszczuk, W. Nowak, J. Krzywanski, Effect of bed particle size on heat transfer between fluidized bed of group b particles and vertical rifled tubes, Powder Technol. 316 (2017) 111–122. https://doi.org/10.1016/j.powtec.2016.12.027.

[56] D. Jia, X. Bi, C.J. Lim, S. Sokhansanj, A. Tsutsumi, Heat transfer in a tapered fluidized bed of biomass particles with pulsed gas flow, Particuology. 42 (2019) 2–14. https://doi.org/10.1016/j.partic.2018.01.007.

[57] H.M. Abdelmotalib, M.A. Youssef, A.A. Hassan, S.B. Youn, I.-T. Im, Numerical study on the wall to bed heat transfer in a conical fluidized bed combustor, Int. J. Precis. Eng. Manuf. 16 (2015) 1551–1559. https://doi.org/10.1007/s12541-015-0205-z.

[58] M. Syamlal, D. Gidaspow, Hydrodynamics of fluidization: Prediction of wall to bed heat transfer coefficients, AIChE J. 31 (1985) 127–135. https://doi.org/10.1002/aic.690310115.

[59] H.M. Abdelmotalib, D.G. Ko, I.-T. Im, A study on wall-to-bed heat transfer in a conical fluidized bed combustor, Appl. Therm. Eng. 99 (2016) 928–937. https://doi.org/10.1016/j.applthermaleng.2016.01.054.

[60] H.M. Abdelmotalib, M.A.M. Youssef, A.A. Hassan, S.B. Youn, I. Im, Influence of the specularity coefficient on hydrodynamics and heat transfer in a conical fluidized bed combustor, Int. Commun. Heat Mass Transf. 75 (2016) 169–176. https://doi.org/10.1016/j.icheatmasstransfer.2016.04.018.

[61] H.M. Abdelmotalib, M.A.M. Youssef, A.A. Hassan, S.B. Youn, I.-T. Im, Numerical study on heat transfer in a conical fluidized bed combustor considering particle elasticity, Int. J. Heat Mass Transf. 92 (2016) 236–243.

https://doi.org/10.1016/j.ijheatmasstransfer.2015.08.069.

[62] G. Gopan, L. Hauchhum, P. Kalita, R. Krishnan, S. Pattanayak, Parametric study of tapered fluidized bed reactor under varied taper angle using TFM, in: 2021: p. 020020. https://doi.org/10.1063/5.0066547.

[63] K. Zhang, S. Wang, Y. Tang, G. Liu, Y. He, Gas pulsation effect on flow behaviors and heat transfer in a tapered fluidized bed, Powder Technol. 361 (2020) 540–547. https://doi.org/10.1016/j.powtec.2019.11.079.

[64] R.P. Levey, A.D.L. Garga, S.C. Jacobs, H.M. Heidt, P.E. Trent, Fluid Bed Conversion of UO3 to UF4, Chem. Eng. Progr. 56 (1960) 43–48.

[65] S. He, H. Sun, C. Hu, J. Li, Q. Zhu, H. Li, Direct reduction of fine iron ore concentrate in a conical fluidized bed, Powder Technol. 313 (2017) 161–168. https://doi.org/10.1016/j.powtec.2017.03.007.

[66] K. Sutherland, Solids Mixing in Gas-Solid Fluidized Beds. Part 1. A Preliminary Comparison of Tapered and Non-Tapered Beds, Trans. Inst. Chem. Eng. 39 (1961) 188–194.

[67] H. Littman, Solids mixing in straight and tapered fluidized beds, AIChE J. 10 (1964) 924–929. https://doi.org/10.1002/aic.690100628.

[68] R. Deiva Venkatesh, J. Chaouki, D. Klvana, Fluidization of cryogels in a conical column, Powder Technol. 89 (1996) 179–186. https://doi.org/10.1016/S0032-5910(96)03181-6.

[69] K. Ridgeway, The Tapering Fluidized Bed—A New Processing Tool, Chem. Process Eng. 6 (1965) 317–321.

[70] Y. Peng, L.T. Fan, Hydrodynamic characteristics of fluidization in liquid-solid tapered beds, Chem. Eng. Sci. 52 (1997) 2277–2290. https://doi.org/10.1016/S0009-2509(97)00061-4.

[71] S. Jing, Q. Hu, J. Wang, Y. Jin, Fluidization of coarse particles in gas – solid conical beds, Chem. Eng. Process. 39 (2000) 379–387. https://doi.org/10.1016/S0255-2701(99)00103-8.

[72] M. Rasteh, F. Farhadi, A. Bahramian, Hydrodynamic characteristics of gas–solid tapered fluidized beds: Experimental studies and empirical models, Powder Technol.

283 (2015) 355–367. https://doi.org/10.1016/j.powtec.2015.06.002.

[73] J.S.N. Murthy, V.S. Reddy, S. Tasleem, D.V. Kumar, C.S. Krishna, T. Sankarshana, Hydrodynamics of gas-solid fluidization in tapered beds, Can. J. Chem. Eng. 87 (2009) 359–374. https://doi.org/10.1002/cjce.20180.

[74] M.H. Khani, Models for prediction of hydrodynamic characteristics of gas–solid tapered and mini-tapered fluidized beds, Powder Technol. 205 (2011) 224–230. https://doi.org/10.1016/j.powtec.2010.09.018.

[75] J. Li, B. Yang, G. Cheng, Affinity adsorption and hydrodynamic behavior in a tapered-bed of upward flow, Biochem. Eng. J. 15 (2003) 185–192. https://doi.org/10.1016/S1369-703X(03)00002-0.

[76] Z. Zhao, J. Zhang, G. Zhang, X. Zeng, X. Liu, G. Xu, Hydrodynamic characterization of a tapered gas–solid bed without a gas distributor, Powder Technol. 256 (2014) 300–309. https://doi.org/10.1016/j.powtec.2014.02.037.

[77] J. Shan, C. Guobin, M. Fan, B. Yu, W. Jinfu, J. Yong, Fluidization of fine particles in conical beds, Powder Technol. 118 (2001) 271–274. https://doi.org/10.1016/S0032-5910(00)00385-5.

[78] T. Maruyama, T. Koyanagi, Fluidization in tapered vessels, Chem. Eng. J. 51 (1993) 121–128. https://doi.org/10.1016/0300-9467(93)80022-G.

[79] D.C. Sau, S. Mohanty, K.C. Biswal, Experimental studies and empirical models for the prediction of bed expansion in gas–solid tapered fluidized beds, Chem. Eng. Process. Process Intensif. 49 (2010) 418–424. https://doi.org/10.1016/j.cep.2010.02.010.

[80] D.C. Sau, S. Mohanty, K.C. Biswal, Bed Fluctuation Ratio for Regular and Irregular Particles in Gas-Solid Tapered Fluidised Beds, Indian Chem. Eng. 51 (2009) 119–128. https://doi.org/10.1080/00194500903123953.

[81] D.C. Sau, S. Mohanty, K.C. Biswal, Minimum fluidization velocities and maximum bed pressure drops for gas–solid tapered fluidized beds, Chem. Eng. J. 132 (2007) 151–157. https://doi.org/10.1016/j.cej.2007.01.036.

[82] D.T.K. Dora, S.R. Panda, Y.K. Mohanty, G.K. Roy, Hydrodynamics of gas–solid fluidization of a homogeneous ternary mixture in a conical bed: Prediction of bed expansion and bed fluctuation ratios, Particuology. 11 (2013) 681–688.

https://doi.org/10.1016/j.partic.2013.02.009.

[83] R.K. Padhi, D.T.K. Dora, Y.K. Mohanty, G.K. Roy, B. Sarangi, Hydrodynamics of three-phase fluidization of homogeneous ternary mixture in a conical conduit — Experimental and statistical analysis, Chinese J. Chem. Eng. 24 (2016) 1335–1343. https://doi.org/10.1016/j.cjche.2016.05.032.

[84] D.C. Sau, S. Mohanty, K.C. Biswal, Critical fluidization velocities and maximum bed pressure drops of homogeneous binary mixture of irregular particles in gas–solid tapered fluidized beds, Powder Technol. 186 (2008) 241–246. https://doi.org/10.1016/j.powtec.2007.12.008.

[85] D.C. Sau, S. Mohanty, K.C. Biswal, Prediction of critical fluidization velocity and maximum bed pressure drop for binary mixture of regular particles in gas–solid tapered fluidized beds, Chem. Eng. Process. Process Intensif. 47 (2008) 2114–2120. https://doi.org/10.1016/j.cep.2007.10.022.

[86] H.G. Kim, I.O. Lee, U.C. Chung, Y.H. Kim, Fluidization Characteristics of Iron Ore Fines of Wide Size Distribution in a Cold Tapered Gas-Solid Fluidized Bed., ISIJ Int. 40 (2000) 16–22. https://doi.org/10.2355/isijinternational.40.16.

[87] M. Wormsbecker, A. Adams, T. Pugsley, C. Winters, Segregation by size difference in a conical fluidized bed of pharmaceutical granulate, Powder Technol. 153 (2005) 72–80. https://doi.org/10.1016/j.powtec.2005.02.006.

[88] S.H. Schaafsma, T. Marx, A.C. Hoffmann, Investigation of the particle flowpattern and segregation in tapered fluidized bed granulators, Chem. Eng. Sci. 61 (2006) 4467–4475. https://doi.org/10.1016/j.ces.2006.01.040.

[89] D. Zhou, S. Dong, H. Wang, H.T. Bi, Minimum Fluidization Velocity of a Three-Phase Conical Fluidized Bed in Comparison to a Cylindrical Fluidized Bed, Ind. Eng. Chem. Res. 48 (2009) 27–36. https://doi.org/10.1021/ie8001974.

[90] Webster, G.H. and Perona, J., The effect of taper angle on the hydrodynamics of a tapered liquid-solid fluidized bed, AIChE Symp. Ser. 86, No. 27 (1990) 104–112.

[91] S. Fang, Y. Wei, L. Fu, G. Tian, H. Qu, Modeling of the Minimum Fluidization Velocity and the Incipient Fluidization Pressure Drop in a Conical Fluidized Bed with Negative Pressure, Appl. Sci. 10 (2020) 8764. https://doi.org/10.3390/app10248764.

[92] S. Fang, Y. Wei, L. Fu, G. Tian, H. Qu, Time-series analysis of the characteristic pressure fluctuations in a conical fluidized bed with negative pressure, Chinese J. Chem. Eng. 32 (2021) 87–99. https://doi.org/10.1016/j.cjche.2020.09.042.

[93] X. Zhang, S. He, H. Sun, Q. Zhu, J. Li, H. Li, Mechanism of surface morphology evolution in the reduction of fine iron ore in a conical fluidized bed reactor, Chem. Eng. Sci. 220 (2020) 115468. https://doi.org/10.1016/j.ces.2019.115468.

[94] L. Kalo, H.J. Pant, M.C. Cassanello, R.K. Upadhyay, Time series analysis of a binary gas-solid conical fluidized bed using radioactive particle tracking (RPT) technique data, Chem. Eng. J. 377 (2019) 119807. https://doi.org/10.1016/j.cej.2018.08.193.

[95] L. Kalo, P. Kamalanathan, H.J. Pant, M.C. Cassanello, R.K. Upadhyay, Mixing and regime transition analysis of liquid-solid conical fluidized bed through RPT technique, Chem. Eng. Sci. 207 (2019) 702–712. https://doi.org/10.1016/j.ces.2019.07.005.

[96] A. Bahramian, The mutual effects between the interparticle forces and mechanical properties on fluidization of TiO2 nanoparticle agglomerates in a conical fluidized bed: nanoindentation and pressure fluctuation analysis, J. Nanoparticle Res. 21 (2019) 196. https://doi.org/10.1007/s11051-019-4640-0.

[97] L.K. Sahoo, S. Sarkar, Experimental Study of Bubble Behavior in a Two-Dimensional Gas–Solid Tapered Fluidized Bed, Ind. Eng. Chem. Res. 60 (2021) 12740–12751. https://doi.org/10.1021/acs.iecr.1c01496.

[98] W. Bai, D. Chu, Y. He, Bubble characteristic of carbon nanotubes growth process in a tapered fluidized bed reactor without a distributor, Chem. Eng. J. 407 (2021) 126792. https://doi.org/10.1016/j.cej.2020.126792.

[99] W. Bai, D. Chu, Y. He, The minimum fluidization velocity and dynamic characteristics of agglomerated carbon nanotube in a tapered fluidized bed at elevated temperature, Chem. Eng. Res. Des. 168 (2021) 239–253. https://doi.org/10.1016/j.cherd.2021.02.014.

[100] W. Bai, D. Chu, F. Wang, Y. He, Research on Fluidization Performance of Different Tapered Fluidized Bed Reactors for Fluidizing Carbon Nanotubes, Ind. Eng. Chem. Res. 59 (2020) 11893–11904. https://doi.org/10.1021/acs.iecr.0c01047.

[101] M. Rasteh, G. Ahmadi, S.H. Hosseini, Effect of Gaussian size distribution width on

minimum fluidization velocity in tapered gas–solid fluidized beds, Particuology. 66 (2022) 71–84. https://doi.org/10.1016/j.partic.2021.09.005.

[102] R.K. Padhi, D.T.K. Dora, Y.K. Mohanty, G.K. Roy, B. Sarangi, Effect of tapered angle on hydrodynamics of homogenous ternary mixture of regular particles in a three-phase tapered fluidized bed, Indian Chem. Eng. 61 (2019) 269–285. https://doi.org/10.1080/00194506.2018.1548950.

[103] T. Hong, E. Jung, D.H. Lee, Segregation of glass beads in three-sectional tapered fluidized beds with ternary system, Powder Technol. 343 (2019) 342–349. https://doi.org/10.1016/j.powtec.2018.11.055.

[104] M. Karimi, B. Vaferi, S.H. Hosseini, M. Rasteh, Designing an Efficient Artificial Intelligent Approach for Estimation of Hydrodynamic Characteristics of Tapered Fluidized Bed from Its Design and Operating Parameters, Ind. Eng. Chem. Res. 57 (2018) 259–267. https://doi.org/10.1021/acs.iecr.7b02869.

[105] S.H. Hosseini, M.A. Moradkhani, M. Rasteh, M. Rahimi, New Smart Models for Minimum Fluidization Velocity Forecasting in the Tapered Fluidized Beds Based on Particle Size Distribution, Ind. Eng. Chem. Res. 60 (2021) 15289–15300. https://doi.org/10.1021/acs.iecr.1c02682.

[106] J.F. Saldarriaga, J. Grace, C.J. Lim, Z. Wang, N. Xu, A. Atxutegi, R. Aguado, M. Olazar, Bed-to-surface heat transfer in conical spouted beds of biomass–sand mixtures, Powder Technol. 283 (2015) 447–454. https://doi.org/10.1016/j.powtec.2015.05.046.

[107] H.M. Abdelmotalib, I.-T. Im, Three dimensional modeling of heat transfer and bed flow in a conical fluidized bed reactor, Int. J. Heat Mass Transf. 106 (2017) 1335–1344. https://doi.org/10.1016/j.ijheatmasstransfer.2016.10.117.

[108] L. Gan, X. Lu, Q. Wang, Experimental and theoretical study on hydrodynamic characteristics of tapered fluidized beds, Adv. Powder Technol. 25 (2014) 824–831. https://doi.org/10.1016/j.apt.2013.12.007.

[109] R. Katiyar, Conical fluidized beds - Case Study for a gas-solid system involving coarse particles, (2017) 864–869.

[110] K.C. Biswal, T. Bhowmik, G.K. Roy, Prediction of pressure drop for a conical fixed bed of spherical particles in gas—solid systems, Chem. Eng. J. 29 (1984) 47–50.

https://doi.org/10.1016/0300-9467(84)80006-4.

[111] K.C. Biswal, T. Bhowmik, G.K. Roy, Prediction of minimum fluidization velocity for gas-solid fluidization of regular particles in conical vessels, Chem. Eng. J. 30 (1985) 57–62. https://doi.org/10.1016/0300-9467(85)80007-1.

[112] R. Kaewklum, V.I. Kuprianov, Theoretical and experimental study on hydrodynamic characteristics of fluidization in air–sand conical beds, Chem. Eng. Sci. 63 (2008) 1471–1479. https://doi.org/10.1016/j.ces.2007.11.033.

[113] J.S. Rao, D.N. Reddy, Fluidisation Characteristics of Tapered Fluidized Bed Reactors with Different Distributors for PFBG Application, J. Inst. Eng. Ser. C. 93 (2012) 63–73. https://doi.org/10.1007/s40032-011-0011-z.

[114] K.C. Biswal, B.B. Samal, G.K. Roy, Dynamics of Gas-Solid Fluidization of Regular Particles in Conical Vessels, J. Inst. Eng. 65 (1984). http://dspace.nitrkl.ac.in/dspace/handle/2080/968.

[115] K.C. Biswal, G. k Roy, Prediction of Fluctuation Ratio for Gas-Solid Fluidization of Irregular Particles in Conical Vessels, J. Inst. Eng. 65 (1985). http://dspace.nitrkl.ac.in/dspace/handle/2080/1263.

[116] K.M. Ali, A.N. Ghanim, Hydrodynamic Simulation Behavior of Two Phase Conical Fluidized Column, Int. J. Sci. Eng. Res. 5 (2014). http://www.ijser.org.

[117] D.C. Sau, S. Mohanty, K.C. Biswal, Correlations for critical fluidization velocity and maximum bed pressure drop for heterogeneous binary mixture of irregular particles in gas-solid tapered fluidized beds, Chem. Eng. Process. Process Intensif. 47 (2008) 2386–2390. https://doi.org/10.1016/j.cep.2007.11.003.

[118] K.C. Biswal, S. Sahu, G.K. Roy, Prediction of the fluctuation ratio for gas—solid fluidization of regular particles in a conical vessel, Chem. Eng. J. 23 (1982) 97–99. https://doi.org/10.1016/0300-9467(82)85011-9.

[119] R.K. Singh, G.K. Roy, A. Suryanarayana, Prediction of Fluctuation Ratio for Binary Mixtures of Non-Spherical Particles in Conical Beds, Indian Chem. Eng. 33 (1991). http://dspace.nitrkl.ac.in/dspace/handle/2080/978.

[120] Y.F. Shi, Y.S. Yu, L.T. Fan, Incipient fluidization condition for a tapered fluidized bed, Ind. Eng. Chem. Fundam. 23 (1984) 484–489. https://doi.org/10.1021/i100016a018.

[121] D.C. Sau, S. Mohanty, K.C. Biswal, Minimum fluidization velocity at elevated temperature in tapered fluidized bed, Chem. Eng. Process. Process Intensif. 47 (2008) 2391–2394. https://doi.org/10.1016/j.cep.2007.11.016.

[122] R. Khodabandehlou, H. Askaripour, A. Molaei Dehkordi, Numerical investigation of gas bubble behavior in tapered fluidized beds, Particuology. 38 (2018) 152–164. https://doi.org/10.1016/j.partic.2017.05.013.

[123] P.P. Thant, P.S. Robi, P. Mahanta, Inclined Fluidized Bed Dryer Performance in Energy Saving Option, Int. J. Sci. Eng. Technol. Res. (2018).

[124] S. Firouzi, M.R. Alizadeh, D. Haghtalab, Energy consumption and rice milling quality upon drying paddy with a newly-designed horizontal rotary dryer, Energy. 119 (2017) 629–636. https://doi.org/10.1016/j.energy.2016.11.026.

[125] M.A. Islam, M.H.T. Mondal, M. Akhtaruzzaman, M.A.M. Sheikh, M.M. Islam, M.A. Haque, M.S.H. Sarker, Energy, exergy, and milling performance of parboiled paddy: an industrial LSU dryer, Dry. Technol. (2021) 1–15. https://doi.org/10.1080/07373937.2021.1919701.

[126] M. Yahya, A. Fudholi, K. Sopian, Energy and exergy analyses of solar-assisted fluidized bed drying integrated with biomass furnace, Renew. Energy. 105 (2017) 22–29. https://doi.org/10.1016/j.renene.2016.12.049.

[127] R. Sivakumar, R. Saravanan, A. Elaya Perumal, S. Iniyan, Fluidized bed drying of some agro products – A review, Renew. Sustain. Energy Rev. 61 (2016) 280–301. https://doi.org/10.1016/j.rser.2016.04.014.

[128] S. Das, P. Mahanta, A. Sinha, L. Mishra, Performance Study of an Inclined Bubbling Fluidized Bed Dryer During Cashew Nut Drying, in: 2022: pp. 71–82. https://doi.org/10.1007/978-981-16-4489-4_8.

[129] Y. Yan, B. Qi, W. Zhang, X. Wang, Q. Mo, Investigations into the drying kinetics of biomass in a fluidized bed dryer using electrostatic sensing and digital imaging techniques, Fuel. 308 (2022) 122000. https://doi.org/10.1016/j.fuel.2021.122000.

[130] O. Taskin, A. Polat, A.B. Etemoglu, N. Izli, Energy and exergy analysis, drying kinetics, modeling, microstructure and thermal properties of convective-dried banana slices, J. Therm. Anal. Calorim. (2021). https://doi.org/10.1007/s10973-021-10639-z.

[131] A. Anand, Y. Gareipy, V. Raghavan, Fluidized bed and microwave-assisted fluidized bed drying of seed grade soybean, Dry. Technol. 39 (2021) 507–527. https://doi.org/10.1080/07373937.2019.1709495.

[132] M.S.H. Sarker, M. Akhtaruzzaman, M.H.T. Mondal, M.M. Kamal, E.A. Plabon, Evaluation of Drying Characteristics, Milling Performance and Nutritional Quality: The Case of Aromatic Rice, J. Food Process. Preserv. (2021). https://doi.org/10.1111/jfpp.16275.

[133] S. Nanvakenari, K. Movagharnejad, A. Latifi, Evaluating the fluidized-bed drying of rice using response surface methodology and artificial neural network, LWT. 147 (2021) 111589. https://doi.org/10.1016/j.lwt.2021.111589.

[134] K. Sandip, H.K. Paliwal, A.K. Sharma, Comprehensive study of fluidization characteristics and variations of moisture content in fluidized bed drying of soybean, IOP Conf. Ser. Mater. Sci. Eng. 1116 (2021) 012069. https://doi.org/10.1088/1757-899X/1116/1/012069.

[135] K. Luthra, S. Sadaka, G. Atungulu, Effects of ambient air dehumidification, air temperature, and drying duration on rough rice quality and pasting properties using fluidized bed and fixed bed dryers, Cereal Chem. 98 (2021) 968–979. https://doi.org/10.1002/cche.10438.

[136] R. Barathiraja, P. Thirumal, D. Thirumalaikumarasamy, A. Kajavali, M. Ashokkumar, J. Thiyagaraj, Investigation of drying kinetics and qualities of turkey berry in fluidized bed dryer, Mater. Today Proc. 46 (2021) 7711–7718. https://doi.org/10.1016/j.matpr.2021.02.217.

[137] M. Akhtaruzzaman, M.H.T. Mondal, M. Biswas, M.A.M. Sheikh, A.A. Khatun, M.S.H. Sarker, Evaluation of Drying Performance, Energy Consumption, and Quality of Two-Stage Dried Maize Grain, J. Biosyst. Eng. 46 (2021) 151–162. https://doi.org/10.1007/s42853-021-00095-w.

[138] S.S. Sadaka, K. Luthra, G.G. Atungulu, Evaluation of the Performance of a Custom-Made Fluidized Bed Drying System, Appl. Eng. Agric. 34 (2018) 1027–1037. https://doi.org/10.13031/aea.12909.

[139] S. Mujaffar, S. Ramsumair, Fluidized Bed Drying of Pumpkin (Cucurbita sp.) Seeds,

Foods. 8 (2019) 147. https://doi.org/10.3390/foods8050147.

[140] Novrinaldi, S.A. Putra, A. Sitorus, Characteristic of Unhulled Rice Drying on Swirling Fluidized Bed Dryer, IOP Conf. Ser. Mater. Sci. Eng. 1096 (2021) 012054. https://doi.org/10.1088/1757-899X/1096/1/012054.

[141] M. Tohidi, M. Sadeghi, M. Torki-Harchegani, Energy and quality aspects for fixed deep bed drying of paddy, Renew. Sustain. Energy Rev. 70 (2017) 519–528. https://doi.org/10.1016/j.rser.2016.11.196.

[142] M. Khanali, A. Khakpour Giglou, S. Rafiee, Model development for shelled corn drying in a plug flow fluidized bed dryer, Eng. Agric. Environ. Food. 11 (2018) 1–8. https://doi.org/10.1016/j.eaef.2017.09.002.

[143] H. Darvishi, M.H. Khoshtaghaza, S. Minaei, Effects of fluidized bed drying on the quality of soybean kernels, J. Saudi Soc. Agric. Sci. 14 (2015) 134–139. https://doi.org/10.1016/j.jssas.2013.09.002.

[144] R. Pourbagher, M.H. Rahmati, M.R. Alizadeh, Air temperature and final grain moisture effects on drying time and milling quality in two types of fluidized bed dryer, Agric. Eng. Int. CIGR J. (2016).

[145] Y. Tatemoto, R. Ogawa, H. Iyota, Measurement of constant drying rate of wet material placed in a fluidized bed of inert particles under reduced pressure, Dry. Technol. 36 (2018) 1380–1386. https://doi.org/10.1080/07373937.2017.1403926.

[146] M. Ranjbaran, B. Emadi, D. Zare, CFD Simulation of Deep-Bed Paddy Drying Process and Performance, Dry. Technol. 32 (2014) 919–934. https://doi.org/10.1080/07373937.2013.875561.

[147] G. Srinivas, S.K. Thamida, Y. Pydi Setty, Simulation and validation of a model for a batch wall heated fluidized bed dryer, Powder Technol. 270 (2015) 368–377. https://doi.org/10.1016/j.powtec.2014.10.011.

[148] M.S.H. Sarker, M.N. Ibrahim, N.A. Aziz, M.S. Punan, Application of simulation in determining suitable operating parameters for industrial scale fluidized bed dryer during drying of high impurity moist paddy, J. Stored Prod. Res. 61 (2015) 76–84. https://doi.org/10.1016/j.jspr.2014.12.004.

[149] V. Sutar, H. and Kumar, The Effect Of Distributor Design On Hydrodynamics Of

Conical Fluidized Bed Dryer, (2012).

[150] S. Hematian, F. Hormozi, Drying kinetics of coated sodium percarbonate particles in a conical fluidized bed dryer, Powder Technol. 269 (2015) 30–37. https://doi.org/10.1016/j.powtec.2014.08.050.

[151] C. Srinivasakannan, A. Al Shoaibi, N. Balasubramanian, Continuous fluidized bed drying with and without internals: Kinetic model, Chem. Biochem. Eng. Q. (2012).

[152] Phyu Phyu Thant, P. Mahanta, P. S. Robi, Effect of Spirals in an Inclined Bubbling Fluidized Bed Paddy Dryer, Int. J. Eng. Res. V4 (2015). https://doi.org/10.17577/IJERTV4IS060466.

[153] E.K. Akpinar, Energy and exergy analyses of drying of red pepper slices in a convective type dryer, Int. Commun. Heat Mass Transf. 31 (2004) 1165–1176. https://doi.org/10.1016/j.icheatmasstransfer.2004.08.014.

[154] E. Kavak Akpinar, A. Midilli, Y. Bicer, Energy and exergy of potato drying process via cyclone type dryer, Energy Convers. Manag. 46 (2005) 2530–2552. https://doi.org/10.1016/j.enconman.2004.12.008.

[155] E.K. Akpinar, A. Midilli, Y. Bicer, The first and second law analyses of thermodynamic of pumpkin drying process, J. Food Eng. 72 (2006) 320–331. https://doi.org/10.1016/j.jfoodeng.2004.12.011.

[156] T. Nazghelichi, M.H. Kianmehr, M. Aghbashlo, Thermodynamic analysis of fluidized bed drying of carrot cubes, Energy. 35 (2010) 4679–4684. https://doi.org/10.1016/j.energy.2010.09.036.

[157] M.S.H. Sarker, M.N. Ibrahim, N. Abdul Aziz, M.S. Punan, Energy and exergy analysis of industrial fluidized bed drying of paddy, Energy. 84 (2015) 131–138. https://doi.org/10.1016/j.energy.2015.02.064.

[158] O. Corzo, N. Bracho, A. Vásquez, A. Pereira, Energy and exergy analyses of thin layer drying of coroba slices, J. Food Eng. 86 (2008) 151–161. https://doi.org/10.1016/j.jfoodeng.2007.05.008.

[159] H. Darvishi, M. Azadbakht, B. Noralahi, Experimental performance of mushroom fluidized-bed drying: Effect of osmotic pretreatment and air recirculation, Renew. Energy. 120 (2018) 201–208. https://doi.org/10.1016/j.renene.2017.12.068.

[160] Y. Devani, P.S. Yelamarthi, Energetic and exergetic analyses of Barnyard millet drying using continuous multistage fluidized bed dryer, J. Food Process Eng. 42 (2019). https://doi.org/10.1111/jfpe.13247.

[161] B. Pattanayak, S.S. Mohapatra, H.C. Das, Energy and exergy analyses of paddy drying process in a vertical fluidised bed dryer, Int. J. Exergy. 28 (2019) 113. https://doi.org/10.1504/IJEX.2019.097975.

[162] S.U. Handayani, I.S. Atmanto, F.T. Putri, S. Fujiwara, Energy and exergy analysis economic of continuous vibrating fluidized bed drying on celery drying, J. Phys. Conf. Ser. 1524 (2020) 012030. https://doi.org/10.1088/1742-6596/1524/1/012030.

[163] K. Luthra, S. Sadaka, Energy and Exergy Analysis of Rough Rice Drying in a Fluidized Bed and Fixed Bed with Ambient Air Dehumidification, in: 2021 ASABE Annu. Int. Virtual Meet. July 12-16, 2021, American Society of Agricultural and Biological Engineers, St. Joseph, MI, 2021. https://doi.org/10.13031/aim.202100225.

[164] G.M. da Silva, A.G. Ferreira, R.M. Coutinho, C.B. Maia, Energy and exergy analysis of the drying of corn grains, Renew. Energy. 163 (2021) 1942–1950. https://doi.org/10.1016/j.renene.2020.10.116.

[165] E. Çelik, N. Parlak, Y. Çay, EXERGY AND ENERGY ANALYSES OF CORN DRYING PROCESS: AN EXPERIMENTAL STUDY IN A LABORATORY-SCALE DRYER, Heat Transf. Res. 52 (2021) 1–13. https://doi.org/10.1615/HeatTransRes.2021036125.

[166] M.H.T. Mondal, M.A. Hossain, M.A.M. Sheikh, Md. Akhtaruzzaman, M.S.H. Sarker, Energetic and exergetic investigation of a mixed flow dryer: A case study of maize grain drying, Dry. Technol. 39 (2021) 466–480. https://doi.org/10.1080/07373937.2019.1709077.

[167] M. Beigi, M. Torki, F. Khoshnam, M. Tohidi, Thermodynamic and environmental analyses for paddy drying in a semi-industrial dryer, J. Therm. Anal. Calorim. 146 (2021) 393–401. https://doi.org/10.1007/s10973-020-09968-2.

[168] I. Golpour, M. Kaveh, R.A. Chayjan, R.P.F. Guiné, Energetic and exergetic analysis of a convective drier: A case study of potato drying process, Open Agric. 5 (2020) 563–572. https://doi.org/10.1515/opag-2020-0058.

[169] S. Suherman, E.E. Susanto, A.W. Zardani, N.H.R. Dewi, H. Hadiyanto, Energy–exergy analysis and mathematical modeling of cassava starch drying using a hybrid solar dryer, Cogent Eng. 7 (2020) 1771819. https://doi.org/10.1080/23311916.2020.1771819.

[170] Z. Wang, Experimental studies and CFD simulations of conical spouted bed hydrodynamics, University of British Columbia, 2006. https://doi.org/10.14288/1.0059036.

[171] C.K.K. Lun, S.B. Savage, D.J. Jeffrey, N. Chepurniy, Kinetic theories for granular flow: inelastic particles in Couette flow and slightly inelastic particles in a general flowfield, J. Fluid Mech. 140 (1984) 223–256. https://doi.org/10.1017/S0022112084000586.

[172] D.G. Schaeffer, Instability in the evolution equations describing incompressible granular flow, J. Differ. Equ. 66 (1987) 19–50. https://doi.org/10.1016/0022-0396(87)90038-6.

[173] P.C. Johnson, R. Jackson, Frictional–collisional constitutive relations for granular materials, with application to plane shearing, J. Fluid Mech. 176 (1987) 67. https://doi.org/10.1017/S0022112087000570.

[174] D.J. Gunn, Transfer of heat or mass to particles in fixed and fluidised beds, Int. J. Heat Mass Transf. 21 (1978) 467–476. https://doi.org/10.1016/0017-9310(78)90080-7.

[175] F.B. Pidduck, S. Chapman, T.G. Cowling, The Mathematical Theory of Non-Uniform Gases, Math. Gaz. 23 (1939) 488. https://doi.org/10.2307/3607024.

[176] P. Singh, P. Kalita, P. Mahanta, Experimental study of food grain drying in a gas–solid vortex reactor, Dry. Technol. (2020) 1–13. https://doi.org/10.1080/07373937.2020.1835948.

[177] Y. a. Çengel, Thermodynamics: An Engineering Approach, McGraw-Hill. (2004).

[178] A. Midilli, H. Kucuk, Energy and exergy analyses of solar drying process of pistachio, Energy. 28 (2003) 539–556. https://doi.org/10.1016/S0360-5442(02)00158-5.

[179] P.A. Idah, J.J. Musa, S.T. Olaleye, Effect of Temperature and Drying Time on Some Nutritional Quality Parameters of Dried Tomatoes, Au J. T. 14 (2010) 25–32.

[180] P. Basu, P.K. Nag, An investigation into heat transfer in circulating fluidized beds, Int. J. Heat Mass Transf. (1987). https://doi.org/10.1016/0017-9310(87)90230-4.

[181] P. Basu, COMBUSTION AND GASIFICATION IN FLUIDIZED BEDS, n.d.

[182] P. Basu, L. Cheng, K. Cen, Heat transfer in a pressurized circulating fluidized bed, Int. J. Heat Mass Transf. 39 (1996) 2711–2722. https://doi.org/10.1016/0017-9310(95)00362-2.

[183] P. Sahoo, A. Sahoo, A Comparative Study on Effect of Different Parameters of CFD Modeling for Gas–Solid Fluidized Bed, Part. Sci. Technol. 33 (2015) 273–289. https://doi.org/10.1080/02726351.2014.952393.

[184] P. Sahoo, A. Sahoo, Computational and experimental studies on bed dynamics of a gas–solid fluidized bed using Geldart-A particle: A comparison, Part. Sci. Technol. 35 (2017) 688–698. https://doi.org/10.1080/02726351.2016.1194348.

[185] S. Sari, G. Kulah, M. Koksal, Characterization of gas–solid flow in conical spouted beds operating with heavy particles, Exp. Therm. Fluid Sci. 40 (2012) 132–139. https://doi.org/10.1016/j.expthermflusci.2012.02.008.

[186] D.T.K. Dora, Y.K. Mohanty, G.K. Roy, Hydrodynamics of three-phase fluidization of a homogeneous ternary mixture of irregular particles, Chem. Eng. Sci. 79 (2012) 210–218. https://doi.org/10.1016/j.ces.2012.04.035.

[187] R.K. Padhi, D.T.K. Dora, Y.K. Mohanty, G.K. Roy, B. Sarangi, Prediction of bed pressure drop, fluctuation and expansion ratios for three-phase fluidization of ternary mixtures of dolomite in a conical conduit, Cogent Eng. 3 (2016) 1181821. https://doi.org/10.1080/23311916.2016.1181821.

[188] A. Reyes, M. Eckholt, P.I. Alvarez, Drying and Heat Transfer Characteristics for a Novel Fluidized Bed Dryer, Dry. Technol. 22 (2004) 1869–1895. https://doi.org/10.1081/DRT-200032837.

[189] F.T. Ademiluyi, M.F.N. Abowei, Y.T. Puyate, S.C. Achinewhu, Effects of Drying Parameters on Heat Transfer during Drying of Fermented Ground Cassava in a Rotary Dryer, Dry. Technol. 28 (2010) 550–561. https://doi.org/10.1080/07373931003622669.

[190] V.S.S. Prasad, A. Hymavathi, V.R. Babu, T. Longvah, Nutritional composition in relation to glycemic potential of popular Indian rice varieties, Food Chem. 238 (2018) 29–34. https://doi.org/10.1016/j.foodchem.2017.03.138.

[191] D.K. Verma, P.P. Srivastav, Proximate Composition, Mineral Content and Fatty Acids Analyses of Aromatic and Non-Aromatic Indian Rice, Rice Sci. 24 (2017) 21–31.

https://doi.org/10.1016/j.rsci.2016.05.005.

[192] A. Abbas, S. Murtaza, F. Aslam, A. Khawar, S. Rafique, S. Naheed, Effect of Processing on Nutritional Value of Rice (Oryza sativa), World J. Med. Sci. 6 (2011) 68–73.

[193] E. Cho, J. Lee, K. Park, S. Lee, Effects of Heat Pretreatment on Lipid and Pigments of Freeze-Dried Spinach, J. Food Sci. 66 (2008) 1074–1079. https://doi.org/10.1111/j.1365-2621.2001.tb16083.x.

[194] G.P. Savage, P.C. Dutta, M.T. Rodriguez-Estrada, Cholesterol oxides: their occurrence and methods to prevent their generation in foods, Asia Pac. J. Clin. Nutr. 11 (2002) 72–78. https://doi.org/10.1046/j.1440-6047.2002.00270.x.

[195] T. Nazghelichi, M. Aghbashlo, M.H. Kianmehr, M. Omid, Prediction of Energy and Exergy of Carrot Cubes in a Fluidized Bed Dryer by Artificial Neural Networks, Dry. Technol. 29 (2011) 295–307. https://doi.org/10.1080/07373937.2010.494237.

[196] I. Dincer, A.Z. Sahin, A new model for thermodynamic analysis of a drying process, Int. J. Heat Mass Transf. 47 (2004) 645–652. https://doi.org/10.1016/j.ijheatmasstransfer.2003.08.013.

[197] M. Yahya, Performance Analysis of Solar Assisted Fluidized Bed Dryer Integrated Biomass Furnace with and without Heat Pump for Drying of Paddy, Int. J. Photoenergy. 2016 (2016) 1–17. https://doi.org/10.1155/2016/3801918.

[198] P. Singh, Thermal and hydrodynamic studies of a rotating fluidized bed dryer with static geometry, 2021.

[199] J.R. Pati, Drying of granular materials in rotating fluidized bed in a static geometry (RFB-SG), 2016.

[200] P. Basu, Combustion and Gasification in Fluidized Beds, Taylor & Francis Group, LLC, Halifax, Nova Scotia, 2006.

APPENDICES

Appendix A

Design of Distributor Plate

The distributor was fabricated based on the design procedure described by Kunii and Levenspiel [13] and Basu [200]. It was a straight hole orifice type of distributor. The design considerations are given below:

Bed inventory, I = 5 kg

Operating velocity, U_{op} = 3 m/s

Voidage at minimum fluidization, ε_{mf} = 0.5

The bottom diameter of beds (D_0) = 150 mm

Top diameter of beds (D_1) = 150 mm, 254.8 mm and 360 mm

Axial height of beds = 1200 mm

Inlet cross-sectional area of the bed, (A_c) = $\frac{\pi}{4} r_0^2$

$= \pi/4\ (0.075)^2$

$= 0.028\ m^2$

Density of the solid particle (sand), ρ_s = 2660 kg/m^3

Density of air, ρ_g = 1.225 kg/m^3

Acceleration due to gravity, g = 9.81 m/s^2

Height of the bed at minimum fluidization (H_{mf}):

$$H_{mf} = \frac{\Delta P}{(1-\varepsilon_{mf}) \times \rho_s \times g} = \frac{I \times g / A_c}{(1-\varepsilon_{mf}) \times \rho_s \times g} = \frac{I}{A_c \times (1-\varepsilon_{mf}) \times \rho_s} \quad \text{(A.1)}$$

$= 0.137$ m

(i) Bed pressure drop (ΔP_b):

$$\Delta P_b = \rho_s \times g \times H_{mf} \times \left(1 - \varepsilon_{mf}\right) \tag{A.2}$$

$$\Delta P_b = 1747.16 \text{ N/m}^2$$

(ii) Minimum distributor pressure drops for uniform distribution (ΔP_D) [13]:

$$\Delta P_D = 0.15\ \Delta P_b \tag{A.3}$$

$$\Delta P_D = 349.43 \text{ N/m}^2$$

(iii) Thickness of the distributor plate (t) = 5 mm = 0.005 m

(iv) Orifice diameter (d_{or}) = 4 mm = 0.004 m

(v) Orifice discharge coefficient (C_D):

$$C_D = 0.82\left(t/d_{or}\right)^{0.13} \tag{A.4}$$

$$C_D = 0.923$$

(vi) Gas velocity through the Orifice (U_{or}):

$$U_{or} = C_D \times \left(2 \times \Delta P_D / \rho_g\right) \tag{A.5}$$

$$U_{or} = 20.37 \text{ m/s}$$

(vii) Number of orifices per square meter of the distributor (N_{or}):

$$N_{or} = \left(U_{op}/U_{or}\right) \times \left(1/A_{or}\right) = \left(U_{op}/U_{or}\right) \times \left(4/\pi d_{or}^2\right) \tag{A.6}$$

$$N_{or} = 9568.43/\text{m}^2$$

(viii) Total number of holes on perforated distributor = $N_{or} \times A_b$ (A.7)

Total number of holes = 591

(ix) Pitch of orifice in the distributor = $\left(1/N_{or}\right)^{1/2}$ (A.8)

= 5 mm

(x) Open area in the distributor = $\pi/4 \times d_{or}^2 \times$ No. of holes (A.9)

= 2.86× 10^{-3} m^2

(xi) Percentage opening = $\frac{\text{Open area in the distributor}}{A_c} \times 100\%$ (A.10)

= 24.16%

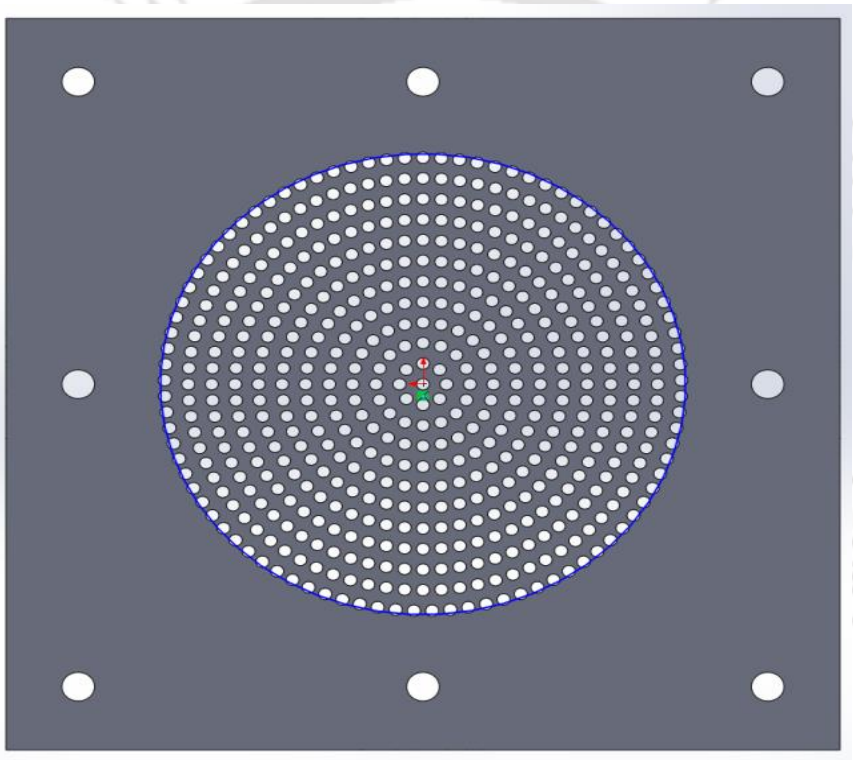

Figure A.1: Design of distributor plate

Appendix B

Measurement of Mean Particle Size of Sand

The actual size and shape of sand particles are different in practice. So, there is a procedure to measure the actual size of a particle. In order to measure the mean size of the particles, the procedure adopted by Kunii and Levenspiel [13] has been followed.

In this context, the following assumptions are to be made

1. Volume remains the same.
2. The surface area remains the same.

Now, let there be:

n_1: Particles of diameter d_1

n_2: Particles of diameter d_2

n_3: Particles of diameter d_3

and so on.

From assumption no. 1:

$$N \times \frac{\pi \bar{d}_p^3}{6} = n_1 \frac{\pi d_1^3}{6} + n_2 \frac{\pi d_2^3}{6} + n_3 \frac{\pi d_3^3}{6} + ... \quad \text{(B.1)}$$

Where N is the number of replaced, uniformly sized particles of diameter $\overline{d_p}$,

$$N \times \bar{d}_p^3 = n_1 \times d_1^3 + n_2 \times d_2^3 + n_3 \times d_3^3 + ... \quad \text{(B.2)}$$

From assumption no. 2:

$$N \times \pi \bar{d}_p^3 = n_1 \pi d_1^2 + n_2 \pi d_2^2 + n_3 \pi d_3^2 + ... \quad \text{(B.3)}$$

$$N \times \bar{d}_p^2 = n_1 \times d_1^2 + n_2 \times d_2^2 + n_3 \times d_3^2 + ... \quad \text{(B.4)}$$

Let X_1 be the weight fraction of solids of diameter d_1.

Therefore,

$$X_1 = \frac{\frac{n_1 \times \bar{d}_1^3}{6} \times \rho_s}{\frac{N \times \bar{d}_p^3}{6} \times \rho_s} = \frac{n_1 \times \bar{d}_1^3}{N \times \bar{d}_p^3} \quad \text{(B.5)}$$

where, ρ_s represents the density of sand.

Similarly,

$$X_2 = \frac{n_2 \times \bar{d}_2^{\,3}}{N \times \bar{d}_p^{\,3}} \tag{B.6}$$

Hence,

$$\begin{aligned} n_1 \times d_1^{\,2} &= X_1 \times N \times \bar{d}_p^{\,3} / d_1 \\ n_2 \times d_2^{\,2} &= X_2 \times \bar{d}_p^{\,3} / d_2 \end{aligned} \tag{B.7}$$

$$\begin{aligned} N \times \bar{d}_p^{\,2} &= n_1 \times d_1^{\,2} + n_2 \times d_2^{\,2} + n_3 \times d_3^{\,2} + \ldots\ldots\ldots \\ &= X_1 \times N \times \frac{\bar{d}_p^{\,3}}{\bar{d}_1} + X_2 \times N \times \frac{\bar{d}_p^{\,3}}{\bar{d}_2} + X_3 \times N \times \frac{\bar{d}_p^{\,3}}{\bar{d}_3} \end{aligned} \tag{B.8}$$

$$\text{Or, } \frac{1}{\bar{d}_p} = \frac{X_1}{d_1} + \frac{X_2}{d_2} + \frac{X_3}{d_3} + \ldots\ldots\ldots\ldots \tag{B.9}$$

$$\text{Or, } \frac{1}{\bar{d}_p} = \sum \frac{X_i}{d_i} \tag{B.10}$$

$$\text{Or, } \bar{d}_p = \frac{1}{\sum \frac{X_i}{d_i}} \tag{B.11}$$

Table B.1 Measurement of particle size

Mesh (BSS)	Mean particle Size (d_i), μm	Weight in grams	Weight fraction (X_i)	X_i / d_i
22-25	649	350	0.350	0.539×10^{-3}
25-30	549.5	320	0.320	0.582×10^{-3}
30-36	461	100	0.100	0.216×10^{-3}
36-44	388	50	0.050	0.128×10^{-3}
44-52	325.5	80	0.080	0.245×10^{-3}
52-60	274	160	0.160	0.583×10^{-3}

Hence, using the equation (B.11), the mean particle size has been calculated and found to be 435 μm.

Appendix C

Specifications of different types of equipment/instruments used

Table C.1 Specification of instruments

Equipments/ Instruments	Specifications
Twin Lobe Blower	Serial No. – 0503468 Model – 710 Capacity- 1275 M3/HP Pressure - 2000 mm of Hg Speed - 1300 rpm Flow rate – 1275 m^3/hr Manufacturer – Everest Transmission
Motor for blower	Primo 3 phase induction motor Power - 20 HP Speed - 1400 rpm Amperes 27.6 Voltage – 445 volts 50 Hz, Manufacturer - Kirloskar
Weighing balance	Model: SP/p1s-15-FLP Measuring range: Max-15 kg, min-0.04 kg Error - 2 gm Manufacturer - M/s. Shyaam Switchgears Pvt. Ltd.
Autotransformer	Output: 0 – 270 Volts Input – 240 Volts Capacity – 6 amps Manufacturer - Varivolt
Sieve machine for particle size	Manufacturer: Scientific Engineering Corporation
Installation of Orifice plate with U-tube water-filled manometer	In-house fabrication
Thermocouple sensor	Chromel-Alumel (K-type)
Non-contact type thermometer	Infrared
Thermocouple calibrator with a constant temperature bath	Manufacturer: Julabo
DC voltage supply	Model: Beetek-3005 Output voltage range: 0 to 30V, 5A

Ceramic Band Heater	110 mm ID × 100 mm L × 1.25 kW × 240 V
Fine wire mesh and cigarette filter	-
Digital grain moisture meter	Make: Indosaw, model: Handy data logging moisture meter, the accuracy of ±0.5
Milling machine	-
Gasket	High pressure
Data acquisition system	Agilent 34970A (Data acquisition switch unit with multiplexer)

Appendix D

Calibration of Thermocouple

The K-type thermocouples were used for the experimental analysis in order to measure the temperature across the risers. These thermocouples were connected to the data acquisition system (DAS) for displaying temperature via a multiplexer. Before the experiments were carried out, pre-calibration of thermocouples was performed to minimize standard measurements error. The error was determined against the standard temperature measurements obtained from the oil temperature bath. One end of the thermocouple was immersed in the oil bath, and the temperature was varied, while the other end of the thermocouple was connected to the data acquisition system. The readings obtained from the oil bath and the data acquisition system were recorded and plotted for calibration. The calibration curve is shown below.

Table D.1 Temperature readings for calibration of thermocouples

Sl. No.	Oil Temperature, °C	Reference Temperature, °C	Temperature difference (X_i)
1	32.9	32.1	0.8
2	34.5	33.7	0.8
3	37	36.4	0.6
4	40.5	39.6	0.9
5	42.6	41.7	0.9
6	45.5	44.9	0.6
7	48	47.5	0.5
8	50.6	50.2	0.4
9	54.5	54.1	0.4
10	60.3	60	0.3
11	64	63.5	0.5
12	67.4	66.8	0.6
13	70.8	70.4	0.4
14	77	76.2	0.8
15	81	80.5	0.5

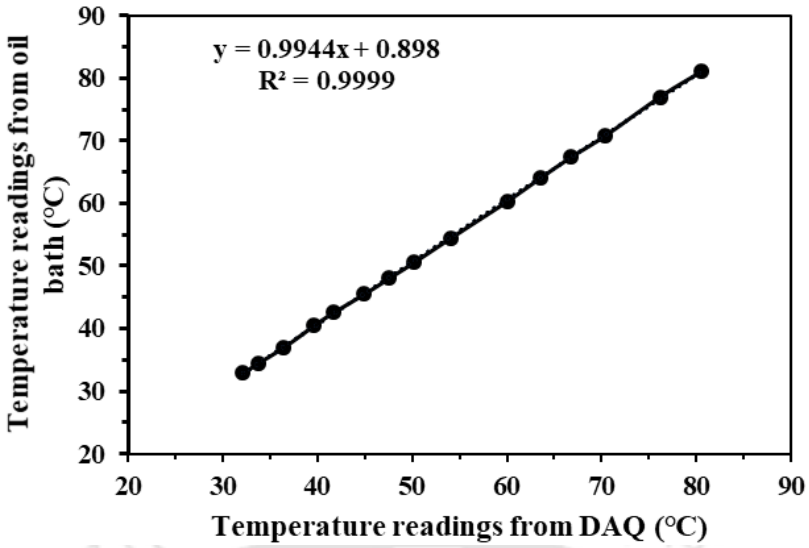

Figure D1: Calibration curve for temperature readings

Appendix - E

Uncertainty Analysis

In conducting the experiments, several measuring devices were used, all of which had a degree of uncertainty. The estimation of uncertainty was implemented as an error bar in experimental outcomes. This was calculated using measuring devices such as U-tube manometers, an orifice plate, weighing machines, a data acquisition system and a measuring scale. All of the experiments were repeated three times in order to determine the percentage of variance that occurs during repeated experiments under the same operating conditions for overall uncertainty measurement, considering the following parameters with uncertainty values in Table E.1.

Table E.1 Experimental parameters with uncertainty values

Experimental parameters	Uncertainty values
Orifice	± 0.5 mm
Manometer	± 0.2 mm
Temperature	± 0.5 °C
Distributor plate	± 0.6 % opening area
Centre to centre pressure tapings	± 1 mm
Loss of inventory	± 1 gm
Visual Error	± 0.5
Bulk temperature calculation	± 1°C
Thermocouple temperature measurement error	± 0.5 °C
Air flow rate	± 1.5
Temperature	± 1.0
Air humidity	± 2.5
Initial moisture content	± 3.5
Final moisture content	± 0.5
Blower	± 0.05

Uncertainty analysis of pressure drop:

Individual uncertainties are

$$\rho_s = 2600 \pm 5\ \text{kg/m}^3$$

$$\rho_g = 1.225 \pm 0.2\ \text{kg/m}^3$$

$$\Delta H = \pm\ 0.002\ \text{m}$$

$$g = 9.81\ \text{m/s}^2$$

Pressure drop is calculated by the following expression

$$\Delta P = \left(\rho_s - \rho_g\right) \times g \times \Delta H \tag{E.1}$$

$$\Delta P = f(\Delta H) \tag{E.2}$$

The overall uncertainty associated with the pressure drop was

$$U_{\Delta P} = \pm \sqrt{\left(\frac{\partial \Delta P}{\partial (\Delta H)}\right)^2 \times (\Delta H)^2} \times 100 \tag{E.3}$$

So, overall uncertainty, $U_{\Delta P}$ = ± 5.43%

Uncertainty analysis in calculating the bed expansion ratio:

The bed expansion ratio was calculated by the following relationship

$$R = \frac{H_{max}}{H_s} \tag{E.4}$$

where,

H_{max} = Maximum height up to which solid particle fluidized

H_s = Initial static bed height

$$R = f\left(H_{max}, H_s\right) \tag{E.5}$$

$$\frac{\partial R}{\partial H_{max}} = \frac{1}{H_s} \tag{E.6}$$

$$\frac{\partial R}{\partial H_s} = -\frac{H_{max}}{(H_s)^2} \tag{E.7}$$

So, overall uncertainty for bed expansion ratio is given by

$$U_R = \pm\sqrt{\left(\frac{\partial R}{\partial H_{\max}}\right)^2 \times (\Delta H_{\max})^2 + \left(\frac{\partial R}{\partial H_s}\right)^2 \times (\Delta H_s)^2} \times 100 \quad \text{(E.8)}$$

So, overall uncertainty, U_R = ± 2.28%

Uncertainty analysis of moisture content:

The percentage of moisture content (MC) available in the paddy was calculated using Eqns. (E.9) and (E.10).

Moisture content wet basis is

$$MC_{w.b.} = \frac{M_i - M_f}{m_i} \times 100\ \% \quad \text{(E.9)}$$

$$MC_{d.b.} = \frac{M_i - M_f}{m_f} \times 100\ \% \quad \text{(E.10)}$$

where, M_i, M_f, MC_{wb} and MC_{db} are the initial weight of paddy, the final weight of paddy, moisture content of paddy (wet basis) and moisture content of paddy (dry basis), respectively. However, the initial and final weight of paddy particles is denoted by W_i and W_f, respectively. It can be seen that; the moisture content depends on the initial and final weight of paddy particles. Therefore, the equation of moisture content can be written as the function of these two independent variables.

$$MC_{w.b.} = f(W_i, W_f) \quad \text{(E.11)}$$

Hence, uncertainty in the measurement of the MC available in the granular material

$$= \frac{\text{Error}}{MC_{db}} \times 100\ \% \quad \text{(E.12)}$$

Percentage of uncertainty

$$= \pm\sqrt{\left(\frac{a_1}{w_f}\right)^2 + \left(\frac{a_2}{w_i}\right)^2} \times 100\ \% \quad \text{(E.13)}$$

where, a_1 and a_2 are uncertainty associated with w_f and w_i, respectively.

For 1000 g of food grain (Paddy)

$w_f = 640 \pm 8g$ where $a_1 = \pm 8g$

$w_i = 1000 \pm 12g$ where $a_2 = \pm 12g$.

Therefore, the percentage of the uncertainty of MC available in food grain (paddy) is

$$= \pm\sqrt{\left(\frac{8}{640}\right)^2 + \left(\frac{12}{1000}\right)^2} \times 100\ \% \quad = \pm 1.73\%$$

So, overall uncertainty is $\pm$ 1.73%

Uncertainty analysis of heat input to the dryer:

The heat input to the dryer can be expressed by the Equation

$$Q = Vit \times P.F. \times 60 \times 10^{-6} \tag{E.14}$$

$$Q = f(V, i, t) \tag{E.15}$$

$$\frac{\partial Q}{\partial V} = it \tag{E.16}$$

$$\frac{\partial Q}{\partial i} = Vt \tag{E.17}$$

$$\frac{\partial Q}{\partial t} = Vi \tag{E.18}$$

The overall uncertainty of heat input is

$$U_Q = \pm\sqrt{\left(\frac{\partial Q}{\partial V}\right)^2 \times (\Delta V)^2 + \left(\frac{\partial Q}{\partial i}\right)^2 \times (\Delta i)^2 + \left(\frac{\partial Q}{\partial t}\right)^2 \times (\Delta t)^2} \times 100 \tag{E.19}$$

So, overall uncertainty, U_Q = ± 3.25%

List of Publications

From the thesis:

A. Journals:

1. **Das, H.J.,** Mahanta, P., Saikia, R., Aamir, M.S., 2020. Performance evaluation of drying characteristics in conical bubbling fluidized bed dryer, ***Powder Technology*, *(Elsevier)***, 374, p. 534-543, https://doi.org/10.1016/j.powtec.2020.06.051.
2. **Das, H.J.,** Mahanta, P., Saikia, R., 2020. Characterization of sand particles in a bubbling fluidized bed with diverging riser, ***International Communications in Heat and Mass Transfer*, *(Elsevier)***, 119 p. 104953, https://doi.org/10.1016/j.icheatmasstransfer.2020.104953.
3. **Das, H.J.,** Saikia, R., Mahanta, P., 2020. Effects of spiral and cone angles on drying characteristics and energy consumption of fluidized bed paddy dryer, ***Drying Technology*, *(Taylor & Francis)***, p. 1-12, https://doi.org/10.1080/07373937.2020.1832512.
4. **Das, H.J.,** Mahanta, P., Saikia, R., Tamuly, P., 2021. Thermodynamic analysis in bubbling fluidized bed paddy dryers with spiral and cone angles, ***Journal of Thermal Science and Engineering Applications*, *(ASME)***, 13 (6): 061019-1, https://doi.org/10.1115/1.4050568.
5. **Das, H.J.,** Mahanta, P., Saikia, R., 2022. Flow dynamics and thermal characteristics of air-sand mixture in a conical bubbling fluidized bed riser, ***International Communications in Heat and Mass Transfer*, *(Elsevier)*, *under review***.
6. **Das, H.J.,** Mahanta, P., Saikia, R., 2022. Influence of cone angle on flow dynamics and heat transfer in bubbling fluidized beds, ***Journal of Heat Transfer (ASME), under review.***

B. International / National Conferences:

1. **Das, H.J.,** Mahanta, P., 2018. Effect of superficial velocity on hydrodynamic behaviour in conical fluidized bed riser, 7th International & 45th National Conference on Fluid Mechanics & Fluid Power (FMFP 2018), 10-12 December 2018, IIT Bombay.
2. **Das, H.J.,** Aamir, M.S., Mahanta, P., 2019. Effect of Spiral on Drying Characteristics in Conical Bubbling Fluidized Bed Paddy Dryer. In: Riffat, Su, Ismail, Ahmad. ed.,

Sustainable Energy Towards the New Revolution: Proceedings of the 18th International Conference on Sustainable Energy Technologies, 20-22 August 2019, Kuala Lumpur, Malaysia. University of Nottingham: Buildings, Energy & Environment Research Group. Volume 2, pp 307-316, ISBN-13: 9780853583318. Available from: nottingham-repository.worktribe.com/.

3. **Das, H.J.,** Saikia, R., Mahanta, P., 2019. Effect of the Specularity Coefficient on Hydrodynamic Behaviour and Heat Transfer Characteristics Across a Variable Cross-Sectional Riser of Bubbling Fluidized Bed, Proceedings of the 25th National and 3rd International ISHMT-ASTFE Heat and Mass Transfer Conference (IHMTC-2019), December 28-31, 2019, IIT Roorkee, Roorkee, India.
4. **Das, H.J.,** Saikia, R., Mahanta, P., 2021. A Comparative Study on the Hydrodynamic and Heat Transfer Behaviour of Conical Fluidized Bed with that of a Columnar Pressurized Circulating Fluidized Bed. In: Pandey K., Misra R., Patowari P., Dixit U. (eds), Recent Advances in Mechanical Engineering. Lecture Notes in Mechanical Engineering. Springer, Singapore. https://doi.org/10.1007/978-981-15-7711-6_53.
5. Singh, P., Kalita, P., Mahanta, P., **Das, H.J.,** 2021. Study of Granular Food Material Drying in a Pilot-Scale Rotating Fluidized Bed with Static Geometry Dryer. In: Pandey K., Misra R., Patowari P., Dixit U. (eds), Recent Advances in Mechanical Engineering. Lecture Notes in Mechanical Engineering. Springer, Singapore. https://doi.org/10.1007/978-981-15-7711-6_55.
6. Tamuly P., **Das H.J.,** Mahanta P., 2021. Experimental Investigation of Drying Characteristics of Tea in a Conical Bubbling Fluidized Bed Dryer. In: Pandey K., Misra R., Patowari P., Dixit U. (eds), Recent Advances in Mechanical Engineering. Lecture Notes in Mechanical Engineering. Springer, Singapore. https://doi.org/10.1007/978-981-15-7711-6_58.
7. **Das, H.J.,** Mahapatro, A., Mahanta, P., Saikia. R., 2020. Comparison of hydrodynamic behaviour of conical fluidized bed risers with a columnar fluidized bed riser. In: S. K. Acharya and D. P. Mishra (eds.), Current Advances in Mechanical Engineering, Lecture Notes in Mechanical Engineering. Springer, Singapore. https://doi.org/10.1007/978-981-33-4795-3_51.

C. Book Chapter:

1. **Das, H.J.,** Mahanta, P., Saikia, R., 2020. A Future Trend on Research Scope of Numerical Simulation on Conical Fluidized Bed, Handbook of Research on Developments and Trends in Industrial and Materials Engineering, ***IGI Global***, p. 401–437, https://doi.org/10.4018/978-1-7998-1831-1.ch017.

D. Review Paper

1. **Das, H.J.,** Mahanta, P., Saikia, R., 2022. Fluid dynamics in conical fluidized beds: A systematic review of the models, ***European Journal of Mechanics B/Fluids***, ***(Elsevier)***, ***(Under Review).***

Outside the thesis:

E. Journals:

1. Saikia, R., Mahanta, P., **Das, H.J.,** 2020. Heat recovery from the Downcomer of a pressurized circulating fluidized bed during various transient conditions, ***Heat and Mass Transfer***, ***(Springer)***, 57, p. 53–61, https://doi.org/10.1007/s00231-020-02945-3.
2. Saikia, R., Mahanta, P., **Das, H.J.,** 2021. Transient hydrodynamics and heat transfer behaviour in a pressurized circulating fluidized bed during abrupt changes in operating pressure, ***International Communications in Heat and Mass Transfer***, ***(Elsevier)***, 125(6), p. 105296, https://doi.org/10.1016/j.icheatmasstransfer.2021.105296.
3. Saikia, R., Mahanta, P., **Das, H.J.,** 2022. Effect of fluctuating load on the hydrodynamics and heat transfer behaviour of a pressurized circulating fluidized bed, ***(Paper to be communicated).***